

ABSTRACT

Title of Dissertation: FAILURE MECHANISMS OF ULTRA HIGH MOLAR MASS POLYETHYLENE SINGLE FIBERS AT EXTREME TEMPERATURES AND STRAIN-RATES

Donald Robert Jenket II, Doctor of Philosophy, 2017

Dissertation directed by: Professor Mohamad Al-Sheikhly, Department of Materials Science and Engineering

The effects of temperature and strain-rate on the mechanical properties of Ultra High Molar Mass Polyethylene (UHMMPE) single fibers was investigated at eleven temperatures from room temperature (20 °C) to the orthorhombic-hexagonal phase transition (148 °C) and at six strain-rates from quasi-static (10^{-3} s^{-1}) to dynamic (10^3 s^{-1}). Dimensional analysis of ballistic limit tests using has shown an underperformance of materials comprised of UHMMPE fibers. A possible explanation is the relatively low melting temperature of UHMMPE fibers (~150 °C) in comparison to other fiber materials, such as poly-aramids (~450 °C).

The mechanical properties of UHMMPE single fibers were investigated through a series of 437 tensile tests at 66 temperature-strain-rate combinations. Changes in stress-strain curve shapes were observed with respect to temperature and strain-rate. The transition of stress-curve shape with increasing temperature was observed to be pseudo-brittle, plateauing, necking, and non-failure and transitions between these phases were observed within a strain-rate dependent temperature

range. For low and intermediate strain rates, a temperature and strain-rate equivalence is observed: a decadal increase of strain-rate is mechanically equivalent to a ~ 20 °C decrease in temperature. Strain to failure for dynamic strain rates was invariant over the temperature range of this study. Strength and modulus properties were observed to decrease with increasing temperature and increase with increasing strain-rate. An orthorhombic to hexagonal phase transition occurs between 145 °C and 148 °C and a sudden decrease in strength and moduli was observed.

The change in dominant stress-relieving mechanism is proposed. Chain slippage is dominant for the majority of conditions in this study except where scission and straightening are the dominant mechanism. At high temperatures for constrained fibers in the hexagonal phase, chain slippage occurs more frequently due to the trans to gauche conformation. Chain scission is only dominant moments before fiber failure and near the failure surface. Chain straightening is dominant at low strain (0 % to 0.5 %) and at temperatures greater than or equal to the necking temperatures for the quasi-static and intermediate strain-rates and at all temperatures for the dynamic strain-rates.

FAILURE MECHANISMS OF
ULTRA HIGH MOLAR MASS POLYETHYLENE SINGLE FIBERS
AT EXTREME TEMPERATURES AND STRAIN-RATES

by

Donald Robert Jenket II

Dissertation submitted to the Faculty of the Graduate School of the
University of Maryland, College Park, in partial fulfillment
of the requirements for the degree of
Doctor of Philosophy
2017

Advisory Committee:

Professor Mohamad Al-Sheikhly, Chair
Professor Manfred Wuttig
Professor Gary Pertmer
Assistant Professor Yifei Mo
Dr. Amanda L. Forster

© Copyright by
Donald Robert Jenket II
2017

Acknowledgements

I would like to thank **Mohamad Al-Sheikhly** for your guidance and patience throughout our journey together. Thank you for your words of encouragement and candid discussions about science, work, and life.

NIST:

Amanda Forster for her guidance and discussions on fiber properties and FTIR.

Nick Paulter for his discussions on experimental design.

Kirk Rice for his discussions about armor materials and policy.

Aaron Forster for his help in the development of the NIST f-SHTB.

Ajay Krishnamurthy for his help with the SEM imaging.

Julie Bitter for her help with the Micro-FTIR.

Kai-Li Kang for her help with the DSC.

The STG group for their support and help: **Jack Leigh, Mike Riley, John Jendurski,**

Dwight Barry, Nathaniel Walters

Richard Allen for his help with the Bose 3100 testing laboratory.

Rusty Hettenhouser for his help in the design of the fiber heater.

Jay Brandenburg for his help in the design of the fiber grips.

ARL:

Tusit Weerasooriya and **C. Allan Gunnarson** for their collaboration with the f-SHTB experiments.

Jan Andzelm for his discussions about PE simulations.

Eric Wetzel for his help in introducing me to the field of ballistic fibers.

UMD:

Dan Taylor for his help with the WAXS experiments.

Zois Tsnias for his useful discussions regarding polyethylene.

Travis Dietz for his help with ChemDraw.

This work was made possible by the Pathways Internship Program at the National Institute of Standards and Technology. Thank you to **Mohamad, Amanda, and Nick** for providing me with this opportunity.

Lastly, I sincerely thank my wife, **Caitlin Murphy**, for supporting me throughout my entire graduate experience and my daughter, **Jackie**, for always giving me a reason to smile.

Table of Contents

Dedication	Error! Bookmark not defined.
Acknowledgements	ii
Table of Contents	iv
List of Tables	vii
List of Figures	ix
Chapter 1: Introduction to Ultra High Molar Mass Polyethylene Fibers.....	1
1.1 Introduction to Ballistic Resistant Soft Body Armor.....	1
1.2 Soft Body Armor Ballistic Testing: V ₅₀ Tests	2
1.3 Dimensional Analysis of Experimental V ₅₀ Test Data	4
1.4 UHMMPE Fibers: Phases and Morphology	6
1.5 UHMMPE Fibers: Viscoelasticity	18
1.6 UHMMPE Fibers: Mechanical Properties	24
1.6.1 Mechanical Property Terms and Definitions	25
1.6.2 Factors Affecting the Mechanical Properties of UHMMPE Fibers	28
1.6.3 Cunniff Parameters Revisited	31
1.6.4 Previous studies of Temperature and Strain-rate Effects.....	32
Chapter 2: Experimental Procedure	35
2.1 Fiber Sample Preparation.....	35
2.2 Diameter Measurements	41
2.3 Single Fiber Heater	42
2.3 Fiber Grips	46
2.5 Tensile Experiments.....	48
2.5.1 Low and Intermediate Strain-Rates	49
2.5.2 High Strain-Rates.....	53
2.6 X-ray Scattering	59
2.6.1 Wide Angle X-ray Scattering.....	59
2.6.2 Heated Wide Angle X-ray Scattering	60
2.7 Fourier Transform Infrared Spectroscopy	62
2.8 Scanning Electron Microscopy	62
Chapter 3: Results	63
3.1 Characterization	63
3.1.1 Wide Angle X-ray Scattering.....	63
3.1.2 Fourier Transform Infrared Spectroscopy	68
3.2 Tensile Tests	69
3.2.1 Categorization and Number of Fibers Tests	69
3.2.2 Diameter Distribution	72
3.2.3 Grip Performance: Percentage of Tensile Failures in the Gage Length of the Fiber	73
3.2.4 Observed Shape Changes in Stress-Strain Curves.....	76
3.2.5 Strain to Failure.....	93
3.2.6 Failure Strength.....	98
3.2.7 Strain to UTS	104

3.2.8 Ultimate Tensile Strength	108
3.2.9 Effects of Fiber Diameter on Failure Strength.....	112
3.2.10 SEM Imaging.....	122
3.2.11 Young’s Modulus.....	130
3.2.12 Failure Toughness	136
3.2.13 Cunniff Parameters	141
4 Discussion	150
4.1 Chapter Overview	150
4.2 Characterization	151
4.2.1 Morphological Characterization	151
4.2.2 Chemical Characterization.....	154
4.2.3 Fiber Diameter Distribution.....	161
4.3 Changes in Strength and Young’s Modulus	162
4.3.1 Failure Strength.....	166
4.3.2 Ultimate Tensile Strength	171
4.3.3 Young’s Modulus.....	172
4.4 Grip Performance.....	175
4.5 Strain Behavior	178
4.5.1 Stress-strain Curve Shapes and the Chain Slippage Mechanism.....	178
4.5.2 Strain to UTS Mechanisms at High Temperature.....	186
4.6 Theoretical Ballistic Performance.....	188
4.6.1 Failure Toughness	188
4.6.2 Cunniff Parameters	189
4.6.3 Ballistic Estimates for the Thermal and Mechanical Energy Dissipation	191
4.7 Chapter Summary	193
5 Conclusions and Future Work	196
5.1 Contributions to Science.....	196
5.1.1 Elucidation of the Change in Dominant Mechanism that Determine the Mechanical Properties of Highly Oriented UHMMPE Fibers.....	196
5.1.2 Improved the Prediction of the Ballistic Response of UHMMPE Fibers	201
5.1.3 Proposed a New Method for Calculating Average Fiber Strength	201
5.2 Future Work.....	202
5.2.1 Dynamic Strain-Rates	202
5.2.2 Quasi-Static and Intermediate Strain-Rates.....	203
5.2.3 Structure-Property Relationships from Additional UHMMPE Fiber Systems	203
Appendices.....	205
A-1 Average Uncorrected Strain to Failure Plots	205
A-2 Average Uncorrected Strain to Failure Values.....	206
A-3 Individual Corrected Strain to Failure Plots	207
A-4 Individual Failure Strength Plots	208
A-5 Average Uncorrected Strain to UTS Plots.....	210
A-6 Individual Corrected Strain to UTS Plots.....	211
A-7 Individual UTS Plots	212
A-8 Individual Young’s Modulus Plots.....	214
A-9 Individual Failure Toughness Plots	215

Bibliography 216

List of Tables

- 1-1 Cunniff parameters for various polymer materials
- 2-1 Key instrument test parameters for the Bose Electroforce 3100
- 2-2 Student t tests for heater standoff force calibrations at 500 s^{-1} strain-rate
- 2-3 Student t tests for heater standoff force calibrations at 10^3 s^{-1} strain-rate
- 3-1 Phase composition of 5 yarn samples with averages and standard deviations
- 3-2 Number of fiber tests per temperature-strain-rate combination including grip failures and non-failures
- 3-3 Number of grip interface failures and success rates
- 3-4 Number of grip interface failures and success rates for the adjusted $20 \text{ }^\circ\text{C}$ data and comparison to Sanborn et. al.
- 3-5 Average strain to failure values and standard deviations for all temperature-strain-rate combinations
- 3-6 Average strain to failure values for the $20 \text{ }^\circ\text{C}$ data and comparison to Sanborn et. al.
- 3-7 Average failure strength values and standard deviations for all temperature-strain-rate combinations for calculations using the average fiber diameter
- 3-8 Linear fit parameters for diameter and failure strength for the 6 strain-rates
- 3-9 Comparison of the experimental average failure strength values and the diameter-strength distribution calculated average values

- 3-10 Linear fit parameters of the slopes of the diameter-strength plots and log of strain-rate
- 3-11 Average diameters for fibers imaged by SEM including diameters for pre-tensile test, zone 1, zone 2, and zone 3
- 3-12 Statistics for the nanofibril dimensions including diameter, length, and spacing
- 3-13 Linear fit parameters for the change in Young's modulus with respect to temperature
- 3-14 Linear fits parameters for the change in the slope and intercepts with respect to strain-rate of the linear fits for the change in Young's modulus with respect to temperature
- 3-15 Linear fit parameters for the change in failure toughness with respect to temperature
- 3-16 Linear fit parameters for the change in Cunniff parameters with respect to temperature
- 3-17 Linear fit parameters for the weighted best fits for the change in Cunniff parameters with respect to temperature
- 4-1 Temperature ranges for the 4 types of stress-strain curves for the quasi-static and intermediate strain-rates

List of Figures

- 1-1 Image of a UHMMPE vest, layers of protective laminate and an individual laminate
- 1-2 Example of a V_{50} velocity probability curve and possible ballistic threat
- 1-3 Fitted Cunniff plot of UHMMPE V_{50} data using 672 m/s
- 1-4 Monomers and adjacent chain interactions for PE and PPTA
- 1-5 Unit cells for the three crystalline phases of PE
- 1-6 Images of lamellar orthorhombic, extended orthorhombic, and oriented amorphous phases
- 1-7 Example plots for creep compliance and stress relaxation tests for a perfectly amorphous polymer material
- 1-8 Types of stress-strain curves for polymer materials
- 1-9 Example plots of pseudo-brittle and necking stress-strain curves
- 1-10 Schematic of a fiber-Split Hopkinson Tension Bar
- 2-1 Spool of Dyneema® SK76 yarn showing the unclean edges and clean middle
- 2-2 Tape clasped yarn being cut by ceramic scissors
- 2-3 Tape-clasped yarn taped to the self-healing mat a single fiber taped on the opposite end
- 2-4 Method for creating a tape-capstan to hold single fiber ends
- 2-5 Autodesk Inventor software rendering of the fiber template showing dimensions
- 2-6 Glue-curing phase of the first 324 fiber samples
- 2-7 Single fiber sample in template

- 2-8 Fiber diameter measurement method
- 2-9 Single fiber heater in the open position and mounted on the supporting stand
- 2-10 Single fiber heater assembly
- 2-11 Single fiber heater thermal calibration using a wire thermocouple mounted on a translation stage
- 2-12 CAD rendering of the custom fiber grips
- 2-13 Image of the Bose Electroforce 3100 gripping area and setup
- 2-14 Loading sequence of a single fiber for tensile testing at elevated temperatures
- 2-15 The Bose Electroforce 3100 area and experimental setup
- 2-16 Optical displacement measurement system on the fiber-Split Hopkinson Tension Bar
- 2-17 Optical displacement calibration setup on the fiber-Split Hopkinson Tension Bar and a sample of the linear fitting
- 2-18 Whisker plots for the force correction for the heater standoff showing comparison of the average fiber diameters, starting force, and peak force for the 500 s^{-1} strain-rate
- 2-19 Whisker plots for the force correction for the heater standoff showing comparison of the average fiber diameters, starting force, and peak force for the 10^3 s^{-1} strain-rate
- 2-20 Bragg-Brentano geometry for Wide Angle X-Ray Scattering experiments

- 2-21 Image of the custom designed fiber constrained for heated Wide Angle X-Ray Scattering experiments
- 3-1 Wide Angle X-Ray Scattering patterns for 5 yarns samples and an example of the fits for each crystalline phase
- 3-2 Heated Wide Angle X-Ray Scattering patterns for a constrained yarn from 30 °C to the melting temperature
- 3-3 Attenuated Total Reflection Fourier Transform Infrared spectroscopy spectra for 5 yarns samples
- 3-4 Histogram of 2164 fiber diameter measurements
- 3-5 Stress-strain curve shape evolution with increasing temperature for the 10^{-3} s^{-1} strain-rate
- 3-6 Stress-strain curve shape evolution with increasing temperature for the 10^{-2} s^{-1} strain-rate
- 3-7 Stress-strain curve shape evolution with increasing temperature for the 10^{-1} s^{-1} strain-rate
- 3-8 Stress-strain curve shape evolution with increasing temperature for the 10^0 s^{-1} strain-rate
- 3-9 Stress-strain curve shape evolution with increasing temperature for the 500 s^{-1} strain-rate
- 3-10 Stress-strain curve shape evolution with increasing temperature for the 10^3 s^{-1} strain-rate
- 3-11 Average strain to failure values for all temperature-strain-rate combinations

- 3-12 Average failure strength values for all temperature-strain-rate combinations using the average fiber diameter and the minimum fiber diameter
- 3-13 Difference in failure strength standard deviations between the average fiber method and the minimum fiber method for all temperature-strain-rate combinations
- 3-14 Average strain to UTS values for all temperature-strain-rate combinations
- 3-15 Average UTS values for all temperature-strain-rate combinations using the average fiber diameter and the minimum fiber diameter
- 3-16 Difference in UTS standard deviations between the average fiber method and the minimum fiber method for all temperature-strain-rate combinations
- 3-17 Diameter vs. failure strength plots for 20 °C for all 6 strain-rates with linear fits
- 3-18 Calculated fiber failure strength distributions for all 6 strain-rates
- 3-19 Fitted slopes of diameter vs. failure strength plotted with log of strain-rate with linear fits with and without the 10^0 s^{-1} strain-rate point
- 3-20 SEM images of the fiber failure surfaces at 20 °C for the 10^{-3} s^{-1} , 10^0 s^{-1} , and 10^3 s^{-1} strain-rates
- 3-21 SEM images of the fiber failure surfaces at the respective plateauing temperatures for the 10^{-3} s^{-1} and 10^0 s^{-1} strain-rates
- 3-22 SEM images of the fiber failure surfaces at the respective necking temperatures for the 10^{-3} s^{-1} and 10^0 s^{-1} strain-rates

- 3-23 SEM images of the fiber failure surfaces at high temperatures for the 10^{-3} s^{-1} , 10^0 s^{-1} , and 10^3 s^{-1} strain-rates
- 3-24 SEM images of the nanofibril bridging structure within fiber cracks at various temperature and strain-rates
- 3-25 Average Young's modulus values for all temperature-strain-rate combinations and linear fits with respect to temperature
- 3-26 Slope of linear fitted Young's modulus with respect to temperature vs. log of strain-rate
- 3-27 Average failure toughness values for all temperature-strain-rate combinations and linear fits with respect to temperature
- 3-28 Average strain-wave speed values for all temperature-strain-rate combinations
- 3-29 Average linear and actual specific toughness values for all temperature-strain-rate combinations
- 3-30 Average linear and actual Cunniff parameter values for all temperature-strain-rate combinations and linear fits with respect to temperature
- 4-1 Micro-Fourier Transform Infrared spectroscopy spectra for a fiber failure surface at $20 \text{ }^\circ\text{C}$ and 10^3 s^{-1} strain-rate
- 4-2 Both differences in failure strength and UTS standard deviations between the average fiber method and the minimum fiber method for all temperature-strain-rate combinations

4-3 Comparison of engineering stress-strain curve to a calculated true stress-strain curve

4-4 Temperature ranges for the 4 types of stress-strain curves

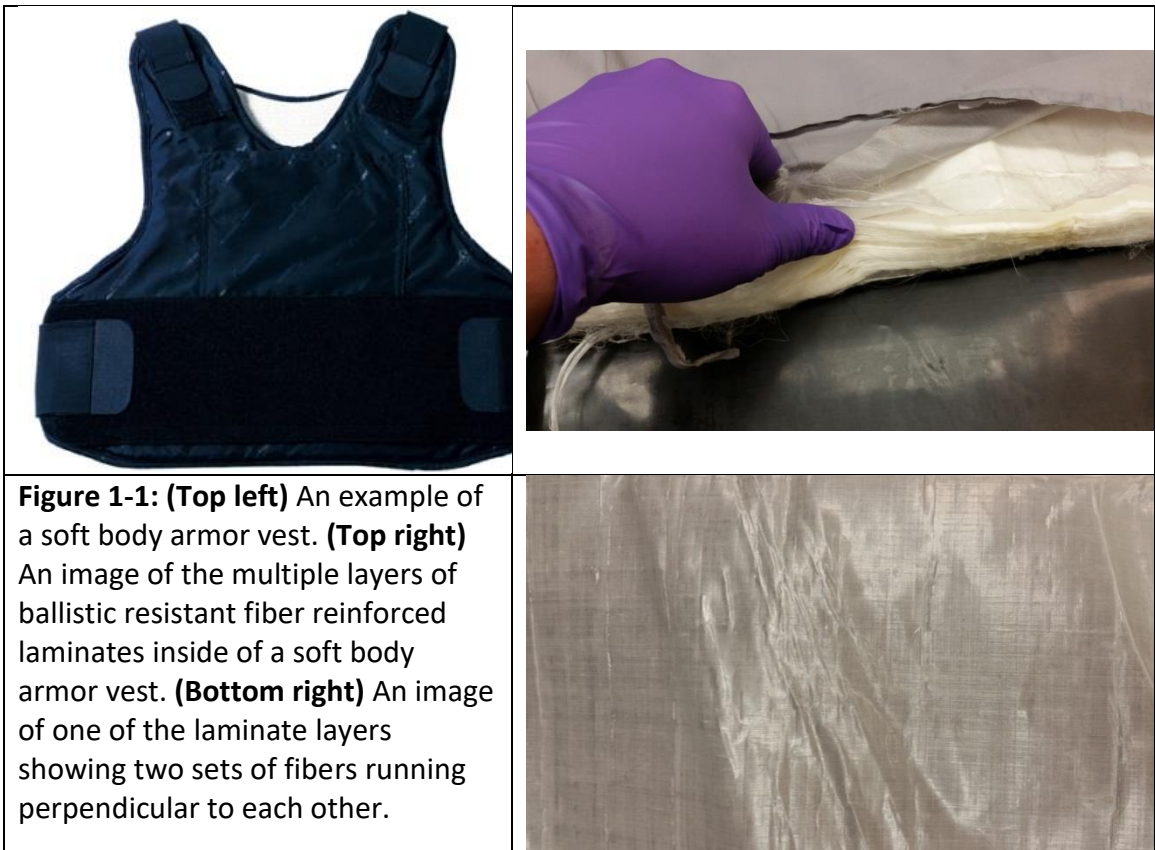
4-5 Plot of the inverse starting temperature for the key temperature regions and the natural log of strain-rate

4-6 Average strain to UTS values for 148 °C and all 6 strain-rates

Chapter 1: Introduction to Ultra High Molar Mass Polyethylene Fibers

1.1 Introduction to Ballistic Resistant Soft Body Armor

Body armor is used by law enforcement and military personnel to protect against fatal injuries. Depending on the anticipated threat, body armor may be comprised of two different types of materials, hard inserts and soft body armor. Soft body armor is engineered to protect the body from handgun and shrapnel threats and covers as much of the vital body areas as possible. The vital areas are primarily located in the torso and soft body armor is usually made in the form of a protective vest as shown in in Figure 1-1 (Top left). Hard inserts, usually comprised of ceramics or composites, can be placed in



pockets of the vest to offer additional protection. In contrast to the hard inserts, soft body armor is made of materials that are flexible and light, as to not hinder the movement of the wearer. Therefore, the materials are usually layers of a woven textiles or fiber reinforced laminates. An example of the multiple layers within a vest and the fibers within a laminate are shown in Figure 1-1 (Top right) and (Bottom right), respectively. The tensile strength of the fibers used is a critical material property governing the protection offered by the soft body armor. Polymer fibers are commonly used due to their flexibility and high tensile strength-to-weight ratio. During a ballistic impact, the polymer fibers are subjected to high temperatures and high strain-rates. Understanding how these materials behave under these conditions is crucial for designing and fabricating ballistic protective apparel.

1.2 Soft Body Armor Ballistic Testing: V_{50} Tests

Ballistic limit, or V_{50} , tests are one method used to characterize and quantify the effectiveness of ballistic resistant materials [1]. In this procedure, an article is first defined to be tested. For soft body armor, it is usually one or several layers of woven textile or fiber reinforced laminate with dimensions large enough to avoid edge effects. A projectile is selected that is representative of the threats encountered in the environment in which the test article is intended to be used. The projectile is then fired at the test article using defined conditions. The velocity of the projectile is varied until a speed is found where the projectile penetrates the test article 50 % of the time. The results are recorded in a binary manner, a 0 for a successful defeat of the projectile or a 1 for the projectile penetrating the article. These tests are repeated and a penetration probability is created as a function of projectile velocity. A logit function is commonly used for

convenience to describe the penetration probability, $p(v)$, as a function of projectile speed, v , where β_0 is a constant and β_1 is the velocity coefficient [2]

$$\text{Logit: } p(v) = \frac{e^{\beta_0 + \beta_1 v}}{1 + e^{\beta_0 + \beta_1 v}} \quad (\text{Eqn 1-1})$$

The logit function has the steepest slope at the 50 % probability and is therefore the easiest location of the penetration probability plot to experimentally determine. An example of a logit plots is shown in red in Figure 1-2. Ballistic resistant apparel is designed so that the V_{50} of an article is below the V_{50} . An example of this is also shown in Figure 1-2 where the velocity probability of a projectile centered at 1350 ft/s is shown in blue and is much lower than the 1563 ft/s V_{50} of the test article. Due to the high

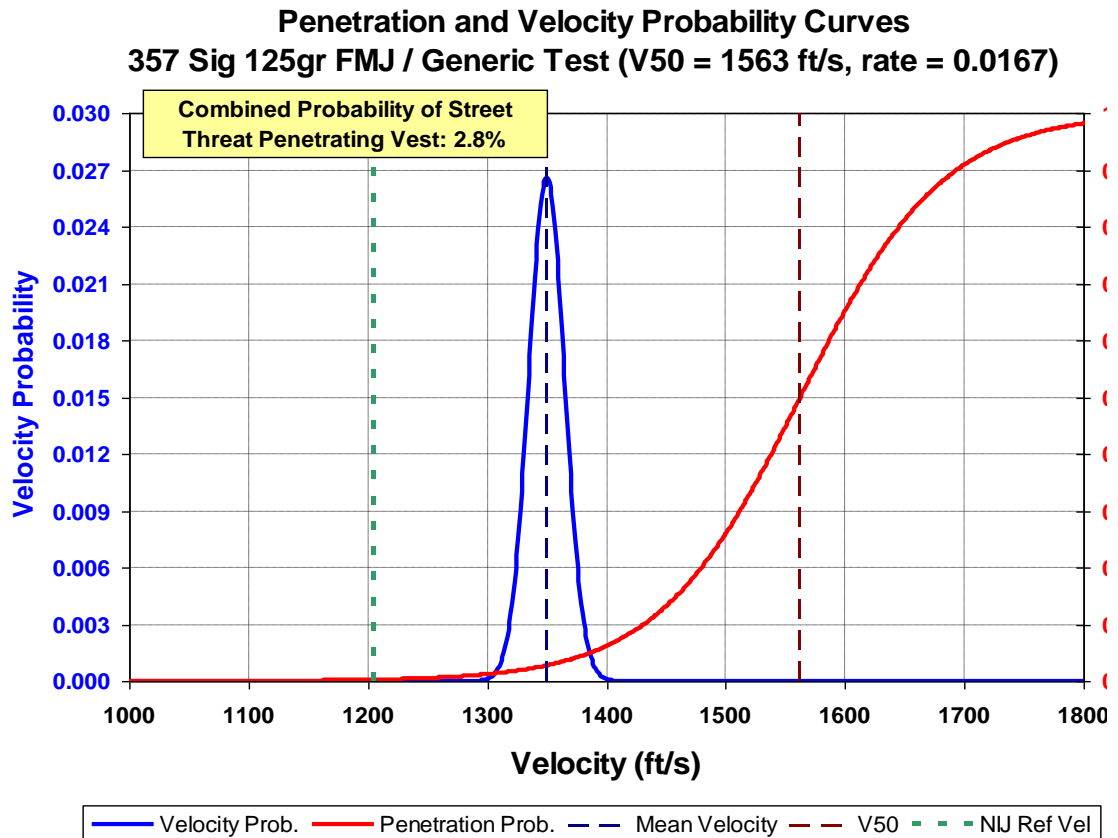


Figure 1-2: An example of the logit function for a V_{50} test shown in red showing a V_{50} of 1563 ft/s and the projectile threat velocity probability in blue.

number of tests required to experimentally determine a penetration probability, these tests are costly and time consuming. Methods to model test articles with fewer or no tests are constantly sought.

1.3 Dimensional Analysis of Experimental V_{50} Test Data

To predict experimental V_{50} values of woven textiles from material properties, Cunniff used dimensional analysis to reduce the complexity of the mechanical response [3]. In his model, he used four axial material properties of the fibers; strain to failure (elongation to failure), failure strength, Young's modulus, and density. These properties were readily available from the manufacturers and required no additional fiber testing or characterization. From these properties, the one-dimensional model calculated the strain-wave speed and the specific toughness, shown in Equations 1-2 and 1-3, respectively. This model has also been derived theoretically and can be used as an initial predictor for two-dimensional materials [4]. The strain-wave speed approximates how quickly mechanical energy can travel away from the point of ballistic impact. This specific toughness is an approximate measure of the mechanical energy per mass a fiber can absorb before mechanically failing. The Cunniff parameter, $U^{*1/3}$, is described as the is the cube root of the product of the strain-wave speed and specific toughness:

$$\text{Strain-wave speed [m/s]: } \sqrt{\frac{E}{\rho}} \quad (\text{Eqn 1-2})$$

$$\text{Specific Toughness [J/kg]: } \frac{\epsilon_f \sigma_f}{2\rho} \quad (\text{Eqn 1-3})$$

$$\text{Cunniff Parameter [m/s]: } U^{*\frac{1}{3}} [m/s] = \left(\sqrt{\frac{E}{\rho}} \frac{\epsilon_f \sigma_f}{2\rho} \right)^{\frac{1}{3}} \quad (\text{Eqn 1-4})$$

where U^* is the product of the strain wave speed and specific toughness, E is the fiber Young's modulus, ϵ_f is the fiber strain to failure, σ_f is the fiber failure strength, and ρ is the fiber density. The Cunniff parameter has units of m/s and was compared to ballistic V_{50} tests for various woven ballistic fabrics impacted with a steel or tungsten fragment-simulating projectile (FSP). Table 1-1 shows the various materials Cunniff tested and their calculated $U^{*1/3}$. The model showed good agreement for the all of the materials

Fiber	Strength (σ) [Gpa: kg/m*s ²]	Failure Strain (ϵ) [%]	Modulus (E) [Gpa: kg/m*s ²]	Density (ρ) [kg/m ³]	Specific Strength ($\sigma\epsilon/2\rho$) [m ² /s ²]	Tensile Wave Velocity ($(E/\rho)^{1/2}$) [m/s]	(U^*) ^{1/3} [m/s]
PBO	5.20	3.10	169	1560	51667	10408	813
Spectra 1000	2.57	3.50	120	970	46366	11123	802
600 denier Kevlar KM2	3.40	3.55	82.6	1440	41910	7574	682
850 denier Kevlar KM2	3.34	3.80	73.7	1440	44069	7154	681
840 denier Kevlar 129	3.24	3.25	99.1	1440	36563	8296	672
1500 denier Kevlar 29	2.90	3.38	74.4	1440	34035	7188	625
200 denier Kevlar 29	2.97	2.95	91.1	1440	30422	7954	623
1000 denier Kevlar 29	2.87	3.25	78.8	1440	32387	7397	621
1140 denier Kevlar 49	3.04	1.20	120	1440	12667	9129	487
nylon 6,6	0.91	9.62	9.57	1135	38565	2904	482

Table 1-1: Material properties for various polymer fabrics investigated by Cunniff. The column on the right is the calculated $U^{*1/3}$ Cunniff parameters.

listed except the Spectra® 1000, which is fiber comprised of Ultra High Molar Mass Polyethylene (UHMMPE). The calculated $U^{*1/3}$ from the manufacturer material properties was 802 m/s. The calculated $U^{*1/3}$ did not fit the V_{50} data and the adjusted fit is shown in Figure 1-3 using a $U^{*1/3}$ value of 672 m/s. The fitted value is approximately 16 % below the predicted value from the model.

Cunniff postulated that the relative melting temperatures for the Kevlar® and the Spectra® was the reason for the underperformance. The Kevlar® fibers, which are made of poly-paraphenylene terephthalamide (PPTA), have a melting temperature of approximately 450 °C [5] and the UHMMPE fibers at approximately 150 °C [6]. The

reasons for the large difference in melting temperature will be discussed in the next section and will form the foundation for this study.

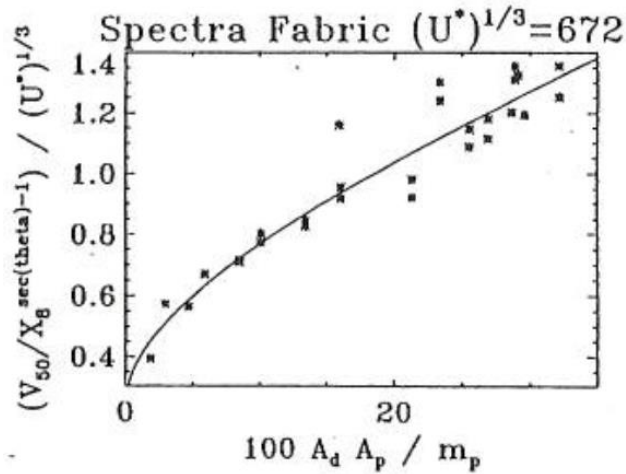


Figure 1-3: Adjusted Cunniff parameter fit for the UHMMPE Spectra 1000 fabric using 672 m/s. The calculated $U^{*1/3}$ from manufacturer material properties was 802 m/s.

1.4 UHMMPE Fibers: Phases and Morphology

To understand the melting temperature difference between the different types of fibers, an understanding of the echelons of protective materials is needed from the vest to the monomer. The protective vests are the highest echelon and are the end-product that an individual would wear. On the outside, there is a shell that holds multiple layers of ballistic-resistant material together and protects the layers from exposure to some environmental conditions such as ultraviolet radiation from the sun. The shell can also include pockets where hard body armor can be inserted for increased protection. The layers are normally woven textiles or fiber reinforced laminates. Woven textiles are comprised of yarns of polymer fibers that have been woven together. Fiber reinforced laminates do not contain yarns and instead have fibers aligned in one direction with some spacing between them to avoid overlap. Fibers are the smallest tangible echelon of the

material and typically have a diameter between 15 μm to 23 μm , depending on the polymer type and processing.

Linear density, with units of g/m, is used to describe and differentiate different types the yarns and fibers. The term denier (den) is used to describe the mass in grams of a yarn that is 9000 m in length. When this term is applied to an individual fiber it is distinguished as denier per filament (DPF). Another term, tex, is used to describe the mass in grams per 1000 m of yarn/fiber. Decitex (dtex) is used to describe the mass in grams per 10000 m of yarn/fiber.

Below the fiber echelon, the polymer fibers exhibit a multi-scale fibrillar structure. These structures have been investigated by Wide Angle X-ray Scattering (WAXS), Small Angle X-ray Scattering (SAXS), Nuclear Magnetic Resonance (NMR) and Atomic Force Microscopy (AFM) showing macrofibrils which are approximately tenths of μm to several μm in diameter [7, 8], and microfibrils which are 10's of nm in diameter. [9-13].

The smallest element is the individual polymer molecule which is comprised of a long chain of covalently bonded monomeric units. The monomers are the building blocks of a polymer and the chemical composition of the monomer influences the polymer material properties. There are two commercial producers of UHMMPE fibers and yarns, Honeywell manufacture Spectra® and DSM manufacture Dyneema®, both of which have similar mechanical properties but different shapes across their cross-sectional area [14].

The difference in monomer chemical composition is the reason why the UHMMPE fibers have a much lower melting temperature than the PPTA fibers. Figure 1-

4 shows the monomer repeat units and a representation of adjacent polymer chains for UHMMPE and PPTA. The carbon atoms are depicted in black, hydrogen atoms in white, nitrogen atoms in blue, and oxygen atoms in red.

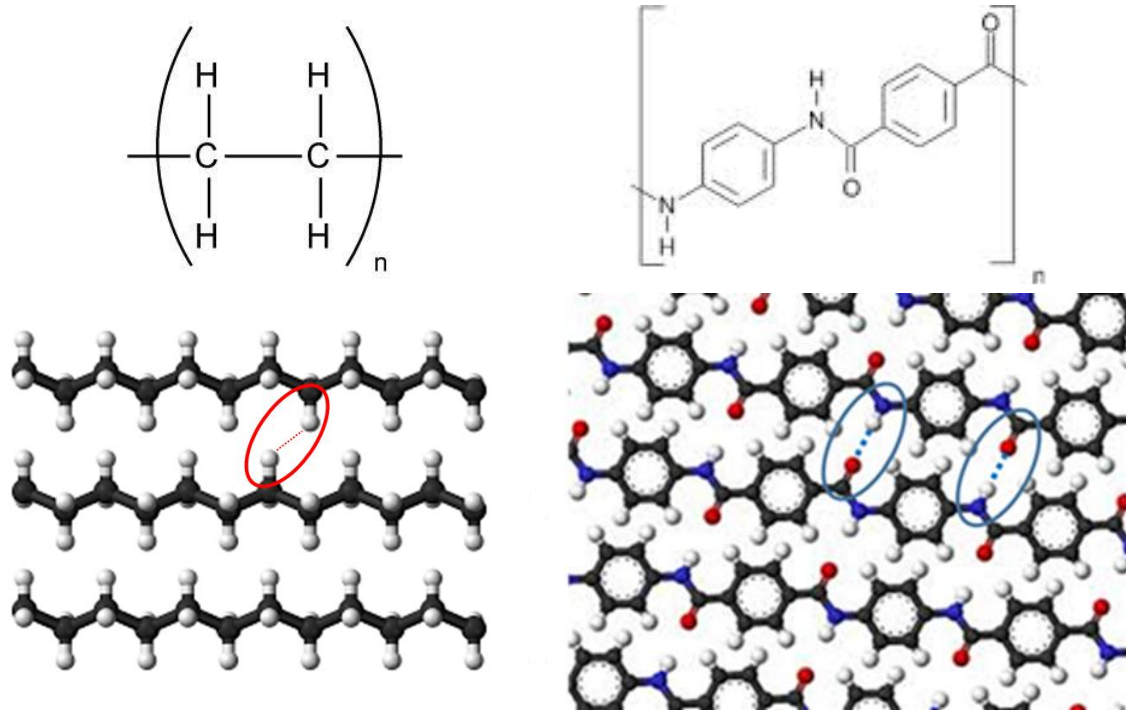


Figure 1-4: (Top left) The monomer repeat unit for UHMMPE. **(Top right)** The monomer repeat unit for PPTA. **(Bottom left)** Adjacent UHMMPE chains showing a Van der Waals forces between chains. **(Bottom right)** Adjacent PPTA chains showing H-bonding between adjacent chains.

The backbone of the UMMWPE chain is comprised of C-C bonds. The UHMMPE chains have no carbon rings and the chains are flexible through rotations of the C-C-C bond angle. The minimum energy for this rotational conformation is called the trans conformation, where the hydrogens are on opposite sides of adjacent carbon atoms in the backbone. There are two other stable states for the rotation and these are called gauche conformations. They are higher energy than the trans conformation and correspond to the decreased distance between hydrogen atoms resulting in repulsive forces between CH₂ units.

There are carbon rings and nitrogen-containing amides in the backbone of the PPTA chain. These create planar covalent bonds in the backbone which increases the stiffness of the chain making them rod-like. The stiffness in the chain reduces the entropy of the chain by not allowing possible degrees of freedom which would be available when the polymer reached its melting temperature. This effect raises the melting temperature for stiff chains because there is not as large of an entropy gain when melted as there is for flexible chains [15].

Another reason for the difference in melting temperature is the secondary bonding between adjacent chains. The UHMWPE chains have two H atoms covalently bonded to each C and the main interactions between chains are weak van der Waals forces, shown in red in Figure 1-4 (Bottom left). The PPTA chains have two carbonyls per repeat unit. These allow hydrogen bonding between the oxygen and hydrogen of adjacent chains, shown in blue in Figure 1-4 (Bottom right). Hydrogen bonding is much stronger than the van der Waals forces and more thermal energy is required to break these bonds to form a melt, increasing the melting temperature [15].

Lastly, the difference in molecular weight of the chains that comprise the two fibers is different. Due to the weak van der Waals forces between chains in the UHMWPE fibers, a high molar mass is required to orient the adjacent chains so they will bind together. UHMWPE molecules have molar masses typically between 3×10^6 g/mol to 6×10^6 g/mol which correspond to a degree of polymerization of approximately 1×10^5 to 2×10^5 . In contrast, the stiff PPTA chains require less of a molar mass to orient because their chemical composition makes them rod-like already and strong H-bonds easily binds adjacent chains. The PPTA molecules form a lyotropic liquid crystalline

solution that self-orient and fibers are fabricated from the self-oriented solution. The change in entropy during melting will be greater for large chains than for smaller chains because there will be more available conformations. This effect also lowers the melting temperature of the UHMMPE fibers compared the PPTA fibers [15]. The difference in chain stiffness, secondary chemical bonding, and molar mass all contribute to the large melting difference between these two polymer fibers.

To discuss the microfibril structure of UHMMPE fibers, the phases of polyethylene must be introduced. Polyethylene can exist in both crystalline and amorphous phases. The chains in the crystalline phases are arranged in periodic arrays with both short and long range order. The amorphous phase has a more random arrangement of the chains with short range order (monomers are still covalently bonded to other monomers with steric limitations) but there is no periodic structure or long range order.

The crystalline phase can exist in three main structures: orthorhombic, monoclinic, and hexagonal [16]. The unit cells and lattice parameters for each phase are shown in Figure 1-5 [16].

The orthorhombic is the lowest energy state at room temperature and pressure and is almost always the predominant crystalline phase in polyethylene. In this phase, a chain folds back on itself to align adjacent segments in the c-direction to form a lamellar orthorhombic structure. The chains are tightly packed and the close proximity creates a low free volume for the system with few degrees of freedom available. The chains are primarily in all trans conformations, except at the folds, and there is a large energy barrier to rotate from trans to gauche.

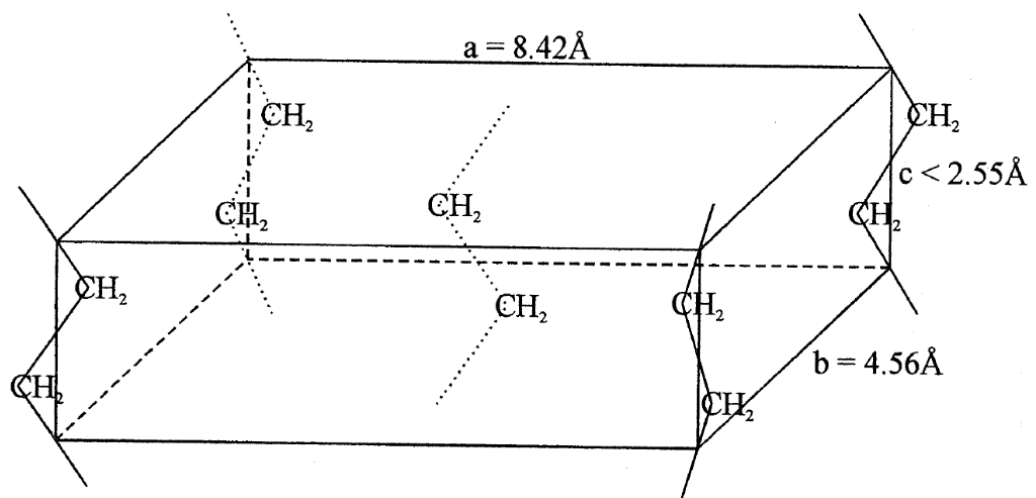
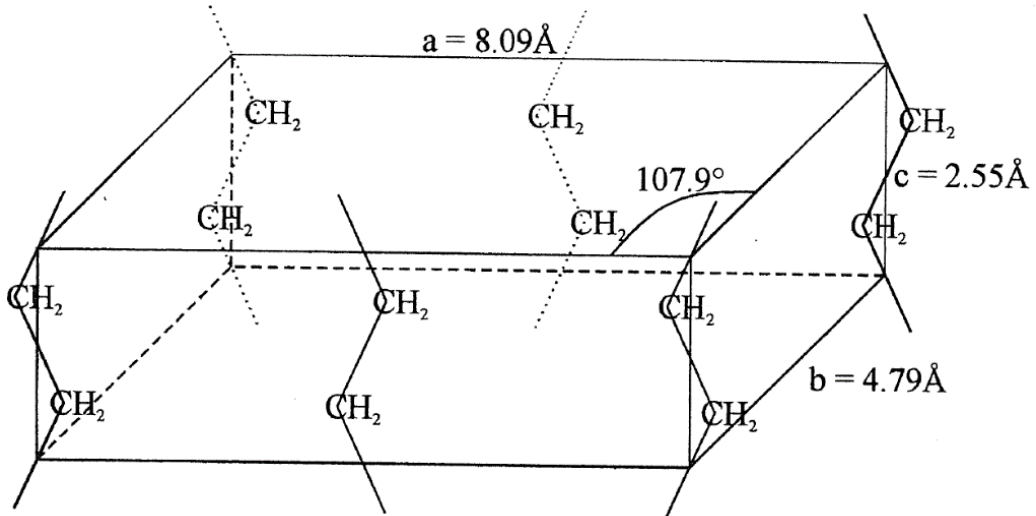
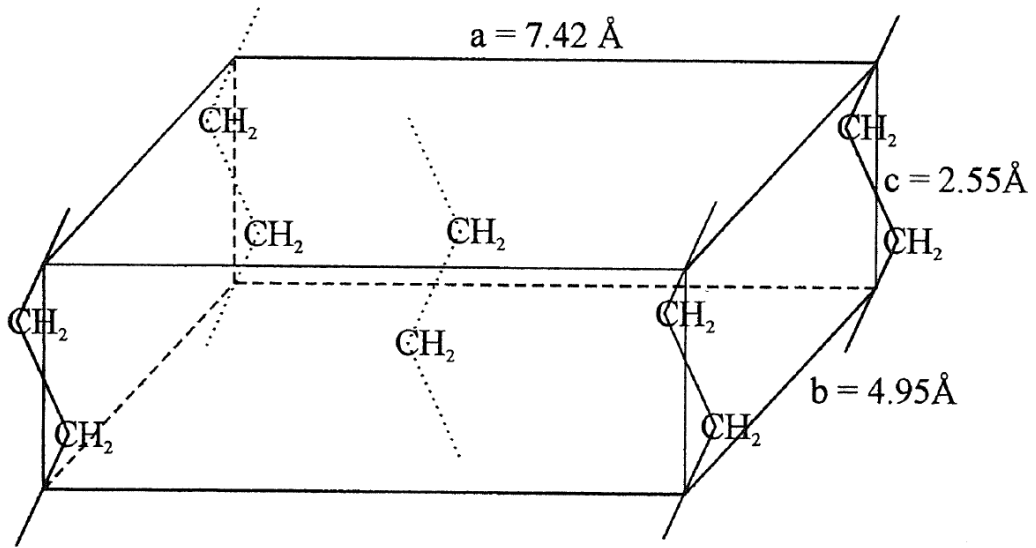


Figure 1-5: The polyethylene crystalline phases and unit cells of orthorhombic (**Top**), monoclinic (**Middle**) and hexagonal (**Bottom**). Images taken from [14].

The monoclinic phase is a shear-induced crystalline phase where the chains have been translated in the a - b plane of the unit cell. The a lattice parameter increases, the b lattice parameter decreases and there is a 107.9° angle between the a and b unit cell vectors. The c unit cell parameter remains the same but there is lower free volume in the monoclinic phase than in the orthorhombic phase. If annealed, the monoclinic phase transitions to the orthorhombic phase [17].

The last crystalline phase is hexagonal which is a mesophase of the orthorhombic phase formed at high temperatures (just below the melting point) and high pressures [18, 19]. The unit cell has an increase in the a lattice parameter, a decrease in the b lattice parameter, and a decrease in the c lattice parameter. There is an increase in the free volume and the trans to gauche rotation has a lower energy barrier from the increased spacing of adjacent chains [20, 21].

The amorphous phase is a region of randomly oriented chains. There is no long-range order and therefore no unit cell. The phase is not homogeneous unless the phase is perfectly random in the orientation of chains. Entanglements between chains normally prevent a perfectly amorphous phase. Due to the heterogeneity, the properties exist over a range of values rather than having specific properties, like those found in crystalline structures. This phase has the largest free volume and the energy barrier for chain conformation changes is the lowest, existing over a range of values.

During solidification, the length of polymer chains cause entanglements to occur that hinder the mobility of part of the chain from reaching the lowest free energy phase (lamellar orthorhombic at room temperature and pressure) and an amorphous region is formed. Entanglements are the reason why single crystal polymers are rare. If a polymer

can crystallize, it is normally described as semicrystalline because the solid is a mixture of crystalline regions where chains were allowed the mobility and time to crystallize and amorphous regions that were hindered before crystallizing.

There are two more phases that are variants of the orthorhombic and amorphous phases. Both of these phases are purposefully created through the specialized processing technique of gel-spinning and drawing. The phases will be described first and the processing technique afterwards.

The first phase is the extended orthorhombic phase. This phase has the same unit cell of the lamellar orthorhombic phase but differs by having adjacent chains aligned in the c -direction to form the crystal. Images of the lamellar and extended orthorhombic phases are shown in Figure 1-6 (Left) and (Middle), respectively. This form of orthorhombic has a higher free energy than the lamellar phase because the chains are almost completely extended and therefore the entropy for each chain is very low. These two phases are still crystallographically identical as are the free volumes and enthalpies. The desired benefit of this phase is that the C-C backbones of the chains are all oriented in the c -direction. Any tensile force in the c -direction is now stressing covalent C-C bonds rather than unraveling the secondary van der Waals bonds in the lamellar structure. This affects the mechanical properties in the c -direction and the strength and stiffness of the extended phase are greatly increased. Therefore, this is the desired phase for high-tensile-strength fibers where the chains are oriented in the fiber direction and the gel-spinning process is designed to maximize the amount of chains that are aligned in the fiber direction.

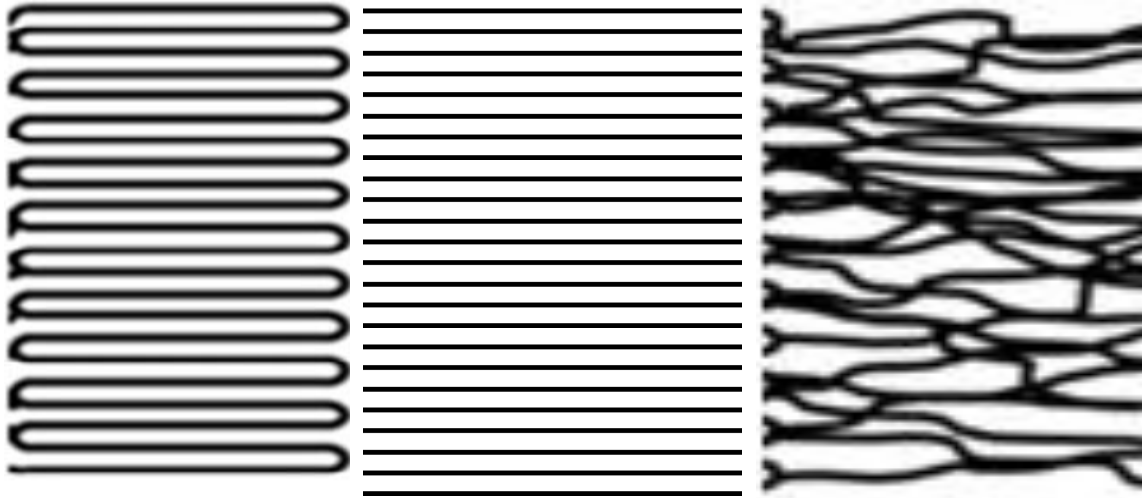


Figure 1-6: (Left): Image of the lamellar orthorhombic phase showing a single chain folding back on itself to create the orthorhombic structure. **(Middle)** An image of the extended orthorhombic phase showing different chains aligned to create the orthorhombic structure. **(Right)** An image of the oriented amorphous phase showing the chains are distributed randomly but there is still a high degree of orientation. Image taken from [22].

The low entropy of this phase creates an interesting thermal effect. As temperature increases, the extended chains are provided more thermal energy to change their conformation. This causes the lower entropy extended phase to transition to the higher entropy lamellar phase. The net effect of this transition in fibers is a retraction force on the fibers that overcomes thermal expansion with increasing temperature [20, 23, 24]. This thermal shrinkage is a concern during the gel spinning and drawing process that occurs at high temperatures and the fibers must be kept under tension (or constrained) to prevent the formation of the undesired lamellar phase.

The second phase is the oriented amorphous phase. This phase still lacks long-range order, but the chains have a higher degree of orientation in direction of the fiber. An image of oriented amorphous phase is shown in Figure 1-6 (Right). The oriented amorphous region still has a higher free volume than the crystalline phases, but the free volume decreases with increasing orientation and the number of chains per volume.

The gel spinning and drawing process orients the chains to create the extended orthorhombic phase from the lamellar orthorhombic phase as shown by XRD and DSC [14, 24-27]. Any residual imperfections in this alignment process, such as entanglements, chain ends, or other impurities comprise the oriented amorphous phase. During the process, UHMPE chains are dissolved in a solvent at high temperature to create a dilute solution where there are few entanglements or locations where the chains cross each other. The solution is then quenched to create a gel that maintains the low number of entanglements. The gel is extruded through spinnerets that align the UHMPE chains in the direction of the extrusion to create fibers. The fibers are heated to remove excess solvent and then mechanically drawn at elevated temperatures to further orient the UHMPE chains, create more extended orthorhombic phase, and to decrease the amount of amorphous phase. In the drawing process, antioxidants or molecular lubricants can be added to enhance disentanglements and maintain the high molecular weight of the chains. As the draw ratio increases, the amount of lamellar orthorhombic amorphous phases decreases while the extended orthorhombic increases and the amorphous phase become oriented. The fiber tensile strength increases with increasing draw ratio [24]. The fibers are then treated to remove the any excess drawing chemicals. The final fibers are approximately 85 % to 90 % extended orthorhombic, 5 % to 10 % oriented amorphous, and a few % monoclinic on the outer sheath of the fibers for highly drawn fibers [11]. These fibers have a draw ratio of approximately 50 to 100 which are much higher than other drawn commercially available fibers. Fourier Transform Infrared spectroscopy of deuterated oriented polyethylene samples has shown as draw ratio increases, the

amorphous regions transitions into crystalline, the lamellar orthorhombic transitions to extended orthorhombic, and crystallites break up at high strains [28].

The fiber morphology is comprised of microfibrils 10's of nm in diameter that have a columnar structure of alternating extended orthorhombic and oriented amorphous with a period of 35 nm to 45 nm [11]. Due to the presence of the oriented amorphous phase and variation in the size of the extended crystallites, the fibers are heterogeneous and the observed mechanical properties fall within a range of values. The semicrystalline morphology of the fibers adds another complexity to the fiber system. Cooperative relationships exist between adjacent crystalline and amorphous regions [29]. For instance, one chain may begin in one crystallite, traverse an oriented amorphous phase, and end in another crystallite. In these chains, the chain ends in the crystalline regions impede movement of chain segment in the amorphous region. The effect of this relationship is that the properties on the crystalline and amorphous regions do not add linearly [29]. For instance, changing the conformation of a chain from mostly trans to trans and gauche conformations is not a simple calculation using one time constant. Both conformations are affected by short range steric interactions including neighboring bonds and frictional forces between the chains, as well as long range steric interactions including entanglements. Similarly, the crystalline and amorphous regions can melt at different temperatures depending on their size, defects, degree of orientation, and these cooperative effects. The melting temperature for UHMMPE fibers ranges from 144 °C to 152 °C [30]. Other mechanical properties such as tensile strength and Young's modulus also fall within a range of values.

Computational studies have been used to understand the molecular motions at the interface of the amorphous and crystalline regions during a tensile stress. A united atom (UA) force field was used in a columnar representative volume element (RVE) comprised of a lamellar orthorhombic crystal on top, an amorphous region in the middle, and another lamellar orthorhombic crystal on bottom showed that failure was caused by a cavitation of melting and crystallization of CH₂ units at the amorphous-crystalline interface [31]. A similar united atom study using extended orthorhombic instead of lamellar orthorhombic showed the same phenomenon [32]. The UA force field does not include specific H atoms and the cavitation results of these two studies is suspected to be a product of incorrect forces between adjacent CH₂ units.

More recent studies of extended orthorhombic crystals using a polymer consistent force field (PCFF) [33] and a Morse modified Adaptive Intermolecular Reactive Empirical Bond Order potential (AIREBO-M) [34, 35] have shown that the energy for chain slippage is smaller than the energy for chain scission and that slippage is the primary failure mechanism of UHMMPE fibers. O'Connor et al. also predicted the slippage mechanism resulting in an upper theoretical strength of a polymer fiber to be near 7 GPa which is close to the strongest fibers DSM has made to date [35].

Lastly, the hexagonal phase was described to form at high temperatures and pressures that is formed from the extended orthorhombic crystals [36] but there is debate about the nature of the phase transition. The debate arises from whether this mesophase is a first order phase transition, a second order phase transition, or not a phase transition and just the continuous thermal expansion of the orthorhombic phase. In support for a first order phase transition, there is a latent heat at the transition temperature [22]. In support

of both arguments for second order phase transition and not a phase transition, the orthorhombic unit cell has been shown to linearly increase in volume as temperature is increased from 40 °C to 120 °C [20]. The same study shows the a lattice parameter increasing, the b lattice parameter decreasing, and the c lattice parameter not changing. The increase in thermal expansion of the a lattice parameter is not linear and the rate of increase is suggested to grow at higher temperatures and approaches the lattice parameter for the hexagonal phase. Phase diagrams have been proposed [37] and there is not agreement on the proper treatment and interpretation of the hexagonal phase [38].

1.5 UHMPE Fibers: Viscoelasticity

Viscoelastic materials have two contributions to their mechanical behavior: an elastic and a viscous component. First, a Hookean relationship describes the elastic portion of the behavior. The engineering version (Cauchy) assumes no change in cross sectional area during the mechanical response of the material takes the form:

$$\varepsilon = \frac{\Delta l}{L_0} \quad (\text{Eqn 1-5})$$

$$\sigma = \frac{F}{A_0} \quad (\text{Eqn 1-6})$$

$$E = \frac{\sigma}{\varepsilon} \quad (\text{Eqn 1-7})$$

where ε is the strain in the material which is a unitless parameter as a ratio of the change in length of a material Δl to the original length L_0 , σ is the stress in the material measured in N/m^2 or Pascals (Pa) which is force, F , normalized by the original cross sectional area of the material, A_0 , E is the Young's modulus which measures the stiffness or linear

elastic response of the material in Pa. The elastic response measures the short range forces or bonding between atoms [40].

The second is the viscous portion which is described by a shearing force, τ , which is a force acting perpendicular to the extension direction. The shearing modulus, G , is also a measure of stress/strain but is defined with the strain measured in radians defined below:

$$G = \frac{\tau}{y} = \frac{F/A}{dx/dy} \quad (\text{Eqn 1-8})$$

The area is no longer the cross sectional area of the material perpendicular to the extension direction, but the area of contact between two sheared bodies in the direction of the extension [40]. Newton's law defines viscosity as the ratio of shearing stress to the velocity gradient:

$$\eta = \frac{F/A}{dv/dy} \quad (\text{Eqn 1-9})$$

where η is viscosity and dv/dy velocity gradient. The formula above shows a linear viscoelastic response, meaning the material is independent of the rate of shear and if the force is doubled then the viscosity is doubled. Many viscoelastic materials show a response to the shear-rate and exhibit either shear thinning (η decreases with increasing shear-rate) or shear thickening (η increases with increasing shear-rate) [40].

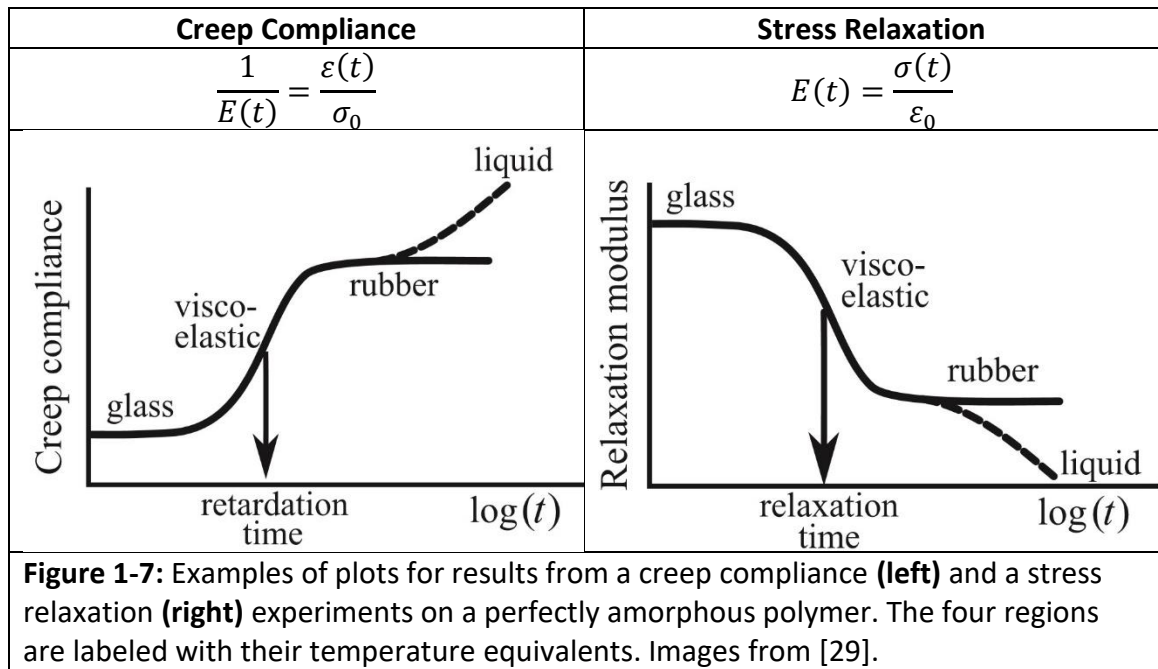
There are three common methods of describing viscoelastic behavior of materials and they are all interrelated [40]. The first method is referred to as the integral model which involves a linear combination of time independent term and a time dependent integral of shear strain and shear stress. The second model is referred to as the differential model and uses a series of elements to represent the elastic and viscous response of the

material using springs and dashpots, respectively. There are various ways to arrange the elements (Voigt/Kelvin, Maxwell, Standard Linear Solid) and the solution is always a sum of linear differential equations describing each elemental ensemble. Lastly, the molecular model experimentally subjects the viscoelastic material to a sinusoidal stress or strain over time and the shift in response time, or phase shift, between stress and strain is recorded. The behavior of the material is then treated as a linear combination of the in-phase component (the elastic response with stored energy) and the out of phase response (the viscous response with dissipated energy).

The issue with each of these models is that they are based on a linear combination of linearly-behaving elastic and viscous terms. These models work well to describe low strain systems ($\epsilon < 1\%$) where both terms can be approximated to behave linearly. However, at high strains such as in tensile failure tests, these models do not accurately model viscoelastic mechanical response for shear thinning or shear thickening materials [40]. These models fail to capture the cooperative response of chains that span more than one phase and behaviors such as trans to gauche rotations or the melting temperature are not considered.

The models can predict the behavior of homogenous systems such as perfectly amorphous polymers. Transient experiments can be used to characterize the time response of these materials. The two most common experiments are creep compliance and stress relaxation. In a creep compliance test, a constant stress is applied to a viscoelastic material and the change in strain is measured as a function of time. In a stress relaxation experiment, the converse of the creep compliance test, an initial strain is imparted on the viscoelastic material and the change in stress as a function of time is

measured. The response of the material varies with the magnitude of the constant stress (σ_0) or strain (ϵ_0) for the tests. Figure 1-7 shows example plots of the response with the log of time for a creep compliance and a stress relaxation experiment with 4 regions of behavior where changes in the modulus or compliance (the inverse of modulus) occur [29]. First, at very small time scales, the behavior of the polymer is glassy and the modulus plateaus at a high value. Second, as the time scale increases, the modulus decreases over a range of time. Third, at long time scales, the modulus plateaus at a low value. Lastly, at very long time scales, the modulus decreases again and approaches null.



To understand the meaning of these regions, the molecular approach will be used. As discussed in the previous section, the polymer molecules are long chains with monomer repeat units. The primary covalent bonds within a chain and the secondary bonds between adjacent chains each have limitations in their conformations from short range steric hindrances and frictional forces [29]. The chains can also be affected by long range interactions, such as entanglements. Each of the bonds is dynamic and oscillates at

a vibrational frequency. The inverse of the frequency gives a time between oscillations. This implies that if an event is given less time to occur than the time between oscillations, then the bond behaves as though the oscillation event was not possible. Additionally, there is a temperature dependence on these events. First, there is a temperature dependence on the oscillation frequency. As temperature increases, the oscillation frequency also increases. There is also an energy barrier for the event to occur and as temperature increases, more of the bonds have enough thermal energy to reach or exceed the barrier, according to a Boltzmann factor. Shown below is the frequency, r , of bonds having energy $\geq U_0$:

$$r = \omega_0 e^{\frac{-U_0}{kT}} \quad (\text{Eqn 1-10})$$

where ω_0 is the vibration frequency for the bond, k is the Boltzmann constant, T is absolute temperature, and U_0 is the energy barrier for the event. Events can be hindered if the time scale is too short or if the temperature is too low. Similarly, the events can become abundant if the time scale is long and the temperature is high. This also implies that and the time can be adjusted at constant temperature or the temperature can be adjusted at constant time scale to observe similar mechanical response [15, 29, 39, 40]. The regions of the plots in Figure 1-7 have been labels with temperature equivalent regions. The first region corresponds to behavior below the glass transition temperature, T_g , of the polymer where the low thermal energy or short time scales prevents conformational changes. Side chains may move of the polymer may move based on their size but the forces responsible for the mechanical response in this region is the primary covalent and secondary bonds making the response linear elastic [29]. As temperature or time scale increase, the events with short time scales or low activation barriers start to

occur and the system transitions into the viscoelastic region near T_g . In this region, cooperative motion of chains is possible but frictional forces make the movements sluggish and the mechanical response is retarded or anelastic [29]. Here, the relaxation time, λ , for the event is crossed and it is the time required for the viscoelastic material to recover to its pre-stressed state (the time analog for T_g). At temperatures above T_g or time scales of λ , conformational rearrangements become possible from the short range interactions. However, the temperature or time scale for long range interaction such as chain disentanglement has not been reached. The result is the entanglements act as crosslinks, creating a rubbery plateau with an approximately constant modulus [29]. Above the melting temperature or at very long time scales, the entanglements can now move past one another similar to a viscous melt and the modulus decreases and approaches null.

The regions described above are for a perfectly amorphous polymer system. Polymer fibers are semicrystalline with approximately 5 % to 10 % of the phase in an oriented amorphous phase and 85 % to 90 % crystalline phase. However, the mechanical properties of oriented amorphous phase in the oriented fibers are still affected by both temperature and time scale. These regions are also affected by the cooperative events of chains spanning more than one phase region [29]. The result is a complex system of cooperative events that occur over a range of temperatures or time scales. These events can be grouped into types of responses based on observation from mechanical behavior experiments and molecular models.

There are three major types of responses to increasing stress that occur in polymer systems [29, 39]. The first is the instant elastic response of the material. This deformation

is recoverable if the stress is removed. The second is the retarded elastic response where a combination of elastic and viscous responses. In this region, the elastic portion is recoverable and some of the viscous portion is recoverable if the stress is removed. The last is the plastic response where permanent deformation of the material occurs and is not recoverable if stress is removed.

There are three families of mechanisms responsible for the mechanical response of polymer systems [29, 41]. The first is, the straightening of unaligned polymer chains. The second is the shearing of chains past one another called chain slippage. Lastly, chain scission is the breaking of covalent bonds in the backbone of the polymer. Determining how each of these mechanisms affects the mechanical behavior of UHMMPE fibers is essential to understand how failure occurs.

Temperature and strain-rate affect each of these mechanisms. The temperature of the fibers at the point of a ballistic impact is difficult to measure directly. Previous studies have attempted to estimate this impact temperature and the estimations vary greatly from a temperature increase of 5 °C to 10 °C measured experimentally by an infrared camera observing the change in temperature on the back face of a PE composite [42] to a peak temperature of 330 °C at the point of impact from computational methods [43] Prevorsek et al. also showed that there is little change in V_{50} performance for PE composites from 604.7 m/s at 23 °C to 558.7 m/s at 120 °C.

1.6 UHMMPE Fibers: Mechanical Properties

Several factors affect the mechanical properties of UHMMPE fibers. Understanding these will help to design experiments to test specific factors. Terms describing the mechanical properties will first be defined for clarification.

1.6.1 Mechanical Property Terms and Definitions

Failure: The loss of the load carrying capability of the fiber. For fibers, this is synonymous with fiber breakage, where one fiber is ruptured into two separate pieces.

Non-failure: A fiber that has been subjected to a loading condition without failure occurring. This is due to the testing machine limits being reached before failure occurs. This term is also used to describe a stress-strain curve shape where non-failure occurs.

Failure Strength (σ_f): The stress in the fiber at failure. [Pa]

Strain to Failure (ϵ_f): The strain in the fiber at failure. [Unitless]

Ultimate Tensile Strength (UTS or σ_{UTS}): The highest stress in the fiber stress-strain curve. [Pa]

Strain to UTS (ϵ_{UTS}): The strain in the fiber at the UTS. [Unitless]

Young's modulus: The ratio of change in stress to the change in strain corresponding to the slope of the stress-strain curve or $d\sigma/d\epsilon$. [Pa]

Failure Toughness: The energy required for fiber failure corresponding to the area under the stress-strain curve to failure or the integral of stress between null strain to the strain to failure.

Pseudo-brittle: A stress-strain curve shape showing a retarded elastic response with point of failure coinciding with the point of UTS.

Plateauing: A stress-strain curve shape showing a retarded elastic response with a region of constant stress with increasing strain occurring at the maximum stress before failure.

Necking: A stress-strain curve shape showing a retarded elastic response with a region of decreasing stress with increasing strain occurring after the maximum stress before failure.

Concave: A curve (or section of a curve) with a negative second derivative

Convex: A curve (or section of a curve) with a positive second derivative

Quasi-static Strain-rate: A term to describe the strain-rates less than or equal to 10^{-2} s^{-1}

Intermediate Strain-rate: A term to describe strain-rates between 10^{-1} s^{-1} and 10^0 s^{-1}

Dynamic Strain-rate: A term to describe strain-rates above 10^0 s^{-1}

The shapes of stress-strain curves can change as testing conditions are varied for polymer fibers. Shown in Figure 1-8 are examples of stress-strain plots observed in polymer systems. Below the T_g , the polymer exhibits brittle behavior with a linear stress-strain relationship. As temperature is increased the short range interactions become available and the behavior transitions to ductile with a concave retarded elastic curve, also called pseudo-brittle, with some plastic deformation before a maximum is reached and the curve then changes to convex before failure. At higher temperatures, the amount of plastic deformation before failure increases and the polymer exhibits a long convex necking region where there is little change in engineering stress over a large strain range. At even higher temperatures, the long range interactions are the only limiting mechanical effect and the polymer exhibits a rubbery behavior

An important distinction is the location of the point of failure and the point of UTS. Figure 1-9 shows two stress-strain curves. The first reaches the maximum stress at

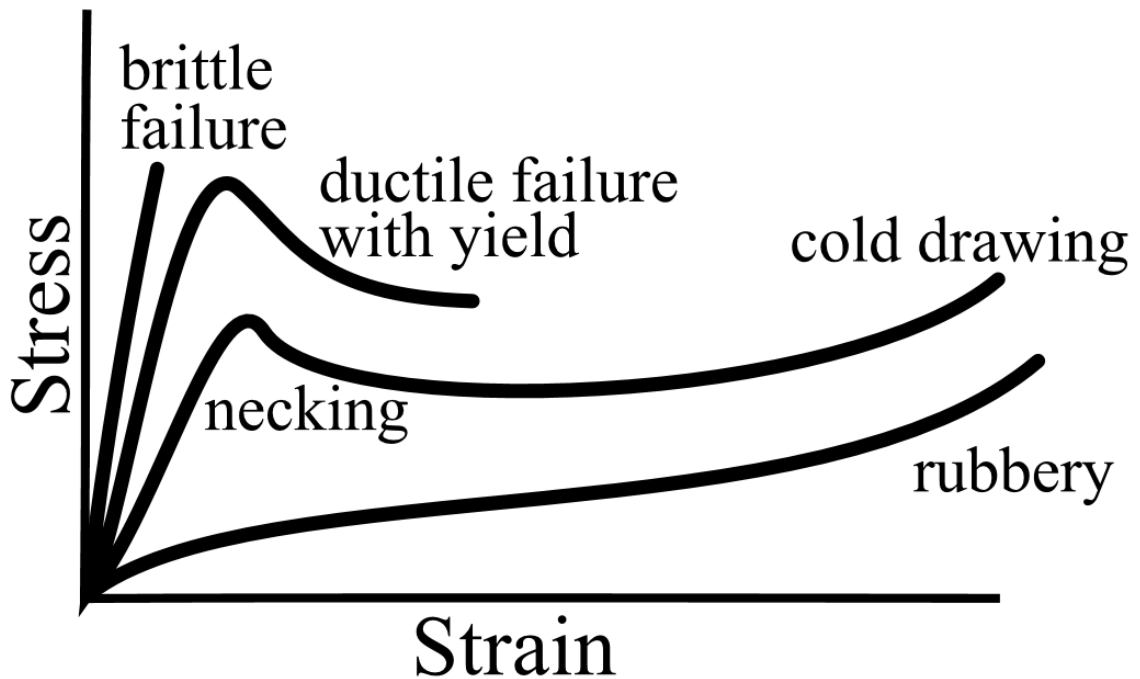


Figure 1-8: Types of stress-strain curves for polymer materials. Image taken from [29].

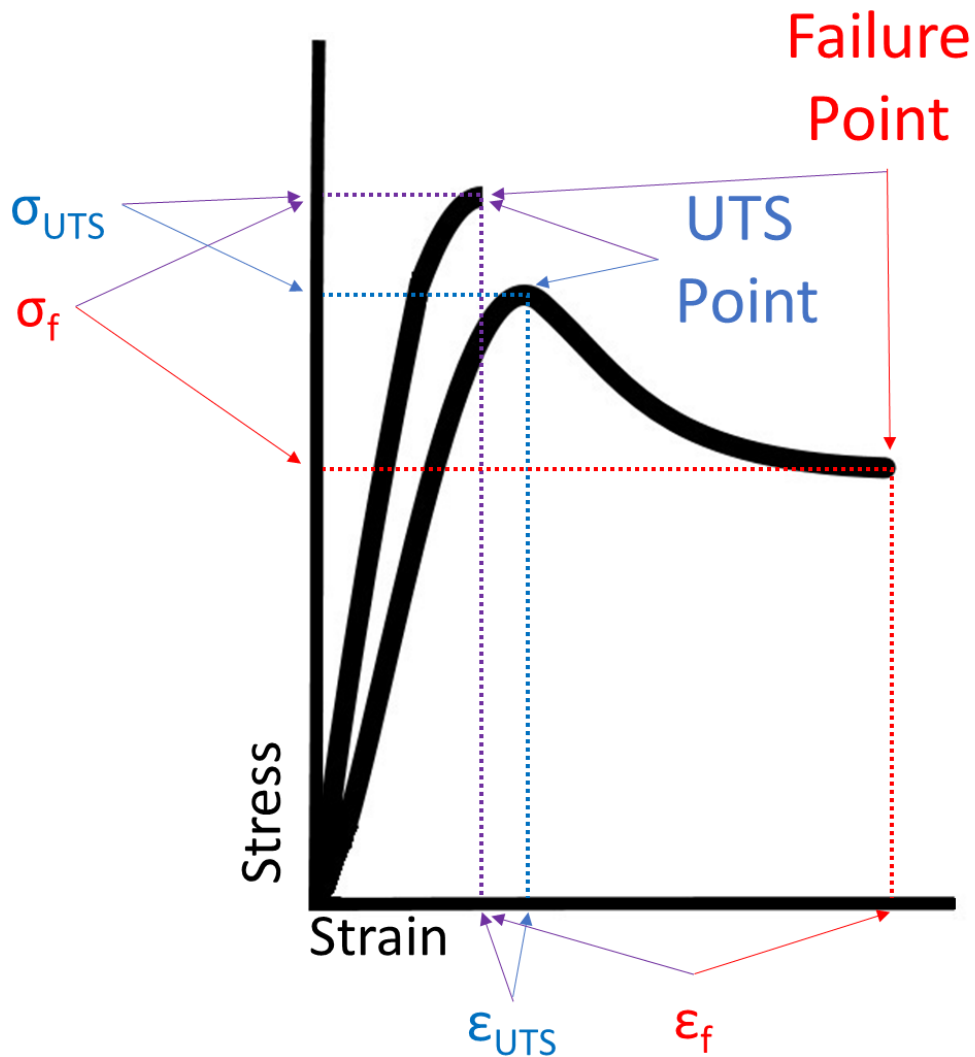


Figure 1-9: Examples of a pseudo-brittle and a necking stress-strain curve showing the possible equivalence and difference between failure strength and UTS.

the point of failure. The other reaches a maximum stress before the point of failure. The failure locations and the corresponding material properties of failure strength and strain to failure are shown with red arrows. The UTS locations and the corresponding material properties of UTS and strain to UTS are shown with blue arrows. In the first curve, the failure occurs at the maximum stress (UTS) and therefore the point of failure and point of UTS are equivalent and these locations are shown with purple arrows. The corresponding

material properties are also equal in this type of stress-strain curve, $\sigma_f = \sigma_{UTS}$ and $\epsilon_f = \epsilon_{UTS}$.

1.6.2 Factors Affecting the Mechanical Properties of UHMMPE Fibers

The mechanical properties of UHMMPE fibers can be influenced by many factors. Discussed in this section are some of the most common factors and their effects on the mechanical properties of UHMMPE fibers and how they can be controlled in an experimental setting.

The fiber morphology is an important factor affecting the mechanical properties [22]. As discussed previously, the process of gel-spinning and drawing changes the phase composition from lamellar orthorhombic to extended orthorhombic and the amorphous to oriented amorphous. The increase in degree of orientation align the backbone of the chains in the direction of the fiber and increase the stiffness and strength in the fiber direction. The number of entanglements prevents orientation of the chains and therefore decreases the strength and stiffness of the fiber. The amount of oriented amorphous phase has less C-C bonds in the cross section of the fiber and therefore decreases the strength and stiffness. The same reasoning can be applied to voids in the fiber which lack any C-C bonds in their cross section. The diameter of the fibers can also affect the mechanical properties. The diameter is a product of the processing conditions and larger diameters can have a negative effect on fiber strength [44, 45] possibly from an increase in void size of population. The morphological effects can be controlled experimentally by conducting experiments using the same spool of fibers. There will still be some variance in morphology but the fibers should be approximately equal.

The gage length is the original length of the fiber to be mechanically investigated. This can affect the mechanical properties if there is defect population and increase in gage length cause an increase in the probability of having a sample with critical defect size [44-46]. The diameter effects can be controlled experimentally by conducting experiments using the same spool of fibers and either selecting fibers with a specific range of values or randomly distributing the fiber diameters over the independent variables of the experiment.

The chain lengths in the fiber can be affected by chemical (oxidation or hydrolysis), radiation (ultraviolet light), mechanical (macroscopic bending), and thermal degradation [47, 48]. Each of these mechanisms can be interrelated and create chain scissions within the fiber. This reduced the average molecular weight of the chains and can decrease the strength and stiffness of the fibers. These degradation effects can be controlled by protecting the fibers from these environmental conditions, particularly by storing in a dark climate controlled location.

Lastly, as discussed in the viscoelastic section, the fibers are affected by both temperature and time scale. Increasing temperature increases the thermal energy available for stress-relieving mechanisms to occur and decreases the strength and stiffness of the fiber. The temperature can be controlled by heating or cooling the environment around the fibers during mechanical testing. Controlling any energy dissipated in the fiber as heat is more challenging experimentally. Increasing the time scale provides time for stress-relieving mechanisms to occur and also decreases the strength and stiffness of the fiber. It is not possible to experimentally control time but by changing the rate at which the fibers are strained, or strain-rate, the time scale allowed for mechanisms can be controlled.

Strain-rate is measured in s^{-1} and for the purposes of this dissertation, quasi-static describes the strain-rates less than or equal to $10^{-2} s^{-1}$, intermediate describes strain-rates between $10^{-1} s^{-1}$ and $10^0 s^{-1}$ and dynamic describes strain-rates above $10^0 s^{-1}$.

A specialized instrument is required to achieve dynamic strain-rates. A fiber-Split Hopkinson Tension Bar (f-SHTB) is specifically designed for high strain-rate of fiber samples and is shown in Figure 1-10 (44, 45, 49-51). The instrument works by imparting

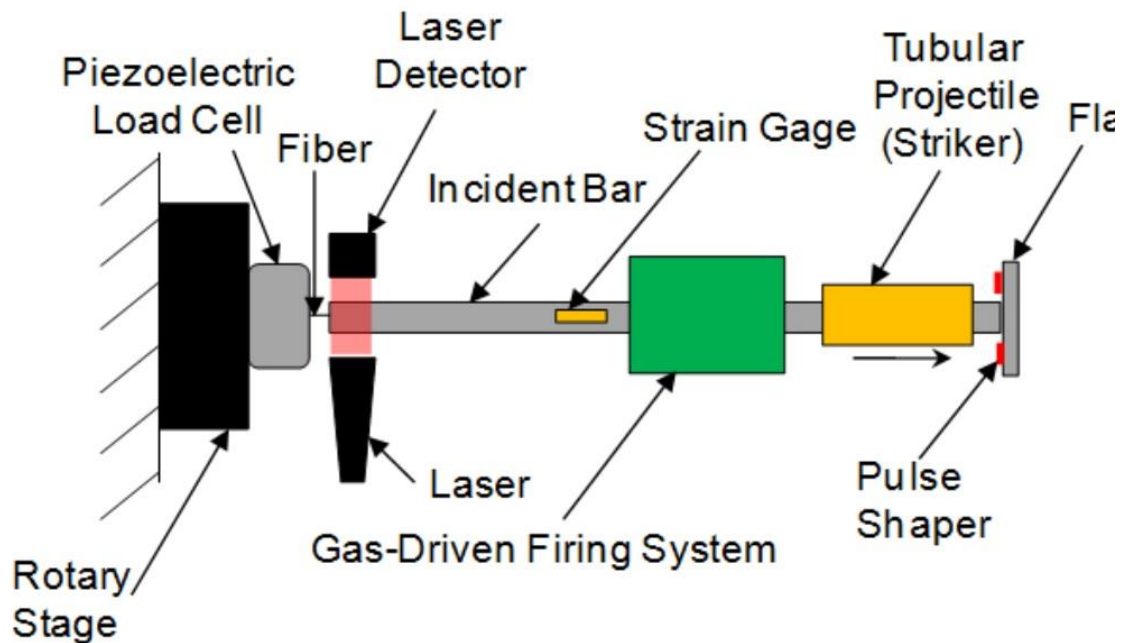


Figure 1-10: A schematic of the fiber-Split Hopkinson Tension Bar (f-SHTB) showing the gas-driven firing system, the brass striker tube, pulse shaper and flange on the end of the incident bar. Also shown are the measurement devices including the strain gages, piezoelectric load cell, and optical displacement setup. Figure taken from [27].

a strain-wave through the fiber material. This is accomplished by starting with an incident bar, normally made of an aluminum alloy or steel. The selected material will have a strain-wave speed according to the Young's modulus and density (Eqn 1-2). The bar must be long enough so that the time for the strain-wave to travel through the bar is longer than the time for fiber failure, normally 100's of μs for dynamic tests. Similarly, the gage

length of the material should be short enough so that the strain-wave in the fiber is not reflecting multiple times during the tensile test. This can be challenging for polymer fibers that have high Young's moduli and low densities. The strain-wave in the incident bar is created by striking a flange at the end of the incident bar with an impact tube. The impact tube is normally a stiff metal and a soft metal pulse shaper is used to smooth the strain-wave. Strain gages are placed on the incident bar and the strain-wave impulse can be observed on a high speed data recorder. An optical system consisting of a laser and an optical detector measure the change in displacement at the end of the incident bar. From this sensor, displacement of the fiber and the strain-rate can be calculated using the fiber gage length, L_0 . The strain-wave passes through the fiber grip and into the fiber. At the other end of the fiber, another grip is attached to a piezoelectric load cell that measures the force exhibited on the fiber by the strain-wave. At each of the locations where there is a change in material or cross sectional area, strain-wave reflections can occur [52-54]. Matching the strain-wave impedance is important to reduce the number and amount of reflection waves, but this is challenging for polymer fibers with diameters of approximately 18 μm .

1.6.3 Cunniff Parameters Revisited

As discussed in the previous sections, the mechanical properties such as Young's modulus, strain to failure, and failure strength had a dependence on both temperature and strain-rate. The manufacturer fiber parameters used by Cunniff are normally conducted at room temperature and at quasi-static strain-rates. The Cunniff parameter can therefore be rewritten and improved to reflect the temperature and strain-rate dependent material properties of E , ϵ_f , and σ_f :

Linear specific toughness:
$$\frac{\varepsilon_f(T, \dot{\varepsilon}) \sigma_f(T, \dot{\varepsilon})}{2\rho} \quad (\text{Eqn 1-11})$$

Linear Cunniff parameter:
$$U_{lin}^* \frac{1}{3} = \left(\sqrt{\frac{E(T, \dot{\varepsilon})}{\rho}} \frac{\varepsilon_f(T, \dot{\varepsilon}) \sigma_f(T, \dot{\varepsilon})}{2\rho} \right)^{\frac{1}{3}} \quad (\text{Eqn 1-12})$$

The equation above assumes the failure toughness is derived from a linear relationship between stress and strain up to the point of failure. It will be referred to as the “linear Cunniff parameter” which is calculated from the “linear specific toughness”. However, the T_g for polyethylene is approximately $-100\text{ }^\circ\text{C}$ [55]. As presented in the previous sections, the stress-strain curves for these fibers are not linear and have a retarded elastic shape when above the T_g . The failure toughness is not captured properly by the linear approximation and the areas under the stress-strain curve give a more accurate representation of the failure toughness for these viscoelastic materials. The equation below replaces the linear approximation for the failure toughness with a temperature and strain-rate dependent integral for the area under the stress-strain curve:

Actual specific toughness:
$$\frac{\int_0^{\varepsilon_f(T, \dot{\varepsilon})} \sigma(T, \dot{\varepsilon}) d\varepsilon}{\rho} \quad (\text{Eqn 1-13})$$

Actual Cunniff parameter:
$$U_{act}^* \frac{1}{3} = \left(\sqrt{\frac{E(T, \dot{\varepsilon})}{\rho}} \frac{\int_0^{\varepsilon_f(T, \dot{\varepsilon})} \sigma(T, \dot{\varepsilon}) d\varepsilon}{\rho} \right)^{\frac{1}{3}} \quad (\text{Eqn 1-14})$$

Equation 1-14 will be referred to as the “actual Cunniff parameter” calculated from the “actual specific toughness” in equation 1-13.

1.6.4 Previous studies of Temperature and Strain-rate Effects

UHMMPE fibers have a low surface energy [56] and a high tensile strength, causing difficulties in proper gripping of the fibers during tensile testing [57, 58].

Capstan methods have been used to gain data about failure stresses but the failure strains

from this method is often questionable due to the unknown amount of gage length within the capstan [57, 59]. Direct gluing to cardboard has shown limited success and is dependent on fiber diameter [45, 60] while a combination of glue and pressing between rubber tabs has reported success but on small numbers of tests performed [58]. Fiber-specific grips have also been developed to directly grip Kevlar fibers between two tabs of poly(methyl methacrylate) [49-51] and the same design using polycarbonate tabs has shown to be successful for UHMMPE single fibers [44]. The gripping tabs in these designs are recessed from the grip edge making it challenging to access the length of fiber in the grip for heating experiments. To investigate the simultaneous effects of strain rate and temperature on the mechanical properties of UHMMPE single fibers, a new set of grips must be created and compliant with a fiber heater.

Previous studies investigating the effects of temperature and strain-rate included UHMMPE fibers between -200 °C to 150 °C at a quasi-static rate (0.005 s^{-1}) [61], 25 °C to 143 °C at a quasi-static rate (0.008 s^{-1}) [46], 21 °C at various quasi-static rates ($6.67 \times 10^{-5} \text{ s}^{-1}$ to 0.016 s^{-1}) [59], -69 °C to 23 °C at multiple quasi-static rates (10^{-4} s^{-1} to 10^{-1} s^{-1}) [57], two temperatures (25 °C and 70 °C) at two dynamic rates (300 s^{-1} and 700 s^{-1}) [62], 20 °C at quasi-static to dynamic rates (10^{-3} s^{-1} , 10^{-2} s^{-1} , and 600 s^{-1}) [45], 20 °C at quasi-static to dynamic rates (10^{-4} s^{-1} to 10^3 s^{-1}) [58], 20 °C at quasi-static to dynamic rates (10^{-3} s^{-1} to 1156 s^{-1}) [44], and bundles of approximately 240 high-modulus polyethylene fibers at 23 °C at dynamic rates (340 s^{-1} to 850 s^{-1}) [63]. These studies have contributed portions of the overall effects of temperature and strain-rate but none has covered a comprehensive investigation of the conditions where chain straightening, slippage and scission are competing mechanisms.

A study is needed to investigate the simultaneous temperature and strain-rate effects on UHMMPE fibers that covers the temperature range from room temperature (20 °C) to melting temperature (148 °C) and strain-rates from quasi-static to dynamic to allow accurate predictions for the mechanical response for a given temperature-strain-rate combination and is the purpose of this dissertation.

Chapter 2: Experimental Procedure

2.1 Fiber Sample Preparation

Single fiber samples were prepared from a single spool of Dyneema® SK76 1760 dtex yarn. The spool has been maintained under climate-controlled laboratory conditions at approximately 22 °C and less than 20 % relative humidity but not sealed in an air-tight container. To minimize effects from contamination on the surface of the spool, approximately 400 m of yarn was removed to reveal yarn that was not directly exposed to the laboratory atmospheric environment. Yarns were selected from the center of the spool to avoid any contamination from table surfaces near the spool edges, as shown in Figure 2-1.

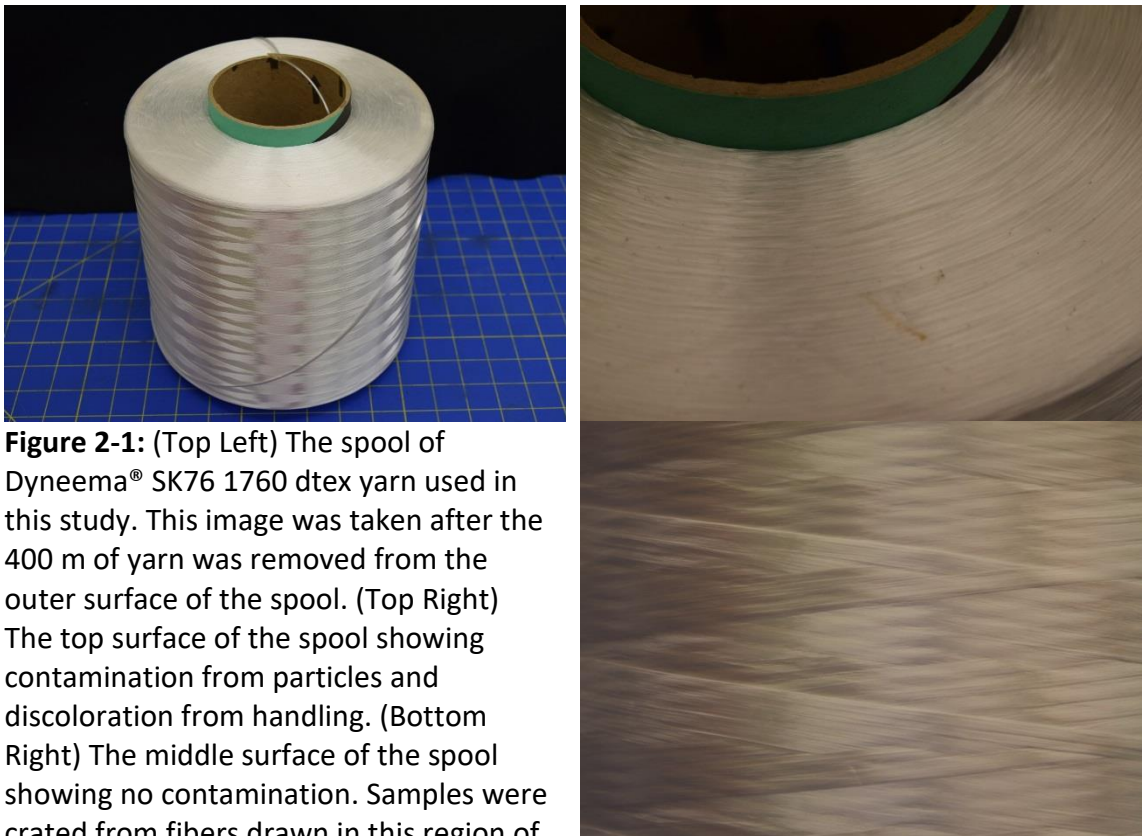


Figure 2-1: (Top Left) The spool of Dyneema® SK76 1760 dtex yarn used in this study. This image was taken after the 400 m of yarn was removed from the outer surface of the spool. (Top Right) The top surface of the spool showing contamination from particles and discoloration from handling. (Bottom Right) The middle surface of the spool showing no contamination. Samples were crated from fibers drawn in this region of the spool.

Maintaining fiber alignment within the yarn is crucial to prevent entanglements and allow the extraction of single fibers. For this reason, the yarn was clasped with tape to prevent bulk yarn splaying but not hindering the teasing of single fibers from the bulk. The yarn was cut through the tape using ceramic scissors to also prevent splaying, shown in Figure 2-2. The yarn was slowly unwound from the spool while kept under slight



Figure 2-2: (Left) An image of the tape-clasped yarn. (Right) The cut tape-clasped yarn maintaining fiber alignment. The top yarn is attached to the spool and is used for extracting samples. The bottom yarn is discarded.

tension to prevent contact with any surrounding surfaces. Yarn lengths of approximately 1 m were unwound and the second end was also tape-clamped and cut as described previously. The double-taped yarns were moved to an ethanol-rinsed self-healing cutting mat. One end of the yarn was taped to the mat and the taped area of the other end was cut away to allow splaying of the individual fibers. The splayed yarn end was carefully spread to expose single fibers. The single fiber end was manually held in place as the surrounding fibers were moved away and a piece of tape was placed directly on the single fiber end, shown in Figure 2-3. The tape was then rolled back on itself approximately every 1 mm to resemble a tape-capstan, shown in Figure 2-4. A small tensile force was manually applied to the tape-capstan end of fiber end to gently tease the single fiber from the tape-clamp on the other end. Careful attention was paid to the amount of force applied

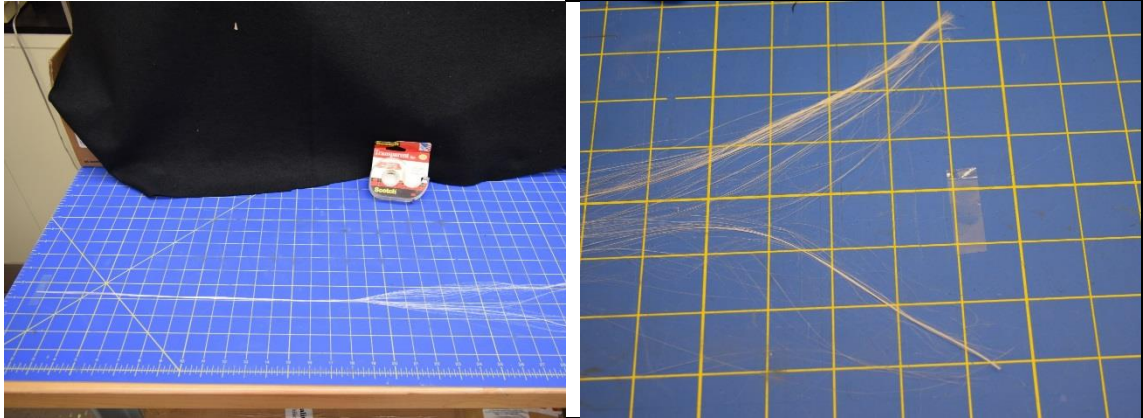


Figure 2-3: (Left) An image of the tape-clasped yarn on the self-healing mat and the splayed end. (Right) A taped single fiber amidst the splayed yarn.

to the single fiber and any tangling encountered during separation from the bulk yarn. If the level of tangling caused permanent deformation in the fiber, visible as large kinks or periodic curvatures along the fiber length, the sample was considered damaged during

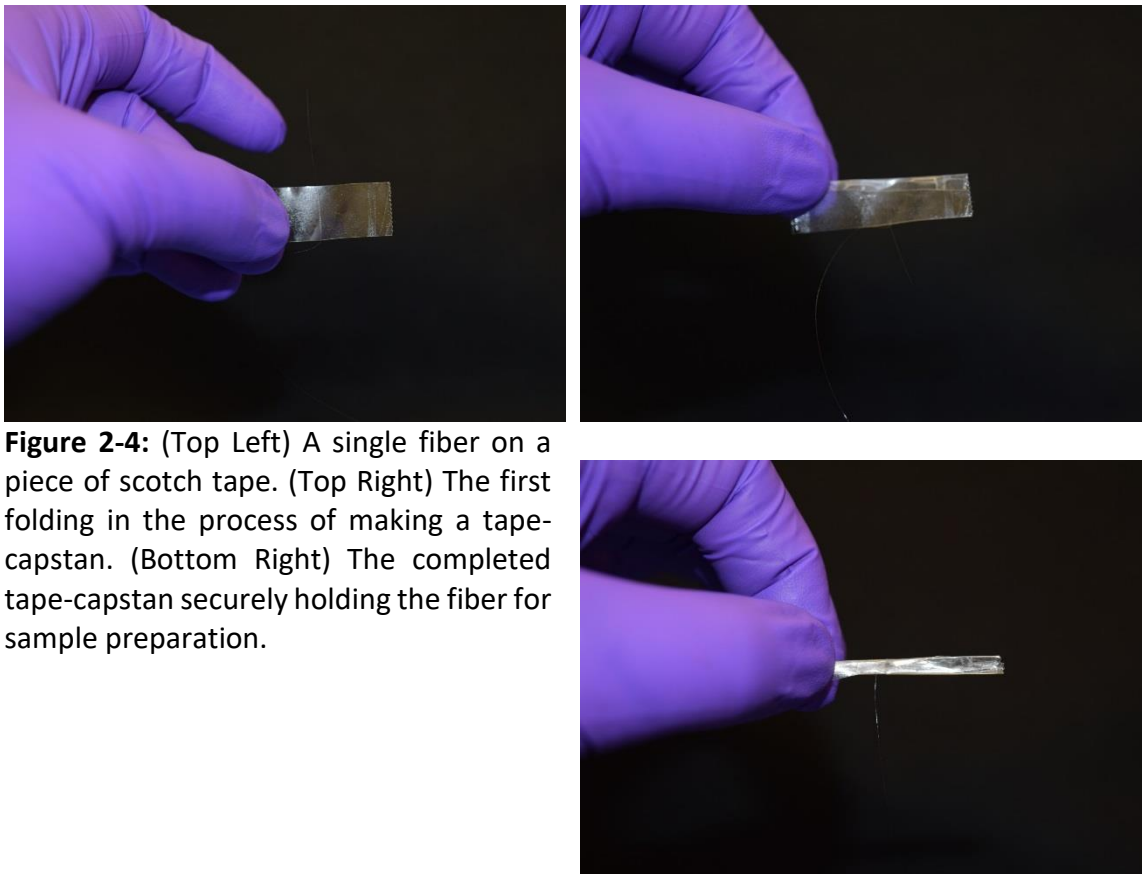


Figure 2-4: (Top Left) A single fiber on a piece of scotch tape. (Top Right) The first folding in the process of making a tape-capstan. (Bottom Right) The completed tape-capstan securely holding the fiber for sample preparation.

extraction and discarded. From each yarn, approximately 5 to 10 single fibers could be extracted before the yarn entanglement became unmanageable, preventing further single fibers from being teased without damage. In total, 57 single fibers were prepared using this method.

A gage length of 10 mm was selected for the temperature-strain-rate tensile test experiments [59]. Hollow-rectangle templates were created to keep the fiber aligned and stationary for directly gripped tensile experiments. The dimensions of the template are 31 mm by 11.5 mm. An inner rectangle with dimensions 24 mm by 6.5 mm is cut away using a hobby knife or razor blade, making the non-cut template dimensions 2.5 mm wide along the long axis and 3.5 mm wide along the short axis. The 24 mm rectangle provides 10 mm of sample gage length and two 7 mm gripping areas on the ends. To maximize the number of samples per 215.9 mm by 279.4 mm (8.5" by 11") sheet of template material, the template was repeated 9 times along the long axis and 18 along short axis.

Transparency sheets were used as the template material (HP color Laserjet transparencies C2934A) due to their higher stiffness than paper stock which provides a more stable template for transporting, storing, and directly gripping the fiber samples. The templates for the first batch of 18 single fibers were created by hand using a ruler and transparency markers. Subsequent fiber batches used a laser-printed sheet from a file created using Autodesk Inventor software to allow more repeatable control of the template dimensions. The Autodesk Inventor software template is shown in Figure 2-5. All templates are lined to show the 10 mm gage for post-failure analysis. The template was cut along the long edge to create strips 9 samples long. Two strips were taped on the mat with their short

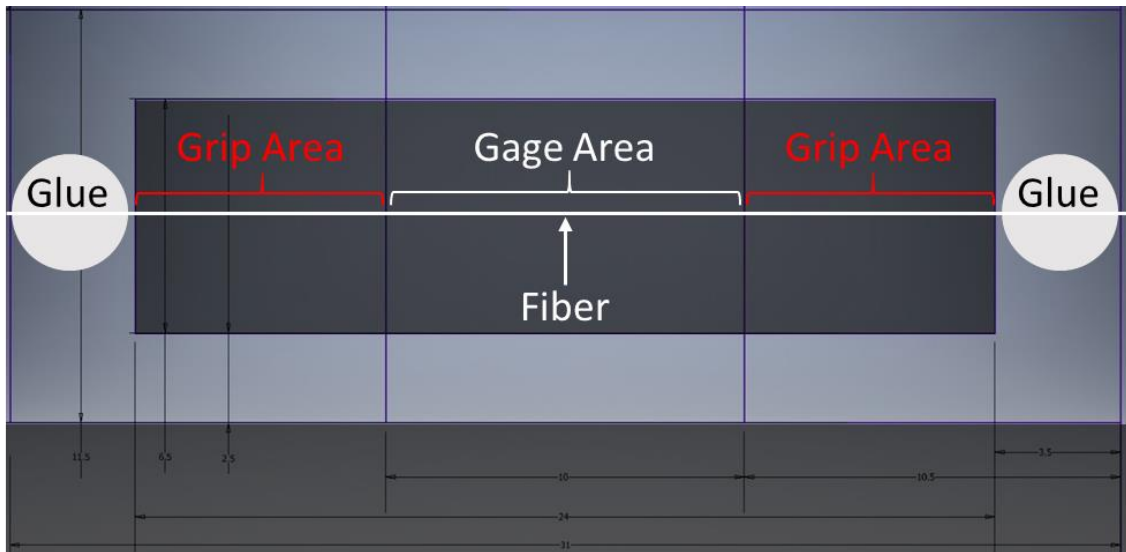


Figure 2-5: The Autodesk Inventor software template illustrating the dimensions used in mm. A single fiber sample showing the glued, gripped, and gage areas has been added for clarity. The darkened region is the inner rectangle that is cut away before the fiber is laid on the template.

edges touching to create an 18-sample strip. The templates were labeled with the fiber number and sample from that fiber. For example, 25-8 is the sample from 25th fiber and 8th sample of that fibers' 18 samples. A single fiber was taped to one end of the strip laid across the center of the hollowed rectangles. A plastic mini spring clamp was placed on the other end of the fiber and hung off the edge of the surface to keep the fibers taught. The clamps have an average mass of 4.209963 g with a standard deviation of .016529 g. Neglecting possible friction at the table edge, the maximum pre-tension force on the fibers during preparation is approximately $.041287 \text{ N} \pm .000162 \text{ N}$. (For reference, the fibers fail at room temperature at approximately 1 N of force.) Each fiber sample was then glued to both sides of its respective template. An image of a batch of fibers in the glue-curing phase is shown in figure 2-6. After at least 24 hours of curing, the samples are cut along the short axis to separate individual fiber samples. A high viscosity

cyanoacrylate glue, 4g Ultra Gel Control Super Glue (model 1363589), was used to create separate glue drops between adjacent templates to prevent having to cut



Figure 2-6: (Left) An image of the glue-curing phase of the first batch of 18 fibers making 324 samples. (Right) A closer image of the glue-curing phase showing the single fibers along the templates.

through a single large glue drop (which can strain the fiber sample). A 10 mm single fiber sample in its template is shown in Figure 2-7. For gage lengths other than 10 mm,

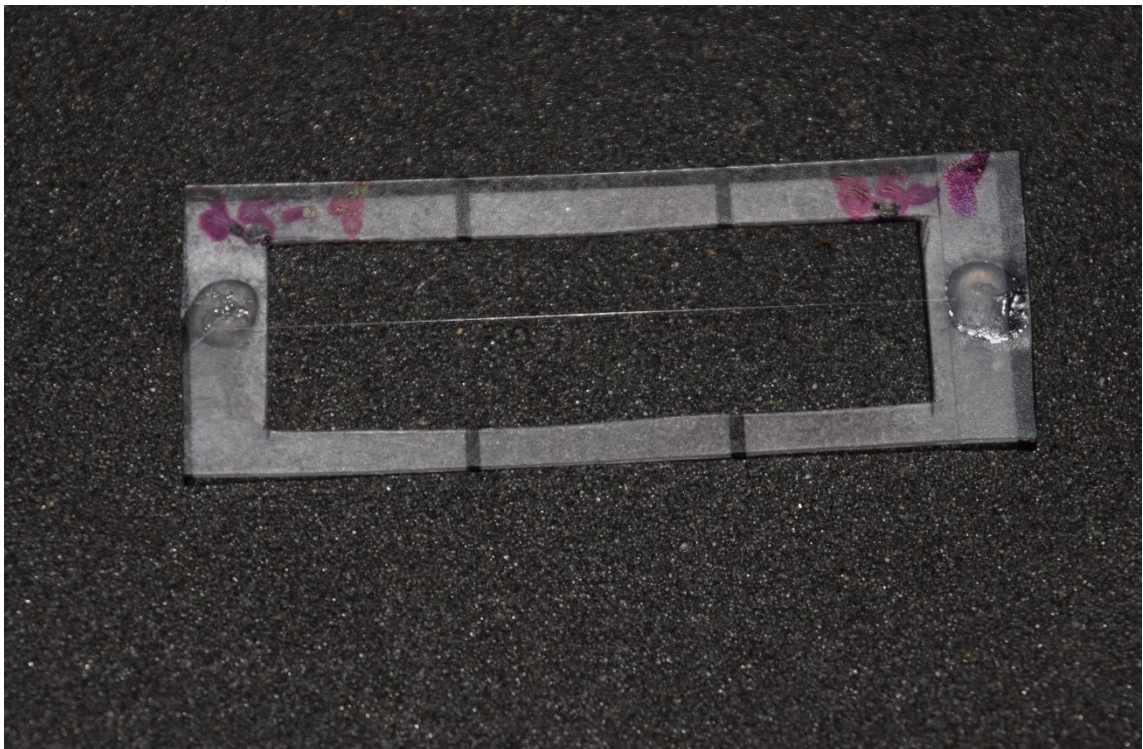


Figure 2-7: Single fiber sample 25-8 glued in its template made from the printed templates using Autodesk Inventor software. The lines on the template indicate the 10 mm gage length and can be used for reference in post-failure analysis.

the same sample preparation procedure was used but the template gage length area was changed to the respective length. Along the 279.4 mm transparency edge, a single strip contained 10 sample templates with two each of the 1, 2, 5, 7, and 12 mm gage lengths.

A total of 828 10 mm samples and 110 samples of other gage lengths were prepared for this study. The samples from a single 18-sample-long fiber showed similar diameters between samples. For this reason, sets of fibers selected for the same temperature-strain-rate combination did not contain two samples from the same 18-sample-long single fiber to avoid the effects of fiber diameters biasing the results.

2.2 Diameter Measurements

Fiber diameters were measured top-down using a Nikon OptiPhot-POL Polarizing Microscope with a 60x magnification lens and a Boeckeler VIA-100 Imaging System with a 3.1x magnification microscope camera. The image was displayed on a Sony Trinitron super fine pitch monitor and the VIA-100 controller was used to translate two horizontal lines. The distance between the lines (in microns) was displayed on the monitor. The translation of the horizontal lines was incremental at either .11 or .12 microns. For the quantized fiber diameters that are possible between 15.8 to 21.02 microns, the average resolution is .1135 microns \pm .0048 microns. The templated fiber sample was placed so one end of the gage length at a 10 mm marker line was centered on the light source and in the microscope image. The microscope camera was rotated to align the fiber length with the VIA-100 lines. The fiber was brought into focus and the top-down diameter was measured by aligning the top of the bottom horizontal line with the bottom of the fiber and the top of the top horizontal line with the top fiber. The viewing stage was connected to an X-Y translator and the diameter measurement was



Figure 2-8: (Left) An image of the diameter measurement process with the fiber in focus before the horizontal lines are moved. (Right) A fiber diameter measurement showing the top of each horizontal line touching an edge of the fiber.

repeated four more times along the 10 mm gage length with a 2.5 mm spacing for a total of five diameter measurements per fiber sample in accordance with current best practices [64-66]. The arithmetic mean of the five was calculated as the average diameter, d_{avg} , and the minimum of the five was recorded as the diameter minimum, d_{min} . A diameter measurement example using the two horizontal lines is shown in figure 2-8. The average diameter of all fibers used in this study was 18.54μ with a standard deviation of 1.44μ , a minimum of 13.86μ , and a maximum of 41.36μ . The maximum was two fibers on top of one another measured at two of the five measurements for that fiber sample.

2.3 Single Fiber Heater

A custom heater was designed and fabricated to heat 10 mm gage length single fiber samples to temperatures between room temperature and the melting temperature (~ 150 °C) [67]. The design took into account the following requirements:

- Allow placement of gripped fibers into the heating channel
- Minimize difficulty in accessing the fiber channel to avoid post-test fiber damage
- Rapidly heat the fiber to minimize artificial annealing
- Provide accurate real-time temperature measurements of the fiber channel

- Maintain a consistent and symmetric thermal profile along the gage length of the fiber
- Maintain repeatable heating profiles between tensile tests

The fiber heater was constructed from oxygen-free high thermal conductivity (OFHC) copper 3.5” in length with a hexagonally-shaped projection in the center. A width of 9.77 mm was chosen to allow for an air insulation layer between the heater surface and the grips for 10 mm gage length samples. The copper heater was cut into two equal halves through the width dimension to allow the heater to be placed around gripped fiber samples. The fiber channel is centered in the hexagon across the width of the heater with a 1.016 mm (.040”) diameter. 20 W resistance cartridge heaters (Omega CSS-10120/120V) were selected for rapid heating rates. Two cartridge heaters are inserted into the top and bottom hexagonal projections and attached to a voltage controller to regulate the heat output. For real-time temperature measurements, small diameter thermocouples (Omega HTTC36-K-116G-2) are inserted in diagonally symmetric positions across the cut surface of the heater. Steel guide posts are located diagonally symmetric and opposite to the thermocouples to provide consistent alignment of the heater and to prevent contact with the fiber sample when closing. Once the fiber sample is loaded, two socket capped machine screws are used to tighten the two heater halves together. The open heater is shown in Figure 2-9 (left). The diagonally opposed components and OFHC copper provide a constant, symmetric, and repeatable heating profile in the fiber channel.

A supporting stand for the fiber heater was 3D printed with ABS plastic and connected to an X-Y-Z translation stage to allow the lower half of the fiber heater to be moved away from the fiber gripping area. ½” Teflon spacers are used to insulate the heater from the ABS stand, as shown in Figure 2-9 (right). A base was also 3D printed with ABS plastic

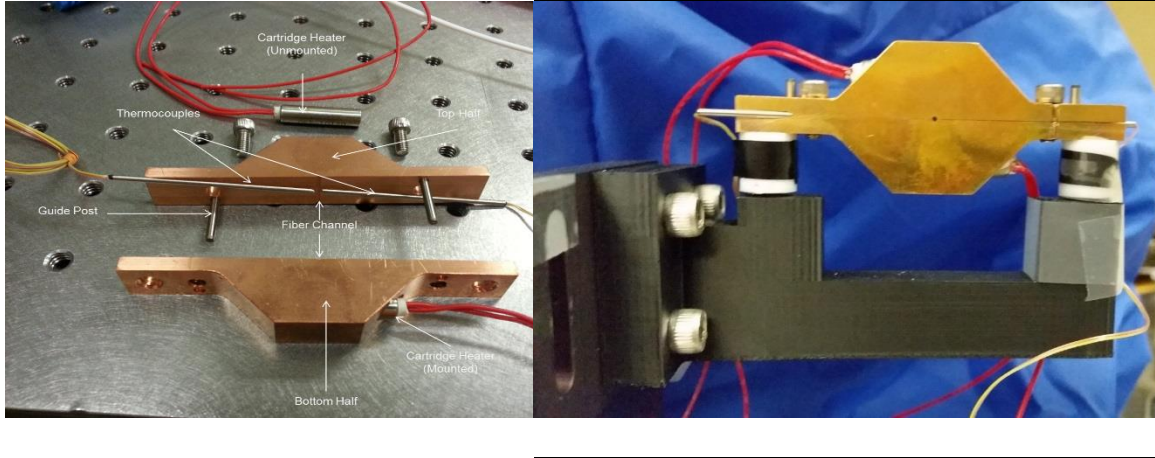


Figure 2-9: (Left)The single fiber heater in the open position. One cartridge heater is shown unmounted for reference. (Right) The single fiber heater on the supporting stand with teflon spacers.

for the X-Y-Z translation stage and for the electrical connections between the cartridge heaters and voltage controller. The heater, stand, and base with translation stage will be referred to as the heater assembly. The heater assembly is shown in Figure 2-10.

The thermocouples in the heater assembly were thermally calibrated using a butt-welded small diameter wire thermocouple (Omega CHAL-005-BW). The wire and heater thermocouples were first calibrated at 0 °C in an ice bath using a dual channel digital thermometer (Omega HH12B) with a .1°C resolution. The wire thermocouple was then glued to a U-shaped 3D printed ABS plastic mount which allowed the wire to be free-floating when placed into the heater channel. The wire mount was then attached to an X-Y-Z translation stage and the thermocouple junction was placed in the center of fiber channel. The calibration setup is shown in Figure 2-11. A voltage controller was set to 120 V and heating cycles were conducted for 4 minutes while measuring thermocouple temperatures every 5 seconds. Between heating cycles, the heater was cooled to 20 °C before the next run was started. An average of three runs for each thermocouple were used to calculate time-temperature curves. Using these curves, the correction between the

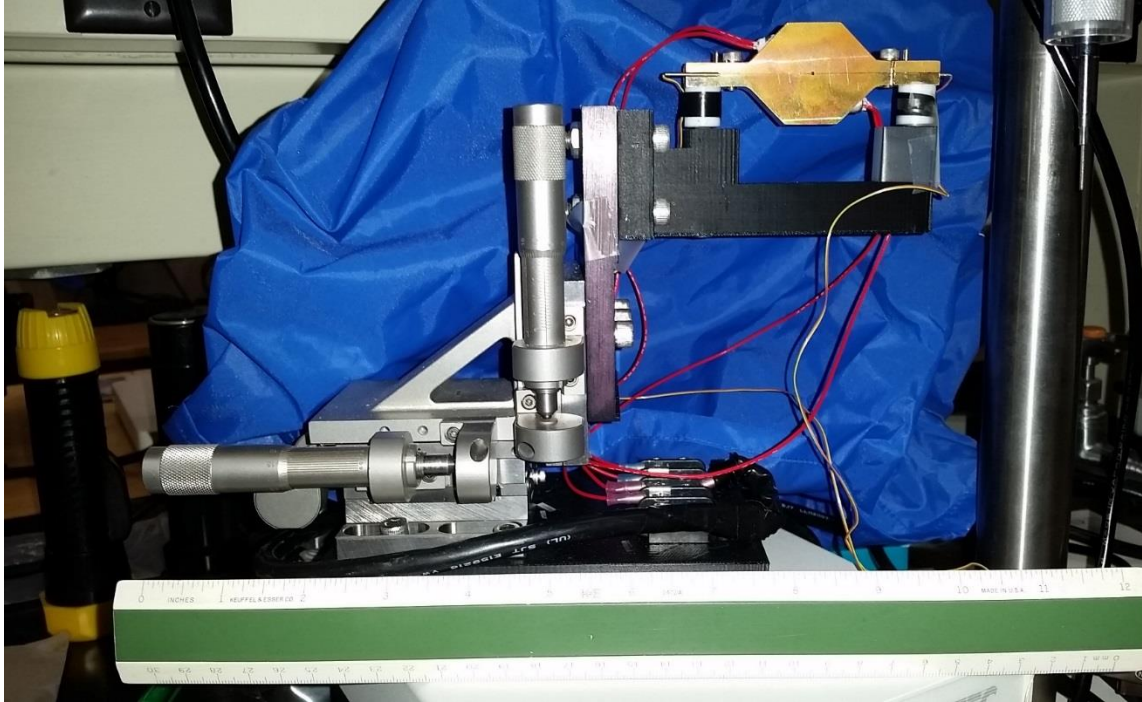


Figure 2-10: The heater assembly with single fiber heater, support stand, X-Y-Z translator and base with electrical wiring. A ruler is included on the bottom of the image for reference.

heater thermocouples and the fiber channel was determined for each temperature for the temperature-strain-rate experiments. The wire thermocouple was then translated in the X, Y, and Z directions using the same heating protocol to determine the change in fiber channel temperature with respect to the position. Heating cycles were conducted in the two circular axes of the channel up to .15 mm from the center with a spacing of .05 mm in both the positive and the negative directions. The change in temperature from the center for these directions was found to be less than 2°C. In the long axis of the fiber channel, tests were conducted to a maximum of 5 mm with a spacing of 1 mm. The change in temperature from the center for the long axis was less than 9°C. It must be noted that for these X-Y-Z tests, the fiber channel was open to air compared to the temperature-strain-rate experiments where the fiber grips almost enclose the fiber channel

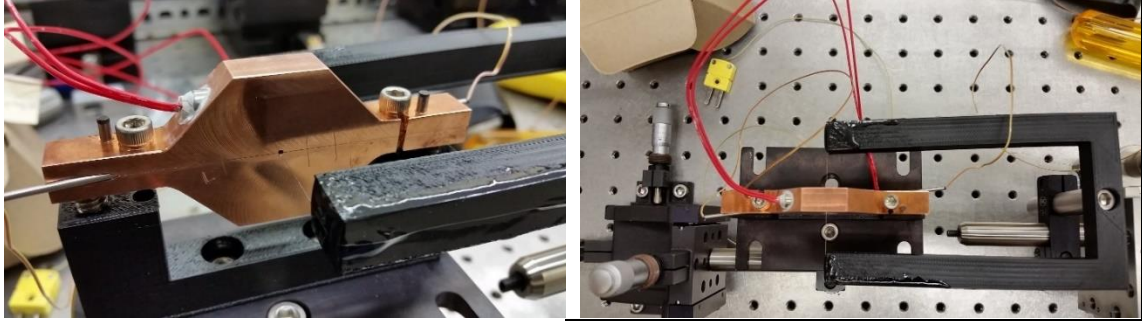


Figure 2-11: (Left) The closed single fiber heater in the open position with the calibration wire thermocouple in the fiber channel. (Right) The top view of the setup displaying the U-shaped wire thermocouple mount and X-Y-Z translation stage setups.

(9.77 mm heater width for 10 mm fiber samples). The physical design of the grips prevented the X-Y-Z tests from being conducted with the grips enclosing the fiber channel. Therefore, the 2°C difference in the circular axes and 9°C difference in the long axis are overestimations of the variation in temperature in the fiber channel.

2.3 Fiber Grips

Fiber grips were design and fabricated to directly grip UHMMPE single fiber samples for uniaxial tensile testing [67]. The design took into account the following requirements:

- Allow templated-fibers to be positioned and gripped
- Minimize the length of fiber sample outside the fiber heater
- Minimized fiber damage from gripping
- Allow for a repeatable gripping force between tests
- Minimize difficulty in accessing the fiber channel to avoid post-test fiber damage
- Impedance match the construction material with the fiber-SHTB

The grip design was based on those used by Kim and Sanborn [44, 50] where the grips consist of a base and a removable top that sandwich the single fiber. The gripping pressure is created by tightening two screws connecting the top and bottom halves. Plastic tabs are used on the top and bottom that contact the fiber. The new design used in this study modified this design by changing from the rectangular edge-recessed plastic

tabs to T-shaped plastic tabs that extend to the grip edge. This allows the gripping area to extend to the edge and minimizes the length of fiber sample that is outside of the fiber heater. This long axis of the T-shape is also approximately 50% longer than the previous tabs (6.58 mm vs. 4.97 mm) allowing for more gripping surface area on each side of the fiber sample. Another difference in the design is the use of two diagonally opposed guide posts to consistently align the top of the grip with the bottom and to keep the gripping pressure normal to the T-surface. This prevents sliding of the top grip from causing damage to the fiber and allows for easy removal of the grip top for post-failure analysis of the fibers. The CAD drawings of the fibers are shown in Figure 2-12.

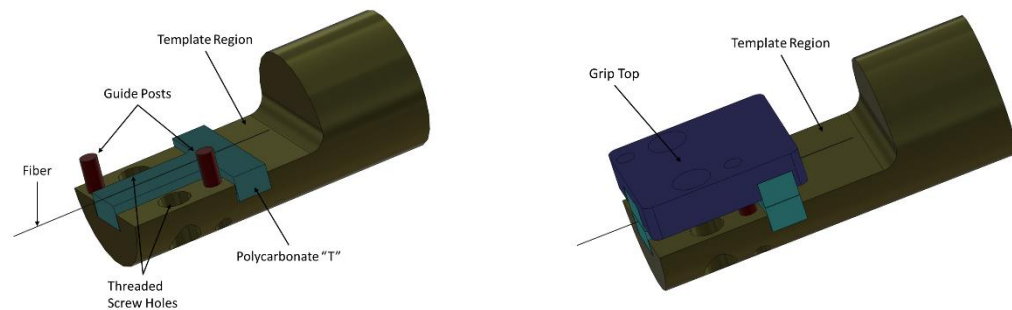


Figure 2-12: (Left)The grip bottom displaying the fiber, polycarbonate “T”, guide posts, screw holes, and template area. (Right) The closed grip showing the top in position without the 0-80 screws.

The gripping pressure is consistently applied by using an electric torque screwdriver to tighten two 0-80 steel screws. Tensile tests were conducted to determine the gripping torque that would maximize gripping while minimizing fiber damage which can induce failure at the interface of the grip edge and the fiber. A torque of .0219 N-m was found to have the best performance as shown by average tensile strength and average strain-to failure analyses. Below is the formula for calculating downward force from an

applied torque where F is the downward force, T is the applied torque, c is the coefficient of friction of the threading, and D is the screw outer diameter. Using parameters for steel 0-80 screws with an outer diameter of 1.524 mm and assuming a steel coefficient of friction of .2, a downward force of approximately 71.9 N is applied in the grips.

$$F = \frac{T}{cD} \quad (\text{Eqn 2-1})$$

First, a set of grips was fabricated with 6061 Al but the strength of the material was affected from the machining process and resulted in shearing of the 0-80 threading when tightening the 0-80 screws.

A new grip material was selected by matching the strain-wave speed with the 6061 Al fiber-SHTB using Eqn 1-2. A second set of grips was made from 303 stainless steel which is strain-wave speed matched to 6061 Al by having both its Young's modulus and density increased by approximately three times. The 303 steel was not affected by the machining process and retained its strength during screw tightening. The 303 steel grips were used for this study.

2.5 Tensile Experiments

Tensile experiments were selected to investigate the change in mechanical behavior between room temperature and the melting temperature and from quasi-static to dynamic strain-rates. A 15 °C temperature step was selected for the entire temperature range with 10 °C step between 65 °C to 85 °C near the α -relaxation temperature. An additional temperature at 148 °C was selected to investigate the mechanical properties of the hexagonal phase. A decade strain-rate step was selected for the entire range of strain-rates from 10^{-3} s^{-1} to 10^3 s^{-1} . No instrument is available to investigate the range between

10^1 s^{-1} to 10^2 s^{-1} . The dynamic instrument has a lower limit of 500 s^{-1} and an upper limit of 10^3 s^{-1} . Both of these limits of the instrument were selected to provide the largest range of dynamic strain-rates possible.

In summary, the 11 temperatures selected were $20 \text{ }^\circ\text{C}$, $35 \text{ }^\circ\text{C}$, $50 \text{ }^\circ\text{C}$, $65 \text{ }^\circ\text{C}$, $75 \text{ }^\circ\text{C}$, $85 \text{ }^\circ\text{C}$, $100 \text{ }^\circ\text{C}$, $115 \text{ }^\circ\text{C}$, $130 \text{ }^\circ\text{C}$, $145 \text{ }^\circ\text{C}$, and $148 \text{ }^\circ\text{C}$. The 6 strain-rates selected were 10^{-3} s^{-1} , 10^{-2} s^{-1} , 10^{-1} s^{-1} , 10^0 s^{-1} , 500 s^{-1} , and 10^3 s^{-1} .

2.5.1 Low and Intermediate Strain-Rates

A Bose Electroforce 3100 with 2.5 mm displacement and 22 N load cell was used to conduct uniaxial tensile tests on UHMPE single fibers at constant strain-rates of 10^{-3} s^{-1} , 10^{-2} s^{-1} , 10^{-1} s^{-1} , and 10^0 s^{-1} . The crosshead displacement speed was .01 mm/s, .1 mm/s, 1 mm/s, and 10 mm/s for 10^{-3} s^{-1} , 10^{-2} s^{-1} , 10^{-1} s^{-1} , and 10^0 s^{-1} , respectively. A maximum displacement was set to 2.49 mm (to prevent software error messages from appearing at the maximum displacement). Data captures were set to trigger on a displacement of .001 mm \pm .05%. Recordings were set to record one scan with scan times of 200 s, 20 s, 2 s, and .4 s for 10^{-3} s^{-1} , 10^{-2} s^{-1} , 10^{-1} s^{-1} , and 10^0 s^{-1} tests, respectively. In the event of a false trigger, the automatic rdr file extension captures data for an extended timeframe of 64 total scans. Points per scan were 2048 for all rates except for the 10^0 s^{-1} rate where the instrument capture limits allowed only 2000 points in a .4 s scan (5000 Samples/s record rate). To reduce the noise in data acquisition, the load cell digital filter was set to 1000 Hz, 100 Hz, 10 Hz, and 1 Hz, for 10^{-3} s^{-1} , 10^{-2} s^{-1} , 10^{-1} s^{-1} , and 10^0 s^{-1} , respectively. Key test parameters for each strain-rate are listed in Table 2-1. The recorded parameters for each tensile test were time in seconds, displacement in mm, and load in N.

Strain-rate [s^{-1}]	Crosshead Displacement Speed [mm/s]	Scan Time [s]	Points per Scan	Load Cell Filter Digital [Hz]
10^{-3}	.01	200	2048	1
10^{-2}	.1	20	2048	10
10^{-1}	1	2	2048	100
10^0	10	.4	2000	1000

Table 2-1: Key instrument test parameters for the Bose Electroforce 3100 Universal Testing Machine.

A ceramic thermal standoff was placed between the load cell and the grips to prevent thermal runoff from affecting the load measurement. A silicon carbide female-threaded cylindrical standoff 1.5" in length with a .75" outer diameter with 18-8 stainless steel screw thread adapters were used and is shown in Figure 2-13.

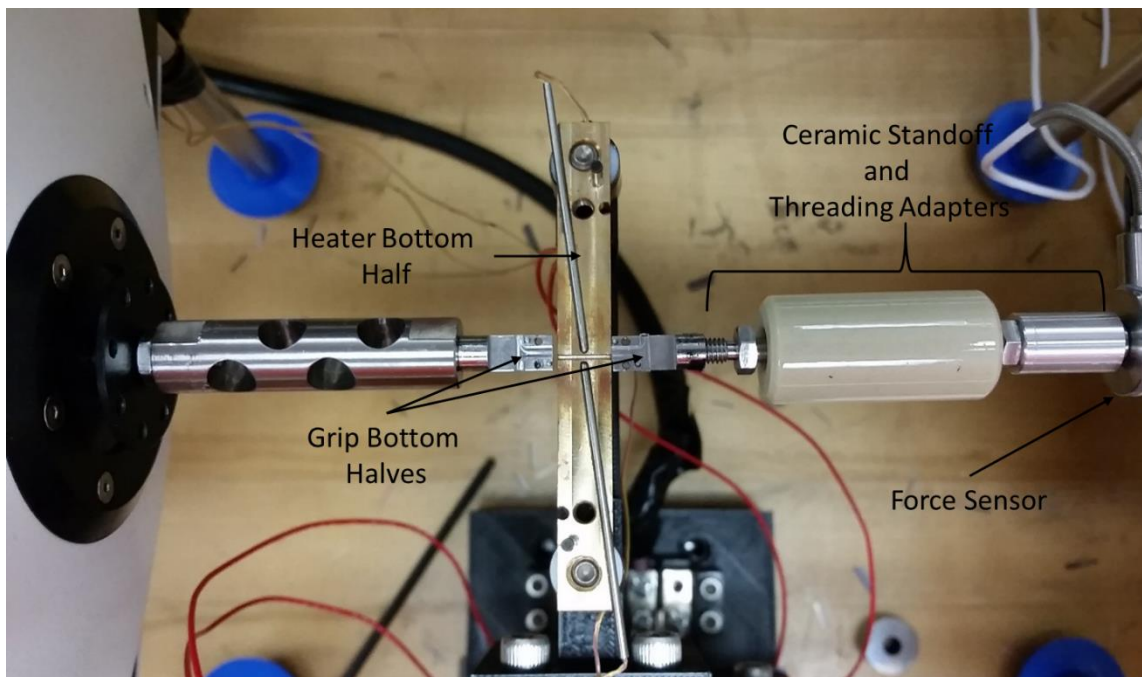


Figure 2-13: The Bose 3100 fiber gripping area including grips, heater, standoff assembly, and force sensor.

For the temperature-strain-rate fibers, the gage length was set by a metal spacer with a thickness of 10.17 mm between the fiber grips. 10.17 mm was used to allow a .2 mm air insulation layer between the heater and the grips to minimize the heating of the

grips and the load sensor. This position was set as the zero-displacement point and the Bose 3100 would return to this position for subsequent tensile tests. For the tensile tests with gage lengths other than 10 mm, an electronic slide caliper with .005 mm resolution was used to set the crosshead spacing.

To load a fiber for tensile testing, the fiber heater would be open and the bottom half is lowered below the gripping area. The grip polycarbonate “T”s are be rinsed with ethanol and wiped with a wooden cotton-tipped swab to remove and residue from previous tests. The grips are be set to the zero-point (10.17 mm spacing). The templated fiber is then place across the open grips (Figure 2-14 Top Right) and a Zeiss Stemi-2000 Stereo Microscope with a 6.5X to 50X magnification range was used to aid in the centering and alignment of the fiber. The grip tops are then placed on top and

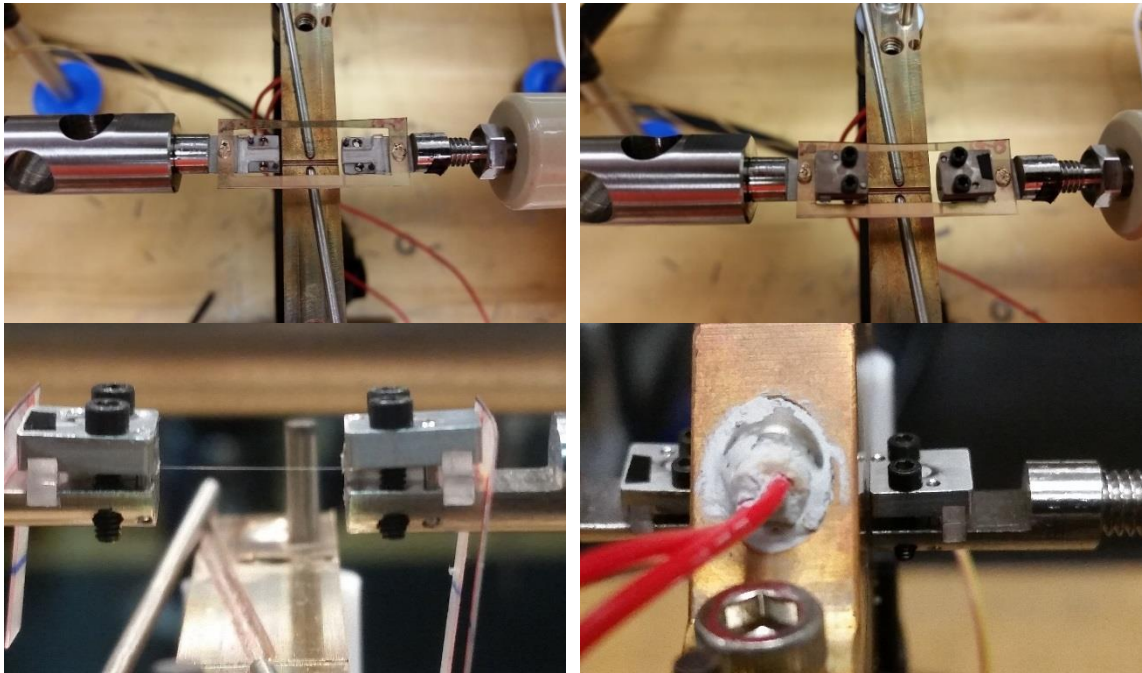


Figure 2-14: (Top Left) A templated fiber sample placed on top of the open grips and aligned. (Top Right) A gripped fiber before the template is cut away. (Bottom Left) A gripped fiber with the template cut away. (Bottom Right) A fiber sample gripped, in the closed heater channel and ready for testing. This image also shows the spacing between the grip and heater.

tightened using a HIOS CL-2000 electric torque driver (Figure 2-14 Top Left). The template is then be cut on both sides in area between the gage length marker lines (Figure 2-14 Bottom Left). With the aid of the stereo microscope, the heater lower half is then raised so the fiber was half way into the lower half of the fiber channel. The fiber is also translated to be in the center of the channel. The heater top is then placed on top and the force sensor readout is watched to see if the fiber is moved during this process. The heater screws are then hand-tightened. The sample is now heated using the voltage controller to provide the correct power to the cartridge heaters and held at the testing temperature. Once at temperature, the tensile test is started. The overall Bose 3100 testing area is shown in Figure 2-15.

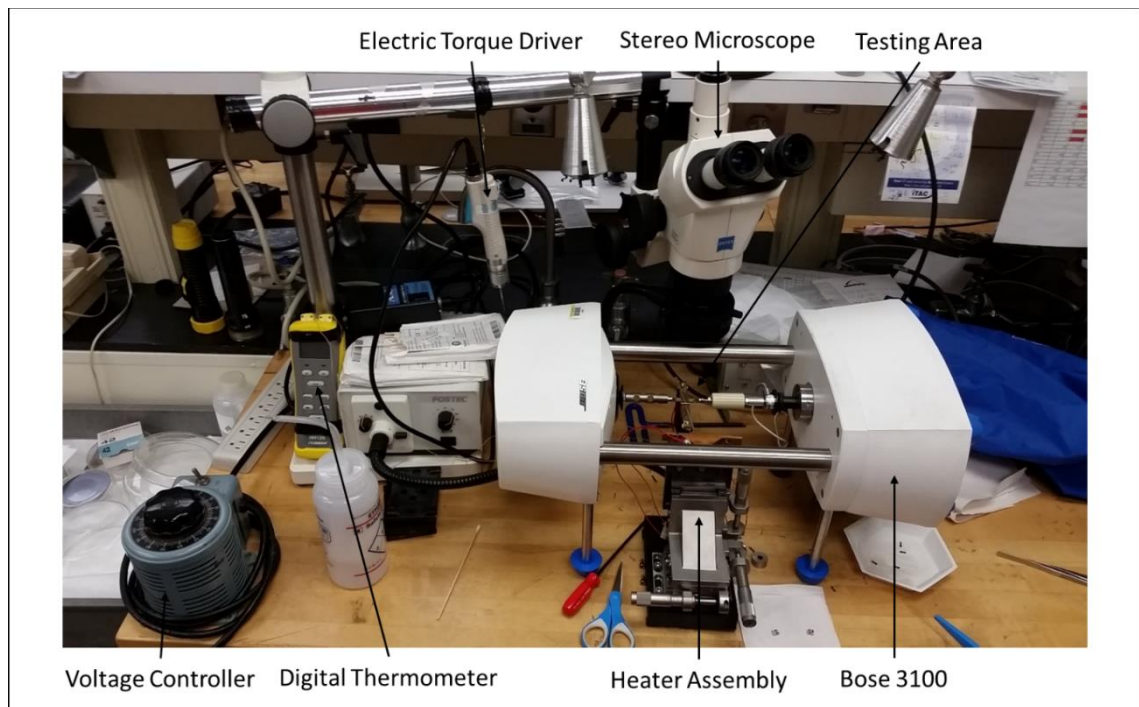


Figure 2-15: The Bose 3100 fiber testing area including Bose 3100, testing area, stereo microscope, electric torque driver, heater assembly, digital thermometer and voltage controller.

2.5.2 High Strain-Rates

A fiber Split-Hopkinson Tension Bar previously with a 22 N dynamic load cell was used to conduct uniaxial tensile tests on UHMMPE single fibers at average strain-rates of 500 s^{-1} and 10^3 s^{-1} . The instrument is located at Aberdeen Proving Ground in Maryland and was used in collaboration with the Weapons Research and Materials Directorate of the Army Research Laboratory. The instrument uses a gas-driven system to fire a brass striker tube into pulse shaper material located on a flange at the end of the incident bar, as shown in Figure 1-9 [44]. For the 500 s^{-1} strain-rate, a gas firing pressure of $20 \pm .20$ psi was used and a soft annealed Cu annulus made of eight .1 mm Cu tapes was used as the pulse shaper. At the 10^3 s^{-1} strain-rate, a gas firing pressure of $80 \pm .20$ psi was used and the striker tube was able to shear off crescent-shaped sections of the .1 mm Cu tapes which would jam the gas firing mechanism and require disassembly of the gas firing system each tensile test. To mitigate this issue, a soft annealed solid Cu annulus 1.09 mm (0.043") thick was used as the pulse shaper. The new solid pulse shaper was not sheared by the striker tube and gave repeatable pulse shapes between subsequent tensile tests. However, at this strain-rate, the impact tube tip became deformed over time and approximately 12.7 mm (0.5") sections for the tube were removed when the deformation prevented reloading in the gas-driven system. An optical setup is used to measure displacement [44, 49-51] and is shown schematically in Figure 1-9 and pictorially in Figure 2-16. The optical system is calibrated weekly at a minimum by using a linear translation stage and a driving plate to move the tension bar increments of .0508 mm (.002") while the optical sensor voltage is recorded. Linear fits are used to get the correlation between sensor voltage and displacement. The setup is shown in Figure 2-17

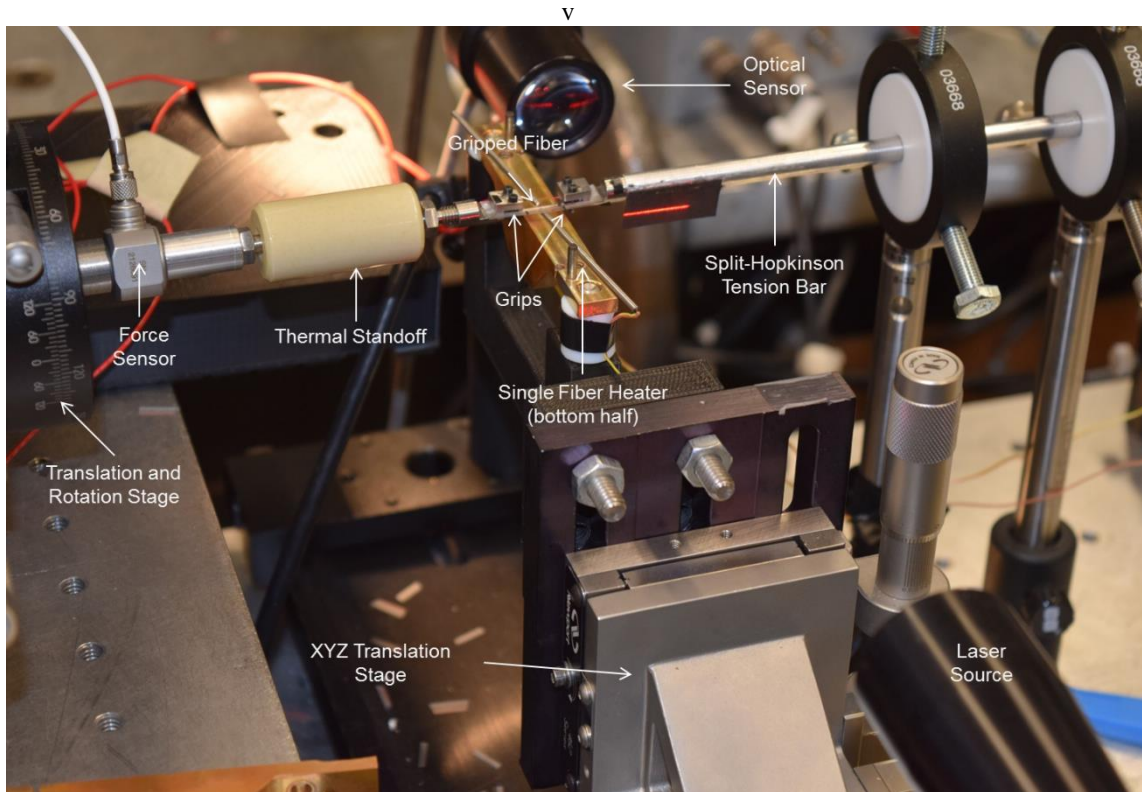


Figure 2-16: An image of the testing area of the fiber-Split Hopkinson Tension Bar (f-SHTB) showing the measurement devices including the piezoelectric load cell, thermal standoff assembly, closed grips with fiber sample, heater bottom half, and optical setup for measuring displacement.

(Left) and an example of a linear fitting is shown in Figure 2-17 (Right). The optical system was calibrated 11 times over the course of this study. Each fiber tensile test was matched to the proper coefficient for calculated strain values. Two strain gages are mounted half way down the bar on opposite sides and are attached to a wheatstone bridge circuit including a variable resistor to set the bridge voltage to near zero before each tensile test, shown in Figure 2-17 (Left). Data capture is triggered off the strain gage voltage when it above 150 mV for more than 25 microseconds. The dynamic load cell has been calibrated to 0.794 lbs/mV and is connected to a Kistler 5010 Dual Mode Amplifier and converts the load cell output voltage into pounds of force. An HBM Genesis High Speed GEN7t Transient Recorder and Data Acquisition System with Differential Input

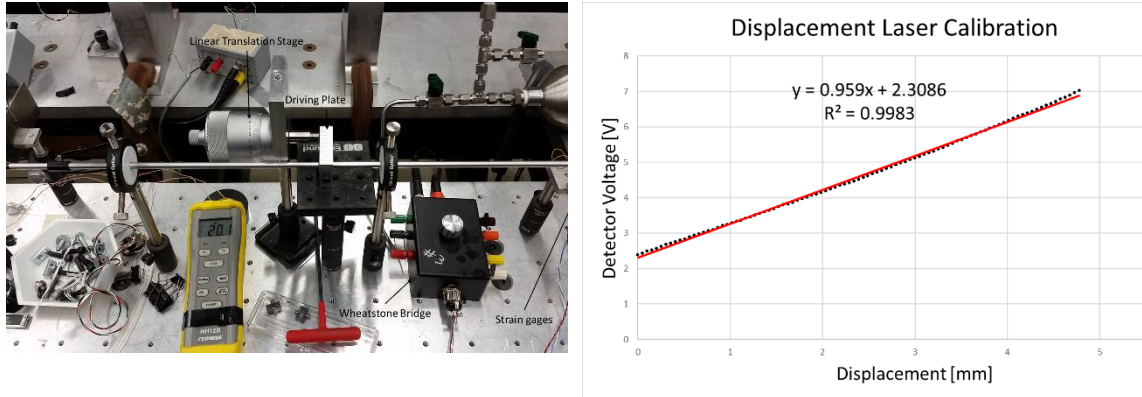


Figure 2-17: (Left)The displacement calibration setup showing the linear translation stage and driving plate. Also shown in this image are the strain gages and wheatstone bridge with variable resistor. (Right) An example of the linear fitting of a voltage-displacement data. The black dots are the measured data and the red line is the linear fit. The line equation and R^2 values are also displayed.

Card and Perception software was used to collect simultaneous time [s], strain gage wheatstone bridge voltage [V], optical displacement voltage [V], and load [lbs]. To prevent heating of the load cell, the ceramic thermal standoff assembly was also used with fiber-SHTB as shown in Figure 2-16. The dynamic load cell has a female socket for attaching a grip. The tightening the thermal standoff assembly, the lever-arm force from the weight of the thermal assembly, and the propagation of dynamic strain wave during these experiments caused the thermal standoff to impart an artificial bias to the load measurements. The bias was corrected by conducting 10 tensile tests at room temperature with and without the thermal assembly. This correction process was done each time the thermal standoff was initially attached or tightened. For this set of experiments, this occurred twice.

For the first calibration, only 500 s^{-1} strain-rate tests had been conducted and the average force difference between the two sets of 10 samples was 0.2258 N (0.05077 lbs). Factors that can affect the failure force of a fiber include the individual fiber diameter and

the pre-tension force from the sample preparation and gripping procedures. To determine if either influenced the change in force values between the sets of samples with and without the thermal standoff assembly, each individual average diameter and the pre-tension force for each fiber in the two sets was compared and are shown as whisker plots in Figure 2-18. Student's t-tests were conducted to test the null hypothesis for the average

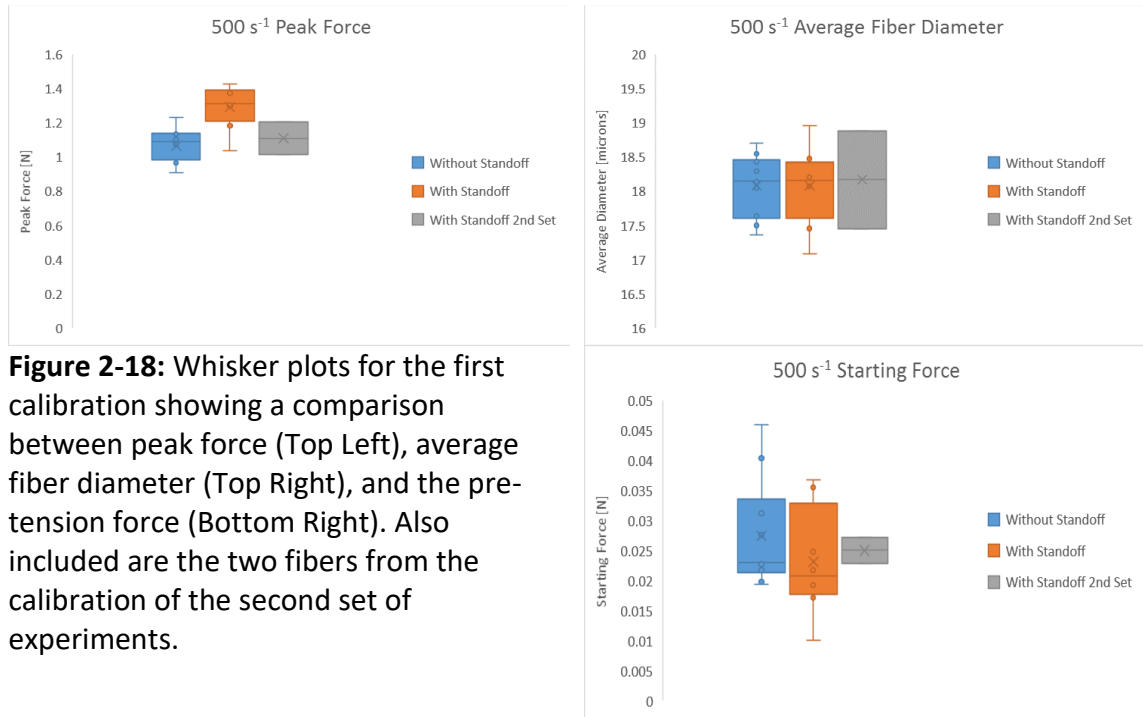


Figure 2-18: Whisker plots for the first calibration showing a comparison between peak force (Top Left), average fiber diameter (Top Right), and the pre-tension force (Bottom Right). Also included are the two fibers from the calibration of the second set of experiments.

differences between peak force, average fiber diameter, and pre-tension force.

Probabilities of 0.001219, 0.9939, and 0.3353 were found, respectively. Using a rejection criterion of 5 %, the tests indicate that there is a statistical difference in peak force but not in the average fiber diameter and starting force. The t-tests are summarized in Table 2-2.

A force correction of 0.2258 N was applied to the samples tested with this calibration.

For the second calibration, the tensile tests consisted of 18 samples at 500 s⁻¹ and all of the 10³ s⁻¹ strain-rate data. For this set of experiments, a conic steel washer was inserted between the load cell and the ceramic thermal standoff assembly to reduce the

	500 s ⁻¹								
	Peak Force [N]			Average Diameter [microns]			Starting Force [N]		
	Without	With	With (2nd set)	Without	With	With (2nd set)	Without	With	With
Mean	1.066	1.291	1.109	18.08	18.08	18.17	0.02744	0.02314	0.02314
Variance	0.010	0.016	0.018	0.20	0.33	1.02	0.00008	0.00008	0.00008
N	10	8	2	10	8	2	10	8	8
P (vs. without)	N/A	0.001219	0.7422	N/A	0.9939	0.9227	N/A	0.3353	0.3353

Table 2-2: The summary of the Student's t-tests for the first set of experiments showing a statistically significant change in peak force and no statistically significant contribution from the average fiber diameters or pre-tension forces.

effects on the load. Two of the 18 500 s⁻¹ strain-rate samples were conducted at room temperature and had a student's t-test probability of .7422 when compared to the previously corrected force values, indicating they were not statistically different. Therefore, the 18 500 s⁻¹ strain-rate samples were not corrected. The average force difference between the 10 samples run with and without the thermal standoff at 10³ s⁻¹ was -.04212 lbs. Student's t-tests were also conducted for this set of experiments and probabilities of .009112, .1702, and .7963 were calculated for peak force, average fiber diameter, and pre-tension force, respectively, indicating that the combination of the washer and the strain wave had a statistically significant compressive effect on the load cell measurements and differences between the average fiber diameters and pre-tension forces were not statistically significant. The whisker plots are shown in Figure 2-19. The plots show a significant difference in average maximum force values but no significant difference in average fiber diameter nor starting force for both sets of calibration. Each force correction value is for the maximum force, corresponding to the Ultimate Tensile Strength (UTS). To correct the stress-strain plots the load values were multiplied by an individual correction factor calculated by dividing the difference between the maximum load [lbs] and the calibration correction load [lbs] by the maximum load [lbs], shown below where C_f is the calculated fiber-specific correction factor, F_{max} is the maximum

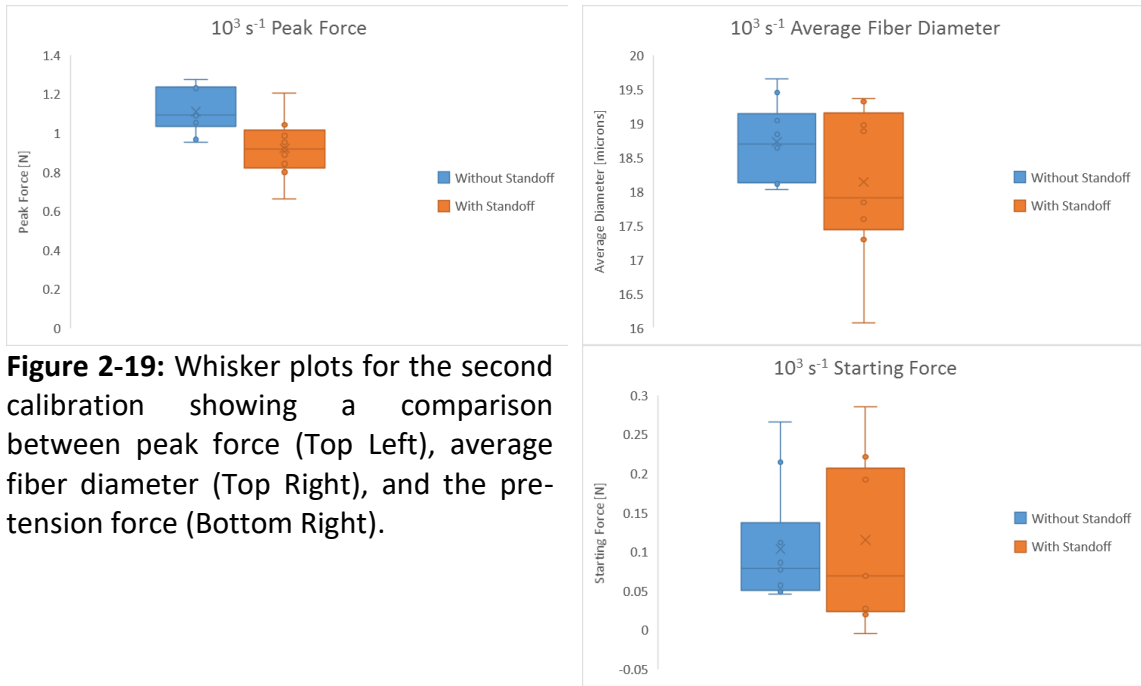


Figure 2-19: Whisker plots for the second calibration showing a comparison between peak force (Top Left), average fiber diameter (Top Right), and the pre-tension force (Bottom Right).

	10^3 s^{-1}					
	Peak Force [N]		Average Diameter [microns]		Starting Force [N]	
	Without	With	Without	With	Without	With
Mean	1.110	0.922	18.73	18.14	0.1037	0.1151
Variance	0.012	0.024	0.30	1.20	0.0057	0.0115
N	10	9	10	9	10	9
P (vs. without)	N/A	0.009112	N/A	0.1702	N/A	0.7963

Table 2-3: The summary of the Student’s t-tests for the second set of experiments showing a statistically significant change in peak force and no statistically significant contribution from the average fiber diameters or pre-tension forces.

experimentally measured load value in lbs for that fiber, F_{calib} is the calibration correction load value in lbs, F_{corr} is the corrected load array in lbs for the entire fiber tensile test, and F_{exper} is the experimentally measured load array in lbs for the entire fiber tensile test. This correction maintains the original shape of the stress-strain curve while shifting the stresses to the corrected load values. These values were converted to newtons and the corrected load arrays are used for stress calculations.

$$\text{Correction Factor} = C_f = \frac{F_{max} - F_{calib}}{F_{max}} \dots \quad \text{..(Eqn 2-2)}$$

$$\text{Corrected Load Array [lbs]} = F_{corr} = C_f F_{exper} \quad \text{(Eqn 2-3)}$$

2.6 X-ray Scattering

Wide Angle X-ray Diffraction was conducted to characterize the crystalline phases of the fibers and their change as a function of temperature. The LeBail method was used to fit collected WAXD spectra. Using this method, known crystalline phases with lattice parameters are used as starting locations to fit the spectra. Two phases were selected for fitting; orthorhombic and monoclinic. The software was then able to fit the spectra by varying the lattice parameters and the crystallite size according to the Scherrer equation, shown below, where τ is the mean size of the crystalline domains, K is a dimensionless shape factor, λ is the x-ray wavelength, β is the line broadening at half the maximum intensity (FWHM) after subtracting the instrumental line broadening, and θ is the Bragg angle:

$$\tau = \frac{K\lambda}{\beta \cos \theta}$$

A Gaussian distribution was used to approximate the amorphous scattering between 19° to 26° values of 2θ . A mean of 22.5°, a variance of 1°, and an area of 187.5. The anisotropic structure of the fibers was corrected using the method described by Litvinov [11].

2.6.1 Wide Angle X-ray Scattering

Wide angle X-ray Scattering (WAXS) was conducted on five Dyneema® SK76 1760 dtex yarn samples. A Bruker D8 diffractometer was used with Cu k_α radiation and a

LYNXEYE detector in a $\theta/2\theta$ Bragg-Brentano geometry. This geometry and use of a sample spinner was selected due to the highly anisotropic nature of the fibers. The sample spinning allows collection of an average of the peaks of differently oriented phases, as shown in Figure 20. Samples were tested with collections between 10° and 60° values of 2θ with a $.02^\circ$ step and one second capture per step. Yarn-sized samples are required over fiber-sized to obtain a measurable diffraction signal during each scan. Yarn samples were aligned on a glass slide coverslips and held in place using scotch tape and scans were collected at room temperature.

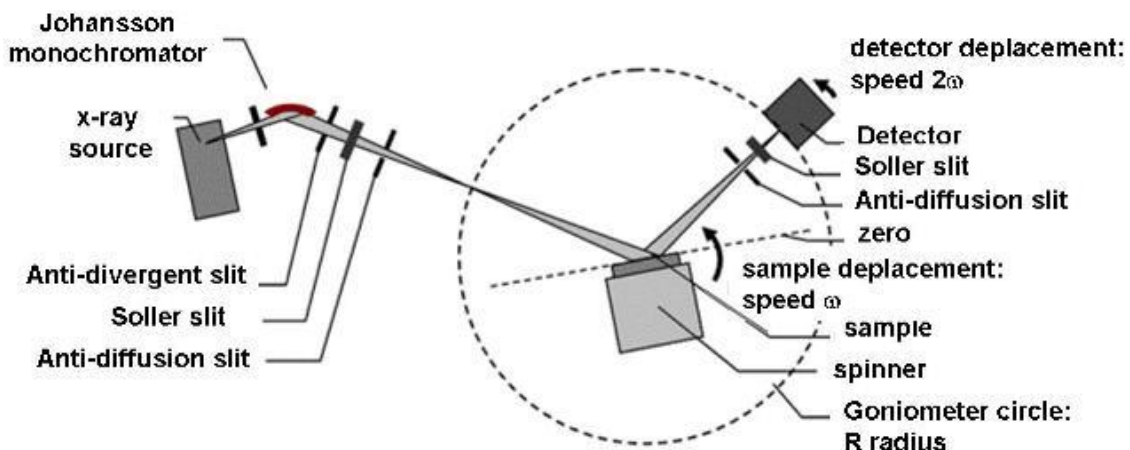


Figure 2-20: A schematic of a Bragg-Brentano geometry and setup for Wide Angle X-ray Scattering showing the spinner location and use for highly anisotropic materials such as fibers. Image taken from [68].

2.6.2 Heated Wide Angle X-ray Scattering

Heated WAXS was conducted on one yarn sample. A Bruker C2 Diffractometer was used with $\text{Cu } k_\alpha$ radiation, and a 2D detector with an Anton Paar DHS 1100 sample stage. The sample stage provided the heating and the sample was constrained using a custom fiber holder. The holder was designed to axially strain the yarn sample while limiting the thermal heating to the fiber region outside of the X-ray beam window. The holder was made from a 19.05 mm x 19.05 mm x 3.175 mm (.75" x .75" x .125") plate of

Al with raised sections to allow the fiber to be wound into an “S” shape with the two ends held in cylindrical capstans. Ceramic pipes, washers, and screws were used to decrease the thermal conductivity to the fiber. A steel set screw was used to apply axial tension and provide thermal conductivity to the fiber region in the X-ray window. The fiber holder is shown in Figure 2-21. The sample was heated from 30°C to the melting temperature with 5°C steps between 30°C and 130°C and 1°C steps above 130°C. The heating rate between steps was 100°C/min and was held at temperature for 5 seconds before a one-minute data capture.

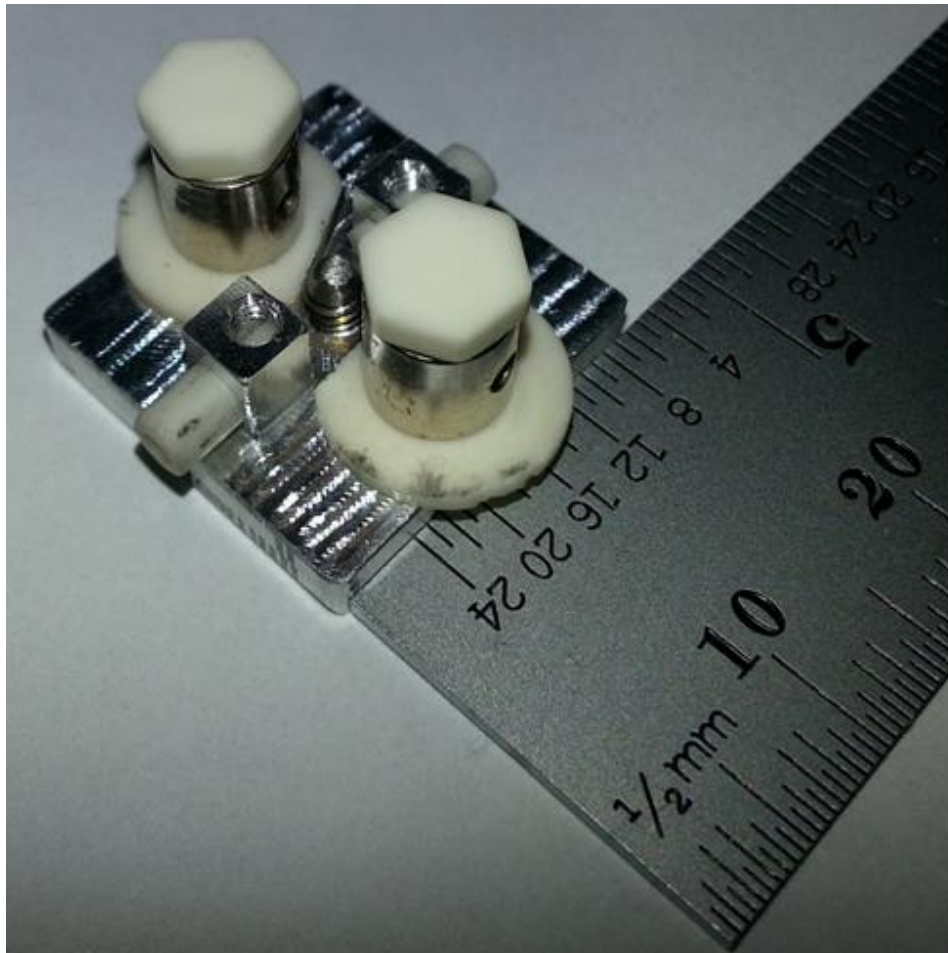


Figure 2-21: An image of the fabricated yarn holder for heated WAXS experiments. The ceramic washers, screws, and tubing insulate the yarn. The steel set screw in the center elevates the yarn to apply a tensile force and conducts heat through the holder to the yarn region in the beam spot.

2.7 Fourier Transform Infrared Spectroscopy

Molecular spectroscopy of UHMMPE yarns was performed using Fourier Transform Infrared (FTIR) Spectroscopy. A Bruker Vertex 80 FTIR Spectrometer equipped with a liquid nitrogen-cooled mercury cadmium telluride (MCT) detector and a Durascope (Smiths Detection) attenuated total Reflectance (ATR) accessory was used in the yarn measurements. Consistent pressure on the yarns was applied using the force monitor on the Durascope. The final scans represent the average of 256 individual scans with a resolution of 4 cm^{-1} between 500 cm^{-1} and 4000 cm^{-1} . Spectral analysis, including spectral baseline correction and normalization, was carried out using the software available with the instrument. Typical standard uncertainties for spectral measurement are 4 cm^{-1} in wavenumber and 5 % in peak intensity. Micro-FTIR was performed using the same instrument, but with the Hyperion microscopy accessory. For this technique, the fiber failure surfaces were enclosed in a diamond anvil cell.

2.8 Scanning Electron Microscopy

Post tensile failure diameter measurements were conducted on fiber failure surfaces using an incident electron beam energy of 2 kV and 0.25 pA probe current, as to not damage the failure surfaces. The fiber samples were viewed under the SEM after sputter coating them with 3 nm to 10 nm of gold. Fiber samples were placed on sample holders using carbon tape. All SEM imaging was conducted on a Helios dual beam FIB. The high contrast images were generated to highlight the crack structure by processing the images on ImageJ software.

Chapter 3: Results

3.1 Characterization

3.1.1 Wide Angle X-ray Scattering

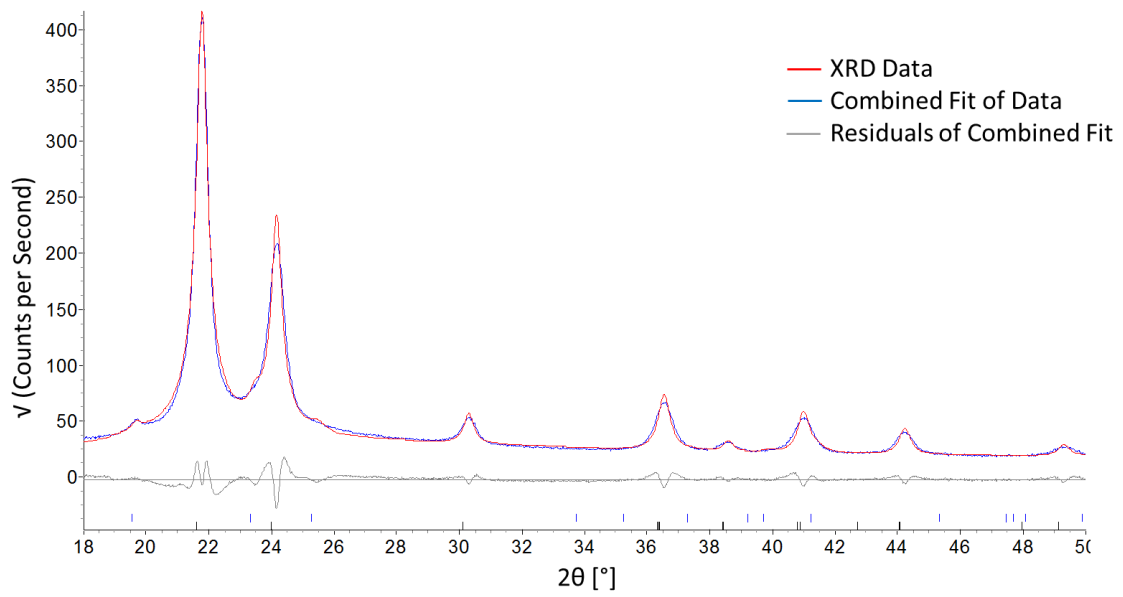
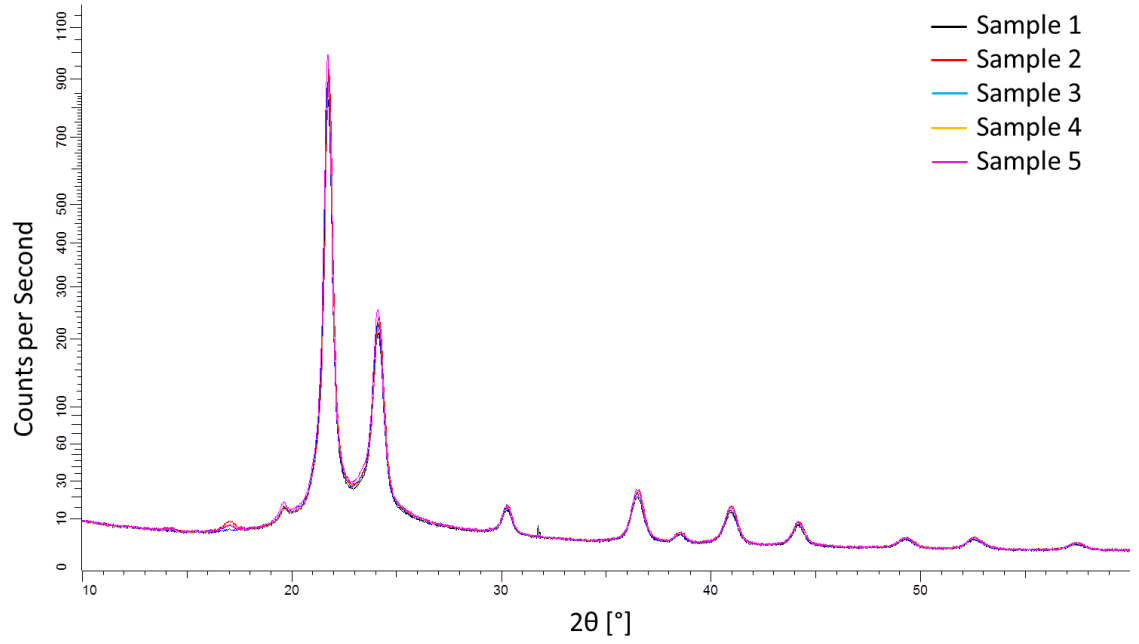
3.1.1.1 Room Temperature Wide Angle X-ray Scattering

X-ray diffraction patterns were collected on five Dyneema® SK76 yarn samples at room temperature. The patterns are shown in Figure 3-1. The patterns were fitted with peaks for the orthorhombic and monoclinic phases. The amorphous phase estimated using a Gaussian distribution centered at $22.5^\circ 2\theta$ with a variance of 1 and an area of 185. The anisotropy of the fibers was corrected for using the method described by Litvinov [11].

The percent phase composition is summarized in Table 3-1 and the average percent phase composition and standard deviation are calculated in the bottom row. The results show that the fibers are highly crystalline with approximately 7.3% oriented amorphous phase composition. The monoclinic comprises approximately 3.2 % of the overall phase composition. The orthorhombic is the most abundant phase comprising approximately 89.5 % of the fiber.

Sample	Orthorhombic	Monoclinic	Amorphous
1	87.8	3.9	8.3
2	90.5	2.7	6.8
3	89.6	3.0	7.4
4	89.5	3.1	7.4
5	90.0	3.3	6.7
Average	89.5	3.2	7.3
Std Dev	1.0	0.4	0.6

Table 3-1: The percent phase composition for five SK76 yarns at room temperature. The average and standard deviation of the five samples is shown in the last row.



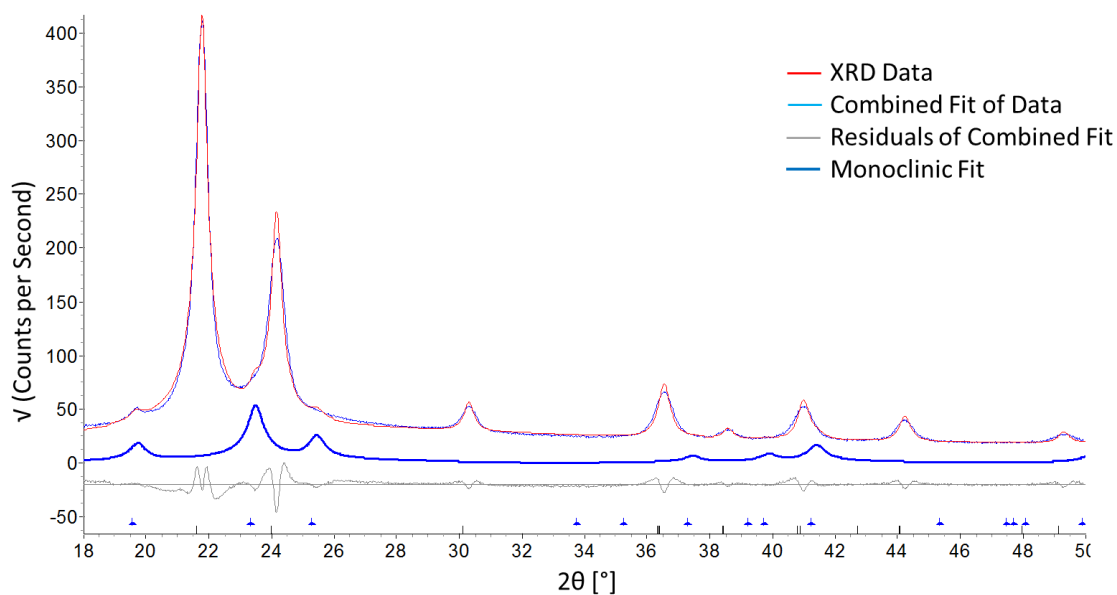
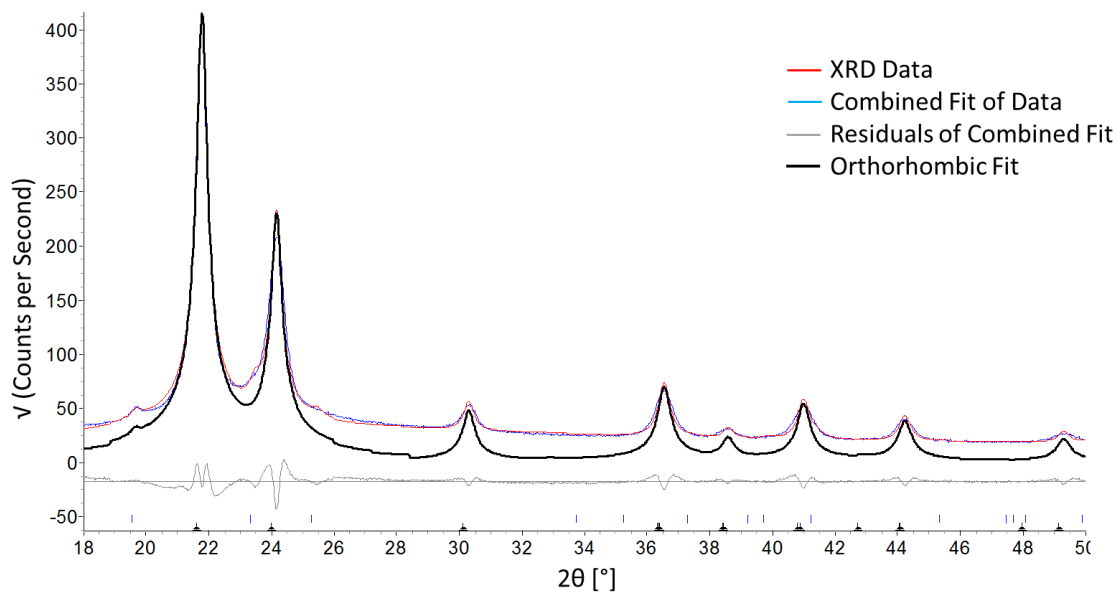


Figure 3-1: (Top) Diffraction patterns for 5 yarn samples. **(Second from top)** An example of the WAXS data for one yarn sample in red and the overall LeBail fitted curve in blue. **(Third from the top)** The orthorhombic fit shown in black and the peak locations shown as black triangles on the x-axis. **(Bottom):** The monoclinic fit shown in dark blue and the peak locations shown as dark blue triangles on the x-axis.

3.1.1.2 Heated Wide Angle X-ray Scattering

Diffraction patterns were taken on a constrained yarn at temperatures from 30 °C to 156 °C using the custom holder described in the experimental section. The patterns are shown in Figure 3-2 (Top). Diffraction patterns were taken from 30 °C to 130 °C with 5 °C steps and from 130 °C to 156 °C with 1 °C steps. The corresponding change in slope of the peak shift with respect to temperature is observed at 130 °C. The temperatures indicate the temperature of the heating stage. Subsequent patterns have been offset by 15 counts in the y-axis direction for clarity.

At low temperatures, the orthorhombic 110 and 200 peaks are observed at approximately 21.5 ° and 23.9 °, respectively. The monoclinic 201 peak is also observed at approximately 36 °. As temperature increases, the peaks become less intense due to thermal scattering and the peak location shift to lower 2-theta values due to thermal expansion. At high temperatures, the extended orthorhombic phase transitions to the hexagonal phase and the hexagonal 100 peak is observed at approximately 20.5°. Figure 3-2 (Bottom) shows a rescaled image between 19.5° to 24.5°. The hexagonal peak begins to form at approximately 151 °C. At this temperature, the orthorhombic peaks begin to decrease rapidly and disappear by 154 °C. The hexagonal phase has the highest peak at 153 °C and the peak disappears at 156 °C. At 156 °C there are no crystallographic peaks for the fiber and it is in the liquid phase. The hexagonal phase is observed to form 5 °C below the melting temperature and there is no longer an orthorhombic phase at 2 °C below the melting temperature.

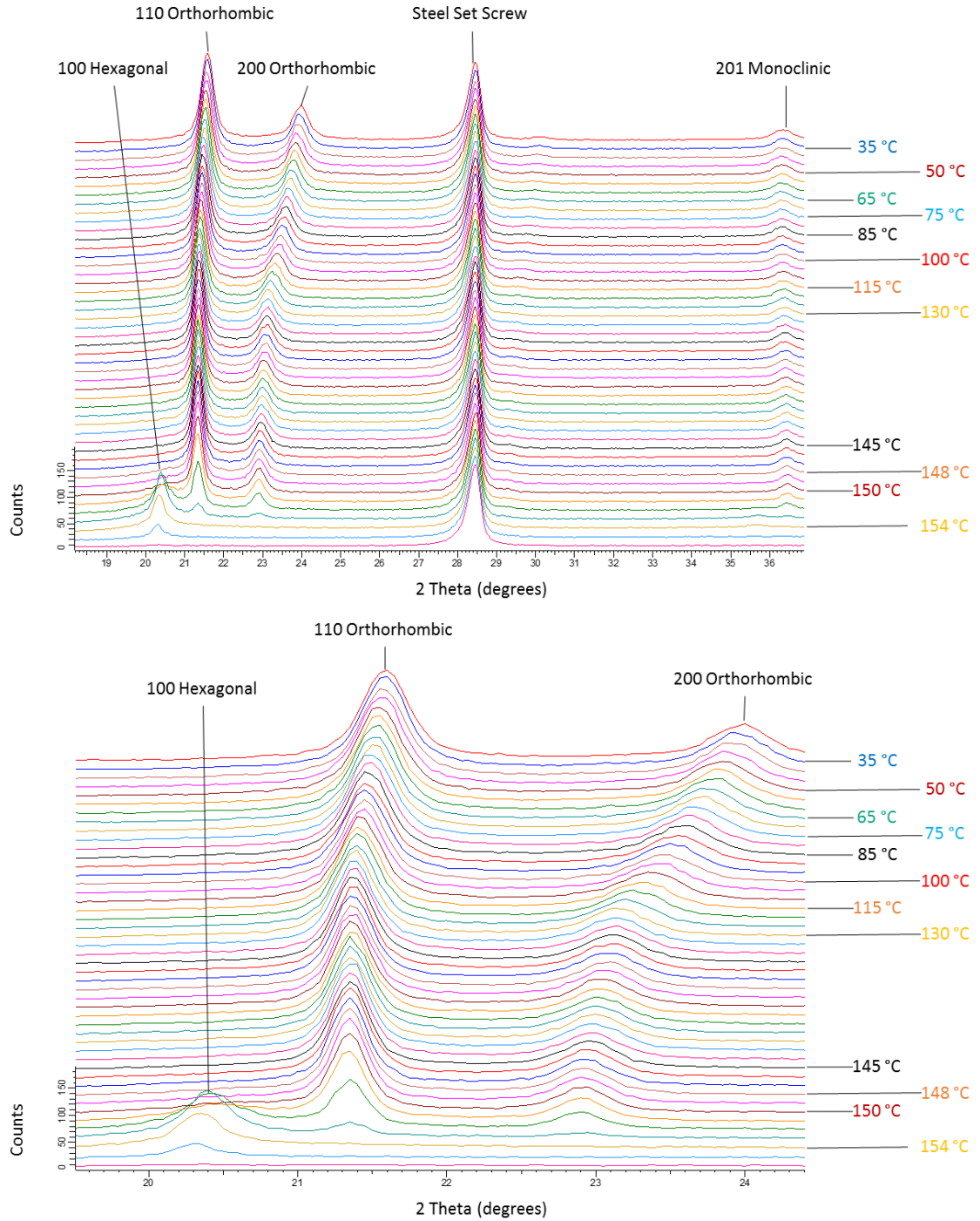


Figure 3-2: (Top) Heated wide angle X-ray scattering of constrained Dyneema® SK76 UHMPE yarn. Temperatures on the right are the temperature of the heating stage. The diffraction patterns were taken from 30 °C to 130 °C with 5 °C steps and from 130 °C to 156 °C with 1 °C steps. The orthorhombic and monoclinic phases are observed at low temperatures. At high temperatures, the extended orthorhombic phase transitions to the hexagonal phase. **(Bottom)** A rescaled image between 19.5° to 24.5° showing the emergence of the hexagonal phase at approximately 151 °C.

3.1.2 Fourier Transform Infrared Spectroscopy

FTIR spectroscopy was conducted on five Dyneema® SK76 yarn samples and the spectra are shown in Figure 3-3. The spectra indicate peaks at 715 cm^{-1} , 1471 cm^{-1} , 2846 cm^{-1} , and 2912 cm^{-1} corresponding to the rocking deformation, bending deformation, CH_2 symmetric stretching, and CH_2 asymmetric stretching, respectively [69]. The CH_2 symmetric and asymmetric stretching have strong intensities. The bending deformation has a medium intensity and the rocking deformation has the lowest intensity. The absent peaks include the CH_2 conformations corresponding to gauche-trans-gauche (gtg at 1368 cm^{-1}), gauche-gauche' (gg' at 1353 cm^{-1}), and end-gauche (eg at 1341 cm^{-1}) [70].

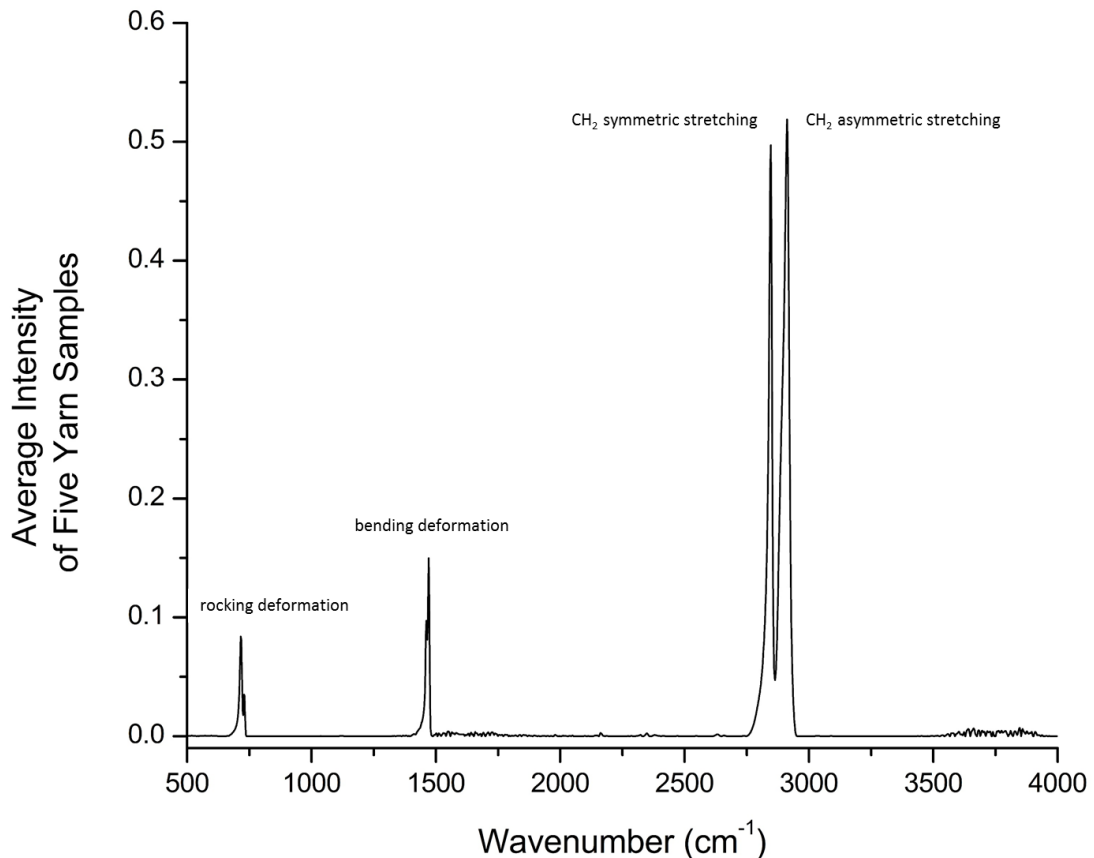


Figure 3-3: The FTIR spectra of five yarn samples showing peaks at peaks at 715 cm^{-1} , 1471 cm^{-1} , 2846 cm^{-1} , and 2912 cm^{-1} which correspond to the rocking deformation, bending deformation, CH_2 symmetric stretching, and CH_2 asymmetric stretching, respectively.

3.2 Tensile Tests

Constant strain-rate to failure tensile tests were conducted on Dyneema® SK76 1760 dtex single fibers at 66 combinations of 11 temperatures from room temperature to the melting temperature (20 °C to 148 °C) and 6 strain-rates from quasi-static to dynamic (10^{-3} s^{-1} to 10^3 s^{-1}). Throughout this chapter, the term strain refers to compliance corrected engineering strain and the term stress refers to engineering stress calculated using the average diameter of the fiber unless otherwise stated. The corrected strain values were calculated according to ASTM C1557-03 [71] using 0.1186 mm/N for the 10^{-3} s^{-1} , 10^{-2} s^{-1} , 10^{-1} s^{-1} , 10^0 s^{-1} strain rates, 0.0692 mm/N for the 500 s^{-1} strain-rate and 0.1365 mm/N for the 10^3 s^{-1} strain-rate.

3.2.1 Categorization and Number of Fibers Tests

864 10 mm gage length fiber samples were prepared. Before tensile testing, 144/864 fibers of the were dedicated for non-tensile purposes including grip torque testing, temperature range selection for the tensile tests, and determining instrument capture settings including data collection rates, load cell digital filters, and trigger parameters. Stress-strain data may not have been recorded for these tests. Tensile testing was attempted on 578/864 fibers leaving 142/864 fiber samples are still available for future studies.

The target number of tensile tests across the temperature-strain-rate study was 440. This includes 5 samples per temperature-strain-rate combination for the four quasi-static and intermediate strain rates, and 10 per combination for the two dynamic strain rates. Of the 578 tensile tests attempted, 23/578 fibers were broken during the grip-loading procedure. 118/578 were repeats of previous tensile tests due to data not being

recorded (from false triggering or human error) or observation of an uncharacteristically low failure strength value coupled with the fiber failing at the grip interface. One of the fibers melted at 148 °C before the tensile test could be conducted. This demonstrates the highest testing temperature of this study is at the lower boundary of the fiber melting temperature range.

After the repeats, 14 had observed failures at the grip-fiber interface, suggesting the grip influenced the failure behavior. However, of these 14, 12 had failure strengths values above the average failure strength for that temperature-strain-rate combination indicating that the grip did not affect the fiber behavior. The data for these 12 were included when calculating the averages for their temperature-strain-rate combination. The remaining two were significantly lower than the average failure strength for that temperature-strain-rate combination, as shown by a student's t-test, and the data were removed before calculating the averages. Both occurred at the 10^3 s^{-1} strain-rate at temperatures of 20 °C and 100 °C. Due to the unavailability of the fiber-SHTB these two tests could not be retested. Additionally, one tensile test in the 500 s^{-1} strain-rate had no recorded data and could also not be repeated resulting in a total of 437 tensile tests used in the temperature-strain-rate study. The issue of availability with the fiber-SHTB will be further addressed in the future work section.

Force-displacement data from the 437 tensile tests were used to calculate fiber mechanical properties for the temperature-strain-rate tensile study. This number is categorized by temperature and strain-rate in Table 3-2. The temperature and strain-rate

Strain-rate [s ⁻¹]	Temperature [°C]											Total	
	20	35	50	65	75	85	100	115	130	145	148		
10 ⁻³	4 (1)	5	5	5	1/4*	0/5	0/5	0/5	0/5	0/5	0/5	55	
10 ⁻²	5	5	5	5	5	5	2/3*	0/5	0/5	0/5	0/5	55	
10 ⁻¹	5	4 (1)	5	5	5	5	5	5	1/4	0/5	0/5	55	
10 ⁰	5	5	5	5	5	5	5	5	5	5	3/2	55	
500	9 (1)	10	9 (1)	8 (2)	10	10	10	10	10	10	9	10	109
1000	4 (4)	10	10	10	9 (1)	10	9 (1)	10	10	10	10	10	108
Total	38	40	39	40	437								

Table 3-2: The number of fibers tests, failures at the grip interface, and non-failures in each testing combination for the temperature-strain-rate tensile study. A total of 437 fibers were tested and used for this study. The 12 grip interface failures are annotated in parenthesis. The non-failures are indicated on the right side of a solidus. The highlighted region depicts the non-failure surface.

where the failures at the grip interface occurred are shown in the table with parentheses. For example, a 4 (1) indicates that there are five total fibers in that temperature-strain-rate combination and one of them was observed to fail at the fiber interface. The highlighted regions of the table indicate regions where the fibers were strained to the instrument maximum of 2.5 mm, or 25% engineering strain for 10 mm fibers, without the fiber failing. Within these regions both the number of fibers that failed and the number that did not fail, called “non-failures”, are presented and separated by a solidus. For instance, a 1/4 indicates that there are five fibers total, one failed, and four were non-failures. A step-like shape of the highlighted area is observed and illustrates that as strain-rate is increased by a decade, the corresponding temperature where non-failures begins increases by two temperature steps. The step sizes between decades are 25 °C, 30 °C, and 18 °C for the 10^{-3} s^{-1} to 10^{-2} s^{-1} , 10^{-2} s^{-1} to 10^{-1} s^{-1} , and 10^{-1} s^{-1} to 10^0 s^{-1} . These steps indicate that there is an equivalence of an increase in one decade of strain-rate to an increase in approximately 15-30 °C temperature for observation of the non-failure behavior.

3.2.2 Diameter Distribution

From the 437 fibers used in this study, 2185 fiber diameter measurements were made. Upper and lower value outliers were found to be diameters with double fibers or fiber halves, respectively. These outliers were not included in the distribution. The distribution for the remaining 2164 fiber diameter measurements is shown in Figure 3-4. The distribution appears to be Gaussian with two possible modes around 17.5 μm and 18.75 μm . These modes are most likely caused from the distribution of spinneret diameters involved in the gel-spinning process. A Gaussian distribution trace is included in the

figure for comparison. The average fiber diameter was calculated to be 18.49 μm with a standard deviation of 1.15 μm .

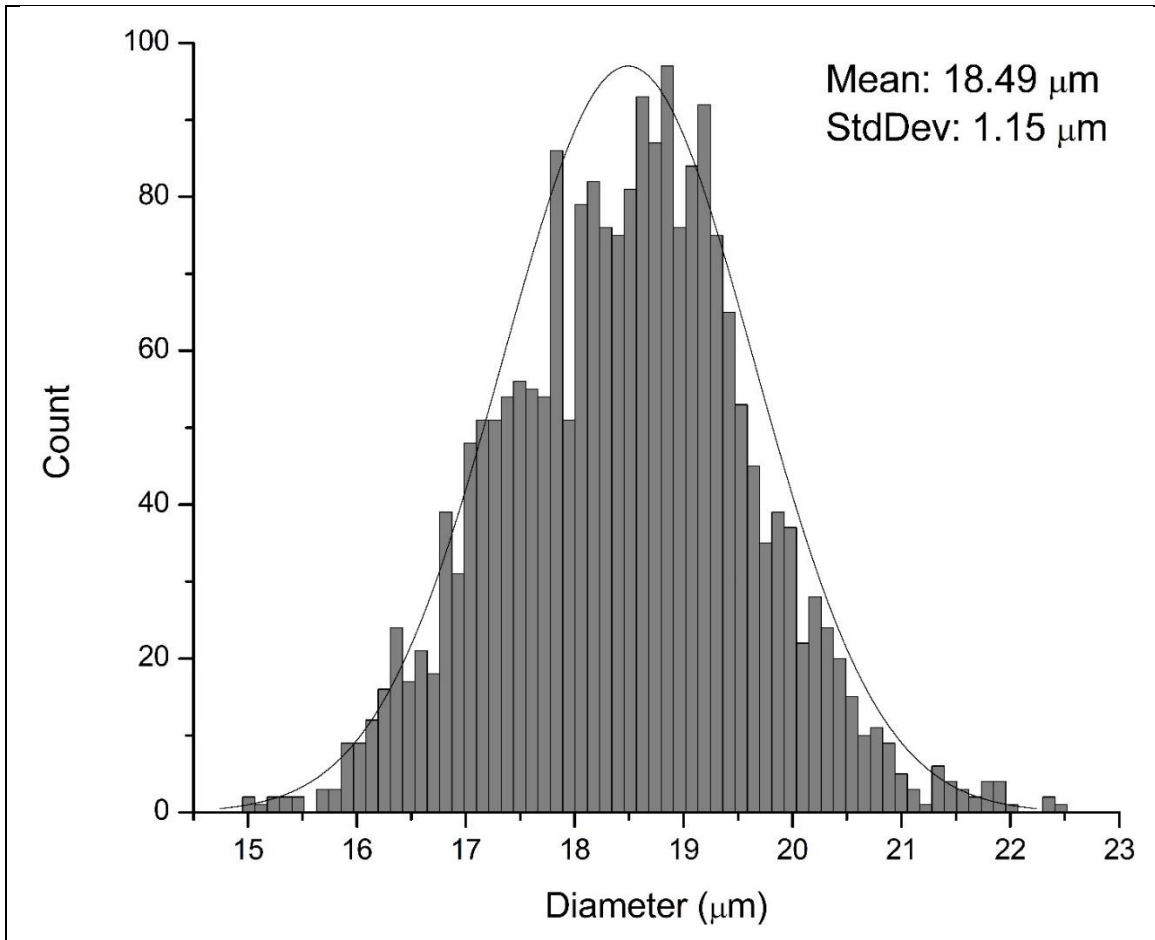


Figure 3-4: Fiber diameter distribution of 2164 fiber diameter measurements. T Gaussian distribution is traced for comparison. The average and standard deviation of the distribution are shown in the top right of the image.

3.2.3 Grip Performance: Percentage of Tensile Failures in the Gage Length of the Fiber

The total number of failures at the grip interface across the temperatures and strain-rates conducted in this study was 12, making the success of a tensile failure occurring within the gage length 425/437 or 97.61%. The distribution by strain-rate of the percentage of successful tests is summarized in Table 3-3. The dynamic strain-rates comprise 10/12 grip interface failures indicating a much lower success rate than the

quasi-static and intermediate rates. At the quasi-static and intermediate strain-rates and higher temperatures, non-failures comprise 73 of the total 437 tensile tests. These tests did not allow for the observation of the failure surface in the gage length or at the grip interface. If these are subtracted from the results the new success rate becomes 352/364 or 96.70%, shown in the last row of Table 3-3. The observed average UTS value decreases as temperature increases for a given strain-rate, signifying the grip experiences less overall force before fiber failure. 20 °C is the lowest temperature utilized in this study and exhibited the highest average UTS values.

To demonstrate the gripping success rate under the highest UTS conditions, the 20 °C data can be analyzed. The number of samples for the quasi-static and intermediate strain-rates at 20 °C is only 5 samples per strain-rate and 10 samples per strain-rate for the dynamic strain-rates. To remedy the low number of tests, the repeat data as well as the fibers that were used for non-tensile purposes are used to expand the population size for the determination of success rates. The non-tensile fibers used are the fibers from the temperature range selection and instrument settings since the location of the failure was recorded. Considering just the 20 °C fibers, the overall success rate of failures in the gage length is 98/119 or 82.35%. Columns 2 to 4 in Table 3-4 shows the distribution of the 20 °C data by strain-rate. The intermediate and dynamic strain-rates show the lowest success rates having 5, 6, and 8 of the failures at the grip interface for the 10^0 s^{-1} , 500 s^{-1} , and 10^3 s^{-1} strain-rates, respectively. Together, the high strain-rates comprising a total of 19/21 or 90.48% of the grip interface failures. Furthermore, the 12 tests presented in the 437 data set were included in the data set because of their higher than average failure strengths at that temperature-strain-rate combination. The number of breaks can be adjusted to

exclude these since the failure strength was unaffected. These adjusted values are shown in columns 5 and 6 of Table 3-4. Also shown are the success rates of Sanborn et al. [27] in column 7. The table shows that the grips used in this study outperformed their grips at 10^{-3} s^{-1} , performed worse at 10^0 s^{-1} , and performed much better at dynamic strain-rates, including a higher strain-rate than they performed. Reasons for this trend will be explored in the discussion section.

Strain-rate [s ⁻¹]	Number of Fiber Samples	Breaks at Grip Interface	% Breaks in Gage Length
10 ⁻³	55	1	98.18
10 ⁻²	55	0	100.00
10 ⁻¹	55	1	98.18
10 ⁰	55	0	100.00
500	109	4	96.33
10 ³	108	2	98.15
Total (Including non-failures)	437	12	97.61
Total (Excluding non-failures)	364	12	96.70

Table 3-3: The number of grip interface failures observed for the 437 tensile tests, categorized by strain-rate. The last row shows the overall success if the non-failures are removed from the calculations.

1	2	3	4	5	6	7
Strain-rate [s ⁻¹]	Number of Fiber Samples	Breaks at Grip Interface	% Breaks in Gage Length	Breaks at Grip Excluding High Failure Strength Samples	% Breaks in Gage Length Excluding High Failure Strength Samples	% Breaks in Gage Length by Sanborn et al.
10 ⁻³	28	1	96.43	0	100	90
10 ⁻²	8	1	87.5	1	87.5	-
10 ⁻¹	8	0	100	0	100	-
10 ⁰	27	5	81.48	5	81.48	91
500	22	6	72.72	5	77.72	-
775	-	-	-	-	-	42
10 ³	26	8	69.23	4	84.61	-
Total	119	21	82.35	15	87.39	-

Table 3-4: The number of grip interface failures and success rates observed for the 20 °C data set including retests and fibers used for non-tensile purposes. The 5th and 6th columns show the number and success rates if the higher than average failure strength fibers are removed from the calculations. The last column shows the grip success rates for Sanborn et al. for the three strain-rates conducted in their study.

3.2.4 Observed Shape Changes in Stress-Strain Curves

For each 437 tensile test, plots of the corrected and uncorrected stress-strain plots were visually inspected and analyzed by a custom R program. The shape of the stress-strain curves was observed to change with respect to both temperature and strain-rate.

These changes in shape will be presented by grouping the quasi-static and intermediate strain-rates together and the dynamic strain-rates together. As discussed in the previous chapter, the reason for this is the f-SHTB is fundamentally different in how it creates strain and how it measures displacement and force. The timescale over which the tensile tests occur are orders of magnitude smaller (on the order of 100 microseconds) than the quasi-static and intermediate strain-rates (on the order minutes to tenths of a second). The stress-strain curves are therefore different and categorized separately.

Two stress trends are observed regardless of the strain-rate. The first is the decrease in the UTS and failure strength observed as the temperature increases. While the UTS and failure strength are strain-rate dependent, the negative correlation between temperature and strength is always observed. The second is the starting stress of the fiber. As temperature increases, the thermal shrinkage of the fiber causes an increase in the starting stress. This can become more apparent in tensile tests conducted at higher temperatures where the shrinkage force is greater. Difficulties can arise trying to determine the initial modulus (slope of the stress-strain curve). Considering these two trends, the stress-strain curves are presented with the stress scale on the y-axis from 0 GPa to the fiber-specific UTS in order to compare similar shapes at different temperature-strain-rate combinations.

3.2.4.1 Quasi-static and Intermediate Strain Rate Curves

The shape of the stress-strain curves changes dramatically as a function of both strain-rate and temperature. Figures 3-5, 3-6, 3-7, and 3-8 show the change in shape as temperature is increased for the 10^{-3} s^{-1} , 10^{-2} s^{-1} , 10^{-1} s^{-1} , and 10^0 s^{-1} strain-rates, respectively.

3.2.4.1.1 Psuedo-brittle

At 20 °C, the lowest temperature used in this study, the stress-strain curve is monotonically increasing with a concave shape until failure. This retarded elastic response is typical for a viscoelastic material (Painter). The steepest slope is observed at the lowest strain values and this region was used to determine the slope for Young's modulus calculations. This curve shape is seen at low temperatures for all of the quasi-static and intermediate strain-rates, with different average values for the strain to failure and failure strength. Examples of 20 °C stress strain curves are shown in the top left images of Figures 3-5, 3-6, 3-7, and 3-8 for the 10^{-3} s^{-1} , 10^{-2} s^{-1} , 10^{-1} s^{-1} , and 10^0 s^{-1} strain-rates, respectively. For this type of curve, the failure strength is the same as the UTS since the point of failure is also the point of the highest stress. Due to the high strength with small strain, this type of curve shape will be referred to as "psuedo-brittle".

3.2.4.1.2 Plateauing

As temperature increases, the curves remain monotonically increasing but show decreasing initial slopes as well as decreasing UTS values. Additionally, a plateau region forms at the UTS across a temperature range that is strain-rate dependent. In this region, a steady state is attained between the strain-rate and the stress relaxation mechanisms, as indicated by an increase in strain with no change in stress. Of the 5 tensile tests for each

temperature-strain-rate combination in the quasi-static and intermediate strain rates, the range was determined to begin when at least 1/5 of the fibers is observed to have the plateauing effect and ends when at least 1/5 fibers display necking which will be presented in the next section. For each individual stress-strain curve, it becomes difficult to determine what constitutes a plateau. Specifically, how many data points of the same value must come sequentially to signify a plateau. For consistency, plateauing was determined for a stress strain curve if the UTS and failure strength points:

- were not overlapping when plotted (indicating a strain separation > 0.0008 strain)
- were within one stress value allowed by the force sensor (± 0.001 N)

Considering the small differences set by the above criteria, example plots for each strain-rate were selected to show a clear plateauing region rather than showing the lowest temperature where plateauing was first observed. Plateauing is observed between 20 °C and 35 °C, at 50 °C only, between 65 °C and 75 °C, and 85 °C only, for the 10^{-3} s^{-1} , 10^{-2} s^{-1} , 10^{-1} s^{-1} , and 10^0 s^{-1} strain-rates, respectfully. Examples of these stress-strain curves are shown in the top right image of Figure 3-5, 3-6, 3-7, and 3-8, respectfully. Within the plateau range, the number of fibers that demonstrate plateauing increases as temperature increases. Also, the slope in the low strain region of the curve is becomes more linear with a shallower slope when compared to lower temperatures. The steepest slope is still observed at the lowest strain values and this region was used to determine the slope for Young's modulus calculations. The combined effects of the plateau and the low strain linearization increases the overall strain to failure. This type of curve shape will be referred to as "plateauing".

3.2.4.1.3 Necking

As temperature continues to increase for a given strain-rate, the UTS values continue to decrease while the plateau region increases in length and begins to curve downward, making the curve no longer monotonically increasing. For these curves, the UTS value is now higher than the failure strength and a necking region of decreasing stress with increasing strain exists between them. Again, the temperature at which this occurs is strain-rate dependent and the necking region occurs over a temperature range beginning when at least 1/5 of the fibers in a temperature-strain-rate combination demonstrates necking behavior and ends when at least 1/5 fibers demonstrate non-failure behavior. For consistency, necking was identified for a stress-strain curve if the UTS and failure strength points were separated by more than 0.5% strain and were separated by more than one stress value allowed by the force sensor (± 0.001 N). Similar to the plateauing, example plots for each strain-rate were selected to show a clear necking region rather than showing the lowest temperature where necking was first observed. For the 10^{-3} s^{-1} , 10^{-2} s^{-1} , 10^{-1} s^{-1} , and 10^0 s^{-1} strain-rates, necking is observed between $50 \text{ }^\circ\text{C}$ and $75 \text{ }^\circ\text{C}$, $65 \text{ }^\circ\text{C}$ and $100 \text{ }^\circ\text{C}$, $85 \text{ }^\circ\text{C}$ and $130 \text{ }^\circ\text{C}$, and $100 \text{ }^\circ\text{C}$ and $148 \text{ }^\circ\text{C}$, respectfully. Examples are shown in the bottom left image of Figures 3-5, 3-6, 3-7, and 3-8, respectfully. The necking region significantly increases the strain to failure with average values over 5% strain. One exception is the 10^0 s^{-1} strain-rate where the strain to failures stayed below 5% strain even though necking was observed. Additionally, an increase in the Young's modulus is observed near the 0.5% strain for all of the strain-rates where the curve is observed to transition from convex to concave. This indicates a stiffening of the fiber at small strains when necking is present in the stress-strain curve. The steepest slope

is observed in this region and this is where the slope was taken for Young's modulus calculations. This This type of curve shape will be referred to as "necking".

3.2.4.1.4 Non-Failure

The last type of stress-strain curve observed is a non-failure curve where a UTS is reached but the fiber continues to be strained to the machine maximum, or 25% uncorrected strain for 10 mm samples, without failing. This type of curve shape will be referred to as "non-failure". These curves are also not monotonically increasing and non-failure is observed over a strain-rate dependent temperature range. The temperature range begins when at least 1/5 of the fibers in a temperature-strain-rate combination demonstrates non-failure behavior. Non-failure is observed between 75 °C and 148 °C, 100 °C and 148 °C, 130 °C and 148 °C, and 148 °C only for the 10^{-3} s^{-1} , 10^{-2} s^{-1} , 10^{-1} s^{-1} , and 10^0 s^{-1} strain-rates, respectfully, and an example of each is shown in the bottom right image of Figures 3-5, 3-6, 3-7, and 3-8, respectfully. The strain to failure is drastically affected to the point that mechanical failure of the fibers is inhibited up to 25% uncorrected strain. (The corrected engineering strains do not reach the 25% values due to the compliance correction previously discussed.) One exception is the 10^0 s^{-1} strain-rate where the data acquisition instrument lacked the recording capacity to record data up to the maximum strain. This was caused by the high acquisition rate needed to capture the initial increase in stress near the 2-3% strain. The 10^0 s^{-1} strain-rate plot also demonstrates the small stress scale observed for the 148 °C tensile tests. The plot shows the 0.001 N resolution of the force sensor creating a granular plot. The necking region of the non-failure curves has a convex shape suggesting a steady state would be reached between

strain-rate and stress relaxation mechanisms if strained above 25% before failure. This type of curve also exhibits the stiffening behavior around 0.5% strain.

To summarize, for a given strain-rate, a transition in curve shape is seen as temperature is increased. The shape transitions order is psuedo-brittle, plateauing, necking, and non-failure. Below are the key points for each curve shape:

- Psuedo-brittle:
 - Monotonically increasing
 - UTS coinciding with the failure strength
 - Low strain to failure values
- Plateauing:
 - Monotonically increasing with a plateauing region
 - UTS spans a range of strain before failing, still same value as the failure strength
 - Strain to failure values slightly increasing
- Necking:
 - Not monotonically increasing with a necking region
 - Failure strength occurs below the UTS
 - Stiffening observed in the 0.5% strain region
 - Strain to failure dramatically increases, above 5%
- Non-failure:
 - Not monotonically increasing with a long non-failure region
 - UTS is present but failure strength is absent
 - Stiffening observed in the 0.5% strain region
 - Fiber does not fail up to 25% uncorrected strain

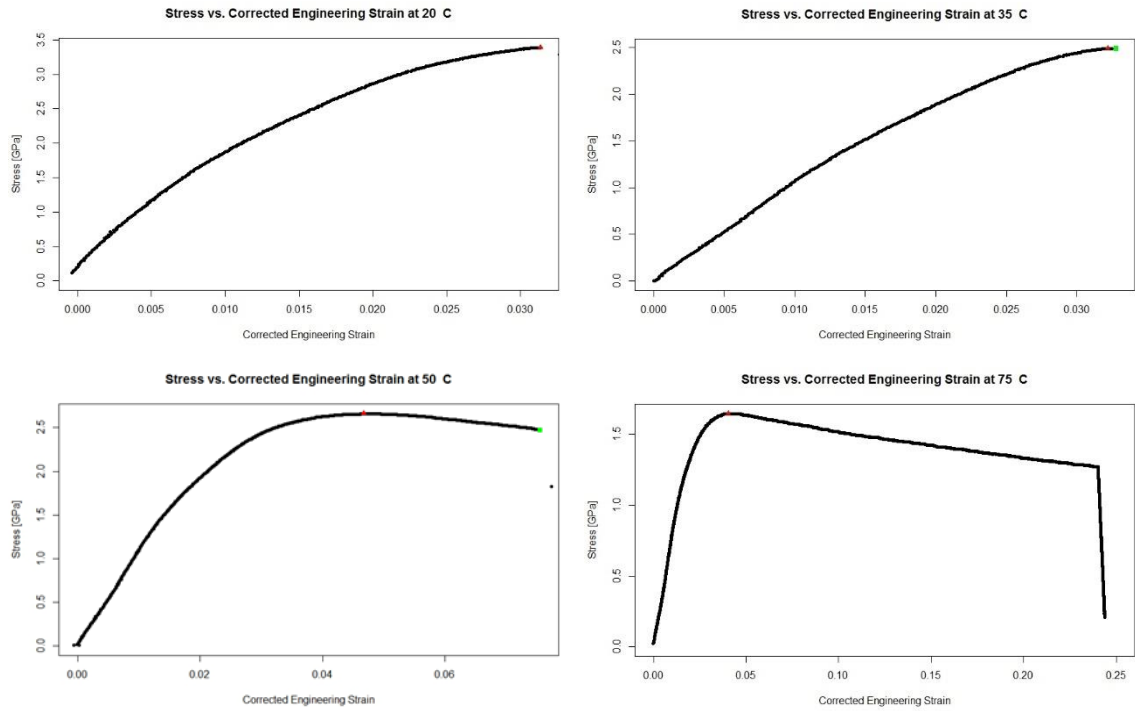


Figure 3-5: 10^{-3} s^{-1} strain-rate shape changes in the stress-strain curves as temperature is increased. **(Top left):** Pseudo-brittle shape at 20 °C where the UTS (red triangle) also corresponds to the failure strength (green square). **(Top right):** Plateauing shape at 35 °C where the UTS (red triangle) is at the same value at the failure strength (green square) but separated by a plateau region of constant stress with increasing strain. **(Bottom left):** Necking shape at 50 °C where the UTS (red triangle) is at a higher value than the failure strength (green square) and they are separated by a necking region of decreasing stress with increasing strain. **(Bottom right):** Non-failure shape at 75 °C where the UTS (red triangle) is present but the fiber does not fail after 25% uncorrected strain.

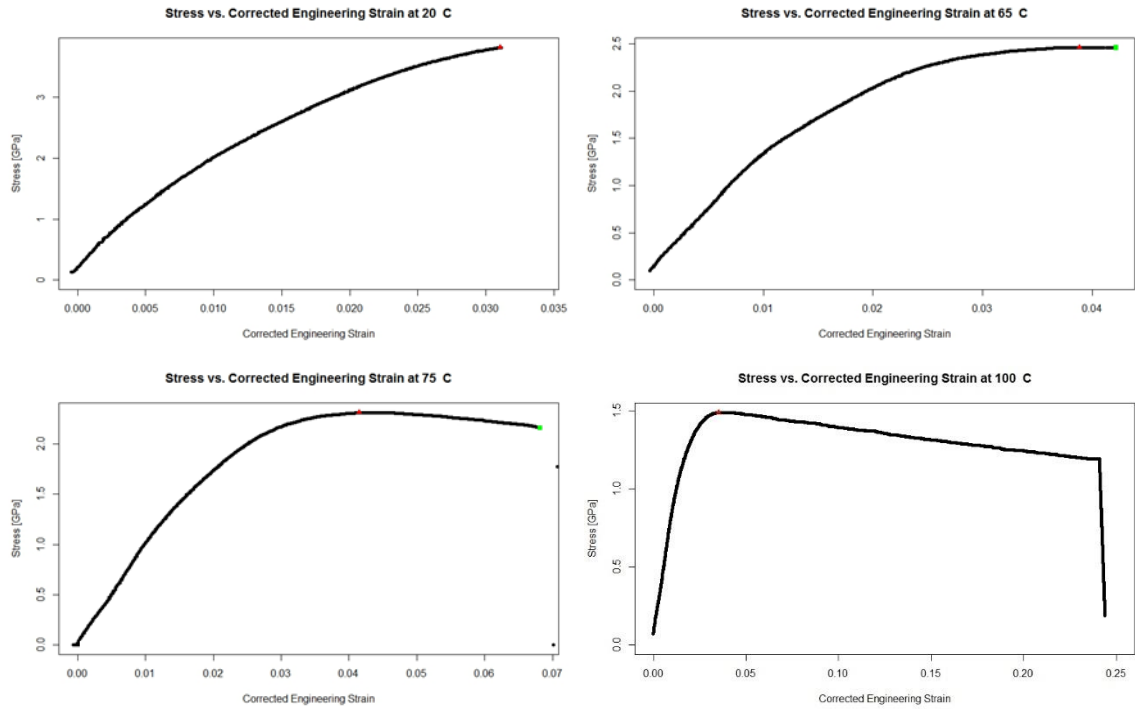


Figure 3-6: 10^{-2} s^{-1} strain-rate shape changes in the compliance corrected stress-strain curves as temperature is increased. **(Top left):** Pseudo-brittle shape at 20 °C where the UTS (red triangle) also corresponds to the failure strength (green square). **(Top right):** Plateauing shape at 65 °C where the UTS (red triangle) is at the same value at the failure strength (green square) but separated by a plateau region of constant stress with increasing strain. **(Bottom left):** Necking shape at 75 °C where the UTS (red triangle) is at a higher value than the failure strength (green square) and they are separated by a necking region of decreasing stress with increasing strain. **(Bottom right):** Non-failure shape at 100 °C where the UTS (red triangle) is present but the fiber does not fail after 25% uncorrected strain.

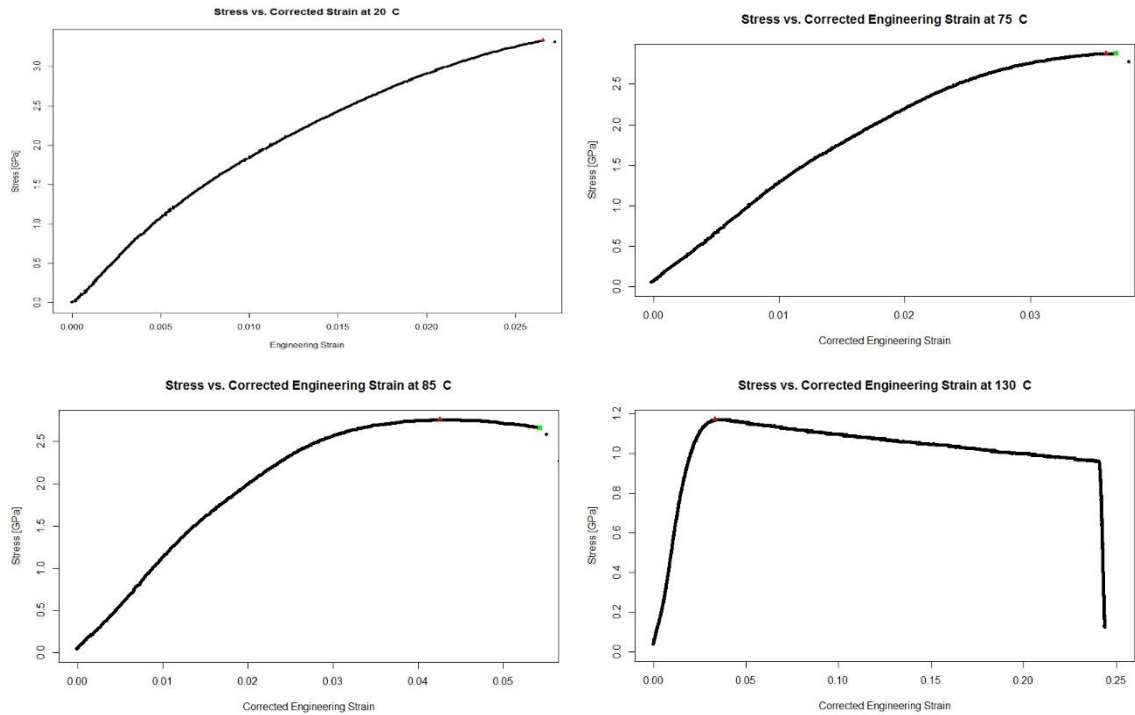


Figure 3-7: 10^{-1} s^{-1} strain-rate shape changes in the compliance corrected stress-strain curves as temperature is increased. **(Top left):** Pseudo-brittle shape at 20 °C where the UTS (red triangle) also corresponds to the failure strength (green square). **(Top right):** Plateauing shape at 75 °C where the UTS (red triangle) is at the same value at the failure strength (green square) but separated by a plateau region of constant stress with increasing strain. **(Bottom left):** Necking shape at 85 °C where the UTS (red triangle) is at a higher value than the failure strength (green square) and they are separated by a necking region of decreasing stress with increasing strain. **(Bottom right):** Non-failure shape at 130 °C where the UTS (red triangle) is present but the fiber does not fail after % uncorrected strain.

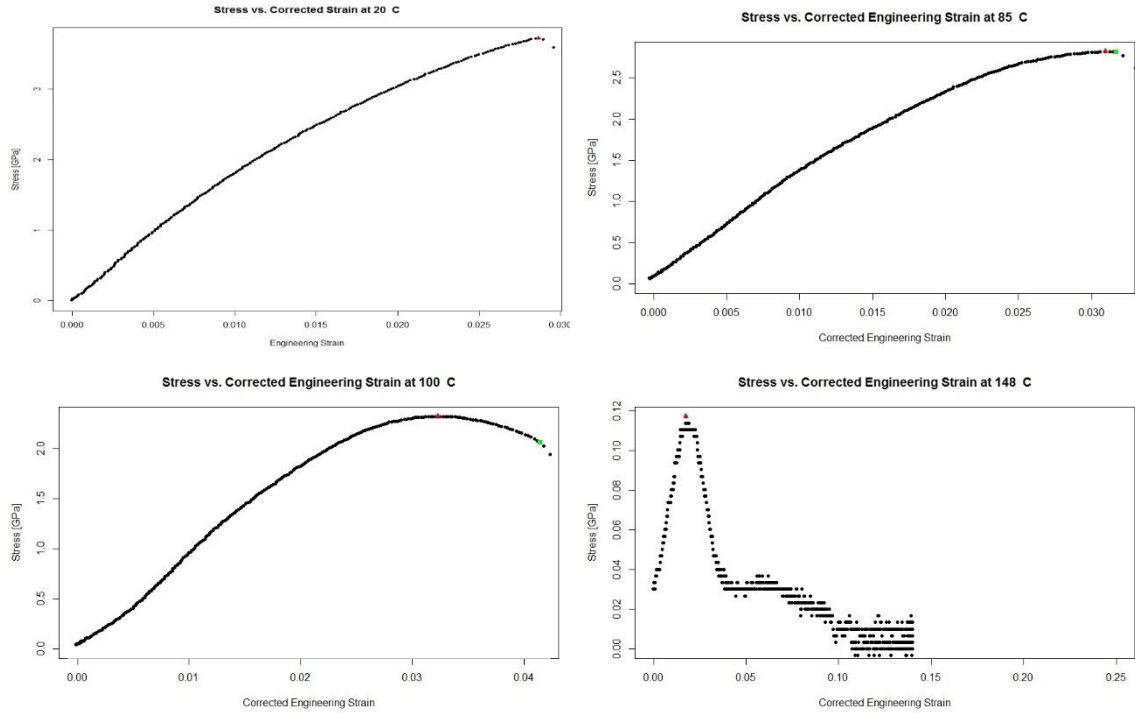


Figure 3-8: 10^0 s^{-1} strain-rate shape changes in the compliance corrected stress-strain curves as temperature is increased. **(Top left):** Pseudo-brittle shape at 20 °C where the UTS (red triangle) also corresponds to the failure strength (green square). **(Top right):** Plateauing shape at 85 °C where the UTS (red triangle) is at the same value at the failure strength (green square) but separated by a plateau region of constant stress with increasing strain. **(Bottom left):** Necking shape at 100 °C where the UTS (red triangle) is at a higher value than the failure strength (green square) and they are separated by a necking region of decreasing stress with increasing strain. **(Bottom right):** Non-failure shape at 148 °C where the UTS (red triangle) is present but the fiber does not fail after being strained to 25% uncorrected strain. Also show at 148 °C is the low UTS value displaying the resolution of the instrument ($\pm 0.001 \text{ N}$) resulting in a granular plot.

3.2.4.2 Dynamic Strain-Rate Curves

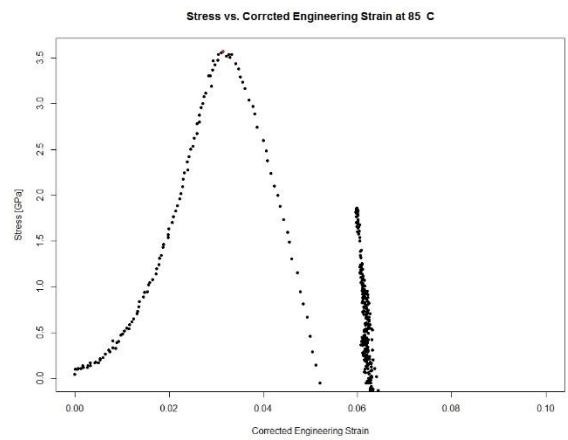
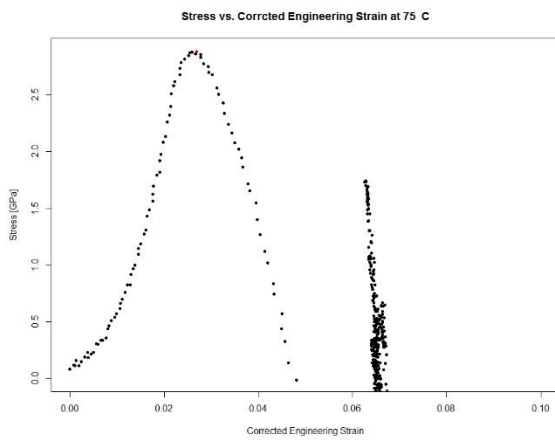
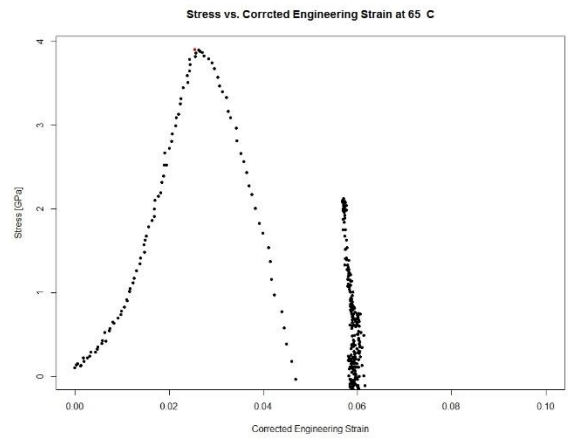
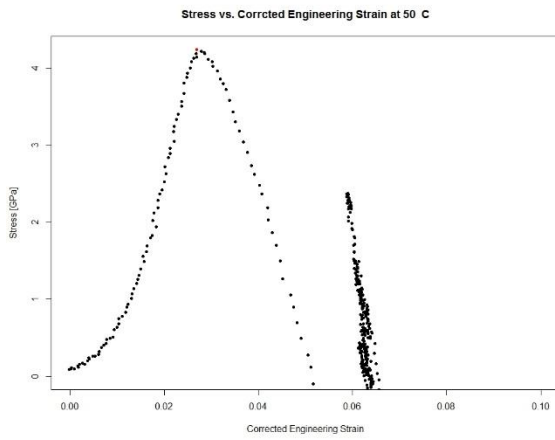
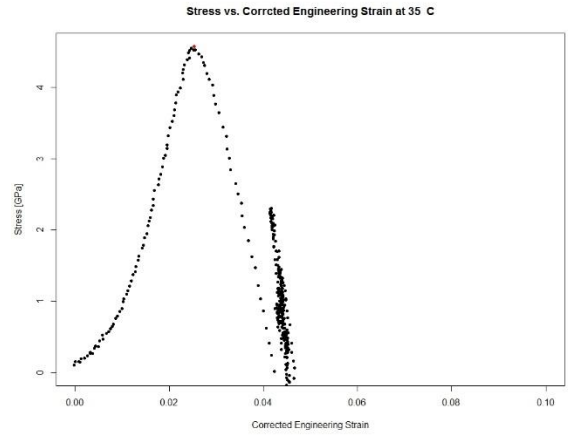
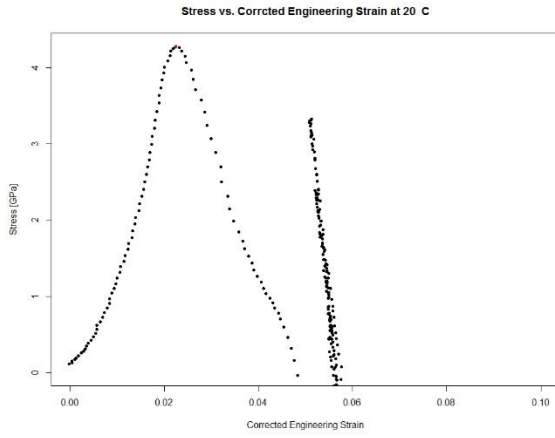
The 500 s^{-1} strain-rate stress-strain curves look different than the curves observed at the quasi-static and intermediate strain-rates. Overall, the shape of the curve does not change as temperature is increased. An example of a stress-strain plot for each temperature in the 500 s^{-1} strain-rate is shown in Figure 3-9. The plots have all been created with the same strain window on the x-axis for comparison but the stress scale on the y-axis is varied to fit the fiber-specific UTS value. The first reflection of the force sensor is also included to observe the rise and fall time of the force sensor without an influence from the fiber. The stress-strain curve shape is observed to be almost parabolic with tapering at the low strain region. The tapering changes from convex to concave, similar to the stiffening behavior seen in the quasi-static and intermediate strain-rate plots at the necking temperature. The stiffening behavior occurs in the 0.5% to 1% strain range. As temperature increases, the shape of the curve does not change and the average strain to failure values remain between 2.5% to 3.5%. Near the melting temperature at $148 \text{ }^{\circ}\text{C}$, the shape of the curve remains the same and there is no observation of a plateauing, necking, or non-failure temperature for this strain-rate. The rise and fall times of the fiber-less force reflection appear to have the same slope and therefore any force sensor effects are symmetric around the UTS. Due to the high strain-rates an instability is observed at fiber failure where the stress-strain curves appear parabolic. The fiber is failing in this region and the failure point is defined as the highest stress value (UTS). This may slightly over estimate the failure strengths and strain to failures.

The 10^3 s^{-1} strain-rate curves behave very similarly to the 500 s^{-1} strain-rate. An example of a stress-strain plot for each temperature in the 10^3 s^{-1} strain-rate is shown in

Figure 3-10. The plots were also created with the same strain window as used in the 500 s^{-1} strain-rate, with the exception of the 148 °C example which displayed a higher strain to failure. The stress scale on the y-axis is also varied with the fiber-specific UTS value. The stress-strain curve shape is similar to the 500 s^{-1} strain-rate where an almost parabolic curve is observed with a tapering at the low strain region. The tapering also demonstrates an increase in the stiffness of the fiber at low strains, in the 0.5% to 1% strain range, where the slope of the curve increases. As temperature increases, the shape of the curve remains the same with an average strain to failure value between 2.5% to 3.5%. Near the melting temperature at 148 °C the shape of the curve changes and linear stress-strain relationship is observed until failure. There is no observed plateauing, necking, or non-failure temperatures for this strain-rate. The speed at which displacement is taking place is higher than the 500 s^{-1} strain-rate curves and a similar loading curve shape is observed. The post-failure fall time of the sensor appears to be broader due to the higher speed. The rise and fall times of the fiber-less force reflection appear to have the same slope and therefore the force sensor effects are symmetric around the UTS. To summarize, the dynamic strain-rate stress-strain curve shapes do not change shape with respect to temperature and strain-rate with the exception of the $10^3 s^{-1}$ strain-rate at 148 °C. The curve shapes have a combination of pseudo-brittle and necking characteristics and will be referred to as “dynamic”. The key points for the curve shape are listed below:

- Dynamic (combination of pseudo-brittle and necking)
 - Does not change shape with temperature or strain-rate (exception below)
 - monotonically increasing
 - UTS coinciding with the failure strength

- Stiffening observed in the .05% to 1% strain range
- Low strain to failure values (exception below)
- Exception: The 10^3 s^{-1} strain-rate at 148 °C curve shows a linear stress-strain relationship to failure and has a higher strain to failure than observed in the other dynamic testing conditions



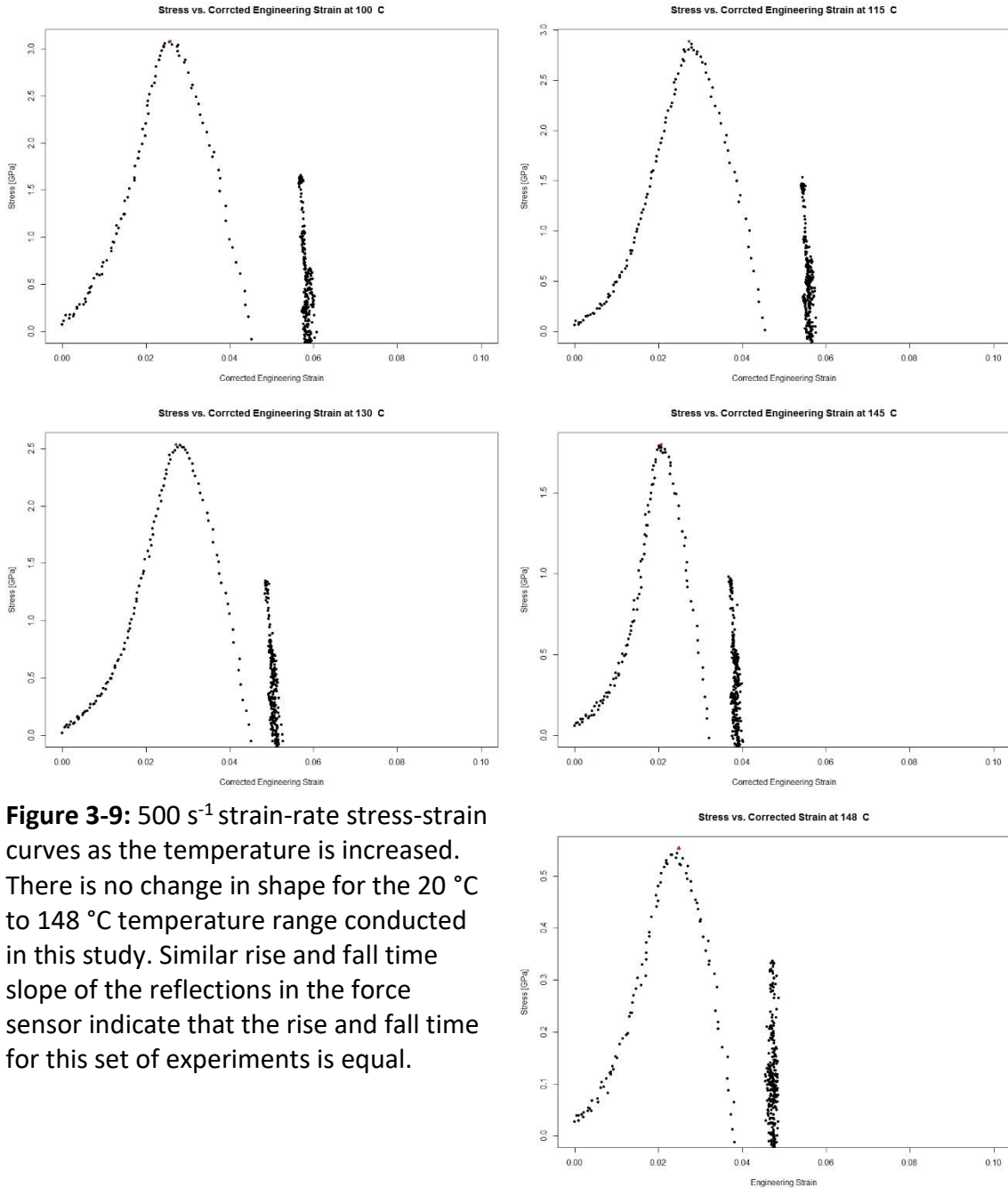
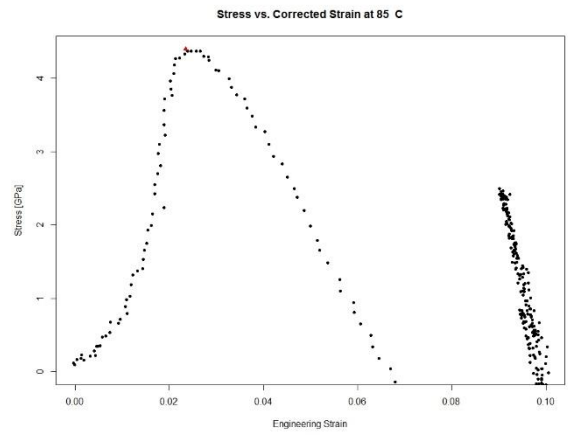
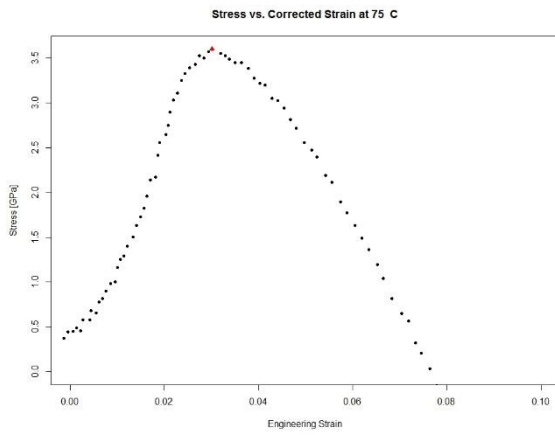
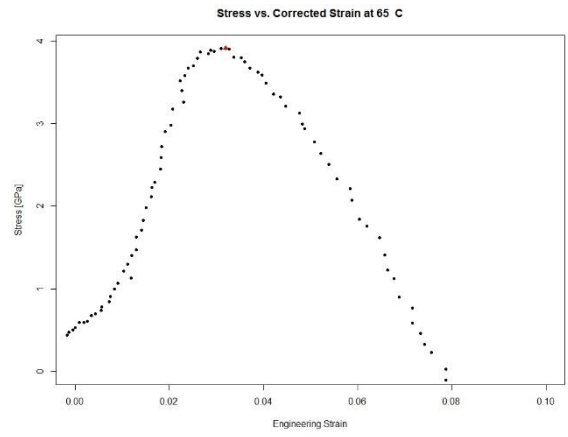
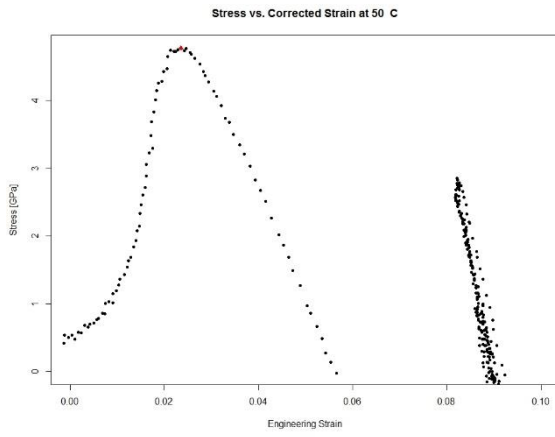
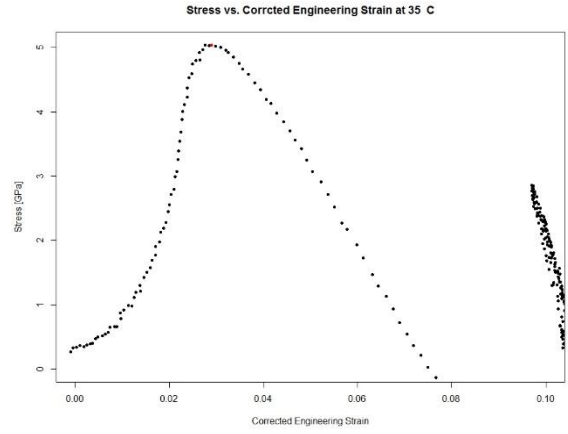
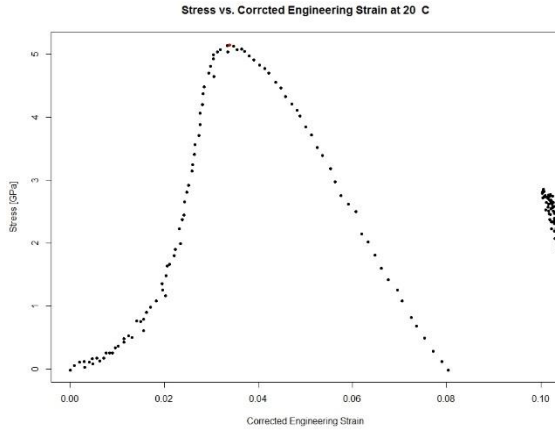


Figure 3-9: 500 s⁻¹ strain-rate stress-strain curves as the temperature is increased. There is no change in shape for the 20 °C to 148 °C temperature range conducted in this study. Similar rise and fall time slope of the reflections in the force sensor indicate that the rise and fall time for this set of experiments is equal.



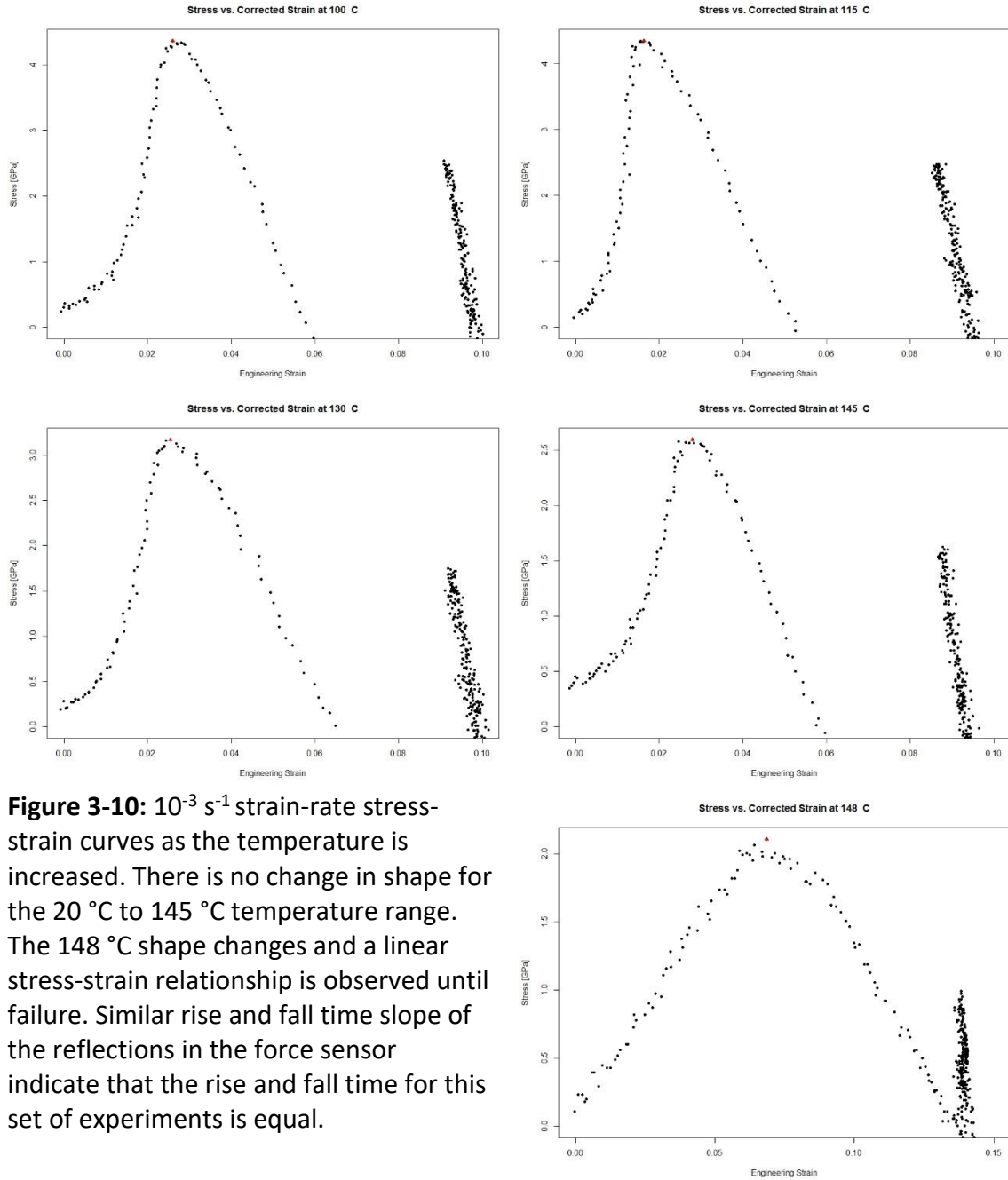


Figure 3-10: 10^{-3} s^{-1} strain-rate stress-strain curves as the temperature is increased. There is no change in shape for the 20 °C to 145 °C temperature range. The 148 °C shape changes and a linear stress-strain relationship is observed until failure. Similar rise and fall time slope of the reflections in the force sensor indicate that the rise and fall time for this set of experiments is equal.

3.2.5 Strain to Failure

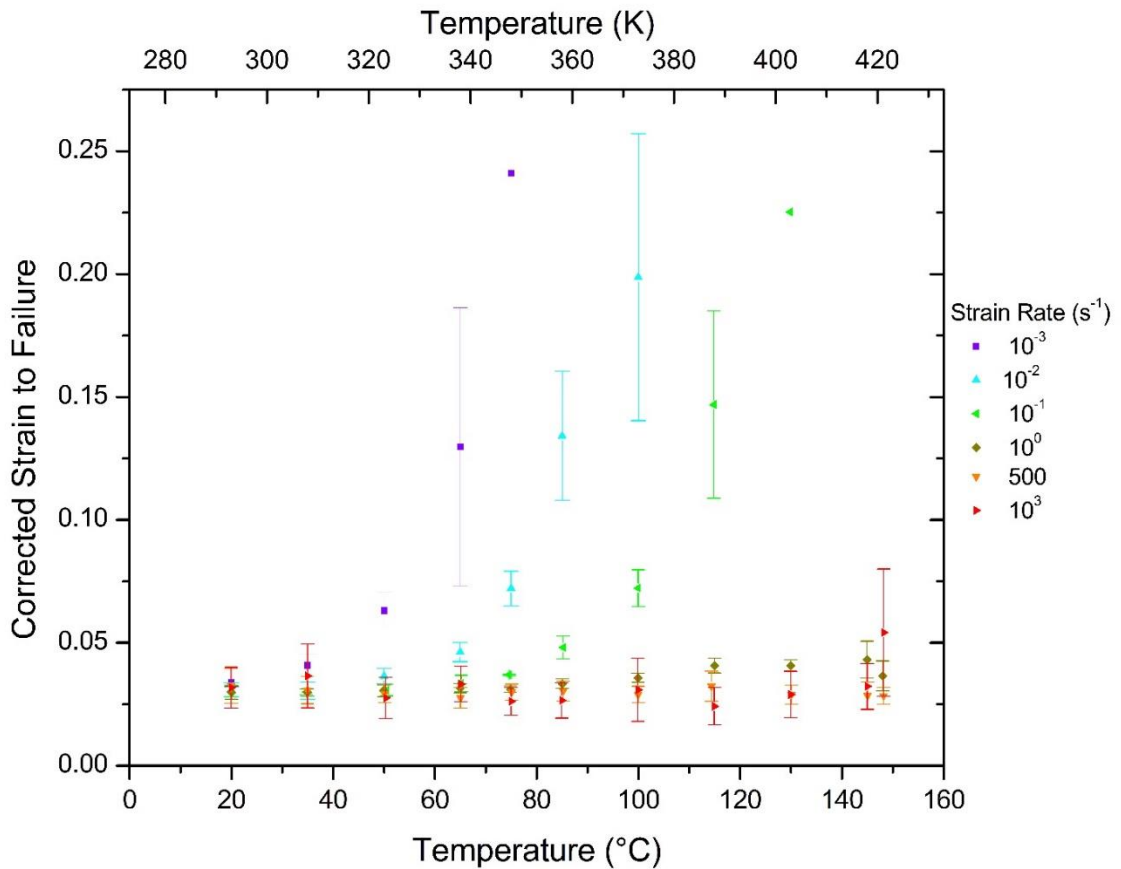
The average strains to failure (or elongation at failure) for the quasi-static and intermediate strain-rates were observed to increase with increasing temperature and decrease with increasing strain-rate. For the dynamic strain-rates, the average strains to failure were observed to remain constant at approximately 3% strain. Each of the 66 temperature-strain-rate combinations are shown in Table 3-5 and plotted in Figure 3-11 (Top). Uncorrected strain to failure plots and tables of these values can be found in Appendix A-1 and A-2, respectfully. The 10^{-3} s^{-1} , 10^{-2} s^{-1} , 10^{-1} s^{-1} , 10^0 s^{-1} , 500 s^{-1} , and 10^3 s^{-1} strain-rates are depicted in violet, blue, green, dark yellow, orange, and red, respectively. The averages are plotted with bars depicting \pm one standard deviation. Standard deviations are observed to be larger for the dynamic strain-rates except in the necking to non-failure regions of the lower strain-rates where a large variation in strain to failure is observed. Individual plots of the strains to failure at each temperature-strain-rate combination can be found in Appendix A-3. Non-failure temperatures are observed at 75 °C, 100 °C, and 130 °C for the 10^{-3} s^{-1} , 10^{-2} s^{-1} , and 10^{-1} s^{-1} , strain-rates, respectively. The 10^{-3} s^{-1} and 10^{-1} s^{-1} strain-rates resulted in only one of the five tensile tests failing and therefore lack a standard deviation bar. The 10^{-2} s^{-1} strain-rate resulted in two of the five tests failing and has a large standard deviation. The non-failure temperature of the 10^0 s^{-1} strain-rate was observed at 148 °C where three of the five tests failed with an average strain to failure value of approximately 3.5%. This average strain to failure value is much lower than values for the lower strain-rates where the curves are approaching the maximum 25% uncorrected strain of the instrument.

Strain-rate [s ⁻¹]	Temperature [°C]											
	20	35	50	65	75	85	100	115	130	145	148	
10 ⁻³	3.38±.17	4.08±.46	6.32±.73	12.97±5.66	24.11±-	-	-	-	-	-	-	-
10 ⁻²	3.09±.28	3.06±.35	3.64±.30	4.62±.39	7.21±.70	13.42±2.63	19.87±5.84	-	-	-	-	-
10 ⁻¹	3.03±.24	3.00±.12	3.07±.24	3.35±.33	3.70±.02	4.80±.46	7.22±.75	14.69±3.81	22.52±-	-	-	-
10 ⁰	2.98±.27	2.98±.15	3.05±.25	3.16±.19	3.10±.13	3.33±.19	3.57±.18	4.07±.30	4.06±.24	4.31±.75	3.65±.61	-
500	3.25±.70	3.07±.56	2.93±.37	2.76±.42	2.99±.33	3.04±.40	2.89±.33	3.23±.61	2.90±.39	2.85±.55	2.84±.34	-
10 ³	3.17±.83	3.65±1.30	2.75±.84	3.32±.72	2.62±.57	2.66±.72	3.09±1.28	2.42±.76	2.89±.94	3.22±.94	5.41±2.59	-

Table 3-5: Average strain to failure values with ± one standard deviation. The highlighted region indicates non-failure behavior. The 10⁻³ s⁻¹ and 10⁻¹ s⁻¹ strain-rates resulted in only one of the five tensile tests failing and therefore lack a standard deviation bar.

A rescaled plot centered around 3% strain is shown in figure 3-10 (bottom). This plot shows the change in behavior for the quasi-static and intermediate strain-rates and the unchanging behavior of the dynamic strain-rates. For clarity, standard deviations have been removed and lines connecting adjacent points have been added. The added lines do not imply interpolated data or trend lines.

The strain to failure remains relatively constant for the 500 s^{-1} and 10^3 s^{-1} strain-rates, with a strain to failure plateau at approximately 3% across the entire temperature range from $20 \text{ }^\circ\text{C}$ to $148 \text{ }^\circ\text{C}$. This agrees with the stress-strain curve shapes where no change in shape was observed across the entire temperature range. The only exception is the 10^3 s^{-1} strain-rate at $148 \text{ }^\circ\text{C}$ where an average strain to failure of approximately 5.5%



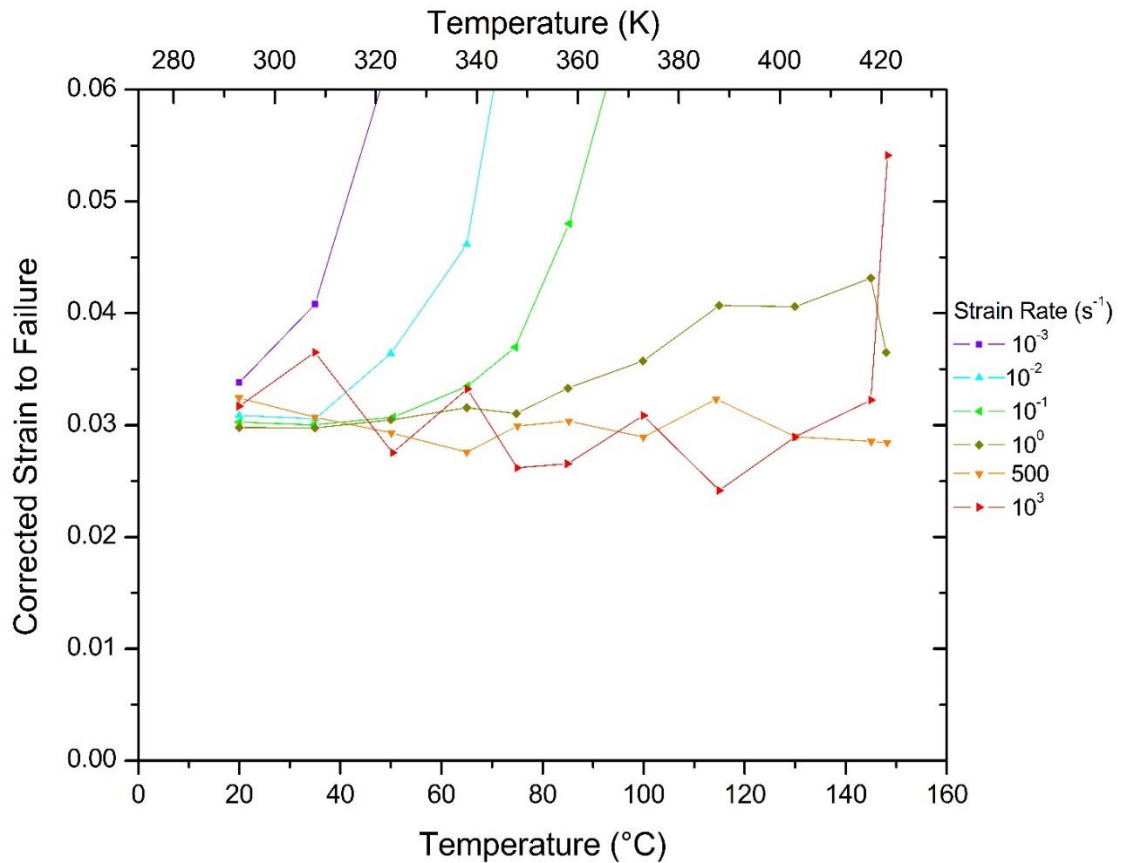


Figure 3-11: (Top) Average values of strain to failure plotted with \pm one standard deviation for all 66 temperature-strain-rate combinations. The non-failure temperatures are observed at 75 °C, 100 °C, and 130 °C for the 10^{-3} s^{-1} , 10^{-2} s^{-1} , and 10^{-1} s^{-1} , strain-rates, respectively. The non-failure temperature of the 10^0 s^{-1} strain-rate is shown at 148 °C where three of the five tests failed with an average value close to 3.5%. **(Bottom)** The same plot rescaled with a centered around 3 % strain. For clarity, standard deviations have been removed and lines connecting adjacent points have been added. The added lines do not imply interpolated or extrapolated data or trend lines. This plot shows the strain to failure not changing for the 500 s^{-1} and 10^3 s^{-1} strain-rates, with a strain to failure of approximately 3 % across the temperature range of 20 °C to 148 °C. The divergence temperatures of 20 °C, 50 °C, 75 °C, and 85 °C, are observed for 10^{-3} s^{-1} , 10^{-2} s^{-1} , 10^{-1} s^{-1} , 10^0 s^{-1} , strain-rates, respectively.

was observed and this agrees with the linear stress-strain relationship to failure observed in the stress-strain curve shape.

Using the dynamic strain-rate plateau of approximately 3% strain, the quasi-static and intermediate strain-rates are observed to follow this plateau and then diverge at a

strain-rate dependent temperature. Divergence temperatures beginning at 20 °C, 50 °C, 65 °C, and 85 °C, are observed for the 10^{-3} s^{-1} , 10^{-2} s^{-1} , 10^{-1} s^{-1} , 10^0 s^{-1} strain-rates, respectively. These temperatures correspond with the start of the plateauing curves observed in the stress-strain curve shapes. Additionally, the 10^0 s^{-1} strain-rate is observed to plateau at approximately 4% strain to failure in the temperature range of 115 °C to 145 °C before decreasing at 148 °C. This behavior is distinct from the lower strain-rates.

The average strain to failure values are also used as a metric for the evaluation of the custom grips used in this study. The values can be compared to other corrected strain to failure values to determine if the custom grips are performing without a significant level of continuous slippage within the grip. The only comparable grip study in the literature comes from Sanborn et al who conducted their study at room temperature. Table 3-6 shows the comparison of corrected strain to failure values for their room temperature and 3 strain-rates and the 20 °C data and 6 strain-rates from this study. The table indicates lower average corrected strain to failure values at all comparable strain-rates except the 10^3 s^{-1} strain-rate where this study found a higher average than the 775 s^{-1} strain-rate conducted by Sanborn [27] and will be explored in the discussion section.

Strain-rate [s ⁻¹]	Uncorrected Strain-to-failure [%]	Uncorrected Strain-to-failure Sanborn et al. [%]	Corrected Strain-to-failure [%]	Corrected Strain-to-failure Sanborn et al. [%]
10⁻³	4.43±.18	5.53±.87	3.38±.17	3.93±.96
10⁻²	4.21±.36	-	3.09±.28	-
10⁻¹	4.20±.06	-	3.03±.24	-
10⁰	4.16±.18	4.83±.72	2.98±.27	3.35±.25
500	3.98±.71	-	3.25±.70	-
775	-	3.71±.26	-	3.00±.24
10³	4.66±.87	-	3.17±.83	-

Table 3-6: Comparison of the uncorrected and corrected average strain to failure values observed in this study at 20 °C and those by Sanborn et al. The corrected strain to failure values observed in this study indicate lower strain to failure values at all comparable strain-rates except the 10^3 s^{-1} strain-rate where this study found a higher average than the 775 s^{-1} strain-rate conducted by Sanborn et al.

3.2.6 Failure Strength

Failure strengths were calculated using two methods. First, the average diameter of the five fiber diameter measurements was used to calculate stresses and these calculations are referred to as failure strength and are used for the majority of this study. Second, the minimum of the five fiber diameter measurements was used to calculate stress to determine if using the smallest cross sectional area of the fiber was a more accurate method. These calculations are referred to as minimum failure strengths. The two methods are compared for shape of trends and difference in standard deviations at the same temperature-strain-rate combination.

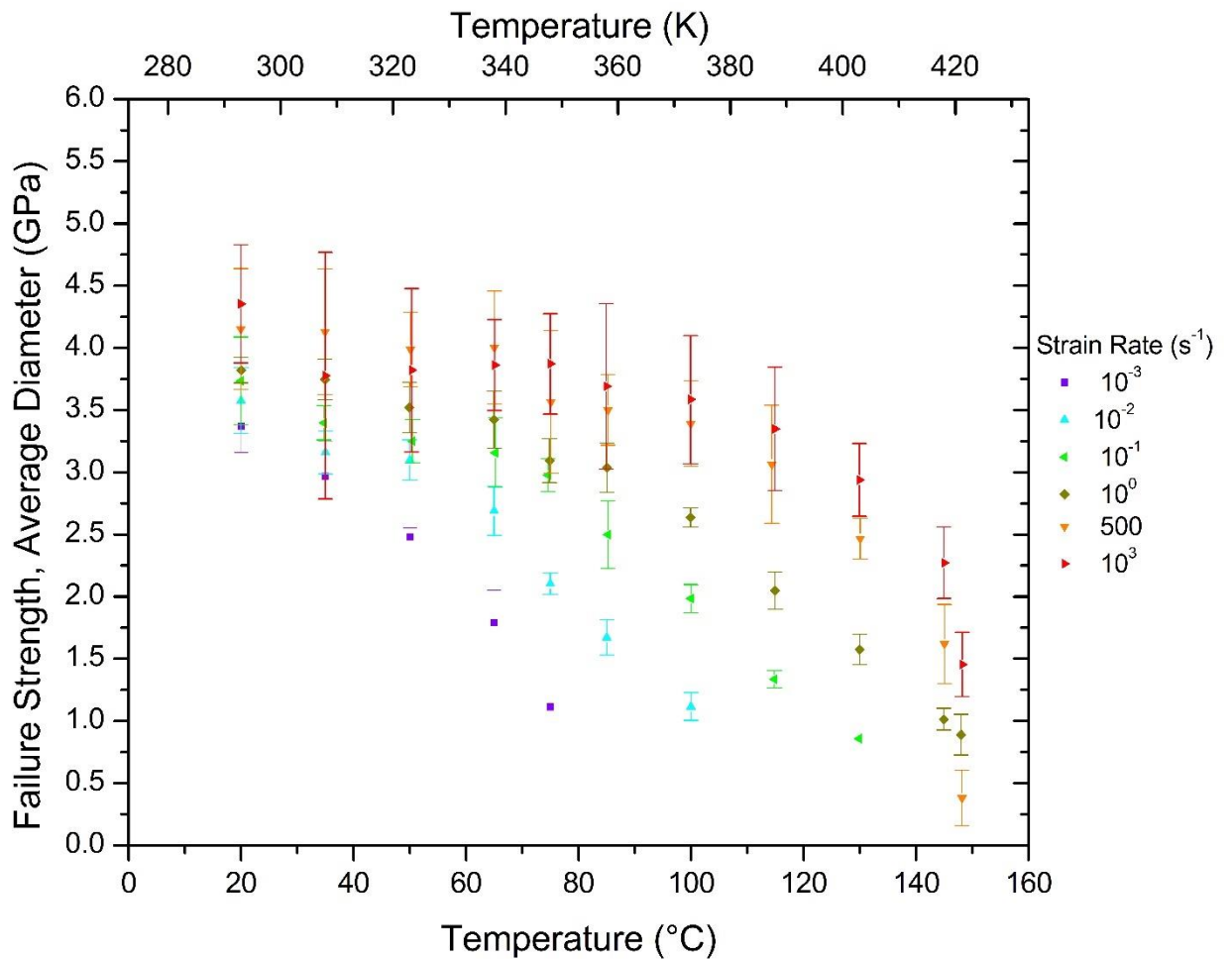
For constant strain-rate, failure strengths were observed to decrease with increasing temperature. For constant temperature, failure strengths were observed to increase with increasing strain-rate. Average failure strengths for each of the 54 temperature-strain-rate combinations where failure occurs are shown in **Table 3-7** and plotted in **Figure 3-12 (Top)**. The 10^{-3} s^{-1} , 10^{-2} s^{-1} , 10^{-1} s^{-1} , 10^0 s^{-1} , 500 s^{-1} , and 10^3 s^{-1} strain-rates are depicted in violet, blue, green, dark yellow, orange, and red, respectively. The averages are plotted with bars depicting \pm one standard deviation. Standard deviations are observed to be larger for the dynamic strain-rates. Individual failure strength plots can be found in Appendix A-4. The highest average failure strength was observed at $4.35 \pm 0.47 \text{ GPa}$ at the 10^3 s^{-1} strain-rate and $20 \text{ }^\circ\text{C}$. At $20 \text{ }^\circ\text{C}$, the average failure strength for 10^{-3} s^{-1} strain rate was $3.37 \pm 0.21 \text{ GPa}$. Non-failure temperatures are observed at $75 \text{ }^\circ\text{C}$, $100 \text{ }^\circ\text{C}$, and $130 \text{ }^\circ\text{C}$ for the 10^{-3} s^{-1} , 10^{-2} s^{-1} , and 10^{-1} s^{-1} , strain-rates, respectively. The 10^{-3} s^{-1} and 10^{-1} s^{-1} strain-rates resulted in only one of the five tensile tests failing and therefore lack a standard deviation bar. The 10^{-2} s^{-1} strain-rate resulted in

Strain-rate [s ⁻¹]	Temperature [°C]													
	20	35	50	65	75	85	100	115	130	145	148			
10⁻³	3.37±.21	2.97±.28	2.48±.07	1.79±.26	1.11±-	-	-	-	-	-	-	-		
10⁻²	3.57±.27	3.16±.17	3.10±.16	2.69±.20	2.10±.09	1.67±.14	1.12±.11	-	-	-	-	-		
10⁻¹	3.73±.35	3.40±.14	3.25±.17	3.16±.28	2.98±.13	2.50±.27	1.98±.11	1.34±.07	.85±-	-	-	-		
10⁰	3.82±.10	3.75±.16	3.52±.20	3.42±.23	3.09±.18	3.04±.20	2.64±.08	2.05±.15	1.57±.12	1.01±.09	.89±.16	-		
500	4.15±.49	4.13±.50	3.99±.30	4.00±.45	3.57±.57	3.50±.28	3.39±.34	3.06±.47	2.47±.16	1.62±.32	.38±.22	-		
10³	4.35±.47	3.78±.99	3.82±.66	3.86±.36	3.87±.40	3.69±.66	3.59±.52	3.35±.50	2.94±.29	2.27±.29	1.45±.26	-		

Table 3-7: The average failure strength values with ± one standard deviation. The highlighted region indicates non-failure behavior. The 10⁻³ s⁻¹ and 10⁻¹ s⁻¹ strain-rates resulted in only one of the five tensile tests failing and therefore lack a standard deviation bar.

two of the five tests failing. The non-failure temperature of the 10^0 s^{-1} strain-rate was observed at $148 \text{ }^\circ\text{C}$ where three of the five tests failed with an average failure strength of approximately 0.75 GPa . This average failure strength is similar to the failure strengths observed at the non-failure temperatures of the lower strain-rates which ranged from approximately 0.75 GPa to 1 GPa . The dynamic strain-rates are observed to have a large decrease in failure strength from $145 \text{ }^\circ\text{C}$ to $148 \text{ }^\circ\text{C}$.

All of the strain-rate plots are monotonically decreasing with increasing temperature and have a concave shape. The quasi-static and intermediate strain-rate plots are observed to exhibit this trend from $20 \text{ }^\circ\text{C}$ to their respective non-failure temperature.



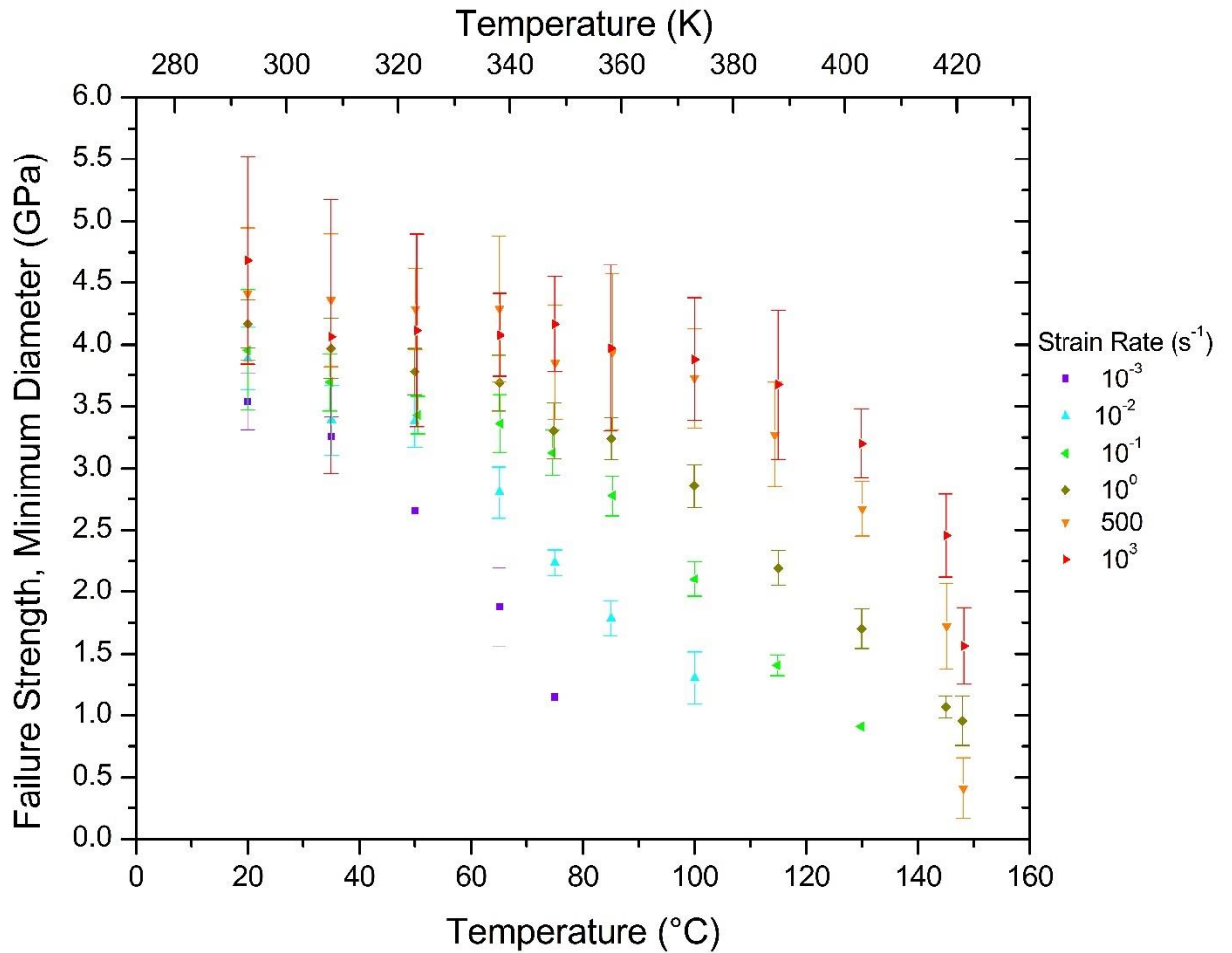


Figure 3-12: (Top) Average values of failure strength plotted with \pm one standard deviation. The non-failure temperatures are observed at 75 °C, 100 °C, and 130 °C for the 10^{-3} s $^{-1}$, 10^{-2} s $^{-1}$, and 10^{-1} s $^{-1}$, strain-rates, respectively. The non-failure temperature of the 10^0 s $^{-1}$ strain-rate was observed at 148 °C. The quasi-static and intermediate strain-rates are observed to be monotonically decreasing. **(Bottom)** Average values of minimum failure strength plotted with \pm one standard deviation. Failure strengths are higher than the average diameter method for all comparable temperature-strain-rate combinations. There does not appear to be a major change in shape of the plots when compared to the average diameter method plots.

The curvature of the strain-rate plot increases with decreasing strain-rate, meaning the failure strength drops off faster for lower strain-rates.

Two trends are observed for the dynamic strain-rates. The plots are observed to display two different behavioral regions. A plateau or slightly decreasing linear region in failure strength is observed for the dynamic strain rates at low temperatures. For the 500

s^{-1} strain rate, the plateau appears in the temperature range of 20 °C to 65 °C with a failure strength of approximately 4 GPa. For the $10^3 s^{-1}$ strain rate, the plateau appears in the temperature range of 20 °C to 65 °C with a failure strength of approximately 4 GPa. At temperatures above the plateau regions, the failure strength decreases with a concave shape, similar to the quasi-static and intermediate strain-rates. Due to the large standard deviations, it is difficult to determine if the failure strength at low temperatures behave in a linear manner or if the shape is always concave with the low temperature region appearing linear.

The minimum failure strengths for each of the 66 temperature-strain-rate combinations are plotted in Figure 3-12 (bottom). The $10^{-3} s^{-1}$, $10^{-2} s^{-1}$, $10^{-1} s^{-1}$, $10^0 s^{-1}$, $500 s^{-1}$, and $10^3 s^{-1}$ strain-rates are depicted in violet, blue, green, dark yellow, orange, and red, respectively. The averages are plotted with bars depicting \pm one standard deviation. Standard deviations are observed to be larger for the dynamic strain-rates. The failure strength values are higher than the values calculated in the average diameter method, at all comparable temperature-strain-rate combinations, as expected from the smaller diameter used for the stress calculations. Despite the increase in failure strengths, no major changes in shape are observed and there does not appear to be any better-fitting trends from the minimum diameter method.

The difference between the standard deviations for each temperature-strain-rate combination where failure occurs were calculated and are shown in Figure 3-13. The zero line is included in the plot to help distinguish the positive values where the minimum diameter method had a higher standard deviation for that temperature-strain-rate combinations and the negative values where the average diameter method had a higher

standard deviation. There were 16 negative values with a minimum of -0.12 GPa. There were 36 positive values with a maximum of 0.37 GPa. The average for all points is $0.04 \pm .03$ GPa, which indicates that there is slight increase in the standard deviations for the minimum diameter method. The plots appear to have a random distribution of positive and negative values and suggest no trend with temperature or strain-rate.

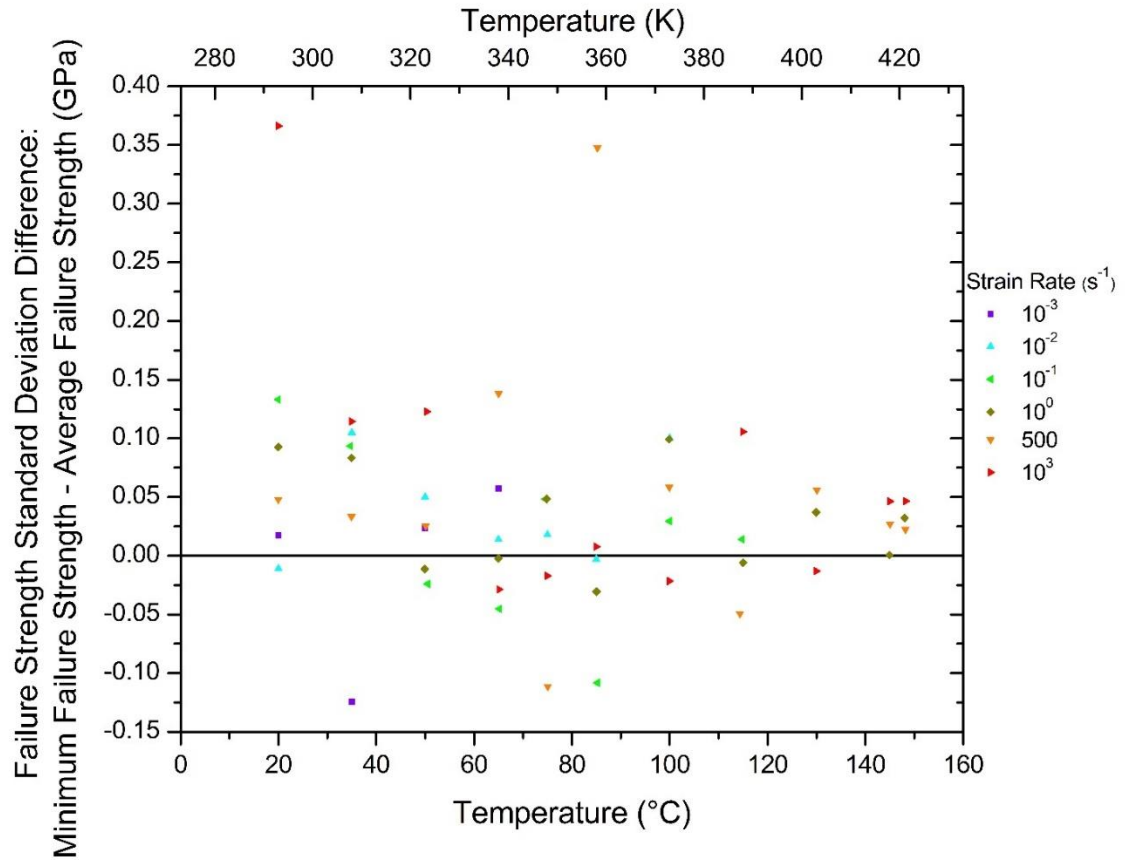


Figure 3-13: The calculated difference in failure strength standard deviations between the minimum diameter method and the average diameter method for each temperature-strain-rate where failure occurs. The positive values indicate temperature-strain-rate combinations where the minimum diameter method has a higher standard deviation and the negative values indicate combinations where the average diameter method has a higher standard deviation. The zero line has been drawn to help distinguish between these regions. The average value for all plots is 0.04 ± 0.03 GPa, indicating the minimum diameter method has slightly higher standard deviations. The plots appear to be randomly distributed suggesting there is no trend with temperature or strain-rate.

3.2.7 Strain to UTS

The strain to UTS values, defined in chapter 1, for each temperature-strain-rate combination were calculated and compared to observe changes in strain behavior in the non-failure temperature regions of the quasi-static and intermediate strain-rates. This is a material property not typically described and it is defined as the strain value at the peak stress (UTS) of the stress-strain curve.

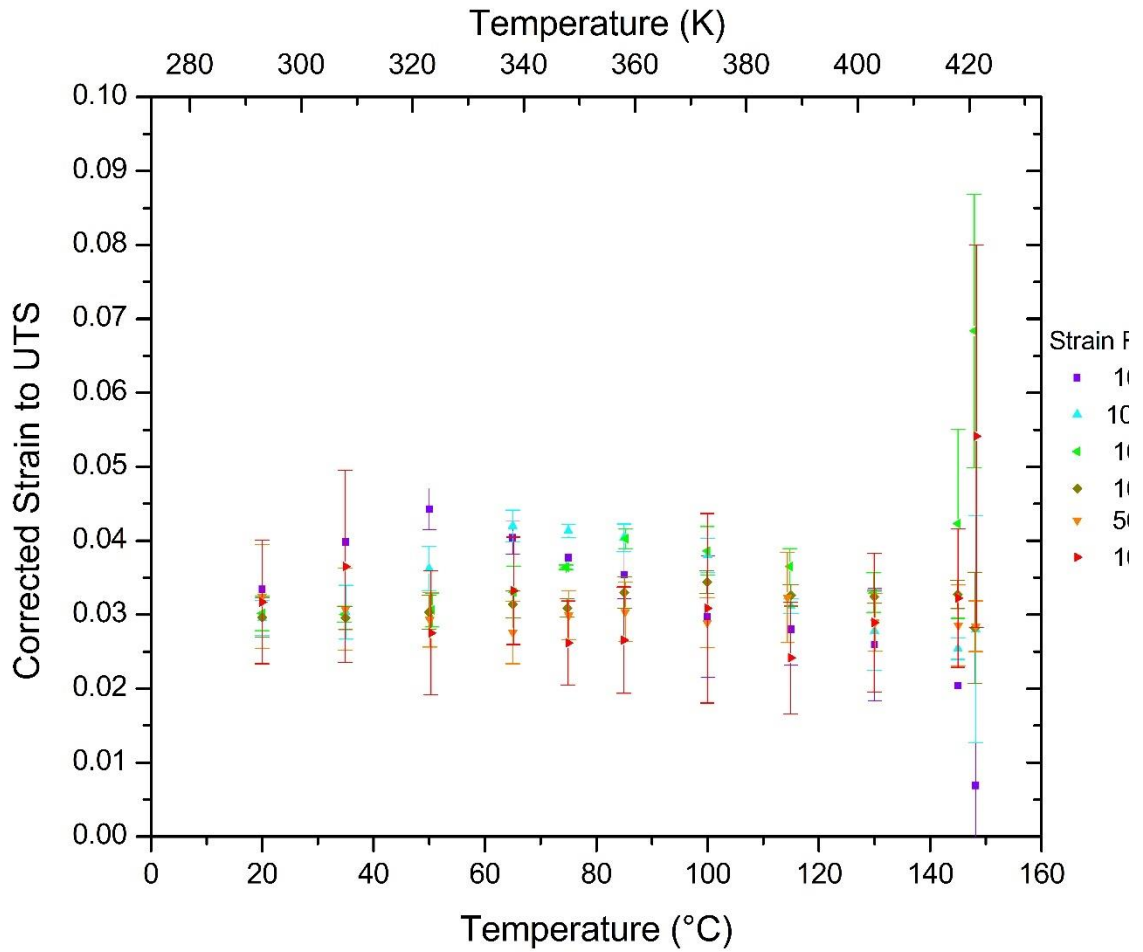
For constant strain-rate, the average strains to UTS were observed to initially increase with increasing temperature and then decrease after a maximum was reached at a strain-rate dependent temperature. This temperature at the peak strain to UTS was observed to increase with increasing strain-rate. As a reminder, for the temperature-strain-rate combinations with pseudo-brittle stress-strain curves, the UTS is the same point as the failure strength and therefore the strain to UTS is the same value as the strain to failure. Each of the 66 temperature-strain-rate combinations are plotted in Figure 3-14 (Top). Uncorrected strain to UTS plots and tables of these values can be found in Appendix A-5. The 10^{-3} s^{-1} , 10^{-2} s^{-1} , 10^{-1} s^{-1} , 10^0 s^{-1} , 500 s^{-1} , and 10^3 s^{-1} strain-rates are depicted in violet, blue, green, dark yellow, orange, and red, respectively. The averages are plotted with bars depicting \pm one standard deviation. Standard deviations are observed to be larger for the dynamic strain-rates except in the region near the melting temperature of the lower strain-rates where a large variation in strain to UTS is observed. Individual plots of the strains to UTS at each temperature-strain-rate combination can be found in Appendix A-6.

The strain to UTS values are observed between 2.5% and 4.5%. for all strain rates in the temperature range from 20 °C to 130 °C. The 10^{-3} s^{-1} strain-rate is observed to have

the maximum within this temperature range at 50 °C with a value of approximately 4.5% strain. The 10^{-3} s^{-1} strain-rate is observed to have the minimum strain value within this temperature range at approximately 2.5% to 3% strain across this temperature range. At temperatures of 145 °C and 148 °C, some behavioral differences emerge between the strain-rates. The 10^{-2} s^{-1} , 10^0 s^{-1} , and 500 s^{-1} all remain in the 2.5% to 4.5% strain range. 10^{-3} s^{-1} strain-rate is observed to decrease outside of the 2.5% minimum and drops sharply at 148 °C. The 10^{-1} s^{-1} strain-rate is observed to have the opposite behavior and increases in strain to UTS with an average value at approximately 7% strain at 148 °C. This is the highest observed average strain to UTS for all temperature-strain-rate combinations in this study. The 10^3 s^{-1} strain-rate is observed to behave similarly and increases in strain to UTS with an average value of approximately 5.5% at 148 °C. These abnormalities suggest changes in different molecular relaxation mechanisms and will be examined in the discussion section.

To show the observed peak strain to UTS values, a rescaled plot centered around 3% strain is shown in figure 3-14 (Bottom). For clarity, standard deviations have been removed and lines connecting adjacent points have been added. The added lines do not imply interpolated data or trend lines. Peak strain to UTS values are observed at temperatures of 50 °C, 65 °C, 85 °C, and 100 °C, for the 10^{-3} s^{-1} , 10^{-2} s^{-1} , 10^{-1} s^{-1} , 10^0 s^{-1} strain-rates, respectively. These temperatures correspond with the beginning of the necking curves observed in the stress-strain curve shapes. This plot shows the strain to UTS remaining relatively constant for the 500 s^{-1} and 10^3 s^{-1} strain-rates, with a plateau of strain to UTS at approximately 3% across the entire temperature range from 20 °C to 148 °C. This is the same observation from the strain to failure due to the UTS and failure

strength corresponding to the same point in the dynamic curve shapes. Similarly, the only exception is the 10^3 s^{-1} strain-rate at $148 \text{ }^\circ\text{C}$ where an average strain to UTS of approximately 5.5% was observed and this agrees with the linear stress-strain relationship to failure observed in the stress-strain curve shape.



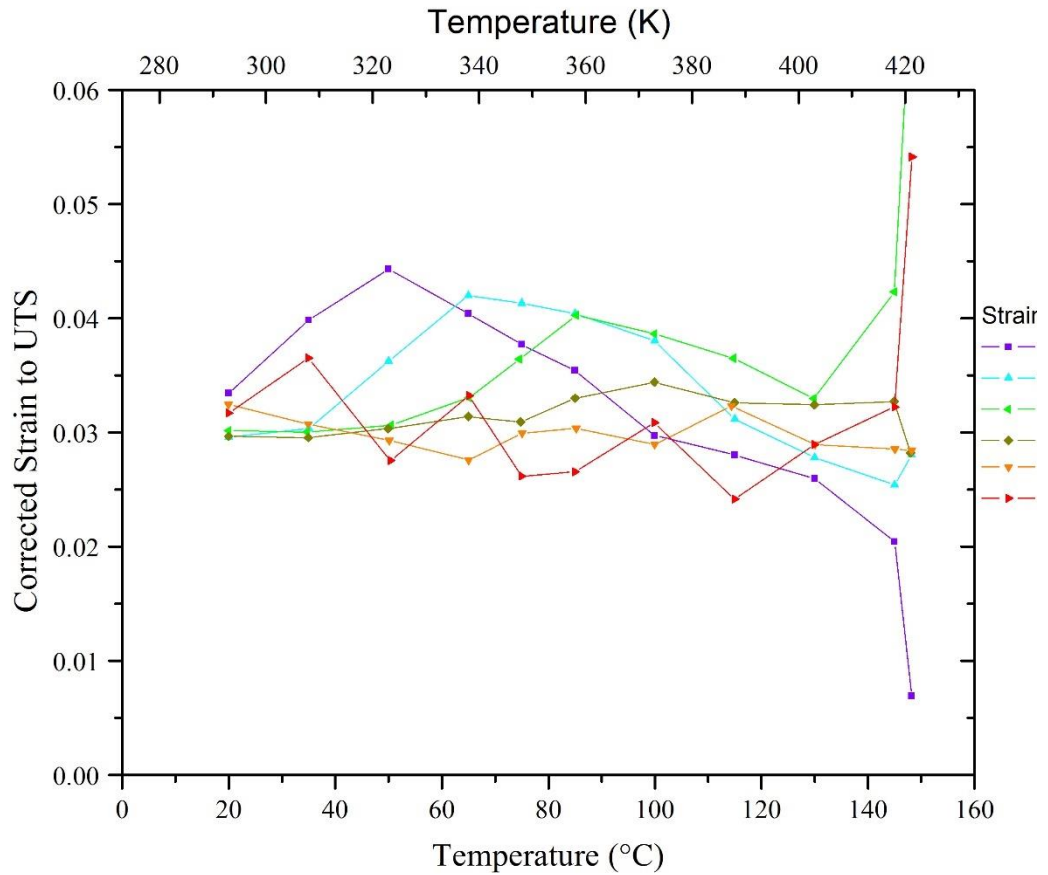


Figure 3-14: (Top) Average values of corrected strain to UTS plotted with \pm one standard deviation showing all strain to UTS values between 2.5% and 4.5% strain in the temperature range of 20 °C to 130°C. Also shown are changes in strain values for some of the strain-rates in the 145 °C to 148 °C temperature range. **(Bottom)** A rescaled plot centered around 3% strain. For clarity, standard deviations have been removed and lines connecting adjacent points have been added. This plot shows the strain to UTS not changing for the 500 s^{-1} and 10^3 s^{-1} strain-rates, with a strain to failure of approximately 3% across the temperature range of 20 °C to 145 °C (just before the melting temperature). The necking temperatures of 50 °C, 75 °C, 85 °C, and 115 °C, are observed as the peaks for 10^{-3} s^{-1} , 10^{-2} s^{-1} , 10^{-1} s^{-1} , 10^0 s^{-1} , strain-rates, respectively. For the 10^{-2} s^{-1} and 10^0 s^{-1} strain-rates, the necking temperature is observed at one temperature higher than the apparent peak in this plot, but the two values of the strain to UTS are very similar and both necking temperatures are within one standard deviation of the strain to UTS values of the apparent peak temperature.

3.2.8 Ultimate Tensile Strength

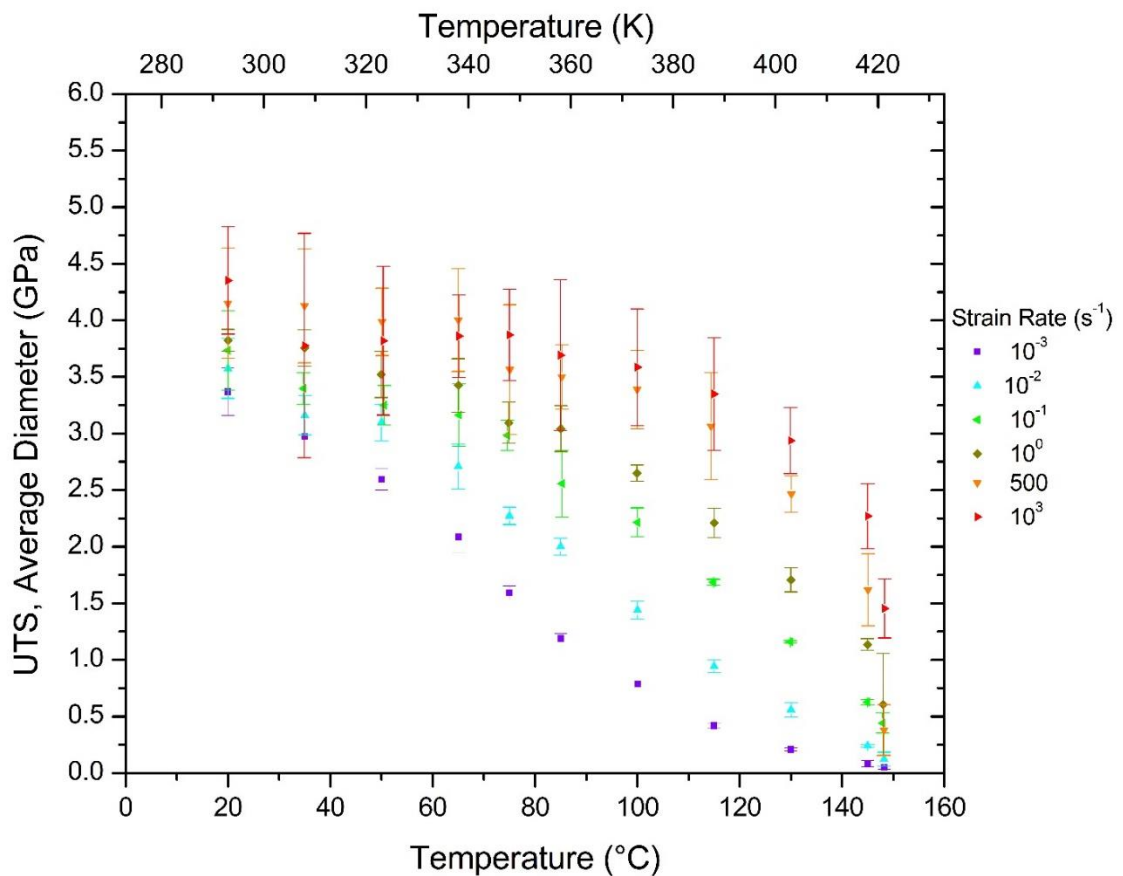
UTS values were calculated using two methods. First, the average diameter of the five fiber diameter measurements was used to calculate stresses and are referred to as UTS. Second, the minimum of the five fiber diameter measurements was used to determine if using the smallest cross sectional area of the fiber was a more accurate method to calculate stresses. These are referred to as minimum UTS.

For constant strain-rate, UTS values were observed to decrease with increasing temperature. For constant temperature, UTS were observed to increase with increasing strain-rate. Average UTS values for each of the 66 temperature-strain-rate combinations are plotted in Figure 3-15 (Top). The 10^{-3} s^{-1} , 10^{-2} s^{-1} , 10^{-1} s^{-1} , 10^0 s^{-1} , 500 s^{-1} , and 10^3 s^{-1} strain-rates are depicted in violet, blue, green, dark yellow, orange, and red, respectively. The averages are plotted with bars depicting \pm one standard deviation. Standard deviations are observed to be larger for the dynamic strain-rates. Individual UTS plots can be found in Appendix A-7.

All of the strain-rate plots are monotonically decreasing with increasing temperature with a concave shape. One exception is the 10^{-3} s^{-1} strain-rate where the plot shape is observed to transition from concave to convex at the inflection point around 75°C . Linear decreases in UTS with increasing temperature are observed for the 10^{-2} s^{-1} , 10^{-1} s^{-1} , and 10^0 s^{-1} strain-rates in the temperature ranges of 65°C to 145°C , 75°C to 145°C , and 85°C to 145°C , respectively. These linear regions are possibly long inflection-transition regions, like the one observed in the 10^{-3} s^{-1} strain-rate. As a reminder, the dynamic strain-rates are observed to exhibit pseudo-brittle stress-strain curve shapes across all temperatures in this study and the UTS points are the same as the failure

strength points. The observation of two possible behavior regions of the dynamic strain-rates was presented in the previous section.

The minimum UTS values for each of the 66 temperature-strain-rate combinations are plotted in Figure 3-15 (Bottom). The 10^{-3} s^{-1} , 10^{-2} s^{-1} , 10^{-1} s^{-1} , 10^0 s^{-1} , 500 s^{-1} , and 10^3 s^{-1} strain-rates are depicted in violet, blue, green, dark yellow, orange, and red, respectively. The averages are plotted with bars depicting \pm one standard deviation. Standard deviations are observed to be larger for the dynamic strain-rates. The UTS values are higher than the values calculated in the average diameter method, at all comparable temperature-strain-rate combinations, as expected. Similar to the failure strength plot comparisons, no major changes in shape are observed and there does not appear to be any better-fitting trends from the minimum diameter method. The difference



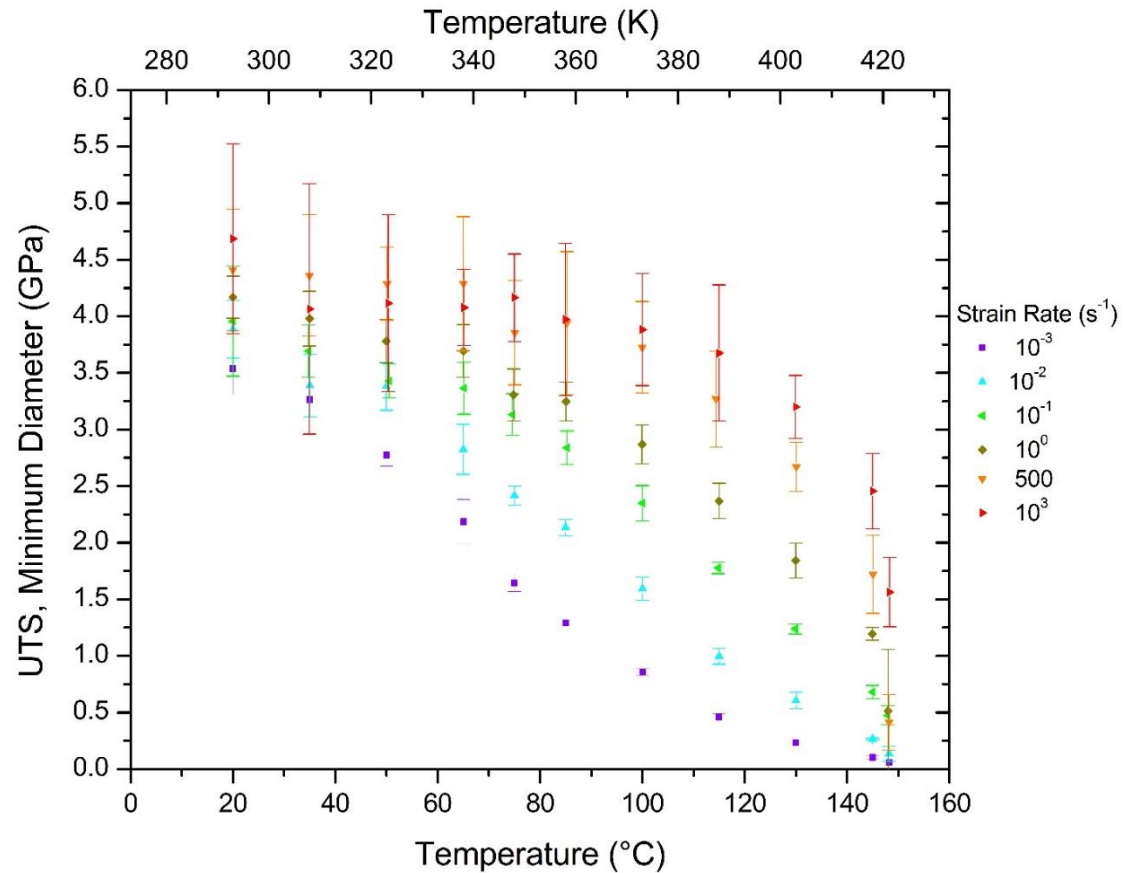


Figure 3-15: (Top) Average values of UTS plotted with \pm one standard deviation. All of the strain-rate plots are monotonically decreasing with increasing temperature and a concave shape. One exception is the 10^{-3} s^{-1} strain-rate where the plot shape is observed to be S-shaped. This plot begins with a concave shape and transitioning to convex at the inflection point around $75 \text{ }^\circ\text{C}$. Linear decreases in UTS with increasing temperature are observed for the 10^{-2} s^{-1} , 10^{-1} s^{-1} , and 10^0 s^{-1} strain-rates in the temperature ranges of $65 \text{ }^\circ\text{C}$ to $145 \text{ }^\circ\text{C}$, $75 \text{ }^\circ\text{C}$ to $145 \text{ }^\circ\text{C}$, and $85 \text{ }^\circ\text{C}$ to $145 \text{ }^\circ\text{C}$, respectively. **(Bottom)** Average values of minimum failure strength plotted with \pm one standard deviation. Failure strengths are higher than the average diameter method for all comparable temperature-strain-rate combinations. There does not appear to be a major change in shape of the plots when compared to the average diameter method plots.

between the standard deviations for each temperature-strain-rate combination were calculated and are shown in Figure 3-16. The zero line is included in the plot to help distinguish the positive values where the minimum diameter method had a higher

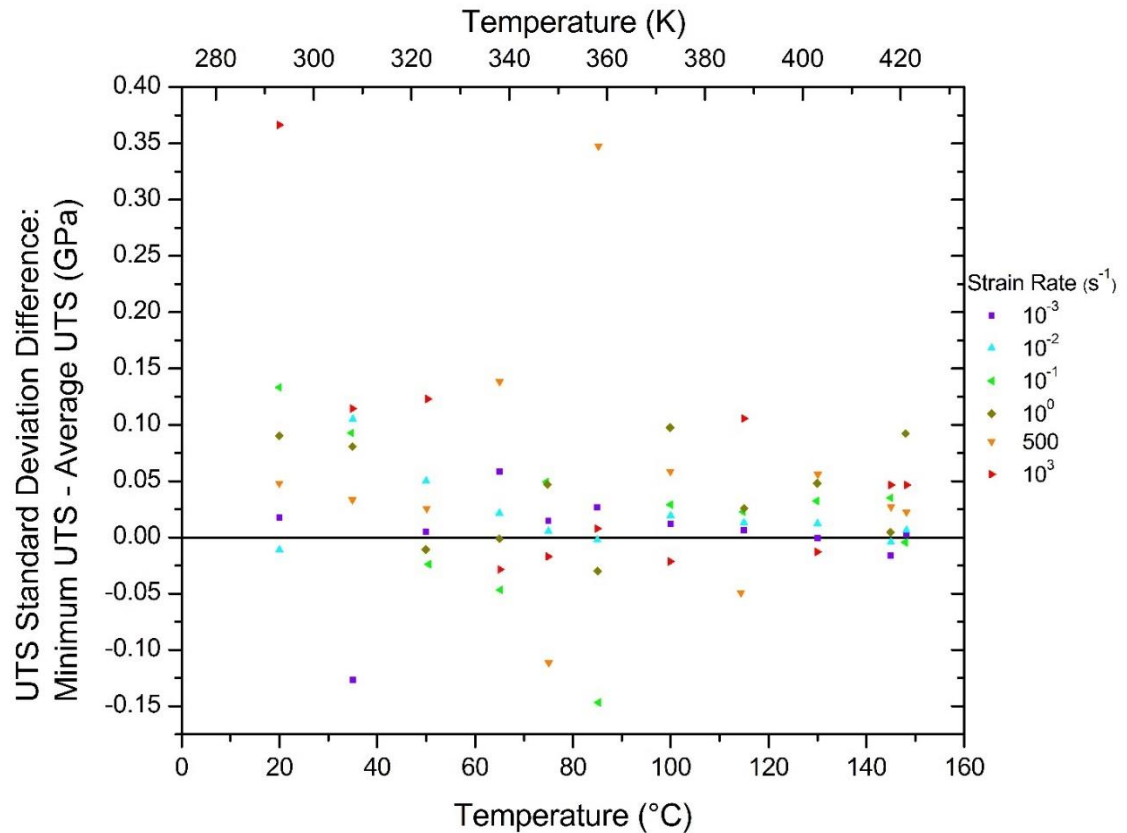


Figure 3-16: The calculated difference in UTS standard deviations between the minimum diameter method and the average diameter method for each temperature-strain-rate. The positive values indicate temperature-strain-rate combinations where the minimum diameter method has a higher standard deviation and the negative values indicate combinations where the average diameter method has a higher standard deviation. The zero line has been drawn to help distinguish between these regions. The average value for all plots is 0.03 ± 0.08 GPa, indicating the minimum diameter method has slightly higher standard deviations. The plots appear to be randomly distributed suggesting there is no trend with temperature or strain-rate.

standard deviation for that temperature-strain-rate combinations and the negative values where the average diameter method had a higher standard deviation. There were 19 negative values with a minimum of -0.15 GPa. There were 47 positive values with a maximum of 0.37 GPa. The average for all points is $0.03 \pm .08$ GPa, which indicates that there is slight increase in the standard deviations for the minimum diameter method. Similar to the failure strength standard deviation difference plots, the UTS standard

deviation difference plots appear to have a random distribution of positive and negative values and suggest that there are not any trends with temperature or strain-rate.

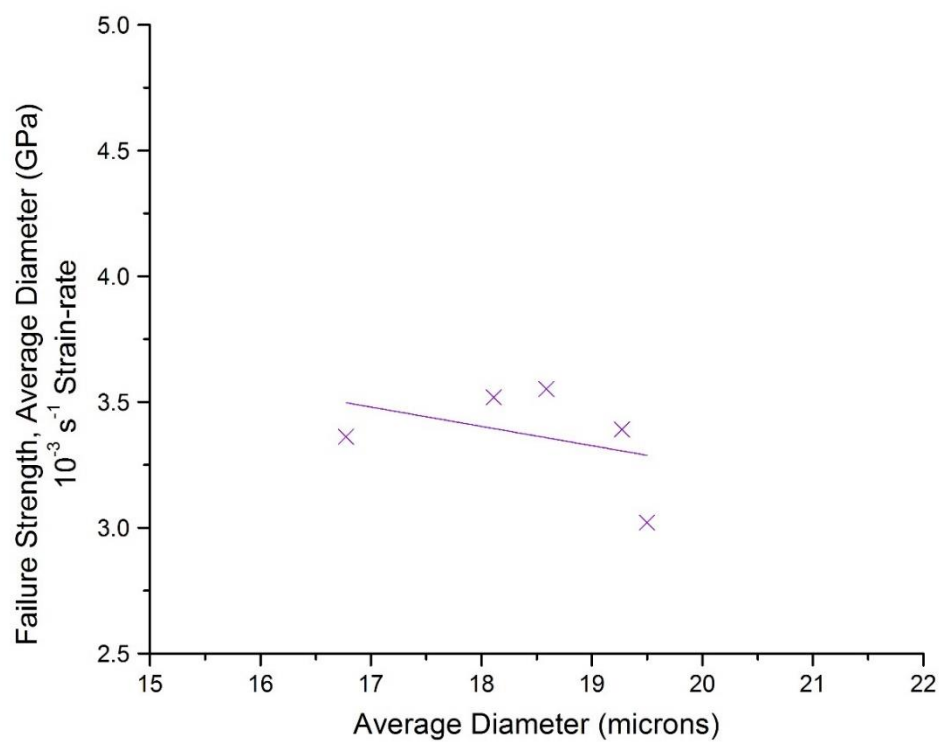
3.2.9 Effects of Fiber Diameter on Failure Strength

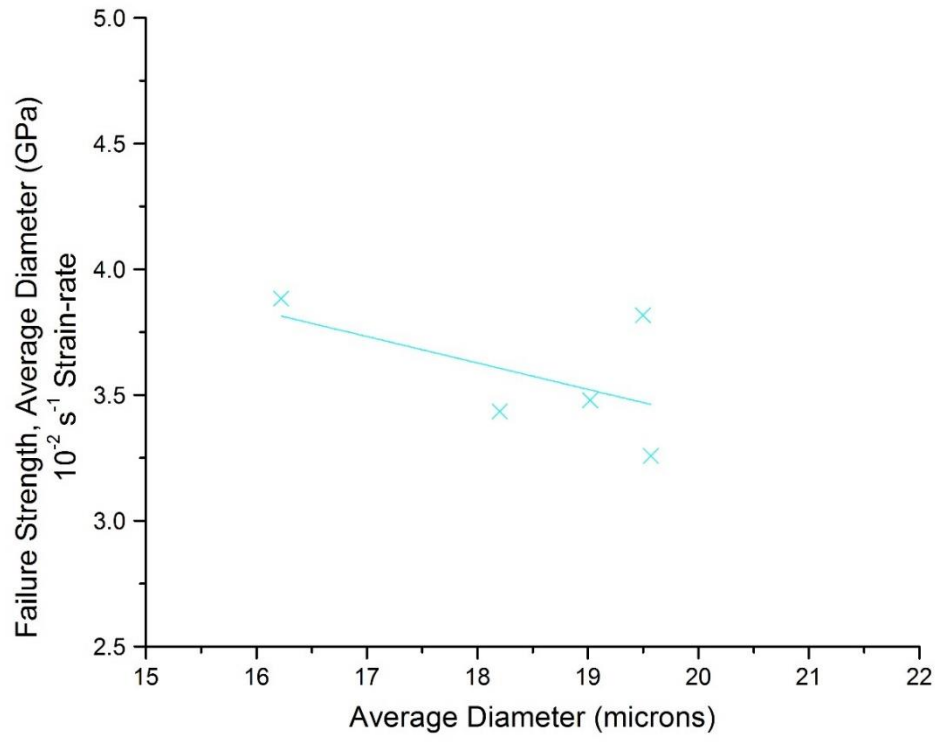
Individual fiber tensile tests at 20 °C were used to determine the effects of average fiber diameter on failure strength. The fit parameters and plots of the average fiber diameter and failure strength for each of the six strain-rates is show in Table 3-8 and Figure 3-17, respectfully. For the quasi-static and intermediate strain-rates, there are 5 data points and for the dynamic strain-rates there are between eight to ten data points. For the change in number of points, adjusted R² values were used for goodness of fit parameters. The fits indicate a negative correlation between average fiber diameter and failure strength. The only exception was the 10⁰ s⁻¹ strain-rate which showed a very small positive correlation.

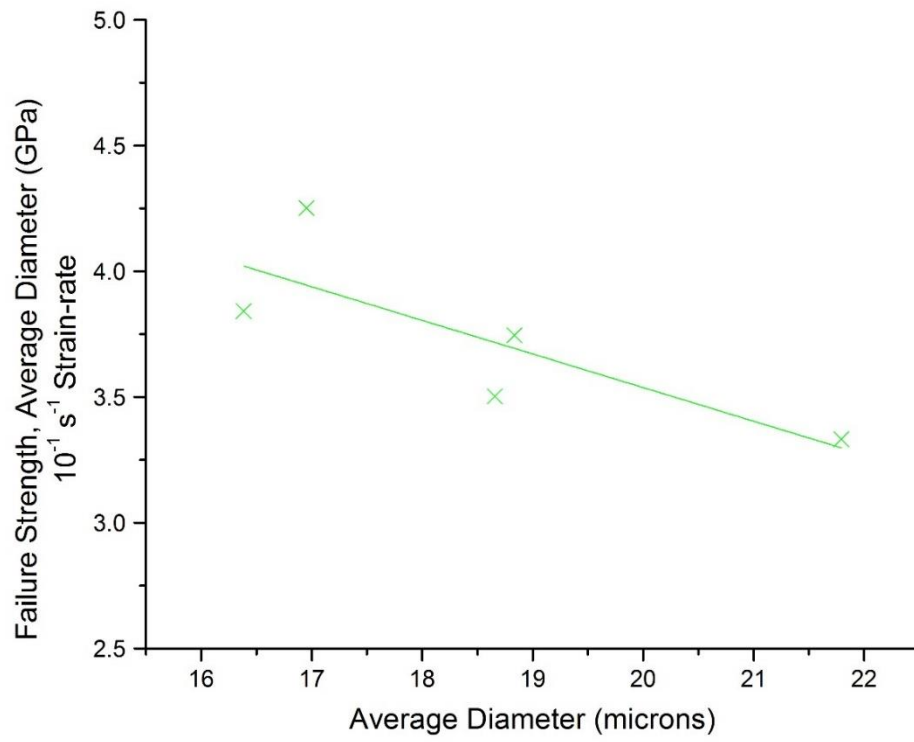
To address the low adjusted R² values of the linear fits, the fits for each strain-rate can be applied to the diameter distribution presented in the previous section to obtain average fiber strength distributions and these average values can be compared with the experimental results. Figure 3-18 shows the distribution plots for the average failure

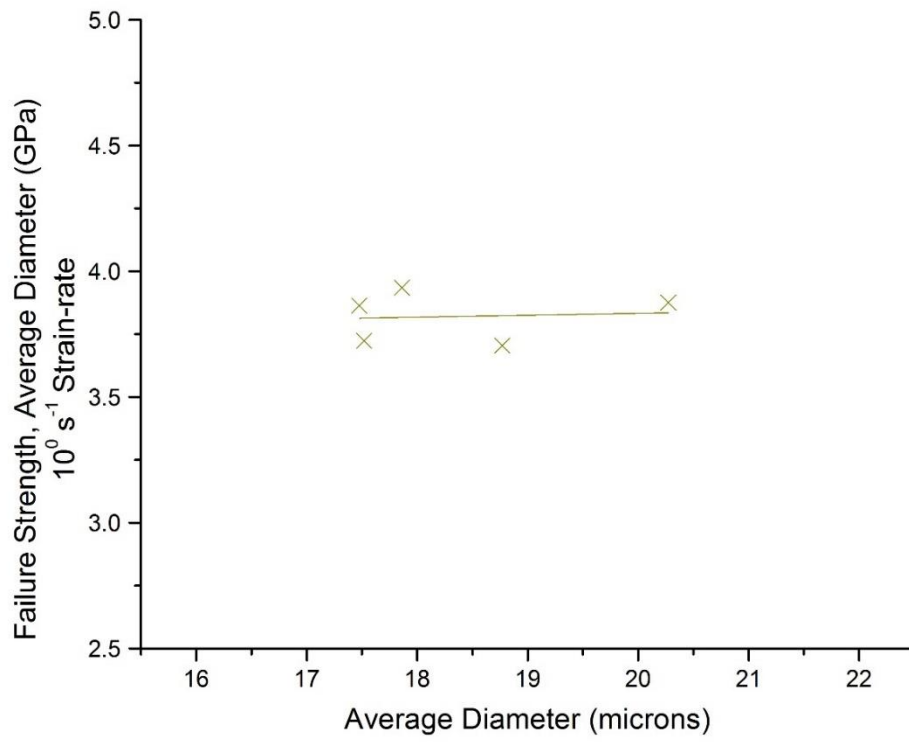
Strain-rate (s ⁻¹)	Slope of linear fit with standard error [GPa/μm]	Intercept of linear fit at 0°C with standard error [GPa]	Adjusted R ² of Fit
10 ⁻³	-0.0767 ± 0.1030	4.78 ± 1.90	-0.1253
10 ⁻²	-0.105 ± 0.093	5.52 ± 1.72	0.06577
10 ⁻¹	-0.134 ± 0.057	6.21 ± 1.07	0.5255
10 ⁰	0.00768 ± 0.04923	3.68 ± 0.91	-0.3226
500	-0.382 ± 0.328	11.0 ± 5.9	0.04248
10 ³	-0.309 ± 0.150	9.96 ± 2.72	0.3174

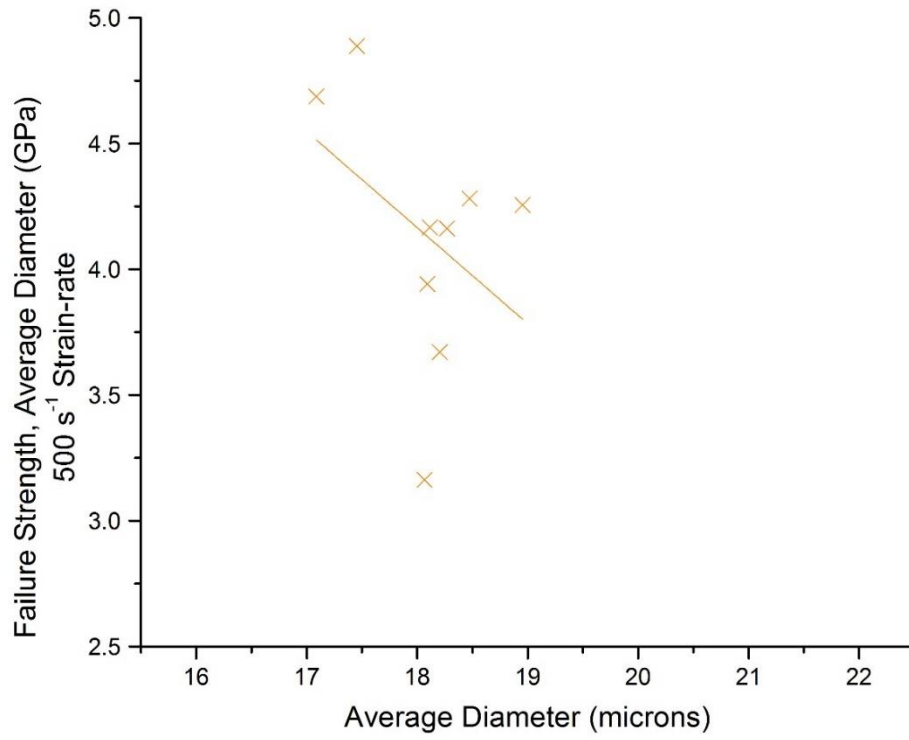
Table 3-8: Fit parameters for 20 °C individual fiber tensile tests for the six strain-rates.











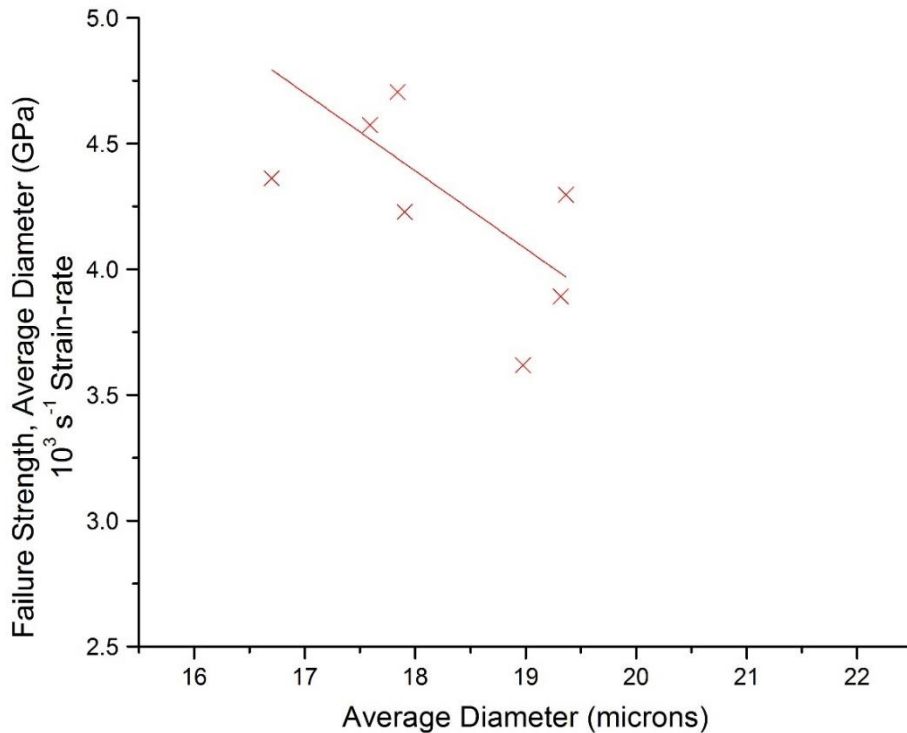


Figure 3-17: Plots of the linear fits of average fiber diameter and failure strength for the six strain-rates. The scales on each plot have been kept constant for comparison. The 10^{-3} s^{-1} , 10^{-2} s^{-1} , 10^{-1} s^{-1} , 10^0 s^{-1} , 500 s^{-1} , and 10^3 s^{-1} strain-rates are depicted in violet, blue, green, dark yellow, orange, and red, respectively.

strength for the six strain-rates. The small positive correlation for the 10^0 s^{-1} strain-rate caused a small range in failure strength (3.80 GPa to 3.88 GPa) to be observed in the distribution.

The averages and standard deviations are compared to the experimental averages and standard deviations in Table 3-9. The table shows excellent agreement between the experimental and calculated distributions for the quasi-static and intermediate strain-rates. The dynamic strain-rates also show good agreement considering the large standard deviations associated with the experimental procedure.

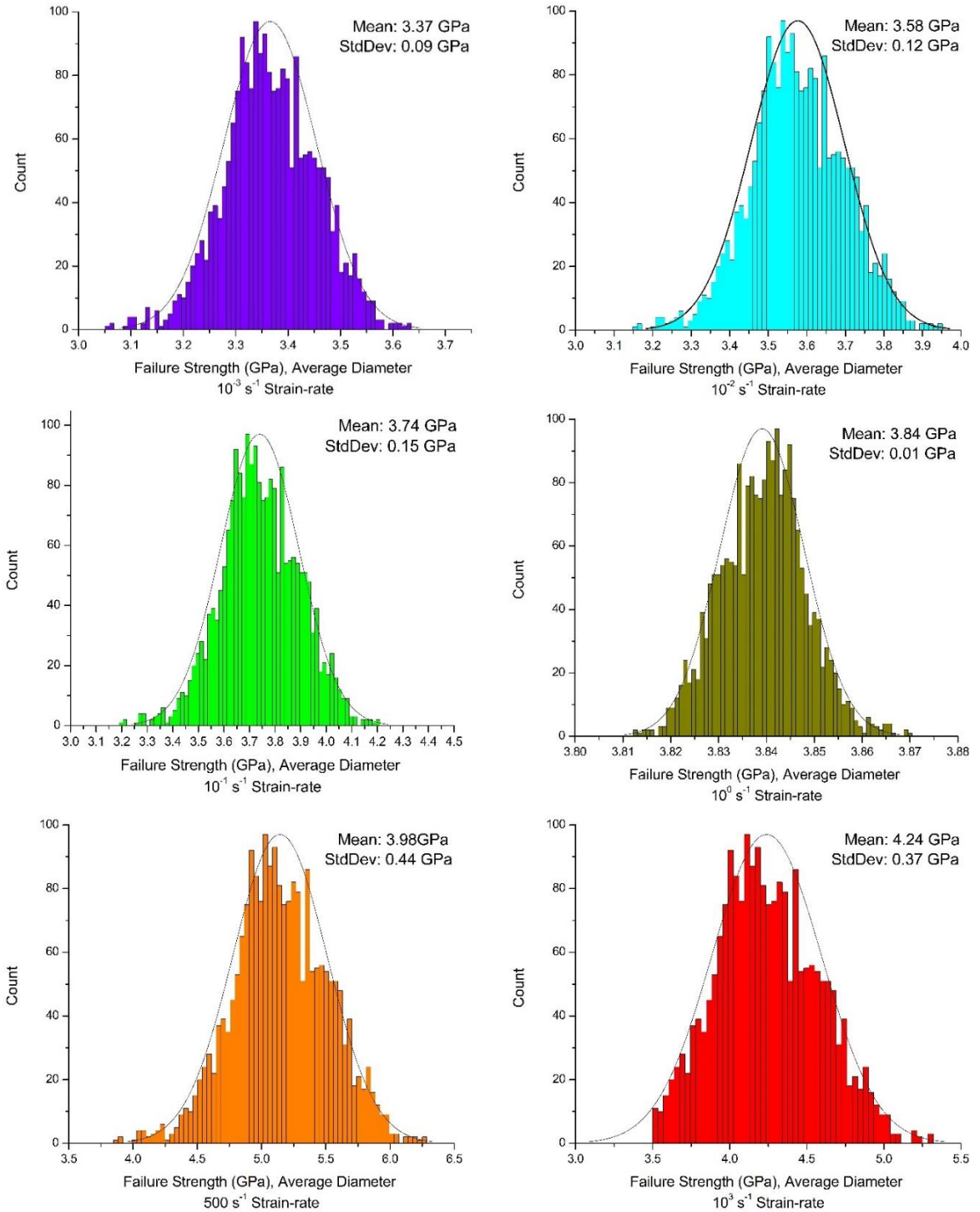


Figure 3-18: The average fiber strength distributions calculated from the diameter distribution and diameter-failure-strength linear relationship for each of the six strain-rates. The 10^{-3} s^{-1} , 10^{-2} s^{-1} , 10^{-1} s^{-1} , 10^0 s^{-1} , 500 s^{-1} , and 10^3 s^{-1} strain-rates are depicted in violet (**Top left**), blue (**Top right**), green (**Middle left**), dark yellow (**Middle right**), orange (**Bottom left**), and red (**Bottom right**), respectively. Gaussian distribution traces have been included for comparison.

Strain-rate (s ⁻¹)	Experimental Average Fiber Failure Strength and Standard Deviation (GPa)	Diameter Distribution Average Fiber Failure Strength and Standard Deviation (GPa)
10 ⁻³	3.37 ± 0.21	3.37 ± 0.09
10 ⁻²	3.57 ± 0.27	3.58 ± 0.12
10 ⁻¹	3.73 ± 0.35	3.74 ± 0.15
10 ⁰	3.82 ± 0.10	3.84 ± 0.01
500	4.15 ± 0.49	3.98 ± 0.44
10 ³	4.35 ± 0.47	4.24 ± 0.37

Table 3-9: A comparison of the experimental and calculated diameter distribution average fiber failure strengths and standard deviations.

To determine if there is a strain-rate dependence on the effect of average fiber diameter on failure strength, the slopes of the fits are plotted with log of strain-rate. The plots are shown in Figure 3-19. Due to the poor fitting of the 10⁰ strain-rate, linear fits of the relationship are shown including and excluding the 10⁰ s⁻¹ strain-rate. The fit parameters are summarized in Table 3-10. The adjusted R² of the fit excluding the 10⁰ s⁻¹ strain-rate is 0.9294 showing an excellent goodness of fit. The slope of this fit is -0.00856 ± 0.03309 GPa/μm/Log(Strain-rate) suggesting that the effect of the average fiber diameter on failure strength increases with increasing strain-rate. For a constant decrease in average fiber diameter, there is a larger decrease in failure strength at higher strain-rates. This will be examined further in the discussion section.

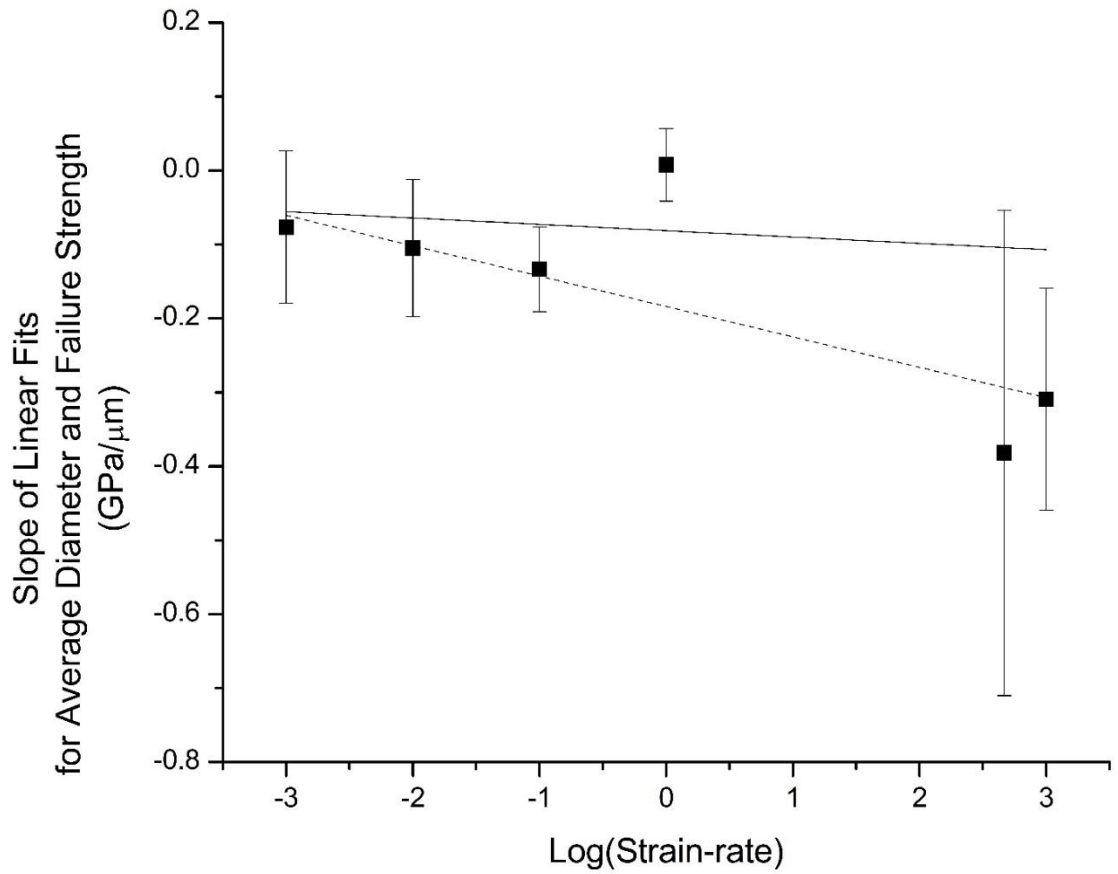


Figure 3-19: Linear fits of the slopes of the relationship between average fiber diameter and failure strength. The fits include the 10^0 s^{-1} strain-rate (solid line) and excluding the 10^0 s^{-1} strain-rate (dashed line).

Fit	Slope of Fit with Standard Error [GPa/μm/Log(Strain-rate)]	Intercept of Fit with Standard Error [GPa/μm]	Adjusted R ² of Fit
Including 10^0 s^{-1}	-0.00856 ± 0.03309	$-.0814 \pm .0482$	-0.2294
Excluding 10^0 s^{-1}	-0.0411 ± 0.0056	-0.184 ± 0.011	.9294

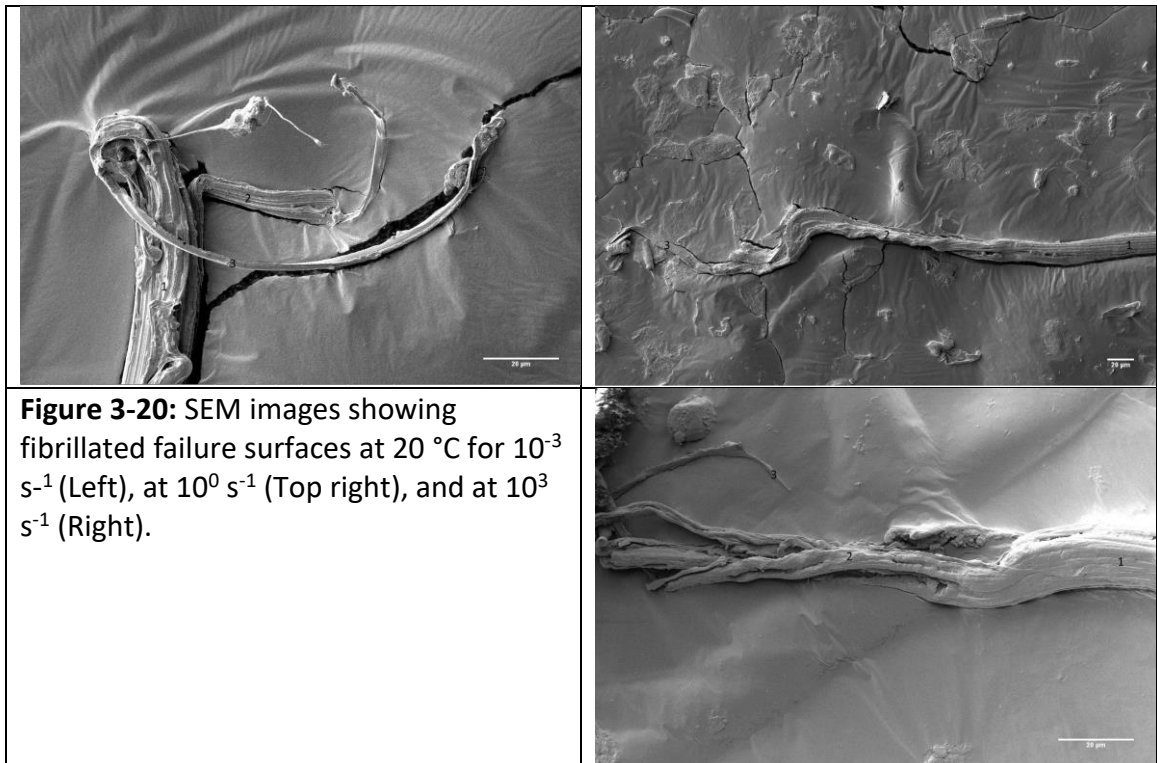
Table 3-10: Fit parameters for the linear fits of the slopes of the relationship between average fiber diameter and failure strength including and excluding the 10^0 s^{-1} strain-rate.

3.2.10 SEM Imaging

SEM imaging was used to observe fiber failure surfaces and changes in fiber cross-sectional area. For the average diameter measurements, three zones are identified in each image. Zone one corresponds to the thickest region of the fiber near the failure surface. Zones two and three measure different regions of the failure surface.

3.2.10.1 Failure Surfaces at 20 °C

The failure surfaces for fibers at 10^{-3} s^{-1} , 10^0 s^{-1} , and 10^3 s^{-1} strain-rates at 20 °C are shown in Figure 3-20. The fibers are observed to fibrillate at all strain-rates. Average diameter measurements were taken at three zones of the image. The average diameters and standard deviations for these zones can be found in Table 3-11. Comparison of the thickest region of the fiber to the pre-tensile test diameter show a decrease in average fiber diameter is observed near the failure surface. This observation suggests that some



level of localized strain occurs at all strain-rates at 20 °C.

3.2.10.2 Failure Surfaces at the Plateauing Temperature

The failure surfaces for fibers at 10^{-3} s^{-1} , 10^0 s^{-1} , strain-rates in their respective plateauing temperature region are shown in Figure 3-21. The fiber is observed to exhibit fibrillation at the 10^{-3} s^{-1} strain-rate. The failure surface for the 10^0 s^{-1} strain-rate does not show a fibrillated failure surface and a large cross-sectional area is observed. The plateauing temperature for the 10^0 s^{-1} strain-rate is 100 °C and the failure surface has been subjected to higher temperatures after failure due to contact with the fiber heater channel walls. Additionally, the fiber is subjected to annealing in the heater channel as the heater is cooled before the fiber is extracted from the test setup. As discussed in the previous chapters, the heating of the fibers causes an entropic shrinking force and these surfaces reflect the shrinkage of a fibrillated failure surface. The average diameters and standard deviations for these zones can be found in Table 3-11. Comparison of the thickest region of the fiber to the pre-tensile test diameter shows a decrease in average fiber diameter is observed near the failure surface in the plateauing temperature range. This suggests that some localized strain occurs at the plateauing temperature.

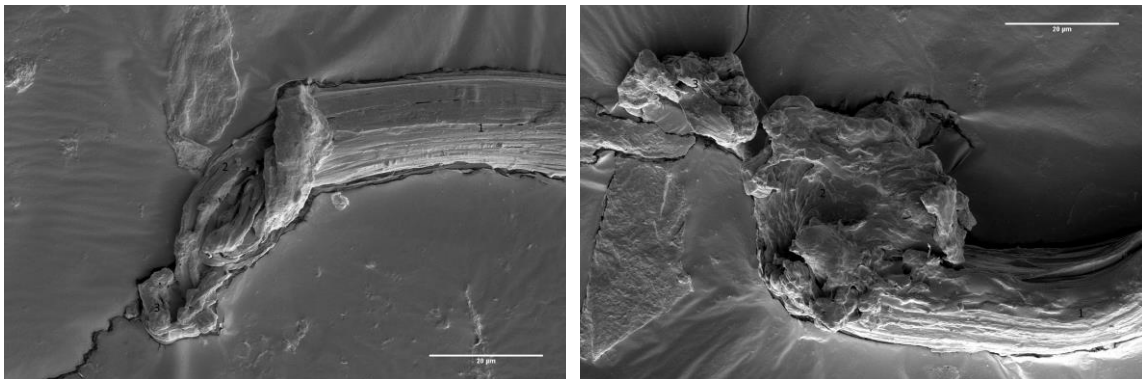


Figure 3-21: Plateauing temperature SEM images showing a fibrillated failure surface at 35 °C for 10^{-3} s^{-1} (Left) and post-failure annealing at 100 °C at 10^0 s^{-1} (Right).

3.2.10.3 Failure Surfaces at the Necking Temperature

The failure surfaces for fibers at 10^{-3} s^{-1} , 10^0 s^{-1} , strain-rates in their respective necking temperature region are shown in Figure 3-22. The fiber is observed to exhibit fibrillation at the 10^{-3} s^{-1} strain-rate. The level of fibrillation is not as high as observed at the lower temperatures at this strain-rate. The fibrils are not as extended and appear to have shrunk. This suggests that $50 \text{ }^\circ\text{C}$ is the lowest temperature where post-failure shrinking is observed. Additionally, necking can be observed in the image for the 10^{-3} s^{-1} strain-rate between zones one and two. The average diameter is observed to taper between these two zones.

The necking temperature for the 10^0 s^{-1} strain-rate is $115 \text{ }^\circ\text{C}$. The failure surface does not show a fibrillated failure surface and is suspected to have annealed in the fiber heater channel. The average diameters and standard deviations for these zones can be found in Table 3-11. Comparison of the thickest region of the fiber to the pre-tensile test diameter shows a decrease in average fiber diameter is observed near the failure surface in the necking temperature range. This suggests that localized strain occurs at the plateauing temperature.

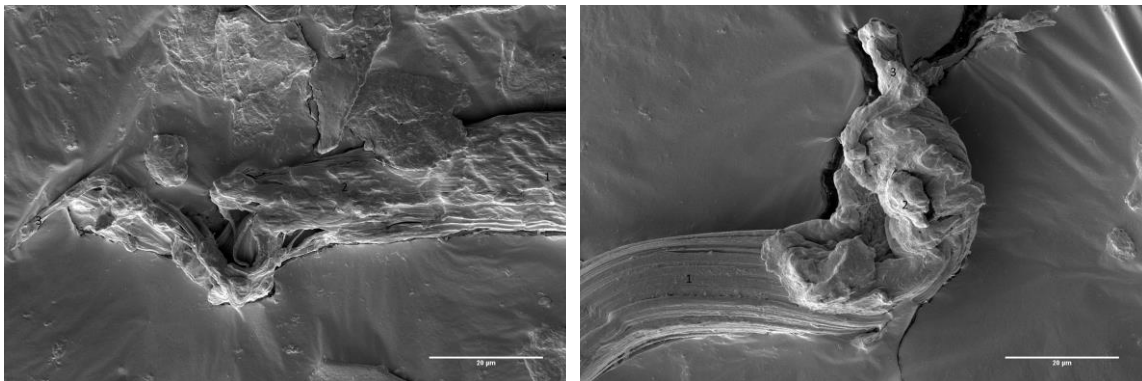
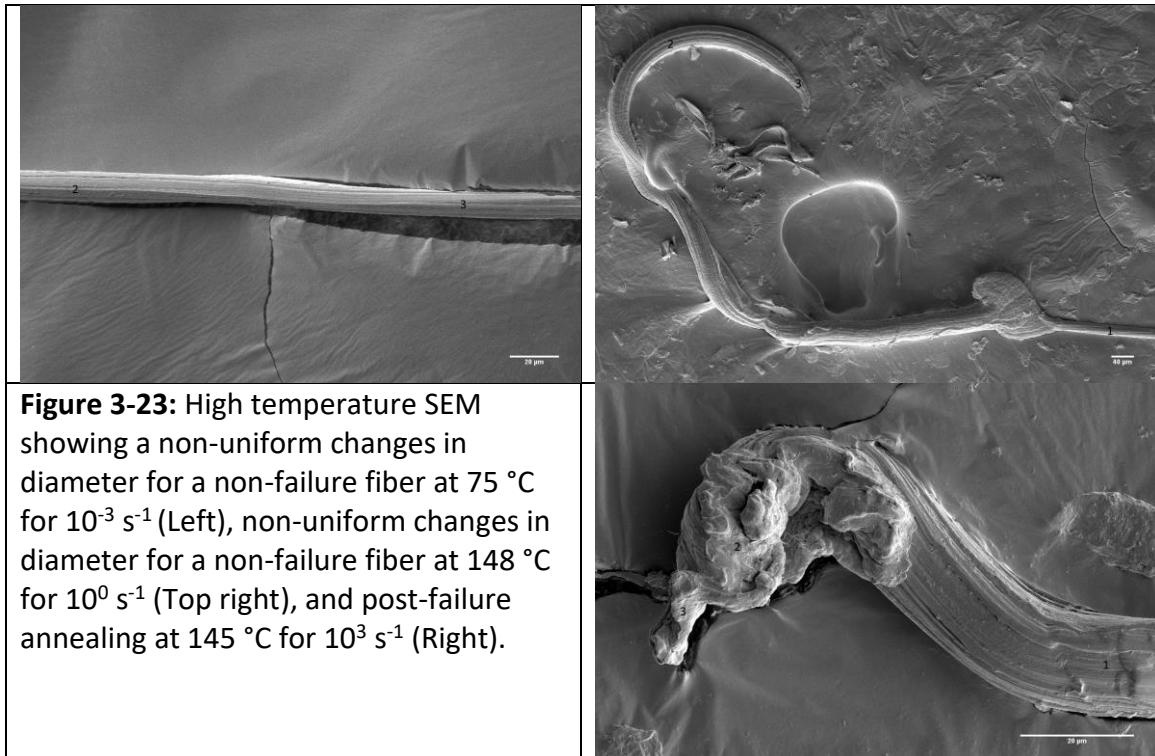


Figure 3-22: Necking temperature SEM images at 1500x showing a fibrillated failure surface at $50 \text{ }^\circ\text{C}$ or 10^{-3} s^{-1} (Left) and post-failure annealing at $115 \text{ }^\circ\text{C}$ at 10^0 s^{-1} (Right).

3.2.10.4 Fibers at Non-failure and High Temperatures

The failure surfaces for fibers at 10^{-3} s^{-1} , 10^0 s^{-1} , strain-rates in their respective non-failure temperature region are shown in Figure 3-23. The average diameters and standard deviations for the zones can be found in Table 3-11. The at the 10^{-3} s^{-1} strain-rate, fourteen images were analyzed spanning the entire gage length of the extended fiber. Zone 1 summarizes the average diameter and standard deviation across the entire gage length. The large standard deviation indicates a non-uniform change in diameter across the gage length. The image demonstrates this non-uniformity showing the difference in average diameter between zones 2 and 3 as approximately $2 \mu\text{m}$.

The 10^0 s^{-1} strain-rate has a non-failure temperature of $148 \text{ }^\circ\text{C}$. At this high temperature, the fiber was fragile after testing and was broken in transit to the storage container. The failure surface does not show a fibrillated failure surface and shows a tapered point with an average diameter higher than the pre-tensile test average diameter.



Comparison of zone 1 of the fiber to the pre-tensile test diameter show a decrease in average fiber diameter near the failure surface in the non-failure temperature range. Combined with the 10^{-3} s^{-1} images, this suggests that there are several possible regions of localized strain occurring at the non-failure temperature.

An image was also taken for a tensile test at $145 \text{ }^{\circ}\text{C}$ and 10^3 s^{-1} strain-rate. The failure surface shows the shrinkage of the fibrillated surface as seen in the 10^0 s^{-1} strain-rate. Comparison of the zone 1 of the fiber to the pre-tensile test diameter show a decrease in average fiber diameter is observed near the failure surface at this high strain-rate. Combined with the previous average diameter measurements, comparison of the average diameter near the failure surface to the average pre-tensile test diameter shows a decrease in average fiber diameter is observed for all temperatures and strain-rates investigated in this study and localized strain is present near the failure surface.

Strain-rate [s ⁻¹]	Temperature [°C]	Pre-tensile Test	Zone 1	Zone 2	Zone 3
10 ⁻³	20	19.50 ± 0.34	17.251 ± 0.190	6.643 ± 1.240	1.938 ± 0.161
	35	17.07 ± 0.77	16.339 ± 0.667	4.549 ± 0.529	3.794 ± 1.001
	50	18.59 ± 0.75	20.792 ± 0.139	15.715 ± 0.742	8.872 ± 1.154
	75	18.11 ± 0.38	17.064 ± 3.991	12.164 ± 0.142	10.610 ± 0.215
10 ⁰	20	17.86 ± 0.79	16.423 ± 0.787	8.570 ± 1.345	7.159 ± 1.477
	100	18.77 ± 0.49	17.349 ± 0.996	30.614 ± 7.744	11.766 ± 1.582
	115	18.37 ± 0.32	17.765 ± 0.271	23.411 ± 0.934	5.703 ± 0.744
	148	19.50 ± 0.64	18.348 ± 0.907	37.501 ± 1.109	20.921 ± 1.281
10 ³	20	18.98 ± 0.21	16.686 ± 0.321	5.569 ± 0.961	0.787 ± 0.254
	145	18.95 ± 0.026	17.969 ± 0.473	18.168 ± 1.281	6.208 ± 0.048

Table 3-11: Average diameters and standard deviations for fibers across the strain-rate and temperature range of this study. Diameter averages are shown for pre-tensile test and in three zones near the failure surfaces. Zone one shows the thickest region near the failure surface. Zones 2 and 3 measure different regions of the failure surface. Zone one in the 10⁻³ s⁻¹ strain-rate at 75 °C is the average diameter and standard deviation for the entire gage length of the non-failure fiber.

3.2.10.5 Nanofibril Bridging

During the failure surface analysis, fibers subjected to bending were observed to have shear separation between adjacent microfibrils and a crack was formed. Within these cracks, fibrils with diameters on the order of 10^3 's of nanometers were observed to connect the opposite sides of the crack. Figure 3-24 shows four cracks with nanofibrils found at 10^0 s^{-1} strain-rate and 100°C (Top left), 10^{-3} s^{-1} strain-rate and 20°C (Top right), 10^0 s^{-1} strain-rate and 115°C (Bottom left), and 10^3 s^{-1} strain-rate and 145°C (Bottom right). The range of strain-rates and temperatures suggest that the nanofibrils are present at all strain-rates and temperatures and a characteristic of the fiber morphology.

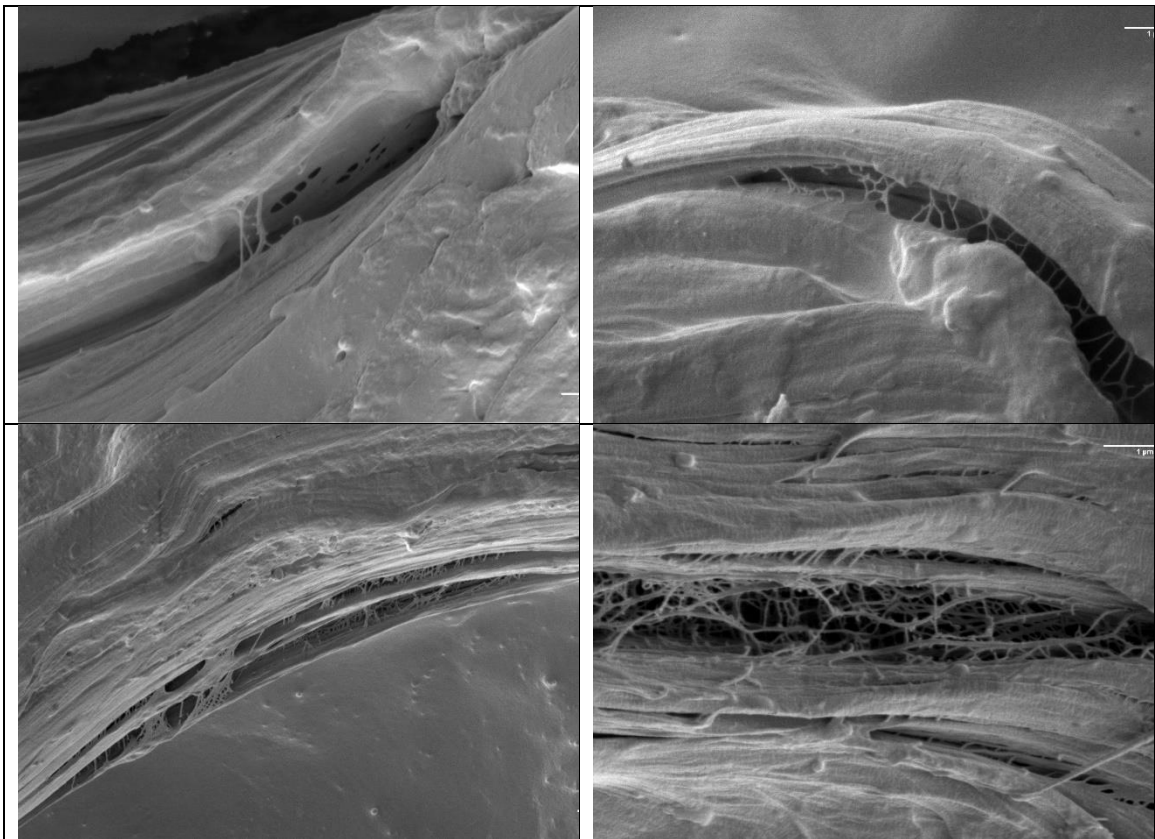


Figure 3-24: Nanofibrils connecting opposite sides of sheared cracks at 10^0 s^{-1} strain-rate and 100°C (Top left), 10^{-3} s^{-1} strain-rate and 20°C (Top right), 10^0 s^{-1} strain-rate and 115°C (Bottom left), and 10^3 s^{-1} strain-rate and 145°C (Bottom right).

Averages for nanofibril thickness, lengths of segments, and spacing along the crack surface can be found for each of the images in Table 3-12. The top left image shows the early stages of the crack formation and was not analyzed for statistics. The maximum thickness measured was 121 nm and the shortest was 10 nm. The maximum length measured was 3591 nm and the shortest was 46 nm. The maximum spacing between nanofibrils along the crack surface was 1595 nm and the shortest was 25 nm.

Strain-rate [s ⁻¹]	Temperature [°C]	Thickness Average and Standard Deviation [nm]	Length Average and Standard Deviation [nm]	Spacing Average and Standard Deviation [nm]
10 ⁻³	20	39 ± 16	265 ± 140	213 ± 093
10 ⁰	115	49 ± 18	203 ± 100	147 ± 175
10 ³	145	35 ± 18	264 ± 400	170 ± 93

Table 3-12: Statistics for the averages and standard deviations for nanofibril thickness, length, and spacing along the crack surface.

The nanofibrils appear to have a larger density between the cracks at higher temperatures. The top right image 10⁻³ s⁻¹ strain-rate and 20°C shows a long spacing between nanofibrils and the relative number of nanofibrils is small. In contrast, the bottom right image at 10³ s⁻¹ strain-rate and 145°C demonstrates the smaller spacing between nanofibrils and a very large number of nanofibrils. This image also shows the complicated structure that must be overcome to for fiber failure to occur at high temperatures. This will be discussed further in the next chapter.

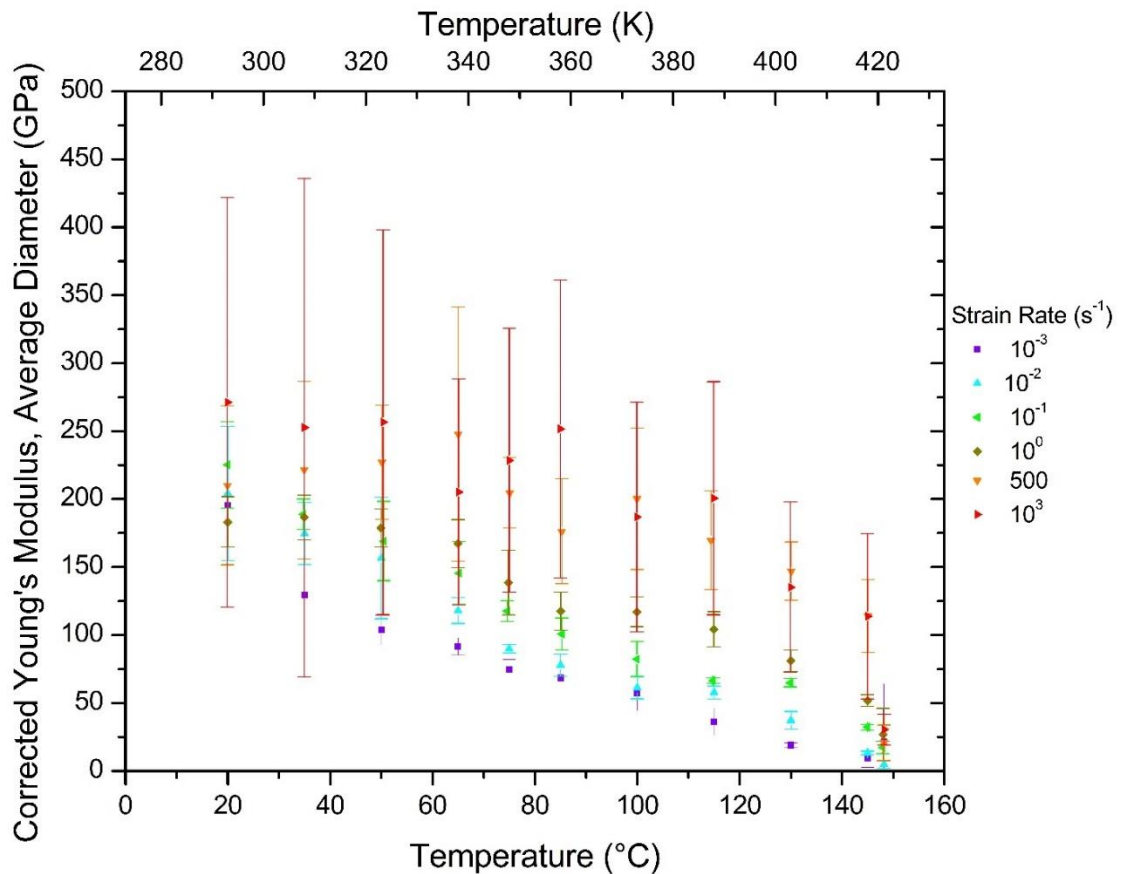
3.2.11 Young's Modulus

Young's modulus values were calculated using corrected strain and the average diameter method for stress. The stress-strain curves of each of the 437 tensile tests were visually inspected to determine the highest slope region of the curve. Points were manually selected to best approximate the slope at this region. The region with the steepest slope on the stress-strain curve changes location with temperature and strain-rate. For the quasi-static and intermediate strain-rates, the steepest region for the pseudo-brittle and plateauing curve shapes is at low strain low strain values near zero strain. For the dynamic strain-rates and the quasi-static and intermediate strain-rates where the curve shape is necking or non-failure, the steepest region is at the stiffening near 0.5% strain. For constant temperature, the Young's modulus was observed to increase with increasing strain-rate. For constant strain-rate, the Young's modulus was observed to decrease with increasing temperature. Each of the 66 temperature-strain-rate combinations are plotted in Figure 3-25 (Top). The 10^{-3} s^{-1} , 10^{-2} s^{-1} , 10^{-1} s^{-1} , 10^0 s^{-1} , 500 s^{-1} , and 10^3 s^{-1} strain-rates are depicted in violet, blue, green, dark yellow, orange, and red, respectively. The averages are plotted with bars depicting \pm one standard deviation. Standard deviations are observed to be larger for the dynamic strain-rates. Individual Young's modulus plots can be found in Appendix A-8.

A large decrease in Young's modulus is observed for all strain-rates at 148 °C with the exception of the 10^{-3} s^{-1} strain-rate where an increase in the Young's modulus was observed. The average Young's modulus converges to a range of 15 GPa to 30 GPa for all strain-rates at 148 °C except the 10^{-2} s^{-1} strain-rate which was observed to decrease to approximately 5 GPa. Excluding the 148 °C, the rest of the values for constant strain-

rate are observed to decrease linearly with increasing temperature. Linear fits for each strain-rate are shown in Figure 3-25 (Bottom). Standard deviations for the quasi-static and intermediate strain-rates have been removed for clarity. The 500 s^{-1} , and 10^3 s^{-1} strain-rates have been included to demonstrate their magnitude. The plot is rescaled and centered on 150 GPa. The fit parameters are listed in Table 3-13.

The slope and intercept appear to change linearly with the log of strain-rate and plots with linear fits of the slopes and intercepts for all strain-rates are shown in Figure 3-26 (Top left) and (Bottom left), respectively. The dynamic strain-rates both have large standard deviations and skew the linear fitting of the quasi-static and intermediate strain-rates. Linear fits excluding the dynamic strain-rates have also been calculated and are shown in Figure 3-26 (Top right) and (Bottom right). The dynamic data points are



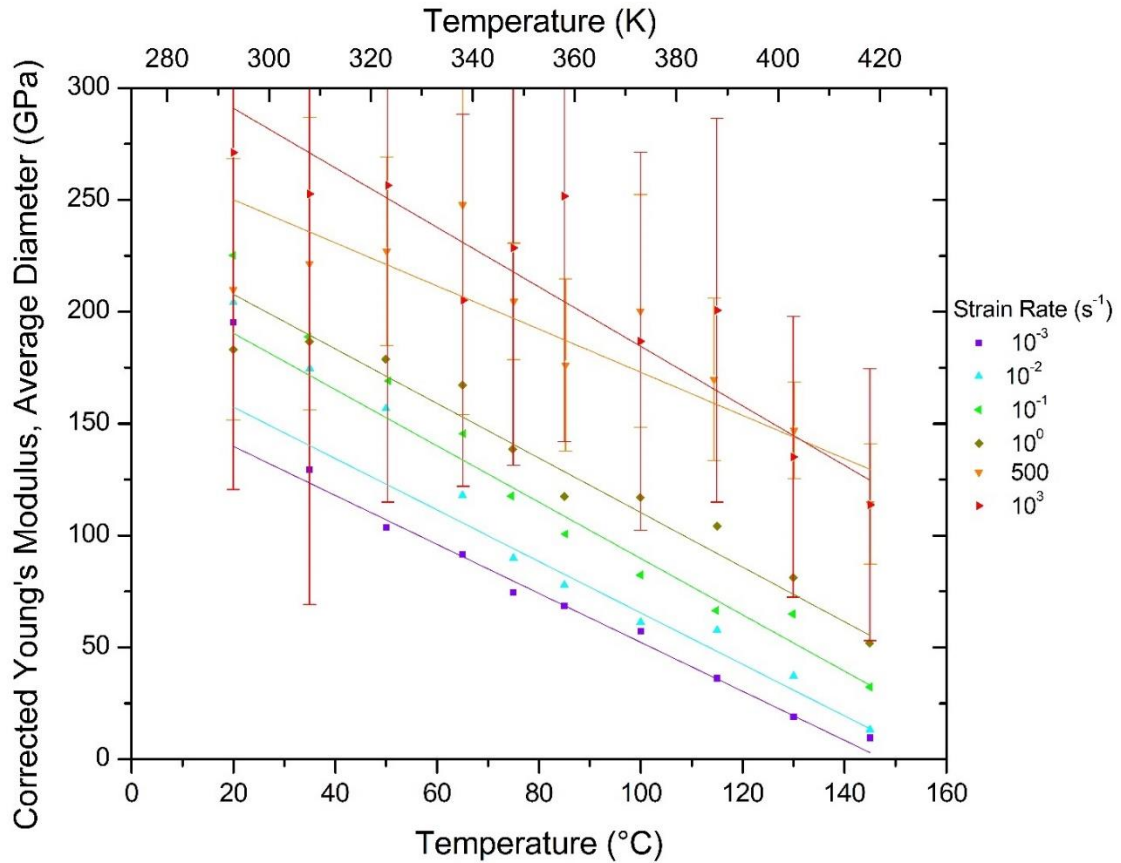


Figure 3-25: (Top) Average values of Young's modulus plotted with \pm one standard deviation for all 66 temperature-strain-rate combinations. A large decrease in Young's modulus is observed for all strain-rates at 148 °C with the exception of the 10^{-3} s^{-1} strain-rate that showed an increase in the Young's modulus at this temperature. The average Young's modulus converges to a range of 15 GPa to 30 GPa for all strain-rates at 148 °C except the 10^{-2} s^{-1} strain-rate which was observed to decrease to approximately 5 GPa. **(Bottom)** A rescaled plot showing the linear fits for each strain-rate excluding the 148 °C data. The \pm one standard deviation bars for the dynamic strain-rates have been included to show the large deviation in Young's modulus values.

included in these plots for comparison of fit. Table 3-13 summarizes the slopes and

intercepts for these fittings of the change in slope with respect to log strain-rate

$(\delta E / \delta T / \delta \log(\text{strain-rate}))$ and the change in intercept with respect to log strain-rate

$(\delta E / \delta \log(\text{strain-rate}))$. The intercepts do not change significantly with the inclusion of

exclusion of the dynamic strain-rates. However the slope fitting changes approximately

4x from $-0.0124 \text{ GPa}/^\circ\text{C}/\log(\text{s}^{-1})$ including the dynamic strain-rates to $-0.0496 \text{ GPa}/^\circ\text{C}/\log(\text{s}^{-1})$ excluding the dynamic strain-rates and the adjusted R^2 value increases from -0.1604 to 0.7816 . These fittings indicate a negative correlation between how quickly the Young's modulus decreases with increasing temperature and strain-rate. Essentially, the same temperature increase results in a larger decrease in Young's modulus for the high strain-rates than it does for the low strain-rates. The plots also show that the behavior of the 10^3 s^{-1} strain-rate appears to be predicted by the quasi-static and intermediate strain-rate fittings but the behavior of the 500 s^{-1} strain-rate possibly falls outside of this prediction. The large standard deviation bars make it difficult to determine if the 500 s^{-1} strain-rate would also be predicted.

Log(Strain-rate)	Slope of linear fit with standard error [GPa/ $^\circ\text{C}$]	Intercept of linear fit at 0°C with standard error [GPa]	Adjusted R^2 of Fit
-3	$-1.09 \pm .05$	162 ± 6	0.9826
-2	$-1.15 \pm .05$	180 ± 7	0.9804
-1	$-1.26 \pm .11$	216 ± 14	0.9363
0	$-1.22 \pm .08$	232 ± 9	0.9668
2.67	$-0.96 \pm .14$	269 ± 15	0.8386
3	$-1.33 \pm .21$	318 ± 23	0.8139

Table 3-13: Parameters for the linear fits for change in Young's modulus with temperature at each strain-rate. All strain-rates show a negative correlation between Young's modulus and temperature. The standard errors for the dynamic strain-rates are larger than the quasi-static and intermediate strain-rates.

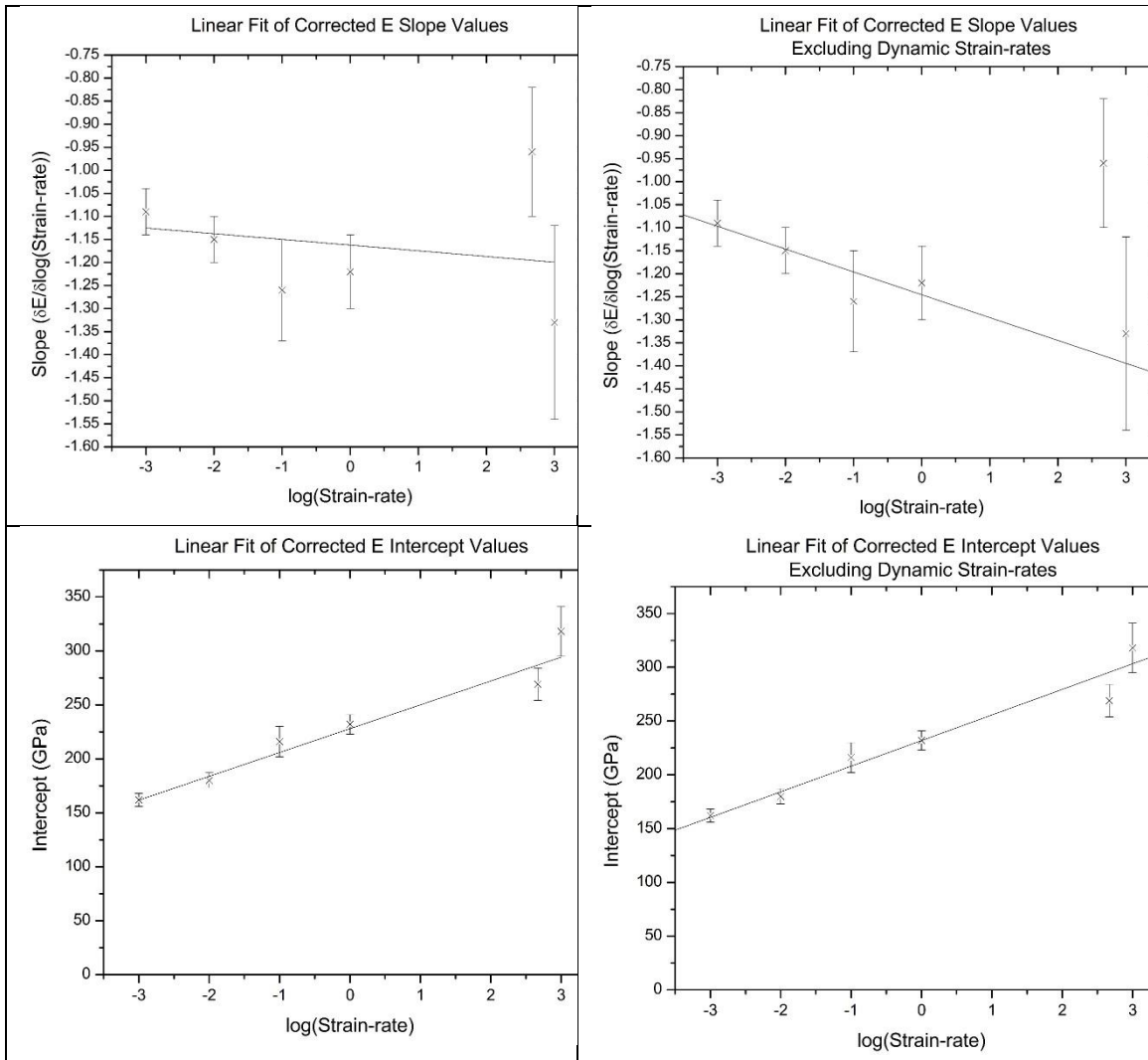


Figure 3-26: (Top left) Plot of the slopes and standard errors calculated from the linear fits of the Young's modulus and temperature data. A linear fit of the slopes is shown including the fitted slopes for all strain-rates. **(Top right)** Plot of the slopes and standard errors calculated from the linear fits of the Young's modulus and temperature data showing the linear fit of the slopes excluding the dynamic strain-rates. The dynamic strain-rate points are shown for comparison. **(Bottom left)** Plot of the intercepts and standard errors calculated from the linear fits of the Young's modulus and temperature data. A linear fit of the intercepts is shown including intercepts for all strain-rates. **(Bottom right)** Plot of the intercepts and standard errors calculated from the linear fits of the Young's modulus and temperature data showing the linear fit of the intercepts excluding the dynamic strain-rates. The dynamic strain-rate points are shown for comparison.

	All Strain-rates	Excluding Dynamic Strain-rates
Slope of linear fit of slopes with standard error [GPa/°C/log(s ⁻¹)]	-0.0124 ± 0.0222	-0.0496 ± 0.0145
Intercept of linear fit of slopes with standard error [GPa/ log(s ⁻¹)]	-1.16 ± 0.05	-1.25 ± 0.03
Adjusted R ² of Fit	-0.1604	0.7816
Slope of linear fit of intercepts at 0 °C with standard error [GPa/°C/log(s ⁻¹)]	22.1 ± 2.0	23.8 ± 2.1
Intercept of linear fit of intercepts at 0 °C with standard error [GPa/log(s ⁻¹)]	228 ± 5	232 ± 5
Adjusted R ² of Fit	0.9588	0.9760

Table 3-14: Parameters for the linear fits for the change in slope of the Young's modulus and temperature linear fits with respect to log(strain-rate). The same fits excluding the dynamic strain-rates are shown in the column on the right. There is an approximately 4x change in the slope of these fits when including or excluding the dynamic strain-rates (from -0.0124 GPa/°C/log(s⁻¹) to -0.0496 GPa/°C/log(s⁻¹)).

3.2.12 Failure Toughness

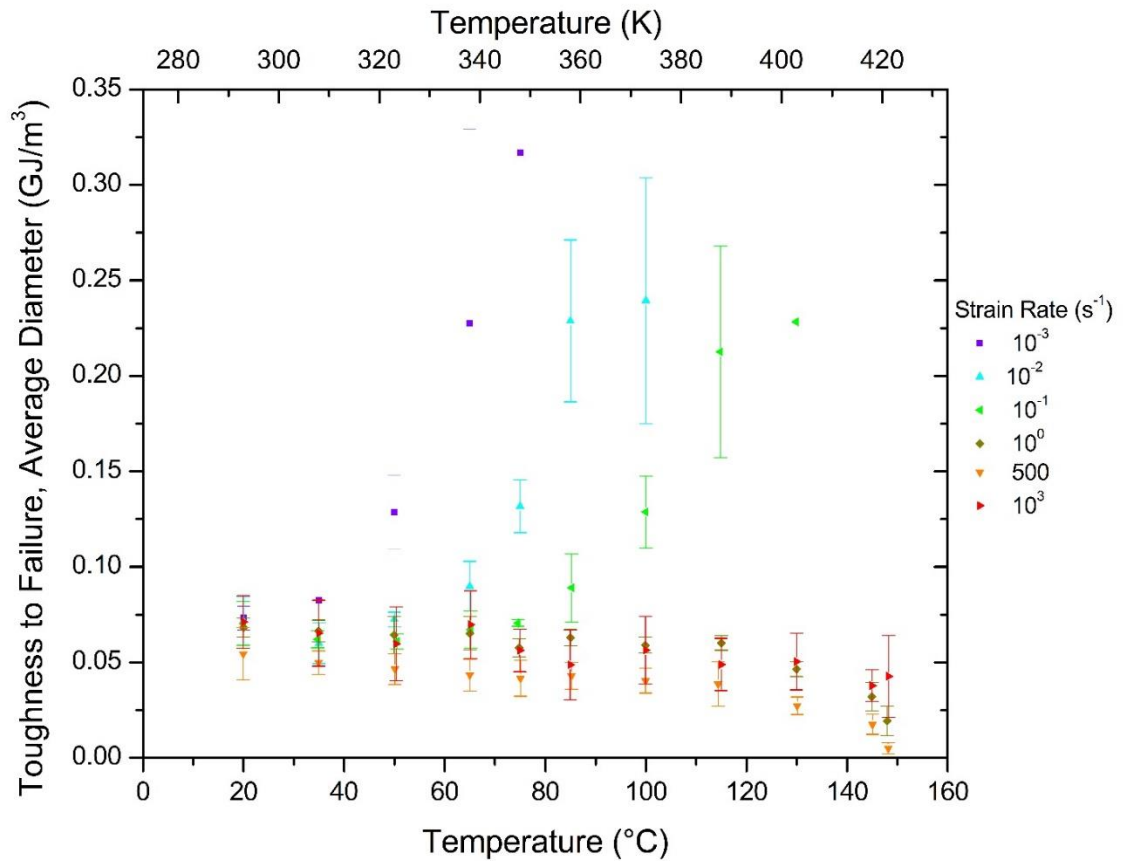
Failure toughness values were calculated to determine the total energy for fiber failure. As discussed in the introduction, the toughness corresponds to the area under the stress-strain curve until failure. The middle Reimann sum method was used on the compliance corrected stress-strain curves to calculate the toughness to failure.

As temperature is increased, an increase in failure toughness is observed for the 10^{-3} s^{-1} , 10^{-2} s^{-1} , and 10^{-1} s^{-1} strain-rates up to the non-failure temperature where a convex curve shape is observed. A decrease in failure toughness is observed for the 10^0 s^{-1} , 500 s^{-1} , and 10^3 s^{-1} strain-rates as temperature is increased. For constant temperature, there is not a consistent trend observed for the average failure toughness with increasing strain-rate. For instance, the 10^{-3} s^{-1} strain-rate has the highest failure strength at all temperatures up to its non-failure temperature and the 500 s^{-1} strain-rate has the lowest average failure toughness at all temperatures. Each of the 54 temperature-strain-rate combinations where failure occurs are plotted in Figure 3-27 (Top). The 10^{-3} s^{-1} , 10^{-2} s^{-1} , 10^{-1} s^{-1} , 10^0 s^{-1} , 500 s^{-1} , and 10^3 s^{-1} strain-rates are depicted in violet, blue, green, dark yellow, orange, and red, respectively. The averages are plotted with bars depicting \pm one standard deviation. Standard deviations are observed to be larger for the dynamic strain-rates. Individual failure toughness plots can be found in Appendix A-9.

The beginning of the non-failure temperatures is observed at $75 \text{ }^\circ\text{C}$, $100 \text{ }^\circ\text{C}$, and $130 \text{ }^\circ\text{C}$ for the 10^{-3} s^{-1} , 10^{-2} s^{-1} , and 10^{-1} s^{-1} strain-rates, respectfully, where the failure strengths rise to values between 0.2 GJ/m^3 and 0.35 GJ/m^3 . Additionally, the 10^{-2} s^{-1} , and 10^{-1} s^{-1} strain-rates show a change in shape from convex to concave between the non-failure temperature and the preceding temperature. This indicates that there is a

plateauing effect on the failure strength as the non-failure temperature is approached. The non-failure temperature for the 10^0 s^{-1} at $148 \text{ }^\circ\text{C}$ does not show a large increase to the range between 0.2 GJ/m^3 and 0.35 GJ/m^3 of failure strength and its value at $148 \text{ }^\circ\text{C}$ drops sharply to a value of approximately 0.02 GJ/m^3 . This is an order of magnitude lower than the observed failure strength values at the non-failure temperatures in the lower strain-rates.

The shape of the 10^0 s^{-1} and 500 s^{-1} show a trend of linearly decreasing failure strength with increasing temperature from $20 \text{ }^\circ\text{C}$ to $115 \text{ }^\circ\text{C}$. In the range from $115 \text{ }^\circ\text{C}$ to $145 \text{ }^\circ\text{C}$ the trend is still linear but the slope of the fit decreases. There is a large decrease in failure toughness at $148 \text{ }^\circ\text{C}$ for both strain-rates.



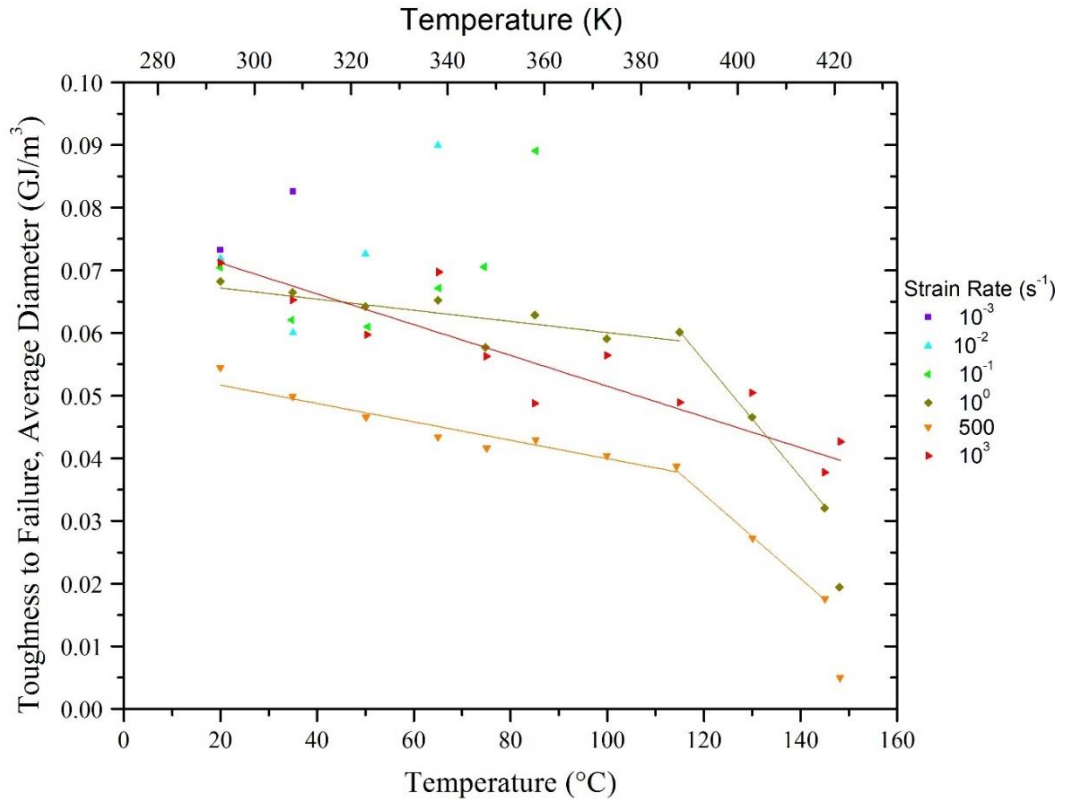


Figure 3-27: (Top) Average values of failure toughness plotted with \pm one standard deviation. For the 10^{-3} s^{-1} , 10^{-2} s^{-1} , and 10^{-1} s^{-1} strain-rates, the failure toughness is observed to increase rapidly with a convex shape as the non-failure temperature is approached. The shape changes from convex to concave between the non-failure temperature and the preceding temperature for the 10^{-2} s^{-1} and 10^{-1} s^{-1} strain-rates indicating a plateauing of the failure strength as the non-failure temperature is approached. **(Bottom)** A rescaled plot centered around 0.05 GJ/m^3 . For clarity, standard deviations have been removed. This plot shows the linear behavior for the low temperature regions of the 10^0 s^{-1} , 500 s^{-1} , and 10^3 s^{-1} strain-rates. Linear plots for the $20 \text{ }^\circ\text{C}$ to $115 \text{ }^\circ\text{C}$ regions for the 10^0 s^{-1} and 500 s^{-1} strain-rate are shown and the $20 \text{ }^\circ\text{C}$ to $145 \text{ }^\circ\text{C}$ for the 10^3 s^{-1} strain-rate.

The 10^3 s^{-1} strain-rate shows a linear trend of decreasing failure strength with increasing temperature across the entire temperature range of this study. Additionally, the 10^3 s^{-1} strain-rate has higher values than the 500 s^{-1} strain-rate at all temperatures conducted in this study and higher than the 10^0 s^{-1} strain-rate at 5/11 temperatures. The

dynamic strain-rates have large standard deviations and these could explain the nonconformities observed in the experimental data.

Linear fits for the 10^0 s^{-1} , 500 s^{-1} , and 10^3 s^{-1} strain-rates are plotted in Figure 3-27 (Bottom) and the fit parameters are shown in Table 3-15. The fit with standard errors for the $20 \text{ }^\circ\text{C}$ to $115 \text{ }^\circ\text{C}$ temperature region of the 10^0 s^{-1} strain rate has a slope of $-8.89 \times 10^{-5} \pm 2.62 \times 10^{-5} \text{ GJ/m}^3/\text{ }^\circ\text{C}$ and an intercept of $0.0690 \pm .0025 \text{ GJ/m}^3$ with the fit having an adjusted R-squared value of 0.6000 while the $115 \text{ }^\circ\text{C}$ to $145 \text{ }^\circ\text{C}$ temperature region has a slope of $-9.28 \times 10^{-5} \pm 2.03 \times 10^{-5} \text{ GJ/m}^3/\text{ }^\circ\text{C}$ and an intercept of $0.167 \pm 0.003 \text{ GJ/m}^3$ with the fit having an adjusted R-squared value of 0.9990. The fit with standard errors for the $20 \text{ }^\circ\text{C}$ to $115 \text{ }^\circ\text{C}$ temperature region of the 500 s^{-1} strain rate has a slope of $-1.47 \times 10^{-4} \pm 1.7 \times 10^{-5} \text{ GJ/m}^3/\text{ }^\circ\text{C}$ and an intercept of $0.0546 \pm 0.0013 \text{ GJ/m}^3$ with the fit having an adjusted R-squared value of 0.9134 while the $115 \text{ }^\circ\text{C}$ to $145 \text{ }^\circ\text{C}$ temperature region has a slope of $-6.73 \times 10^{-4} \pm 2.7 \times 10^{-5} \text{ GJ/m}^3/\text{ }^\circ\text{C}$ and an intercept of $.115 \pm .004 \text{ GJ/m}^3$ with the fit having an adjusted R-squared value of 0.997. The entire temperature range was fit for the 10^3 s^{-1} strain-rate having a slope of $-2.45 \times 10^{-4} \pm 3.1 \times 10^{-5} \text{ GJ/m}^3/\text{ }^\circ\text{C}$ and an intercept of $0.0761 \pm 0.0033 \text{ GJ/m}^3$ with the fit having an adjusted R-squared value of 0.862. Also seen in the rescaled plot is a decrease in failure toughness observed for the 10^{-2} s^{-1} and 10^{-1} s^{-1} strain-rates at $35 \text{ }^\circ\text{C}$, and the $35 \text{ }^\circ\text{C}$ to $50 \text{ }^\circ\text{C}$ range, respectively.

Strain-rate Region [s^{-1}]	Temperature Region [$^{\circ}C$]	Slope of Fit [$GJ/m^3/^{\circ}C$]	Intercept [GJ/m^3]	Adjusted R^2 of Fit
10^0	20 $^{\circ}C$ to 115 $^{\circ}C$	$-8.89 \times 10^{-5} \pm 2.62 \times 10^{-5}$	0.0690 ± 0.0025	0.6
	115 $^{\circ}C$ to 148 $^{\circ}C$	$-9.28 \times 10^{-5} \pm 2.03 \times 10^{-5}$	0.167 ± 0.003	0.999
500	20 $^{\circ}C$ to 115 $^{\circ}C$	$-1.47 \times 10^{-4} \pm 1.7 \times 10^{-5}$	$0.0546 \pm .0013$	0.9134
	115 $^{\circ}C$ to 148 $^{\circ}C$	$-6.73 \times 10^{-4} \pm 2.7 \times 10^{-5}$	0.115 ± 0.004	0.9969
10^3	20 $^{\circ}C$ to 148 $^{\circ}C$	$-2.45 \times 10^{-4} \pm 3.1 \times 10^{-5}$	0.0761 ± 0.0033	0.862

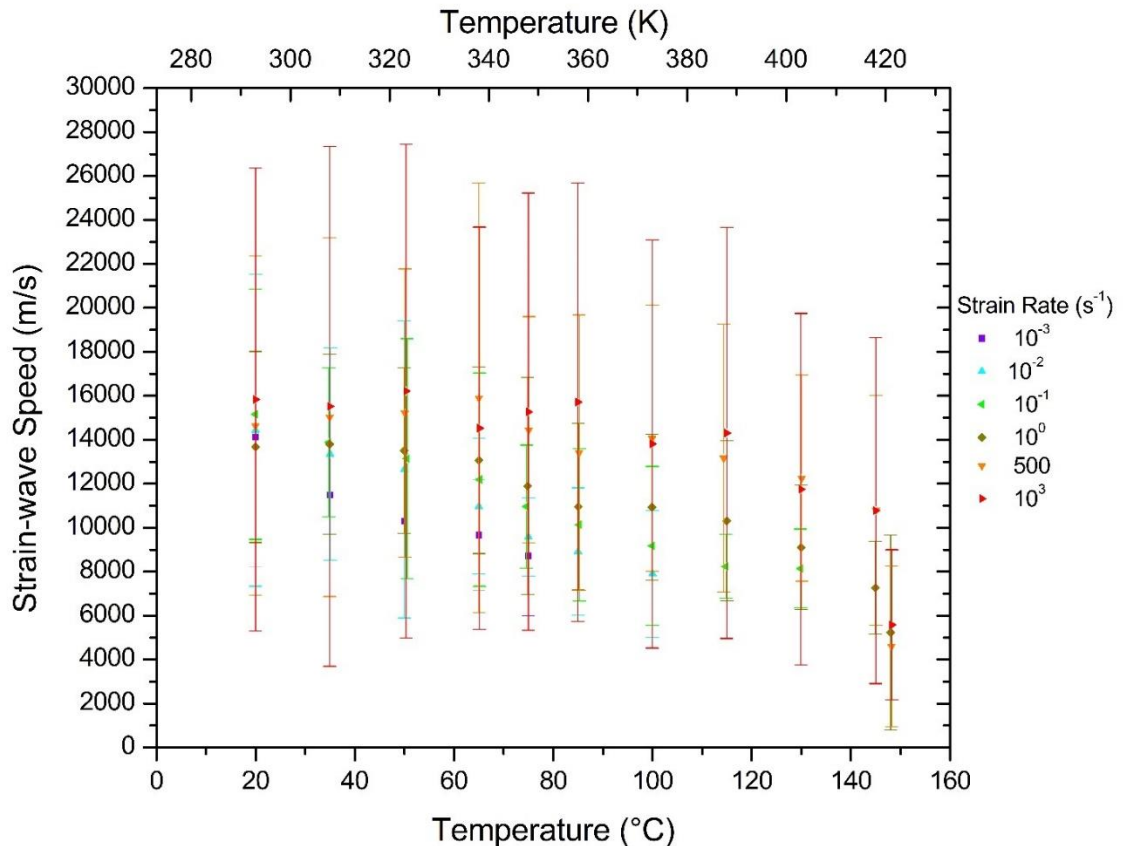
Table 3-15: Linear fit parameters for the change in failure toughness with respect to temperature. For the $10^0 s^{-1}$ and $500 s^{-1}$ strain-rates, two regions were fitted; the low temperature region spanning 20 $^{\circ}C$ to 115 $^{\circ}C$ and the high temperature region spanning 115 $^{\circ}C$ to 145 $^{\circ}C$. For the $10^3 s^{-1}$ strain-rate., one linear fit was conducted for the entire temperature span of 20 $^{\circ}C$ to 145 $^{\circ}$. The adjusted R-squared for each fit is included in the last column.

3.2.13 Cunniff Parameters

Strain-wave speed, linear and actual specific toughness, and linear and actual Cunniff parameters were calculated using the experimental average values for each applicable temperature-strain-rate combination.

3.2.13.1 Strain-wave Speed

The strain-wave speeds were calculated from the temperature-strain-rate dependent Young's modulus and a density of 980 kg/m^3 . Figure 3-28 (Top) shows the calculated strain-wave speeds for all 66 temperature-strain-rates combinations used in this study. The 10^{-3} s^{-1} , 10^{-2} s^{-1} , 10^{-1} s^{-1} , 10^0 s^{-1} , 500 s^{-1} , and 10^3 s^{-1} strain-rates are depicted in violet, blue, green, dark yellow, orange, and red, respectively. The averages are plotted with bars depicting \pm one standard deviation. Standard deviations are



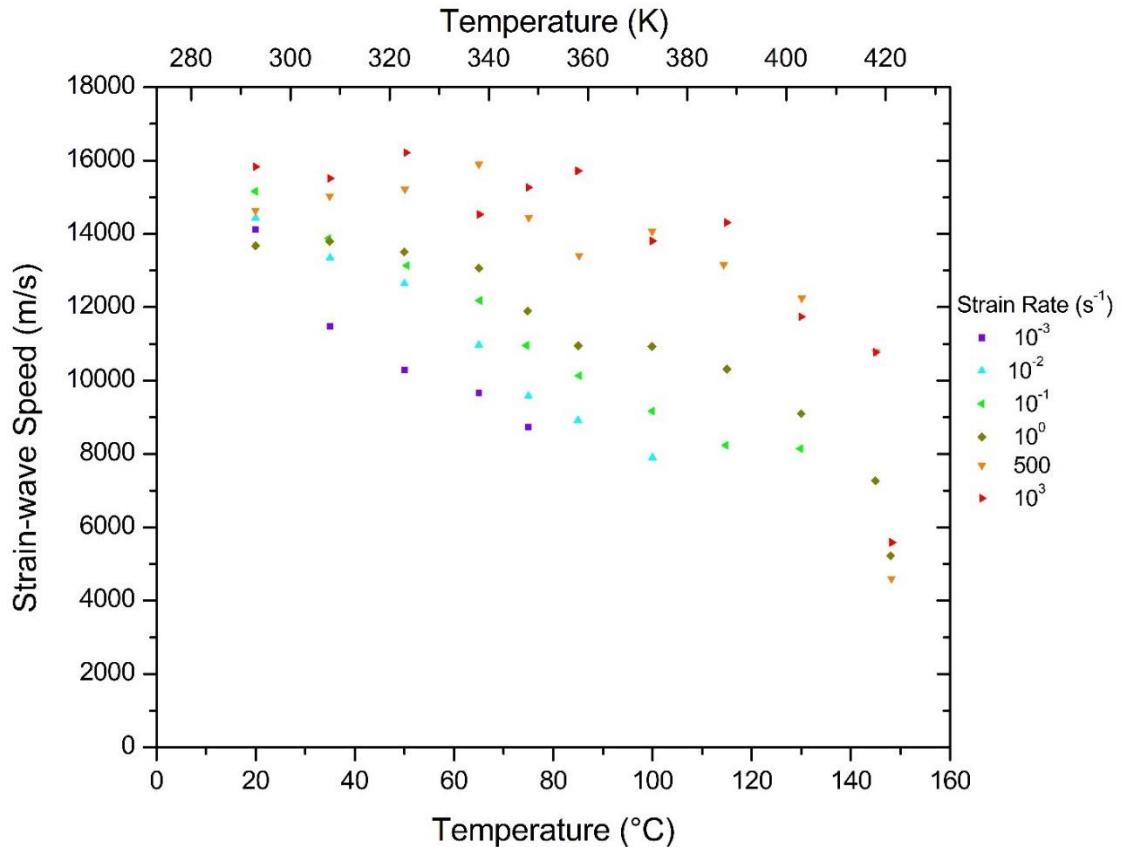


Figure 3-28: (Top) Average values of strain-wave speed plotted with \pm one standard deviation for all 66 combinations of temperature-strain-rate. Large standard deviations are observed for the dynamic strain-rates. **(Bottom)** A rescaled plot centered around 9000 m/s. For clarity, standard deviations have been removed.

observed to be larger for the dynamic strain-rates, similar to those observed in the Young's modulus section. A rescaled plot centered around 9000 m/s is shown in Figure 3-28 (Bottom). For clarity, standard deviations have been removed. Trends with respect to temperature and strain-rate are similar to those observed in the Young's modulus section. The square-root of the Young's modulus values are taken for these calculations and the plots reflect the square-root of a linearly decreasing behavior with respect to temperature. For constant strain-rate, strain-wave speed is observed to decrease with increasing temperature. For constant temperature, strain-wave speed is observed to increase with strain-rate.

3.2.13.2 Specific Toughness: Linear Approximation vs. Actual

Comparisons between the average linear and actual specific toughness for each of the 54 temperature-strain-rate combination where failure occurs are shown in Figures 3-29 (Top left) and (Top right), respectively. The 10^{-3} s^{-1} , 10^{-2} s^{-1} , 10^{-1} s^{-1} , 10^0 s^{-1} , 500 s^{-1} , and 10^3 s^{-1} strain-rates are depicted in violet, blue, green, dark yellow, orange, and red, respectively. The averages are plotted with bars depicting \pm one standard deviation.

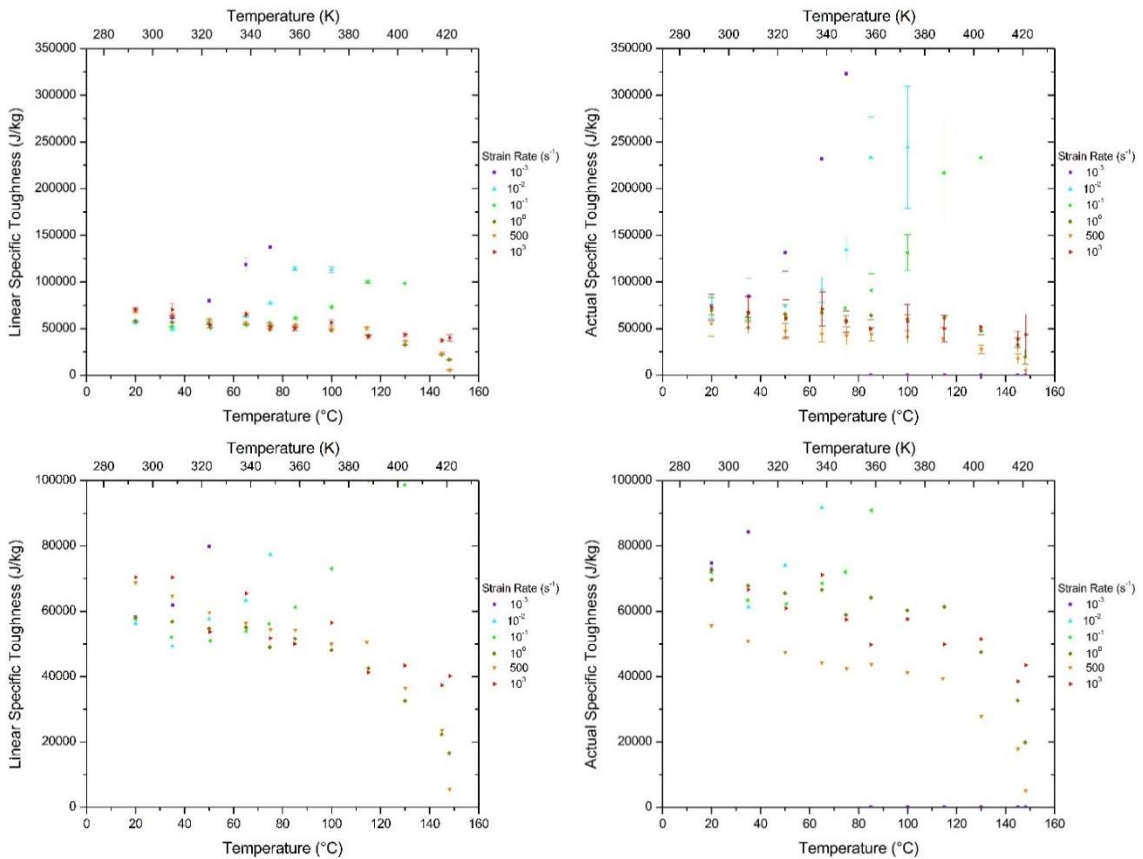


Figure 3-29: A plot of the average linear specific toughness (**Top left**) and average actual specific toughness (**Top right**) for all 54 temperature-strain-rate combinations where failure occurs. The 10^{-3} s^{-1} , 10^{-2} s^{-1} , 10^{-1} s^{-1} , 10^0 s^{-1} , 500 s^{-1} , and 10^3 s^{-1} strain-rates are depicted in violet, blue, green, dark yellow, orange, and red, respectively. The averages are plotted with bars depicting \pm one standard deviation. The actual average specific toughness values for the 10^{-3} s^{-1} , 10^{-2} s^{-1} , and 10^{-1} s^{-1} strain-rates are considerably higher than the values for the linear specific toughness as the strain-rate dependent non-failure temperature is approached. Rescaled plots for the linear and actual specific toughness centered around 50 kJ/kg are shown in the (**Bottom left**) and (**Bottom right**), respectively. For clarity, standard deviations have been removed.

Standard deviations are observed to be larger for the dynamic strain-rates except in the necking to non-failure regions of the lower strain-rates where a large variation in strain to failure is observed. The actual specific toughness is the same as the failure toughness plots in the presented in the previous section divided by the density and therefore show the same trends. Non-failure temperatures are observed at 75 °C, 100 °C, and 130 °C for the 10^{-3} s^{-1} , 10^{-2} s^{-1} , and 10^{-1} s^{-1} , strain-rates, respectively. The linear specific toughness show significantly lower average specific toughness values for the 10^{-3} s^{-1} , 10^{-2} s^{-1} , and 10^{-1} s^{-1} strain-rates as the non-failure temperature is approached.

To show the comparison for the higher strain-rates, rescaled plots for the linear and actual specific toughness centered around 50 kJ/kg are shown in figure 3-29 (Bottom left) and (Bottom right). For clarity, standard deviations have been removed. In general, the specific toughness for the 10^0 s^{-1} , 500 s^{-1} , and 10^3 s^{-1} strain-rates, the average specific toughness values for both plots were observed to decrease with increasing temperature. For identical temperature-strain-rate combinations, the actual specific toughness values are observed be higher than the values for the linear specific toughness. The exception is the actual toughness for the of 500 s^{-1} strain-rate where the values were below the linear specific toughness values for almost all of the temperatures. A large decrease is observed in both plots between 145 °C and 148 °C for the 10^0 s^{-1} and 500 s^{-1} strain-rates while and increase at this temperature is observed for the 10^3 s^{-1} strain-rate.

3.2.13.3 Cunniff Parameters: Linear Approximation vs. Actual

Linear and actual Cunniff parameters were calculated using the strain-wave speed and the linear and actual failure toughness for each of the 54 temperature-strain-rate combinations where failure occurs. Plots for the average linear and actual Cunniff

parameters are shown in Figure 3-30 (Top left) and (Top right), respectively. The 10^{-3} s^{-1} , 10^{-2} s^{-1} , 10^{-1} s^{-1} , 10^0 s^{-1} , 500 s^{-1} , and 10^3 s^{-1} strain-rates are depicted in violet, blue, green, dark yellow, orange, and red, respectively. The averages are plotted with bars depicting \pm one standard deviation. Standard deviations are observed to be larger for the dynamic strain-rates.

The 10^{-3} s^{-1} , 10^{-2} s^{-1} and 10^{-1} s^{-1} strain-rates are observed to increase with increasing temperature up to their respective non-failure temperature. The actual Cunniff parameter shows a much larger increase than the linear Cunniff parameter as the non-failure temperature is approached for these strain-rates.

Rescaled plots centered around 500 m/s for the linear and actual Cunniff parameters are shown in Figure 3-30 (Middle left) and (Middle right), respectively. For clarity, standard deviations have been removed. The 10^0 s^{-1} , 500 s^{-1} , and 10^3 s^{-1} strain-rates are observed to have a similar shape over the entire temperature range. All are observed to decrease linearly from 20 °C to 115 °C, then decrease rapidly from 115 °C to

145 °C, and lastly have a sharp decrease from 145 °C to 148 °C. The 148 °C did not appear to align with the linear any of the linear regions and these points were excluded from fitting calculations. Within the 20 °C to 115 °C regions of the 10^0 s^{-1} , 500 s^{-1} , and 10^3 s^{-1} strain-rates, two different linear regions from 20 °C to 65 °C and 75 °C to 115 °C may also be fitted with a drop in average value between 65 °C and 75 °C. The 10^3 s^{-1} strain-rate does not show a large decrease at 115 °C and fit attempts can also be made with a single line from 20 °C to 115°C, 20 °C to 130 °C and 20 °C to 145 °C.

Each of these linear regions have been fit for both the linear and actual Cunniff parameters and are summarized in Table 3-16. Lines were not fit for regions that have

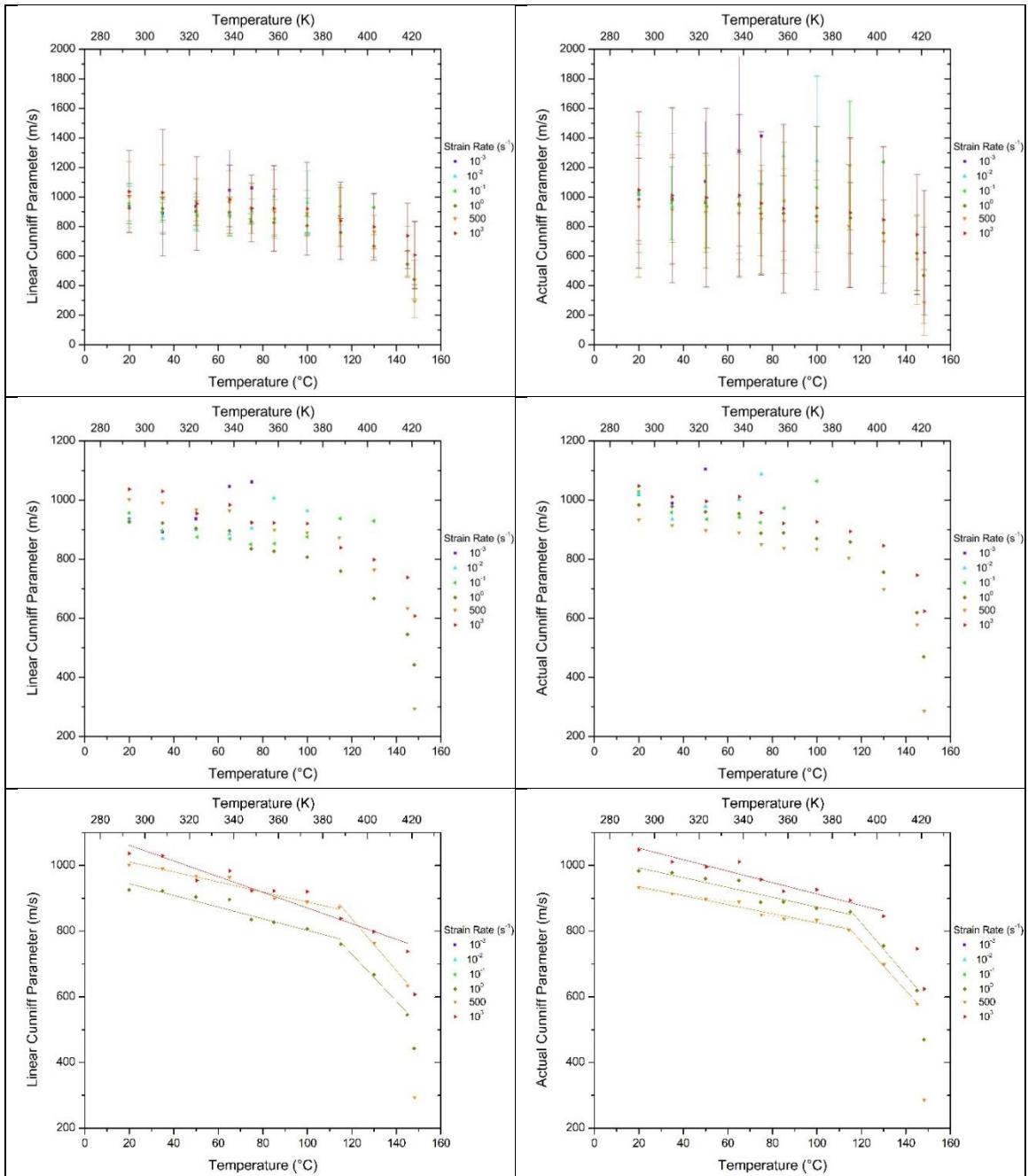


Figure 3-30: A plot of the average linear Cunniff parameters (**Top left**) and average actual Cunniff parameters (**Top right**) for all temperature-strain-rate combinations where failure occurs. Rescaled plots for the linear and actual average Cunniff parameters centered around 500 m/s are shown in the (**Middle left**) and (**Middle right**) plots, respectfully. For clarity, standard deviations have been removed. Best Linear fits for the linear and actual average Cunniff parameters for the 10^0 s^{-1} , 500 s^{-1} , and 10^2 s^{-1} strain-rates are shown in the (**Bottom left**) and (**Bottom right**) plots.

Strain rate [s ⁻¹]	Temperature Region [°C]	Linear Cunniff Parameter			Actual Cunniff Parameter		
		Slope of Fit [m/s/°C]	Intercept [m/s]	Adjusted R ² of Fit	Slope of Fit [m/s/°C]	Intercept [m/s]	Adjusted R ² of Fit
10 ⁰	20 to 65	-0.71 ± 0.13	940 ± 10	0.9014	-0.70 ± 0.12	1000 ± 10	0.9227
	75 to 115	-1.74 ± 0.42	970 ± 40	0.8416	-0.83 ± 0.16	950 ± 20	0.9016
	20 to 115	-1.77 ± 0.19	980 ± 10	0.9264	-1.49 ± 0.17	1020 ± 10	0.9126
	115 to 145	-7.17 ± 0.63	1590 ± 80	0.9849	-7.96 ± 0.70	1780 ± 90	0.9846
500	20 to 65	-0.93 ± 0.20	1020 ± 10	0.8753	-0.98 ± 0.13	950 ± 10	0.9499
	75 to 115	-1.18 ± 0.23	1010 ± 20	0.8917	-1.03 ± 0.29	930 ± 30	0.7988
	20 to 115	-1.53 ± 0.14	1040 ± 10	0.9465	-1.37 ± 0.11	960 ± 10	0.9550
	115 to 145	-7.90 ± 0.67	1790 ± 90	0.9856	-7.45 ± 0.45	1660 ± 60	0.9929
	115 to 145	-7.90 ± 0.67	1790 ± 90	0.9856	-7.45 ± 0.45	1660 ± 60	0.9929
10 ³	20 to 65	-1.34 ± 0.74	1060 ± 40	0.4323	-0.83 ± 0.52	1050 ± 20	0.3487
	75 to 115	-1.97 ± 0.81	1080 ± 80	0.6209	-1.39 ± 0.42	1060 ± 40	0.7687
	115 to 145	-3.39 ± 0.40	1230 ± 50	0.9727	-5.03 ± 0.93	1480 ± 10	0.9338
	20 to 115	-1.93 ± 0.30	1080 ± 20	0.8563	-1.59 ± 0.21	1080 ± 20	0.8934
	20 to 130	-2.15 ± 0.23	1090 ± 20	0.9125	-1.74 ± 0.17	1090 ± 10	0.9252
	20 to 145	-2.38 ± 0.21	1110 ± 20	0.9331	-2.24 ± 0.26	1120 ± 30	0.8908

Table 3-16: Linear fit parameters for the change in failure toughness with respect to temperature regions for the linear and actual Cunniff parameters.

two points or less. To determine the best fit, adjusted R^2 values were used to account for the change in number of points for each linear region and average adjusted R^2 values weighted by the number of points fitted were calculated and are summarized in Table 3-17.

Strain-rate [s^{-1}]	Number of Regions and Temperature Ranges [$^{\circ}C$]	Weighted Average R^2 for Linear Cunniff Parameter	Weighted Average R^2 for Actual Cunniff Parameter
10^0	3 Regions: 20 to 65 75 to 115 115 to 145	0.9024	0.9319
	2 Regions: 20 to 115 115 to 145	0.9424	0.9322
500	3 Regions: 20 to 65 75 to 115 115 to 145	0.9113	0.9067
	2 Regions: 20 to 115 115 to 145	0.9572	0.9653
10^3	3 Regions: 20 to 65 75 to 115 115 to 145	0.6483	0.6610
	2 Regions: 20 to 115 115 to 145	0.8880	0.9044
	1 Region: 20 to 115	0.8563	0.8934
	1 Region: 20 to 130	0.9125	0.9252
	1 Region: 20 to 145	0.9331	0.8908

Table 3-17: Weighted average adjusted R^2 values for the linear fit of the temperature regions. The highlighted values show the best fit at each strain-rate for the linear and the actual Cunniff parameters.

The best fits for the both the linear and actual Cunniff parameters for the 10^0 s^{-1} and 500 s^{-1} strain-rates were the two linear region fits from $20 \text{ }^\circ\text{C}$ to $115 \text{ }^\circ\text{C}$ and $115 \text{ }^\circ\text{C}$ to $145 \text{ }^\circ\text{C}$. The linear Cunniff parameter was best fit by a single line from $20 \text{ }^\circ\text{C}$ to 145 ° . The actual Cunniff parameter was best fit by a single line from $20 \text{ }^\circ\text{C}$ to $130 \text{ }^\circ\text{C}$. The best fits for the linear and actual Cunniff parameters are highlighted in Table 3-17 and are plotted in Figure 3-30 (Bottom left) and (Bottom right), respectively. The best fits suggest that the linear and actual Cunniff parameters predict different trends at the high strain-rate and high temperature regions. This is important for ballistic applications and will be discussed in the next chapter.

4 Discussion

4.1 Chapter Overview

In this chapter potential chain mechanisms responsible for the fiber mechanical properties will be discussed and the likelihood at different temperatures and strain-rates. The three major mechanisms are chain scission, chain slippage, and chain straightening. Chain scission is the breaking of C-C bonds in the backbone of the chain. Chain slippage is the enthalpic motion of one chain (or group of chains) relative to the matrix surrounding it. Chain straightening is the entropic extension of slacked chains. All of the mechanisms are time-dependent and therefore are affected by strain-rate. Their temperature dependence is also evident in the form of a Boltzmann factor, $e^{-\Delta E/kT}$. This implies that it is possible for the dominant mechanism to change as temperature and strain-rate are varied. The ΔE for the chain scission are estimated at 260 kJ/mol to 400 kJ/mol (Schnabel), for the chain slippage at 112 kJ/mol, and are not estimated for the conformational changes due to the competing effects of thermal expansion and thermal shrinkage but are expected to be lower than 112 kJ/mol. The evolution of dominant mechanisms at constant temperature and strain-rate is proposed as straightening at low strains, slippage at strains greater than 0.5 % strain, and scission occurring primarily just before failure. At temperatures just below the melting temperature, an additional mechanism is available due to a phase transformation from extended orthorhombic to hexagonal. The hexagonal phase has a high degree of gauche conformations and rotations of the CH₂ units allow the chain slippage mechanism to be dominant.

4.2 Characterization

4.2.1 Morphological Characterization

Wide angle X ray scattering analysis (WAXS) was used to characterize the morphology of the UHMMPE fibers. The diffraction patterns shown in Figure 3-1 indicate that the single fibers are highly crystalline with a phase composition of approximately 89.5 % orthorhombic, 3.2 % monoclinic, and 7.3 % amorphous. The amorphous scattering is widespread and overlaps of several crystallographic peaks. This indicates that it is highly oriented, as is observed in many highly oriented polymer fibers (paper to be re-found for XRD fitting). The orthorhombic phase can exist as an extended or lamellar phase and remain identical in diffraction pattern. Previous studies have investigated the effects of draw ratio on the mechanical properties of UHMMPE fibers and characterized the phases using Differential Scanning Calorimetry [22]. At high draw ratios the lamellar phase is almost completely removed and the tensile strength increases to the 3 GPa to 4.5 GPa range. Comparable failure strengths and phase compositions were found in this study indicating a high draw ratio and negligible amount of the lamellar orthorhombic phase.

The highly oriented crystalline and amorphous phases of the fibers indicate the system has few degrees of freedom due to hindrances from adjacent chains and therefore a low entropy. The thermal shrinkage observed in the heated single fibers is an indicator of the low entropy. As the chains are heated, the thermal energy causes the extended conformation to become a higher energy state and the chains attempt to lower their free energy by folding back on themselves and changing their conformation back to lamellar. Chain motions will be restricted by adjacent chains and any form of chain slippage in the

crystal or near the amorphous-crystalline domains will likely be a cooperative motion of several chains.

WAXS analysis was also performed to investigate the transition of the extended orthorhombic phase to the hexagonal phase in constrained fibers. The transition was observed to begin at approximately 4 °C to 5 °C below the melting temperature, where diffraction peaks disappeared. The disappearance of the orthorhombic peaks occurs 3 °C after the start of the hexagonal phase formation. The 148.2 °C testing condition is at the lower limit of melting temperature as one fiber demonstrated by melting before the tensile test could be conducted and agreed with the manufacturer melting temperature range of 144 °C to 152 °C for similar fibers [30]. As discussed in the introduction, the fibers melt over a temperature range based on the individual fiber morphology. If the lower bound of this melting range is estimated to be 148.2 °C, then the orthorhombic-hexagonal phase transition for the tensile tests can be estimated to begin with a lower temperature bound of approximately 143 °C. At 145 °C, the extended orthorhombic phase is therefore likely to have a small percentage of hexagonal phase and at 148 °C is likely to be almost completely hexagonal phase with a possible small percentage of extended orthorhombic phase. This phase transition across 145 °C to 148 °C reveals that the crystal structure and morphology of the fiber changes across this temperature and may cause sudden changes in the mechanical properties.

The hexagonal phase, as discussed in the introduction, has a larger spacing between adjacent chains and therefore a higher free volume than the orthorhombic phase. Due to the higher free volume, the energy barrier for CH₂ rotations is lowered and the system can reach a lower free energy by increasing the entropy through the rotation of

trans to gauche conformations. This phase transition occurs at temperatures close to the melting temperature and Raman spectroscopy by Tashiro et al. [21] indicated that the spacing between gauche conformations in the hexagonal phase was no more than 5 CH₂ units. The hexagonal phase is highly dynamic and slippage between chains can occur through rapid CH₂ rotations.

It is important to note that the heated WAXS patterns were from constrained yarn samples subjected to heating but the yarn was not actively strained. In contrast, the fibers in the tensile tests were heated while constrained but then subjected to strain at rates that spanned seven decades of strain-rate. There are two competing effects that will the formation of the hexagonal phase. First, the strain in the fiber system creates stress and high pressure is required for the formation of the hexagonal phase. The thermal shrinkage also acts to induce stress in the system. This is the reason why constrained fibers will form hexagonal phase and unconstrained fibers will form orthorhombic lamellar phase instead. The competing effect is the increased number of gauche conformations in the hexagonal phase chains. The chains start in almost all trans conformation in the extended orthorhombic phase. When the phase transitions to hexagonal, the number of gauche conformations increase and the kinks caused by these conformations decrease the end to end length. For this to occur, the individual chains within the hexagonal phase must slip past one another to decrease their end to end length. This requires the slippage mechanism to allow this decrease in chain length. The slippage mechanism is time dependent and therefore affected by strain-rate. The competing effects of required stress for the formation of the hexagonal phase and the time allowed for the gauche conformations to form the hexagonal phase make the system dependent on instantaneous

strain and strain-rate. The effect of strain or strain-rate on the formation of the hexagonal phase in the fibers has not been studied in situ to date and will be discussed in the future work section.

4.2.2 Chemical Characterization

Fourier Transform Infrared (FTIR) Spectroscopy was performed on the as-received yarns to examine the original chemical composition. This analysis indicated the presence of rocking, bending, CH₂ symmetric and CH₂ asymmetric stretching. The intensities were strongest for the CH₂ symmetric and asymmetric stretching and medium intensity for the bending and rocking modes. The absent peaks for polyethylene include the wagging and twisting modes. The spectra indicate a limited number of modes available to oriented polymer chains. In particular, Gafurov and Nowak [72] showed that the wagging vibrations of polyethylene CH₂ groups in gauche conformations decreased as the strain increased. The lack of the wagging mode in the as received yarns indicates that there is little initial gauche conformation in the fiber.

The scission of a C-C bond creates two carbon-centered free radicals. The free radicals are highly reactive and have a short lifetime, on the order of minutes. To detect free radicals from scission, the characterization technique, such as Electron Paramagnetic Resonance, must be conducted within minutes after the scission-inducing event. To overcome this characterization challenge, the products from the free radical reactions can be used to indicate the occurrence of chain scission. Most of the chemical reactions occur in the amorphous phase where tie chains are subjected to higher stresses than the rest of the fiber and impurities such as molecular oxygen are present due to the free space. The carbon-centered free radicals created during scission can react with other carbon-centered

free radicals in two possible ways. First, the reaction can create a vinyl functional group on the backbone of a chain with a C double bond which has an IR absorption near 980 cm^{-1} . Second, the reaction can form a single covalent bond between the two carbon atoms, repairing one of the scission bonds. Another possible carbon-centered free radical reaction involves reacting with molecular oxygen (O_2) trapped from the gel-spinning and drawing process or from diffusion from air. This reaction creates a peroxy free radical which is still highly reactive and through various reactions can create functional groups with carbon atom single or double bonded to an oxygen atom including aldehydes, carboxyl groups, and ketones which cause degradation of the C-C backbone. These oxidation products have adsorption peaks near 1730 cm^{-1} to 1740 cm^{-1} [73-76].

The spectra for the manufacturer as-received yarns did not show absorption at 980 cm^{-1} or 1700 cm^{-1} indicating that they are absent or have very small adsorptions. The lack of scission products suggests that few chain scissions have occurred in the fibers when received from the manufacturer.

As the fibers are subjected to uniaxial tensile tests to failure at high temperature and strain-rates, the probability of chain scission increases. Chain scission is affected by both temperature and chain stress. The temperature affects the probability of chain scission by providing the chain with a range of phonons according to a Boltzmann distribution. As temperature increases, the total thermal energy stored in the chain increases and the average phonon energy stored per C-C bond also increases. The Boltzmann distribution of the phonon energy stipulates that the likelihood of having several high-energy phonons within a segment of the chain also increases. The phonons

can cumulatively add their effects on a single C-C bond and once the C-C bond strength is reached, chain scission can occur. The rate of a single scission, k_b , can be expressed as:

$$k_b = \alpha \frac{kT}{h} e^{\frac{\Delta S}{k}} e^{\frac{-U_0}{kT}} = \omega_0 e^{\frac{-U_0}{kT}} \quad (\text{Eqn 4-1})$$

Where α is the transmission constant which indicates how many of the C-C bonds that reach the bond energy will actually fail, k is the Boltzmann constant, h is Plank's constant, T is absolute temperature, ΔS is the change in entropy from the C-C bond scission, and U_0 is the energy barrier for C-C bond scission, between 260 kJ/mol and 400 kJ/mol [41]. The first terms can be combined into the vibration frequency for chain scission, ω_0 , which has a temperature dependence but is much less than the temperature dependence in the exponential term. This equation describes the rate of thermally-induced chain scission [29].

This equation can be modified to account for the effects of stress in a single chain. The effect of the chain stress lowers the energy barrier for chain scission. There has long been a debate about what form this function should take [77-79] and theories include a linear relationship suggesting uniform loading throughout the fiber and chains, a quadratic relationship suggesting the elastic energy stored in the fiber is the critical property for the rate of chain scission, and the difference of square root functions suggesting a Morse potential describes the C-C bond for chain scission. Infrared adsorption studies investigating the shifts in the C-C bonds as a function of applied macroscopic fiber stress [79, 80] have suggested a linear correlation between chain stress and macroscopic fiber stress. This agrees with the linear function and difference between square roots function, since the difference of square roots over the range of the Morse potential can be approximated as linear. The rate of chain scission, k_c , as a function of

temperature and chain stress can be expressed as the product of the rate of a single chain scission, k_b , and the total number of C-C bonds in the chain, n_c , where β is the activation volume for chain scission and ψ is the chain stress [29]:

$$k_c = n_c k_b = n_c \omega_0 e^{\frac{(-U_0 + \beta\psi)}{kT}} \quad (\text{Eqn 4-2})$$

This model has two key assumptions. The first is that the stress in each chain, in both the crystalline and amorphous regions, is not affected by the strain of adjacent chains. Due to the three different phases in the fibers (extended orthorhombic, monoclinic, and oriented amorphous), the distribution of the phases, and the phase heterogeneity, this is most likely an inaccurate assumption. Some chains are likely to experience higher strains and therefore stresses due to their location in the fiber. For instance, the amorphous regions have a lower C-C cross sectional area than the crystalline phases, have a lower Young's modulus, and will experience higher strains given the same stress as the surrounding crystalline regions. Individual tie chains in the amorphous regions can therefore be subjected to higher stresses than the average chain stress and scission is likely to first occur in the amorphous regions.

The second assumption is that the stress on each C-C bond within a chain is subjected to the same stress. Similar to the first assumption, the number of different phases in the fibers, the distribution of the phases, and the phase heterogeneity also make this assumption most likely inaccurate. The amorphous phase will be subjected to higher individual stresses, as discussed previously. The stress may also be localized at crystal-amorphous interfaces where the obliquity of the entrance and exit points of a tie chain may impose an angle on the C-C bonds at the phase interface. The angled area acts as a

stress concentrator and the angled C-C bonds at the interface will experience higher stresses than the rest of the n_c bonds.

The crystalline regions also are not expected to have uniform stresses throughout the C-C bonds. Polymer chains in a viscous solution subjected to different flow rates have shown a strain-rate dependence on the stress on individual C-C bonds. [81]. The distribution of forces within the chain were described as:

$$\psi = \frac{\xi_0 \dot{\epsilon} \rho N_L}{M_0} \left(\frac{L^2}{8} - \frac{z^2}{2} \right) \quad (\text{Eqn 4-3})$$

where ψ is the axial stress in the z^{th} bond, ξ_0 is the frictional force experienced by each CH_2 unit, $\dot{\epsilon}$ is the strain-rate, ρ is the density of the polymer, N_L is the number of CH_2 units in the chain, M_0 is the molar mass of the CH_2 unit, L is the length of the chain, and z is the distance of the bond from the center of the chain. The maximum stress is at the center of the chain, where $z = 0$, and is given by:

$$\psi_{max} = \frac{\xi_0 \dot{\epsilon} M^2 L_{mon}}{8M_0^2} \quad (\text{Eqn 4-4})$$

where M is the molecular mass of the chain and L_{mon} is the length of a CH_2 unit. This study was conducted on high molecular weight polymers in solution subjected to high shear forces from viscous liquid flow but the same principles can be applied to crystalline systems by changing the ξ_0 to reflect the frictional forces of a sheared CH_2 unit in the crystalline region. This assumes that the chains within a crystal move relative to one another. Due to the close-packing discussed in the WAXS section, this is most likely a cooperative mechanism. For polyethylene, the shear forces come from Van der Waals forces between CH_2 units, which are relatively weak when compared to aramid fibers with hydrogen bonding between chains, so the frictional value for polyethylene is

expected to be low for oriented polymer fibers. Lastly, the strain-rate term in the numerator indicates that the stress in the chain bonds (or cooperative collection of chain bonds) increases linearly with strain-rate. The highest strain-rate in this study was at 10^3 s^{-1} and scissions should have the highest probability of occurrence at this strain-rate.

The sections above described models for the effects of temperature and chain stress on the probability of chain scission and discussed their applicability to highly oriented polyethylene fibers. As temperature, strain-rate, and fiber stress increase, the chain stress increases and the probability of chain scission increases. More energy is required to break C-C bonds than to straighten or slip adjacent chains. The three main mechanisms for relieving stress energy in fiber are chain scission, enthalpic slippage between chains, and entropic changes in the conformation also called straightening of non-taut chains. The competing mechanisms of chain slippage and conformational changes of straightening have smaller energy barriers than chain scission. The higher temperature tensile tests are more likely to affect these low energy barrier mechanisms than the scission mechanism.

To investigate the presence of chain scission products, a Bruker Vertex 80 FTIR spectrometer equipped with a Hyperion microscope accessory was used to perform analysis on the failure surfaces of the fibers. Failure surfaces from the 10^3 s^{-1} strain-rate at $20 \text{ }^\circ\text{C}$ were selected to have the highest probability of chain scission and free radical products. The transmittance method was first attempted but the signals were not strong enough to detect a single fiber and is attributed to the thickness of the fiber. Attenuated total reflection was attempted on the free-floating fiber ends but fiber ends could not be constrained well enough without affecting the ends. The fiber failure surfaces were

pressed in a diamond anvil cell. The ATR crystal has a collection size of 32 μm and, as shown in the SEM images, the fibrillated failure surfaces can have microfibril diameters close to 5 μm . In an attempt to overcome the discrepancy between ATR crystal collection size and failure surface diameter, knife edges slits were used to localize the collection window to just the failure surface. The collected spectra showed a large background absorption in the areas of interest (980 cm^{-1} and 1700 cm^{-1}). A small absorbance is seen near 1700 cm^{-1} and no absorbance was observed at 980 cm^{-1} . The results are shown in Figure 4-1 and indicate the possibility of oxygen containing functional groups near the failure surface as products of chain scissions. There are two possible explanations for this observation. First, the number of chain scissions at the failure surface are relatively small. Second, a number of scissions occur but the carbon-centered free radicals react with other carbon-centered free radicals through the reparation reaction discussed earlier. However, the absorbance at 1700 cm^{-1} is small relative to the background absorption and it is difficult to quantize.

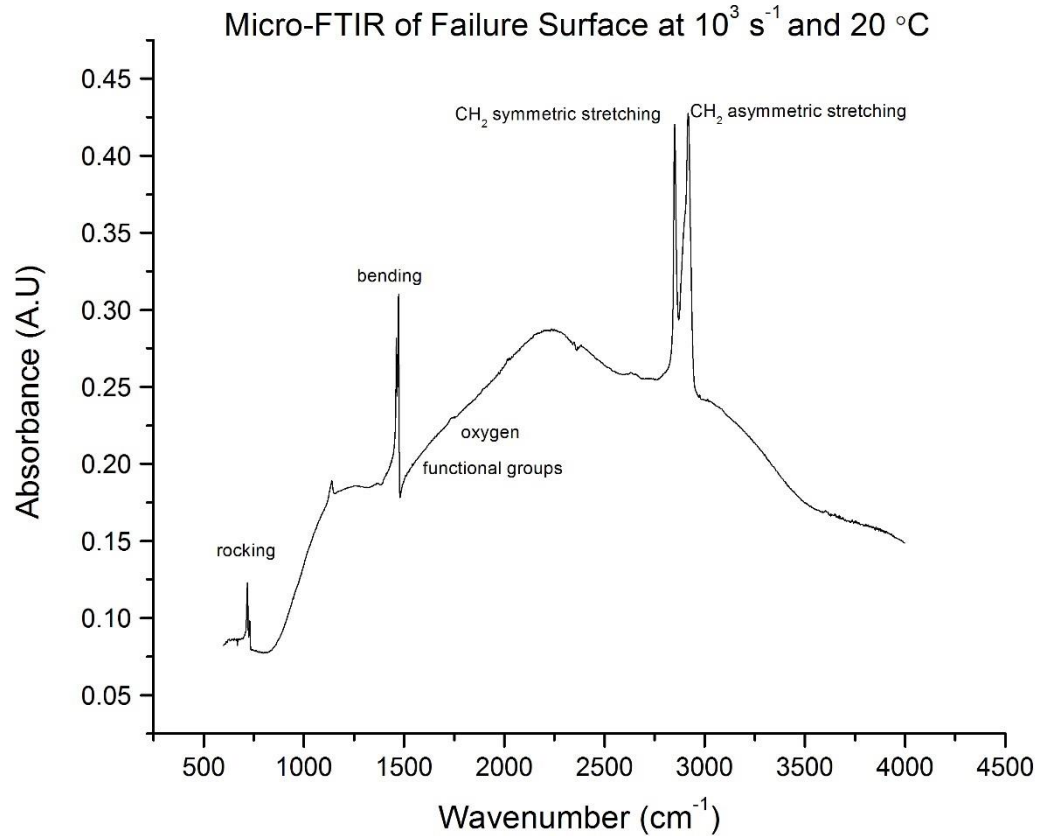


Figure 4-1: Micro-FTIR of a failure surface at 10^3 s^{-1} strain-rate and $20 \text{ }^\circ\text{C}$. The small size of the failure surface (approximately $5 \text{ }\mu\text{m}$) created a large background absorbance in the 1700 cm^{-1} region.

4.2.3 Fiber Diameter Distribution

The fiber diameter distribution showed an average diameter of $18.49 \text{ }\mu\text{m}$ with a standard deviation of $1.15 \text{ }\mu\text{m}$. Similar values have been reported for Dyneema SK76 fibers [19, 28, 54] The distribution is fit fairly well by Gaussian distribution with two possible modes near $17.5 \text{ }\mu\text{m}$ and $18.75 \text{ }\mu\text{m}$. It is likely that this distribution is a result of the combination of the change in polymer concentration of the gel, the initial spinneret diameters, and imperfections in the drawing process.

Outliers were excluded if the diameter measurement was greater than 23 μm or less than 15 μm . The fibers with these measurements had one or two of their fiber diameter measurements in this range. There was only one diameter measurement smaller than 15 μm with a diameter of 13.86 μm and at this location part of the fiber had separated into two smaller fibers at one location along the fiber gage length. This fiber was still used in tensile tests due to both fiber pieces appeared to be load bearing and a normal failure strength was observed. The rest of the excluded outliers had diameters ranging from 23.41 μm up to 41.36 μm , indicating that another whole fiber or part of a separated fiber had wrapped around part of the gage length. These fibers were still used for tensile tests as the additional diameter was not assumed to be load bearing since it did not span the entire gage length.

4.3 Changes in Strength and Young's Modulus

The possibility of the minimum fiber diameter playing a critical role in the failure mechanics was investigated. Plots for the failure strength and UTS were created to determine if the average fiber diameter or minimum fiber diameter stress calculation method would provide better fits of the data or lower standard deviations.

For both failure strength and UTS, the shape of the plots did not change for all strain-rates between the two methods. While the average stress values for the minimum method are always higher than the average diameter method, the same trends are observed for each strain-rate. All of the plots displayed the same general decreases and drops at the same temperature-strain-rate combinations. The relative changes in curve shape as temperature increases are equivalent for each method.

The standard deviations at each temperature-strain-rate combination were also compared and the differences between the methods were calculated and plotted for the failure strength and UTS. These plots are shown again in Figure 4-2. For the failure strength comparison, the minimum method had a higher standard deviation at 36/52 or 69% of the temperature-strain-rate combinations. The maximum difference was 0.37 GPa and the minimum was -0.12 GPa, where the average method had a higher standard deviation than the minimum method. The average for all points is $0.04 \pm .03$ GPa indicating that the minimum method will produce a slightly higher standard deviation on average. For the UTS, the minimum method had a higher standard deviation at 47/66 or 71% of the temperature-strain-rate combinations. The maximum difference was 0.37 GPa and the minimum was -0.15 GPa. The average for all points is $0.03 \pm .08$ GPa indicating that the minimum method will give slightly higher standard deviation on average but with a high standard deviation of that average.

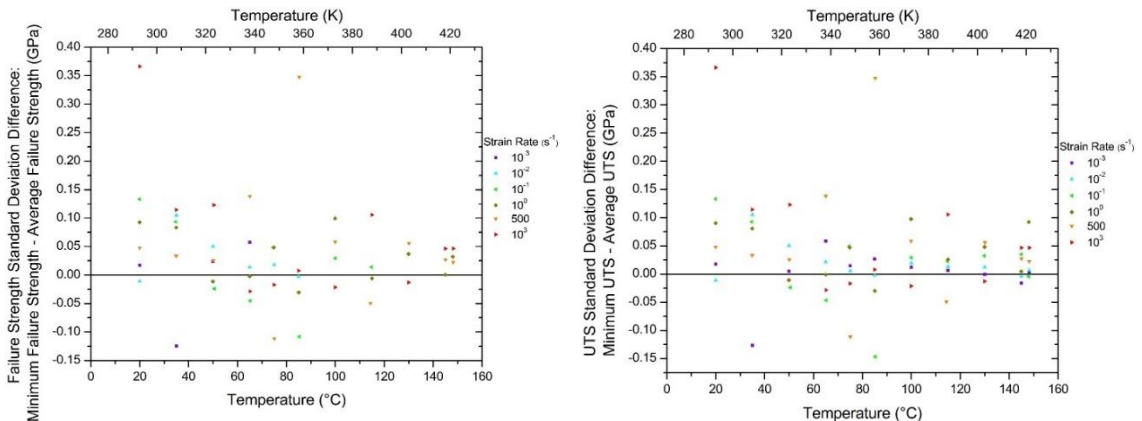


Figure 4-2: The calculated difference in failure strength (right) UTS (left) standard deviations between the minimum diameter method and the average diameter method for each temperature-strain-rate. The positive values indicate temperature-strain-rate combinations where the minimum diameter method has a higher standard deviation and the negative values indicate combinations where the average diameter method has a higher standard deviation. The zero line has been drawn to help distinguish between these regions.

The average diameter method is suggested by this study to be the better method for calculating stress in UHMMPE single fibers. The curve shapes between the two methods appear to be equivalent but on average the standard deviations of the minimum diameter method are higher than the average diameter method. This indicates that the average diameter method will provide the same changes in curve shape but with more reproducible results. The differences appear to be randomly distributed over the temperature-strain-rate combinations indicating there is no apparent trend for the conditions where one method would have the lower standard deviation than the other. For this reason, only the average diameter method was presented in the Young's modulus and failure toughness sections.

A key conclusion from the same shapes and lower standard deviations is that the mechanical properties are not dominated by the lowest diameter region of the fiber. In contrast, ceramic materials would fail at the lowest diameter where the stress is highest, and the lack of this behavior emphasizes the viscoelastic mechanical behavior of the fiber. This also suggests that there is a complex loading path within the fiber and it does not scale directly with the macroscopic diameter of the fiber. However, as seen in the SEM images of failure surfaces, a decrease in fiber diameter near the failure surface when compared to the pre-tensile test average fiber diameter is observed at all temperatures and strain-rates. The failure strengths presented were calculated using engineering stress, where the original fiber diameter is kept constant. As discussed in the introduction, true stress and true strain plots would provide a more accurate measure of stress and strain at the failure surfaces. However, these are difficult to measure and create

due to the unknown location of fiber failure and the complicated fibrillated failure surfaces. True stress-strain curves were created using the constant volume approximation:

$$\sigma_{True} = \sigma_{Eng}(1 + \varepsilon_{Eng}) \quad (\text{Eqn 4-5})$$

$$\varepsilon_{True} = \ln(1 + \varepsilon_{Eng}) \quad (\text{Eqn 4-6})$$

where σ_{True} and ε_{True} are the true stress and strain, respectively, and σ_{Eng} and ε_{Eng} are the engineering stress and strain, respectively. Figure 4-3 shows a comparison between the engineering and true stress-strain curves for a necking curve at 10^{-3} s^{-1} and $50 \text{ }^\circ\text{C}$. There is little difference between the plots due to the small strains to failure and the true stress-strain plot does not provide further insight into the mechanics of fiber failure.

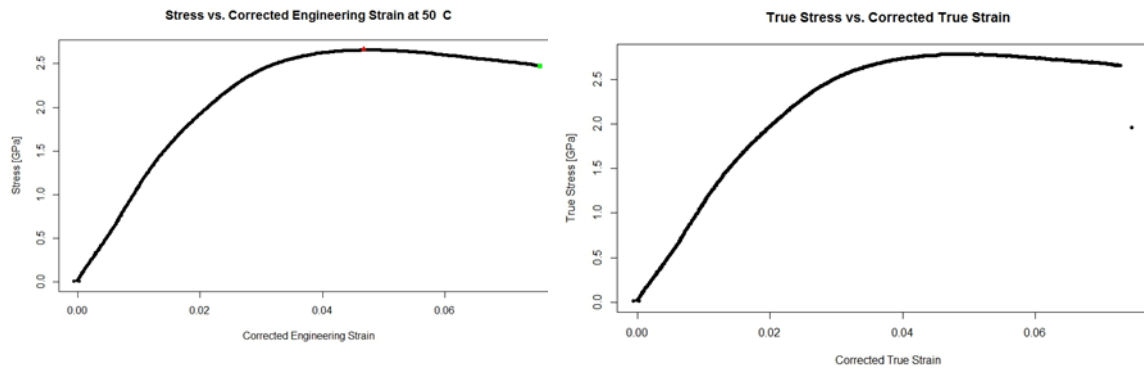


Figure 4-3: Comparison of the engineering (left) and true (right) stress-strain plots using the constant volume approximation.

It is possible that the location and cause for the strain localization is correlated to the minimum diameter area for the fiber gage length. Understanding the location and local morphology where the failure occurs could provide insight in the failure mechanism and will be discussed in the future work section.

An important detail is that there was no discussion about the accuracy of either diameter method. It is possible that the minimum diameter measurement is the more accurate

method for measuring strengths and the single fibers have a larger distribution of failure strength and UTS values for a given diameter.

4.3.1 Failure Strength

The failure strength is observed to decrease monotonically with increasing temperature and to increase with increasing strain-rate. The fibers were observed to not fail up to 25% uncorrected strain at strain-rate dependent temperatures with non-failure temperatures at 75 °C, 100 °C, and 130 °C for the 10^{-3} s^{-1} , 10^{-2} s^{-1} , and 10^{-1} s^{-1} , strain-rates, respectively.

The highest average failure strength was observed at $4.35 \pm 0.47 \text{ GPa}$ at the 10^3 s^{-1} strain-rate and 20 °C. The average failure strength for 10^{-3} s^{-1} strain rate at 20 °C was $3.37 \pm 0.21 \text{ GPa}$. At 20 °C the other four strain-rates are between these two values with failure strength increasing with increasing strain-rate. This trend is observed for all temperatures with four exceptions. The first three are attributable to the large standard deviation observed at the dynamic strain-rates at 35 °C 50 °C and 65 °C where the 10^3 s^{-1} strain-rate has an average failure strength lower than the 500 s^{-1} strain-rate but both rates are within one standard deviation or each other at each of these three temperatures.

The second exception occurs at 148 °C where the 10^0 s^{-1} , 500 s^{-1} , and 10^3 s^{-1} strain-rates have average failure strengths of $0.89 \text{ GPa} \pm 0.16 \text{ GPa}$, $0.38 \text{ GPa} \pm 0.22 \text{ GPa}$, and $1.45 \text{ GPa} \pm 0.26 \text{ GPa}$, respectively. In this region, the fiber is predominantly hexagonal phase and the dynamic strain-rates are observed to have a large decrease in failure strength from 145 °C to 148 °C. The 10^0 s^{-1} strain-rate does not exhibit this large decrease in average failure strength and appears to follow the decrease observed for the higher temperatures. This is an interesting observation because for the 10^0 s^{-1} strain-rate

only 3/5 fibers failed and the other 2/5 were non-failures. This demonstrates that at the 10^0 s^{-1} strain-rate, the competing strain-rate and frequency of the mechanism controlled by the rotations of the CH_2 units are approximately the same magnitude. The increase in failure strength in the 10^0 s^{-1} strain-rate relative to the 500 s^{-1} strain-rate suggests that a different mechanism is responsible for failure at dynamic strain-rates.

As temperature increases, the thermal energy stored within each primary and secondary bond increases and the equilibrium distance between the bonding atoms increases. Increasing temperature therefore decreases the strength of the fundamental bonds of the fiber. The weakening of all bonds within the fiber contributes to the decrease in failure strength as temperature increases.

Another temperature effect is the thermal shrinkage of the fibers as temperature is increased. As discussed in the first chapter, the lamellar orthorhombic phase has a lower free energy than the extended orthorhombic phase due to the higher entropy in the lamellar phase. As temperature increases, there is a retraction force on the fiber from the increase in the thermal energy of the chains and their attempt to create a folded confirmation. This effect is larger than the thermal expansion of bonds discussed earlier and the gripped fiber are observed to have a thermally-induced pretention before the tensile test is conducted. The amount varies based on the gripping procedure and if any slack or tension was introduced in the fiber during this process. The retraction force is typically around 5 % of the UTS for temperatures above $100 \text{ }^\circ\text{C}$ which agrees with the manufacturer estimation of thermal shrinkage at $100 \text{ }^\circ\text{C}$ for similar fibers [30] which agrees with a study that showed no change in crystal structure for tightly constrained fibers at $100 \text{ }^\circ\text{C}$ [23]. The retraction force was observed to be as high as 25 % of the UTS

for temperatures of 148 °C, where the chain mobility from the hexagonal phase allows the retraction force to be the highest and causes the UTS to be at its lowest.

The three possible stress-relieving mechanisms including scission, slippage, and straightening are all described by a Boltzmann distribution where an energy barrier is overcome by thermal energy. This creates another temperature effect on the strength of fibers. As temperature increases, the probability of each mechanism successfully overcoming the barrier increases. Chain scissions will occur more often as presented in Equation 4-1, the degree of chain slippage will increase, and the chain straightening will possibly require less force but can be countered by the thermal retraction force. The combined effect of all the mechanisms is the reduction in stress energy stored in the fiber and tensile failure occurring at lower failure strengths.

Another observation is at strain-rates above 10^0 s^{-1} and at 148 °C, the dynamic average failure strengths show a dramatic decrease between the 500 s^{-1} to 10^3 s^{-1} strain-rates. This large change in failure strength with a small increase in strain-rate suggests that there are different mechanisms responsible for failure within the hexagonal temperature range.

One possible mechanism is the CH₂ rotations or the gauche conformations becoming more likely in the hexagonal phase. As previously discussed, approximately 1/5 CH₂ units are in the gauche conformation indicating that in the hexagonal phase, these rotations are frequent. The ease with which the CH₂ units can rotate allows another mechanism for adjacent chain slippage. In this mechanism, the rapid cycling between trans and gauche conformations increases the free volume between adjacent chains and decreases the energy barrier for chain slippage from the precursor extended orthorhombic

phase. The increased slippage can lower the stress in the fiber and causes the failure strength to decrease suddenly across this phase transition.

4.3.1.1 Effect of Diameter on Fiber Strength

A negative linear correlation was observed between average fiber diameter and failure strength at 20 °C across all strain-rates. The exception to this was the 10^0s^{-1} which showed a small positive correlation that was most likely attributable to one large diameter fiber that had a similar failure strength to the lower diameter fibers at this temperature-strain-rate combination. Application of the linear correlation to the diameter distribution resulted in average failure strengths that were in agreement with the experimental data. There are several possible reasons for the negative correlation between average fiber diameter and failure strength.

First, the processing technique may have introduced a morphology in the larger diameter fibers where there are less load bearing microfibrils before failure. One possibility that would cause this effect is the presence of more amorphous regions or voids in the fiber. Both of these increase the volume of the fiber and could lead to weaker failure strengths due to the decrease in C-C bond density in the cross sectional area near the failure surface. The increase in voids could also increase the number of chain scissions due to fewer chains having to distribute the stress and a few experiencing an increased chain stress. These few with high chain stress will have an increased probability for scission, as indicated by Equation 4.-2.

An additional effect from an increase in amorphous regions or voids is the decrease in the frictional forces of adjacent microfibrils. The amorphous regions and voids in the fiber have smaller concentrations of chains and a smaller degree of

orientation in the fiber direction. At the interface of a crystalline phase with one of these regions, the number of secondary bonds from CH₂ interactions decreases. This can result in slippage energy barriers to decrease and increases the probability of slippage occurring. WAXS can be used to determine the relative volume of amorphous phase in a fiber. Most WAXS facilities require large samples, and therefore cannot distinguish small and large fiber phase compositions. Individual fibers could possibly be examined using a synchrotron source, which will be discussed in the future work section.

The second possible reason the increase in the fiber diameter possibly creating larger voids or amorphous areas. In this possibility, the total volume percentage of amorphous or void region remains the same as smaller diameter fibers, but they are fewer in number but larger in size. The regions can act as critical flaw initiation locations. As the fiber diameter increases, there is a larger population of these regions and a higher probability the presence of regions on the large size end of the distribution. This explanation assumes that a single critical flaw will propagate through the fiber. This is not a strong possibility due to the propagation across the plane of the fiber being arrested by crystalline regions. However, it does allow for a more complicated failure surface of fibrillation where the “crack” can continue to propagate by following a microfibril crystalline boundary in the direction of the fiber to reach the next amorphous or void region. The SEM images showed fibrillation failure surfaces across all temperature and strain-rates with the higher temperature regions. Again, WAXS at synchrotron sources might be able to determine the change in size of the amorphous population. For the voids, Positron Annihilation Lifetime Spectroscopy can be used to investigate the size of voids,

but the resolution of available instruments may prove challenging for single fiber samples.

The slopes corresponding to the negative correlations were observed to decrease with increasing strain-rate. This suggests that the dynamic strain-rates are more sensitive to changes in the average fiber diameter. As mentioned in the previous section, one possible explanation for this is a limited number of microfibril load-bearing paths in the fiber due to an increase in the volume of amorphous regions or voids. The effect of strain-rate on the probability of chain scission was presented in Equation 4-3. As strain-rate increases, the probability of chain scission also increases due to the increase in potential shear forces. The decrease in the number of C-C bonds in the cross sectional area of the fiber due to strain-rate induced scission could also decrease the failure strength of the fiber.

4.3.2 Ultimate Tensile Strength

The UTS is observed to decrease monotonically with increasing temperature and to increase with increasing strain-rate. The same trends are observed for the UTS as were for the failure strength with the major differences observed for the low strain-rates where failure strengths are absent at high temperatures. At constant temperature, the highest UTS values are observed at the 10^3 s^{-1} strain-rate and UTS values decrease with decreasing strain-rate with 10^{-3} s^{-1} strain-rate having the lowest UTS. This trend is observed for all temperatures with same four exceptions for the dynamic strain-rates as discussed previously, where the first three are attributable to the large standard deviations at high strain-rates. The fourth is attributable to the hexagonal phase at 148 °C, as is the sudden decrease in UTS from 145 °C to 148 °C. The largest difference between the

failure strength and UTS plots is the shape of the two lowest strain-rate curves that appear to be “S”-shaped with inflection points near 75 °C. for the 10^{-3} s^{-1} strain-rate and 100 °C. for the 10^{-2} s^{-1} strain-rate.

The presence of the inflection point suggests two possibilities. First, there is a temperature-strain-rate combination where the temperature increase allows the success rate of the dominant mechanism become to become comparable as the strain-rate. Second, there are two competing mechanisms and at the inflection point there is a change between which one is dominant. These two possibilities can also explain the nearly linear regions observed in the higher strain-rates. For the higher strain-rates, the inflection region occurs over a larger temperature range and therefore it is possible for the “S”-shaped curve to appear linear in this region. For these strain-rates, the melting temperature is reached before the inflection is apparent.

4.3.3 Young’s Modulus

Young’s modulus was observed to decrease with increasing temperature and increase with increasing strain-rate. A linear correlation is observed between increase in temperature and decrease in Young’s modulus up to 145 °C and agrees with previous tensile studies of oriented UHMMPE fibers conducted at quasi-static strain-rates [82]. The slopes ($\delta E/\delta T$) are negative and observed to decrease with increasing strain-rate. The change in slope with respect to the log of strain-rate shows a negative correlation ($\delta E/\delta T/\delta \dot{\epsilon}$) with the slope of the 500 s^{-1} strain-rate possibly being an outlier due to the large standard deviations for the dynamic strain-rate tests. Linear fitting without the dynamic strain-rates showed a slope of approximately $-0.0496 \text{ GPa}/^\circ\text{C}/\log(\text{s}^{-1})$

¹). This fit shows reasonable fitting of the 10^3 s^{-1} but not of the 500 s^{-1} strain-rate slope. Similar to the discussions for failure strength and UTS, there are several mechanisms that can affect the change in Young's modulus with respect to temperature.

First, increasing temperature decreases the strength of the primary and secondary bonds that are responsible for the fiber morphology. The decrease in the strength of these bonds also results in a decrease in the Young's modulus. This suggests that the strength of the primary and secondary bonds of the fibers are strain-rate dependent and are more affected by increases in temperature at higher strain-rates.

Second, the attempt of the constrained chains to increase their conformational entropy by creating lamellar structures create a retraction force in the chains. This effect causes the Young's modulus to increase with temperature due to the constrained taut chains becoming stiffer from the thermally induced stress.

Third, the degree of slippage will affect the Young's modulus. As slippage increases, the amount of strain needed to obtain the same level of stress increases. Since Young's modulus is defined as the change in stress with respect to strain, the increase in required strain for the same stress level causes a decrease in the Young's modulus.

Lastly, an increase in chain scissions will also affect the Young's modulus. As described in Equations 4-2 and 4-3, scission is affected by temperature and strain-rate. As temperature and strain-rate increase, the probability of chain scission also increases. At elevated temperatures and strain-rates, more chain scissions are likely and the C-C cross sectional density is reduced. This reduction causes a decrease in Young's modulus since there are less C-C bonds per area and corresponds to a lower stress.

Stiffening is observed at the necking and non-failure temperatures for the quasi-static and intermediate strain-rates and at all temperatures for the dynamic strain-rates. The stiffening indicates that there is a region within the fibers that increases in stiffness as it is stressed to low values of strain. One possible explanation for this phenomenon is the straightening mechanism within the oriented amorphous regions of the fibers. Marko and Siggia found that the relationship between force and extension for long chains is “S”-shaped according to:

$$fA = kT \left(\frac{z}{L} + \frac{1}{4} \left(\frac{L-z}{L-z} \right)^2 - \frac{1}{4} \right) \quad (\text{Eqn 4-7})$$

where f is force, A is persistence length (twice the Kuhn length), k is the Boltzmann constant, T is temperature, z is the end to end distance, and L is the chain contour length [83]. This relationship predicts high forces required for small extensions as the chain end-to-end distance approaches the contour length. With high forces, tie chains that are not yet taut can become more oriented as the amorphous region is strained. The chains can also become taut at higher temperatures by the effects of thermal shrinkage discussed earlier. The stiffening at approximately 0.5 % strain suggests that at this point, the highest number of tie molecules have become aligned and taut, the fiber has the highest average cross-sectional density of C-C bonds, and the fiber displays the highest Young’s modulus. At strains higher than this, the degree of slippage or scission begin to affect the C-C cross sectional density and act to absorb some of the stress resulting in a decrease in fiber stiffness. One possibility for this phenomenon not being observed at lower temperatures in the quasi-static and intermediate strain-rates is the large time for other mechanisms to successfully relieve stress energy and preventing the stress from

accumulating in the tie chains. Without stress in the tie chains and low thermal energy for thermal shrinkage, the tie chains do not change their conformations to an aligned state.

Lastly, the Young's modulus for all strain-rates appear to converge to a small range of values of 5 GPa to 30 GPa at 148 °C. To demonstrate the convergence from the most extreme strain-rates, the dynamic strain-rates show a decrease of approximately 100 GPa over the temperature range from 20 °C to 145 °C where the average Young's modulus is approximately 115 GPa. A decrease of approximately 100 is observed again from the temperature increase from 145 °C to 148 °C. The phase transition to hexagonal is the likely explanation for this observation. The Young's modulus for this phase at 148 °C appears to be unaffected by strain-rate. This suggests that the mobility of the chains in the hexagonal phase is high enough that frequency of successful chain motions allowed by the CH₂ gauche rotations is higher than time limitation imposed by the 10³ s⁻¹ strain-rate. All strain-rates are controlled equally by this dominant mechanism and observed Young's modulus are all equivalent. At the 10³ s⁻¹ strain-rate, the stress strain curve is observed to have a linear stress-strain relationship until failure. One possible explanation for this is that the 10³ s⁻¹ strain-rate is approaching the limit of how quickly the CH₂ rotations can allow chain slippage. This linear relationship might be a measure of adjacent gauche conformations hindering the chain slippage due to the low time for rotations dictated by the strain-rate.

4.4 Grip Performance

As discussed in the introduction and experimental sections, gripping UHMMPE single fibers is challenging. The "T" design of the custom grips used in this study allowed for a heater to be placed over the entire fiber gage length and also allowed for a longer

area for the fiber to be gripped compared to previous studies [44, 50]. The performance of the custom grips used in this study was demonstrated by the success rate of failures in the gage length and the values of compliance corrected strain.

The success rates exceeded those conducted in previous reports (Sanborn et. al. [44]) at the 10^{-3} and 10^3 s^{-1} strain-rates. There was a dramatic improvement in the 10^3 s^{-1} strain-rate where previous studies reported success rates of 42% and the success rate of this study was between 77% to 85 %. At the 10^0 s^{-1} strain-rate, this study had lower success rate of 81% compared to the 91% reported by Sanborn et al. Only five fiber tests were conducted in this study at room temperature ($20 \text{ }^\circ\text{C}$) and this strain-rate. The number was increased to 27 by including the fibers that were used for non-tensile purposes such as determining instrument settings for data capture. Some of the settings that were being investigated may have had an impact on the number of failures at the grip interface. Another possible reason for the lower success rate at this strain-rate was due to the non-tensile fibers not being properly aligned. It was not discovered until after the non-tensile fibers were tested that the grips were misaligned when mounted in the Bose 3100. The offset was in the direction perpendicular to the table surface underneath the Bose 3100. The angle between the gripped fiber and the edges of the polycarbonate “T”s caused stress to be localized at the grip interface and part of the tensile force to be directed in the transverse direction of the fiber. The curvature of the fiber also creates a shear stress in the fiber since the strain on the top of the fiber is higher than the bottom of the fiber. Additionally, the stress localization is amplified at higher strain-rates. The 10^0 s^{-1} strain-rate was the highest strain-rate conducted on the Bose 3100 and therefore would have the greatest effect on success rate. The offset was corrected for the tensile tests by

fabricating polycarbonate “T”s that were 0.397 mm (1/64”) thicker to compensate for the offset but this likely had a negative effect on the success rate at the 10^0 s^{-1} strain-rate.

The other metric of success for the grips was the average strain to failure values. A value close to or lower than previous studies indicates there is little to no slippage in the grips during a tensile test. The observed average strain to failure values were lower than others reported (Sanborn et al.) for the quasi-static and intermediate strain-rates but slightly higher for the dynamic strain-rates. One possible explanation for the higher average strain to failure values at the dynamic strain-rates is strain-wave reflections within the thermal standoff apparatus. The standoff was inserted between the grip and the load cell and the reflections are caused by the change in material and cross sectional area within the thermal standoff. These changes occurred at each material change from the grip to steel thread adapters to the ceramic thermal insulator to another steel thread adapter. These mismatches in impedance cause strain wave reflections and can delay the peak load in the force sensor which causes a longer failure time. A longer failure time results in higher strain to failure values at constant strain-rate. To verify this, the fibers used for the force correction did not use the thermal standoff. The average corrected strain to failure for the 10 tests at 10^3 s^{-1} was 0.0280 ± 0.0027 which is lower than previous reports (Sanborn et al) at dynamic strain-rates. Another possibility is the interpretation of the unstable region of the stress-strain curve. The stress-strain plots of Sanborn et al. did not discuss an unstable region near failure. It is possible that the authors interpreted the beginning of the unstable region as the point of fiber failure and would therefore have lower strain to failure values.

The custom grips were verified to perform well at all strain-rates and allowed the observation of strain measurements across the 20 °C to 148 °C temperature range and seven decades of strain-rate. The strain to failure values for the dynamic strain-rates are likely slight overestimates due to the strain-wave reflections in the thermal standoff. The relative changes in strain to failure across the temperature range can still be compared for trends.

4.5 Strain Behavior

Average strain to failure, or elongation at failure, was observed to increase with increasing temperature and decrease with increasing strain-rate. The quasi-static and intermediate strain-rates showed an evolution of stress-strain curve shape as temperature increased from pseudo-brittle, to plateauing, to necking, to non-failure. These transitions occurred for all four of the quasi-static and intermediate strain-rates at strain-rate dependent temperatures. These curves have a characteristic retarded elastic stress strain behavior observed for viscoelastic materials (Painter) where a combination of coupled elastic and viscous behavior dominate the mechanical response. The dynamic strain-rates showed no change in average strain to failure or stress-strain shape. At 148 °C where there is a hexagonal phase transition, the 10^3 s^{-1} strain-rate was observed to have an increase in the average strain to failure to approximately 5.5% with a linear stress-strain relationship to failure.

4.5.1 Stress-strain Curve Shapes and the Chain Slippage Mechanism

The pseudo-brittle stress-strain curve shapes were observed at strain-rate dependent temperatures below the plateauing temperature. In this pseudo-brittle region,

the stress-strain curve increases monotonically with a decreasing slope until failure, the UTS coincides with the failure strength, and the average strain to failure values are approximately 3%, varying slightly above or below with decreasing or increasing strain-rate, respectively. The 500 s^{-1} and the 10^3 s^{-1} strain-rates were observed to exhibit pseudo-brittle behavior across all temperatures and showed a strain to failure plateau of approximately 3% for the entire temperature range in this study.

The plateauing stress-strain curve shapes were observed at strain-rate dependent temperatures when the average strain to failure values begin to increase above from the 3% plateau and correspond to the beginning of a plateau at the UTS value in the stress-strain curves. In the plateauing region, the stress-strain curve increases monotonically with a decreasing slope until failure, a plateau of constant stress with increasing strain exists at the UTS, the UTS and the failure strength have the same stress value but are separated by a strain plateau, and the strain to failure values are above 3%.

The necking stress-strain curve shapes are also strain-rate dependent and are observed when the average strain to UTS values reach a peak strain value and correspond to the beginning of a necking region after the UTS in the stress strain curves. In the necking region, the stress-strain curve does not increase monotonically due to the necking region, a necking region of decreasing stress with increasing strain is observed after the UTS, the failure strength has a lower stress value than the UTS, stiffening of the fiber is observed in the 0.5% strain region, and the strain to failure values are above 5%.

Lastly, the non-failure stress-strain curves are also strain-rate dependent and are observed when the fibers were strained to 25% uncorrected strain without failure. In the non-failure region, the stress-strain curve does not increase monotonically with a long

necking region, the failure strength is absent, a stiffening is observed in the 0.5% strain region, and the strain to failure values are absent.

Table 4-1 lists these key temperature regions and Figure 4-4 depicts these regions graphically. Based on the temperature-strain-rate trends, interpolation for 5 °C steps and the strain-rates not conducted in this study are included for clarity. Observing similar values diagonal from one another on Table 4-1 and Figure 4-4 suggests that there is a temperature-strain-rate equivalence to observe similar mechanical behavior. The diagonals suggest that for similar mechanical behavior, increasing the strain-rate by a decade can be equalized by an increase of approximately 20 °C. For example, starting at the 10^{-2} s^{-1} plateauing temperature of 50 °C if the strain-rate is increased by a decade to 10^{-1} s^{-1} then the temperature must be increased to 65 °C to observe plateauing stress-strain curves at this higher strain-rate.

This behavior across all of the temperatures for the quasi-static and intermediate strain-rates suggests that the same temperature and strain-rate dependent mechanism is

Strain-rate [s ⁻¹]	Pseudo-brittle	Plateauing	Necking	Non-failure
10^{-3}	< 20 °C	20 °C-35 °C	50 °C-65 °C	75 °C-148 °C
10^{-2}	< 50 °C	50 °C	65 °C-85 °C	100 °C-148 °C
10^{-1}	< 65 °C	65 °C-75 °C	85 °C-115 °C	130 °C-148 °C
10^0	< 85 °C	85 °C	100 °C-145 °C	148 °C
500	< 20 °C-148 °C *	-	-	-
10^3	< 20 °C-148 °C **	-	-	-

Table 4-1: The key temperature regions for the temperatures and strain-rates conducted in this study. The asterisk indicates that the 500 s^{-1} strain-rate stress-strain curve was not the same as the pseudo-brittle shape observed in the quasi-static and intermediate strain-rates. The double asterisk indicates that the 10^3 s^{-1} strain-rate stress-strain curve was not the same as the pseudo-brittle shape observed in the quasi-static and intermediate strain-rates and the 148 °C had a unique stress-strain curve shape with a linear stress-strain relationship to failure.

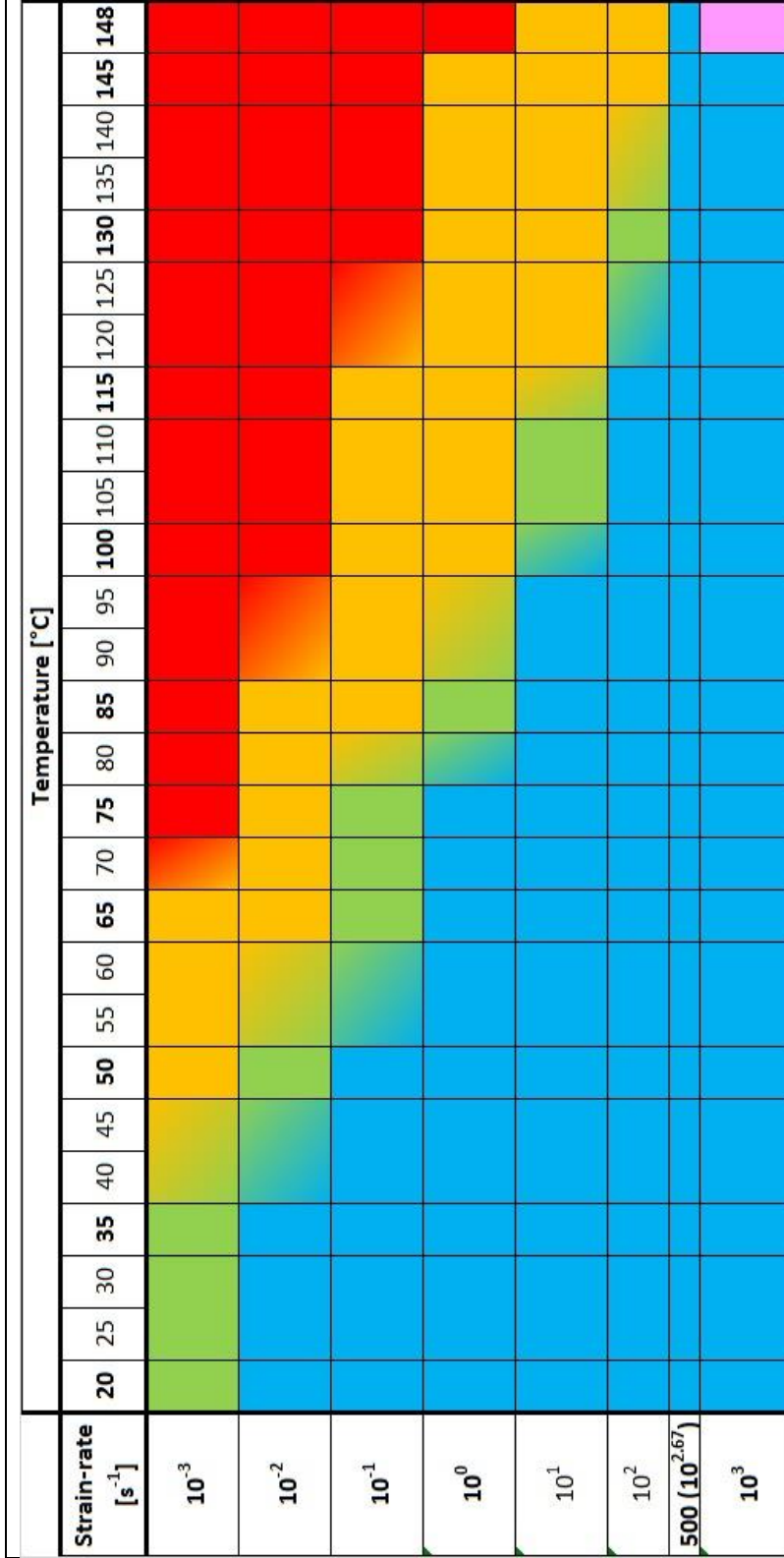


Figure 4-4: A graphical representation of the key temperature regions and their shifts with increasing strain-rate. The blue, green, orange, and red areas correspond to the pseudo-brittle, plateauing, necking, and non-failure regions. The pink square indicates the unique observed stress-strain curve shape at the 10³ s⁻¹ strain-rate and 148 °C where the average strain to failure increased to approximately 5.5% and the shape of the curve was observed to have a linear stress-strain relationship to failure. 5 °C temperature steps as well as 10¹ s⁻¹ 10² s⁻¹ strain-rates have been added and interpolated for visual clarity. The 10² s⁻¹ strain-rate row was divided to show the experimental data for the 500 s⁻¹ strain-rate which corresponds to 10^{2.67} s⁻¹. The interpolated temperature regions are grouped into one box and diagonal shading fills have been used to indicate a temperature range over which a transition occurs but the exact

responsible for all of the transitions. This behavior is similar to that seen in creep experiments where an initial stress is applied to the viscoelastic sample and the decay in strain is observed as a function of time according to the general equation:

$$\frac{d\varepsilon}{dt} = \dot{\varepsilon} = \frac{C\sigma_0^a}{d^b} e^{\frac{-\Delta E}{kT}} \quad (\text{Eqn 4-8})$$

where ε is the strain, t is time, σ_0 is the initial stress, ΔE is the energy barrier of the mechanism, d is the grain size, k is the Boltzmann constant, T is absolute temperature, and C , a , and b are a material and mechanism dependent constants. For this study, strain rate ($d\varepsilon/dt$ or $\dot{\varepsilon}$) was held constant while the change in strain and stress were measured.

Regardless of the form taken by the stress, grain size, and constants, the creep compliance equation indicates an exponential temperature dependence exists according to a Boltzmann factor with constant strain-rate:

$$\dot{\varepsilon} = \text{constant} = f(\sigma_0, d) e^{\frac{-\Delta E}{kT}} \quad (\text{Eqn 4-9})$$

$$\ln(\dot{\varepsilon}) \propto -\frac{\Delta E}{k} \left(\frac{1}{T}\right) \quad (\text{Eqn 4-10})$$

To determine if the mechanism is the same, plots were created using the inverse of the starting temperatures for the key temperature regions and the natural log of the strain-rate to determine if the activation energy (ΔE) of this mechanism changes between these transitions.

Figure 4-5 shows the creep compliance plots and the slopes of the calculated linear fits. Fitted slopes for the plateauing, necking, and non-failure mechanisms were calculated to be -10385, -13677, and -13368, respectively, with units of $-\Delta E/k$. For comparison, the slopes can be multiplied by k to obtain the calculated activation energies of 86 kJ/mol (0.89 eV), 113 kJ/mol (1.18 eV), and 111 kJ/mol (1.15 eV) for the

plateauing, necking, and non-failure regions respectively. These values agree well with previously determined activation energies obtained from other methods that ranged from 107 kJ/mol to 120 kJ/mol [84-89].

The plateauing mechanism is observed to have a lower energy than the necking and non-failure mechanisms. An important note for 10^{-3} s^{-1} strain-rate is that the fibers were considered to already be within the plateauing temperature range at 20 °C, the lowest temperature in this study. However, in comparison of the average strain to failure

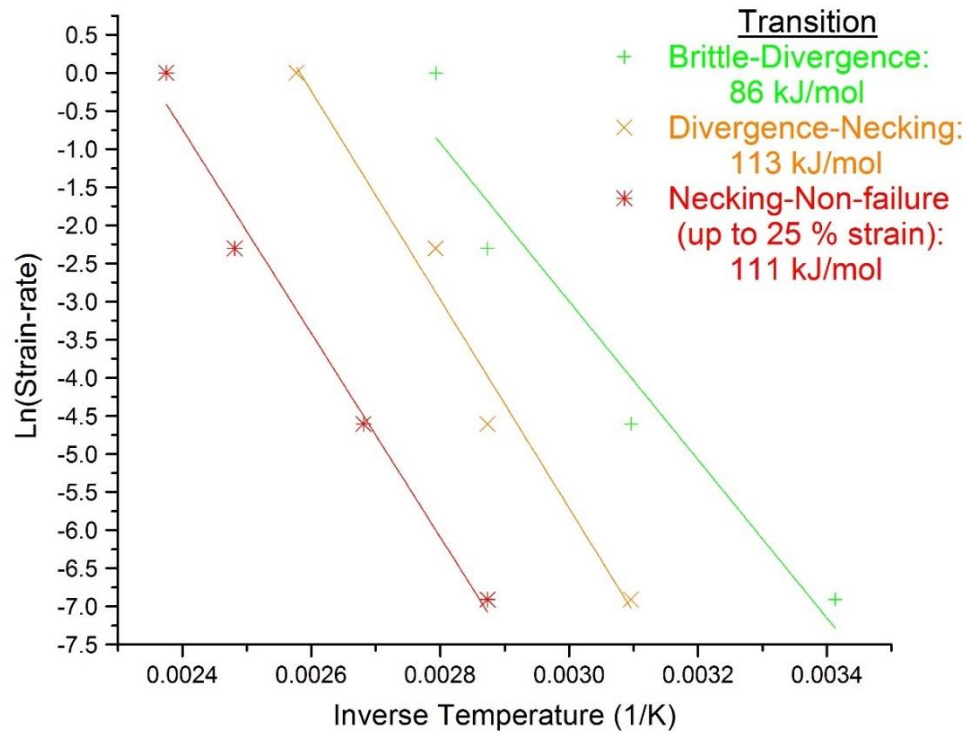


Figure 4-5: Plots of the inverse starting temperature for the key temperature regions and the natural log of strain-rate.

values at the start of the plateauing range for the 10^{-2} s^{-1} and 10^{-1} s^{-1} strain-rates, the 20 °C average strain to failure value at the 10^{-3} s^{-1} strain rate is lower and at 35 °C it to be higher. This implies that for comparable plateauing temperatures between strain-rates, the

starting temperature for plateauing range for the 10^{-3} s^{-1} strain-rate should be higher than 20 °C and lower than 35 °C. The inverse temperature value at 35 °C is .0032 and would shift the linear fit closer to the approximate 13500 $\Delta\text{Energy}/k$ values observed for the necking and non-failure fits. This could account for why the slope of this fit has a lower value than the necking and non-failure fits and suggest that all of the mechanisms have the same energy barrier.

The similarities in the values indicate that the same mechanism is responsible for the all three behaviors; plateauing, necking, and non-failure. The most likely mechanism is the slippage mechanism due to the observation of 25 % strains without failure. The straightening mechanism could not account for 25% strains without failure since the amorphous regions are already highly oriented. Chain scission is also not a likely candidate because the number of scissions that would be needed to approach 25 % strain without failure would be very high and the fiber would have likely failed due to the decrease in C-C cross sectional density. While the straightening and scission mechanism will still be active and play some role in the 25 % strains, the slippage mechanism is the dominant mechanism for this behavior. SEM imaging of crack interfaces showed a microfibril network exists between macrofibrils and has been observed previously in Spectra® fibers [90]. Therefore, the slippage mechanism allows motion between adjacent macrofibrils or microfibrils to alleviate stress in the fiber without drastically altering the morphology inside the macrofibril or microfibril. Given enough successful rates of slippage from high temperatures and enough time for successful attempts from low strain-rates, this mechanism allows the fiber to be drawn to large strains without failure. At dynamic strain-rates, the strain-rate limits the time for attempts of successful slippage

and even at temperatures up to the melting temperature, the mechanism is not the dominant mechanism.

As the strain in the fiber increases, the stress increases. The stress experienced by each individual chain in the fiber is not the same due to the three different phases in the fibers (extended orthorhombic, monoclinic, and oriented amorphous), the distribution of the phases, and the phase heterogeneity. The difference in stress of adjacent chains causes a shear stress between them and increases as the macroscopic stress in the fiber increases. Chain slippage is the main mechanism to alleviate the shear stress. The result is a competition between the buildup of stress and the relaxation from the slippage mechanism. The parameters that control the interaction between these two competing effects are the temperature of the fiber and the strain-rate. As the temperature increases, thermal shrinkage can add stress to the chains increasing the shear-driving force for slippage and increasing temperature also provides the thermal energy for the slippage mechanism to successfully occur. As strain-rate increases, the time for slippage to occur decreases and therefore increasing strain-rate hinders the slippage mechanism.

In the strain-rate dependent pseudo-brittle temperature regions, the stress-strain curve has a concave shape due to the chain slippage causing some relaxation in the fiber as it is strained at a constant rate. The stress accumulates based on the strain-rate, the temperature in this region is not high enough to allow chain slippage to keep up with stress above a certain strain value (approximately 3 %), and failure occurs. At higher temperatures in the plateauing temperature region, the thermal energy allows the slippage mechanism to keep up with the accumulating stress at higher strain values and a stress-strain plateau forms where there is a steady-state between the accumulation of

stress from increasing strain and the ability of the slippage mechanism to alleviate the stress up a higher strain value (approximately 3 % to 5 %). At even higher temperatures in the necking temperature regions, the slippage mechanism occurs more frequently and can alleviate the stress accumulation to higher strains (greater than 5 %). At these higher strain levels, the combination of high temperature and the high shear driving force allow relaxation from the slippage mechanism to occur faster than the strain-rate stress accumulation and a necking region is observed for a range of strain where stress decreases as strain increases. This region does not last indefinitely and necking causes strain localization in the fiber where the relaxation mechanism cannot keep up with the increased stress accumulation from the decrease in cross sectional area and failure occurs. Lastly, in the non-failure temperature regions, the rate of chain slippage is high enough that the slippage mechanism can alleviate stress even in the strain localization areas of the fiber and failure is prevented up to at least 25 % uncorrected strain.

SEM imaging of diameter measurements near the failure surface indicated that there is a degree of localized strain near the failure surface for at all temperatures and strain-rates. The localized strain indicates that there is some degree of plastic deformation observed in the fibers at all temperatures and strain-rates and that this accumulates over time until failure. The fibrillated failure surfaces observed at all temperatures and strain-rates also suggests that the slippage mechanism is the dominant failure mechanism.

4.5.2 Strain to UTS Mechanisms at High Temperature

At temperatures of 145 °C and 148 °C, some behavioral differences emerge for the strain to UTS values between the strain-rates. The 10^{-2} s^{-1} , 10^0 s^{-1} , and 500 s^{-1} are all observed to have strain to UTS values between 2.5 % and 4.5 % for all temperatures. The

10^{-3} s^{-1} strain-rate is observed to decrease outside of the 2.5 % range at 145 °C and drops sharply at 148 °C. The 10^{-1} s^{-1} strain-rate is observed to have the opposite behavior and increases in strain to UTS at 145 °C and sharply increases at 148 °C to a value of approximately 7 % strain. This is the highest observed average strain to UTS for all temperature-strain-rate combinations in this study. The 10^3 s^{-1} strain-rate is observed to behave similarly and increases in strain to UTS with an average value of approximately 5.5% at 148 °C. The plots of the average strain to UTS and $\log(\text{strain-rate})$ are shown in Figure 4-6. These observations suggest complicated relaxation mechanisms with the presence of the hexagonal phase. The increase in the strain to UTS for the 10^3 s^{-1} strain-rate was suggested to be associated with adjacent gauche conformations hindering chain slippage due to the high strain-rate limiting the time allowed for the CH_2 rotations to rotate past one another. The peak in strain to UTS for the 10^{-1} s^{-1} strain-rate and the lower value in the 10^{-3} s^{-1} strain-rate may possibly be explained by some of the free radical reactions discussed previously in this chapter. This behavior requires further investigation and will be discussed in the future work section.

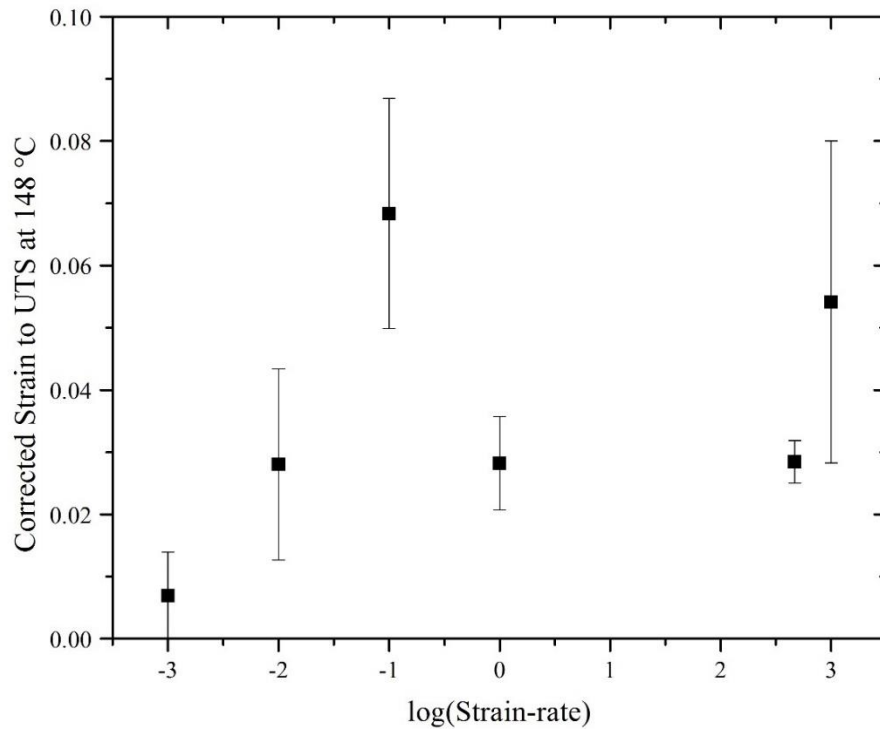


Figure 4-6: Plots of the average strain to UTS values with log(strain-rate) showing a complicated combination of competing mechanisms.

4.6 Theoretical Ballistic Performance

4.6.1 Failure Toughness

The failure toughness was observed to increase monotonically with increasing temperature for the 10^{-3} s^{-1} , 10^{-2} s^{-1} , and 10^{-1} s^{-1} strain-rates. This corresponds to the large increase in strain to failures as these strain-rates approach their respective non-failure temperature. The slippage mechanism is the dominant mechanism at these temperature and strain-rates and the failure toughness is increased dramatically. The highest value was at 75 °C and 10^{-3} s^{-1} strain-rate where a failure toughness of approximately 0.325 GJ/m^3 .

The non-failure temperature for the 10^0 s^{-1} strain-rate at $148 \text{ }^\circ\text{C}$ does not show a large increase to the range between 0.2 GJ/m^3 and 0.35 GJ/m^3 of failure strength and its value at $148 \text{ }^\circ\text{C}$ drops sharply to a value of approximately 0.02 GJ/m^3 . This is an order of magnitude lower than the observed failure strength values at the non-failure temperatures in the lower strain-rates.

The 10^0 s^{-1} , 500 s^{-1} , and 10^3 s^{-1} strain-rates were observed to decrease monotonically with increasing temperature. The trend for the 10^3 s^{-1} strain-rate appears to be a linear decrease in toughness with increasing temperature. At these strain-rates, the strain to failure is not as affected and the dynamic strain-rates plateau at approximately 3 % strain to failure across all temperatures except $148 \text{ }^\circ\text{C}$. The only contributing parameter to the toughness is the decrease seen in the failure strength, discussed previously.

The comparison between the linear approximation and the actual failure toughness showed that the actual failure toughness had higher values at every temperature-strain-rate combination except the 500 s^{-1} strain-rate where the actual toughness was observed to have lower values at all temperature-strain-rate combinations. This decrease is caused by the stiffening mechanism which causes an inflection point in the stress-strain curve. The linear approximation overestimates the toughness at the 500 s^{-1} strain-rate.

4.6.2 Cunniff Parameters

Based on Equation 1-4 for the original Cunniff parameter, the value of the Cunniff parameter should vary with Young's modulus to the $1/6$ power and toughness to the $1/3$ power. The Young's modulus was found to decrease linearly with increasing temperature and the higher strain-rates showed a larger decrease in Young's modulus

with increasing temperature than the lower strain-rates. The strain-wave speed impact on the Cunniff parameter should therefore be a linear function raised to the 1/6 power that is more affected by increases in temperature at higher strain-rates. The power of 1/6 indicate that there would have to be a large change in Young's modulus for this strain-wave speed term to have an impact on the Cunniff parameter.

The toughness was observed to increase monotonically at the three lowest strain-rates and decrease monotonically at the three highest strain rates. The decrease was attributed to the decrease in failure strength since the strain to failure for the dynamic strain-rates was observed not to change with respect to increasing temperature up to 145 °C.

The linear approximation is observed to predict lower values of the Cunniff parameter than the actual toughness with the exception of the 500 s⁻¹ strain-rate. The best fits for the actual Cunniff parameter was found to be linear in two temperature regions of 20 °C to 115 °C and 115 °C to 145 °C for the 10⁰ s⁻¹ and 500 s⁻¹ strain-rates. For the 10³ s⁻¹ strain-rate, a single line was found to fit the data from 20 °C to 130 °C. The linear approximation was also best fitted using the same regions for the 10⁰ s⁻¹ and 500 s⁻¹ strain-rates but for the 10³ s⁻¹ strain-rate the best fit was a single line from 20 °C to 145 °C. This suggests that the linear approximation does not accurately predict the high temperature regions of the 10³ s⁻¹ strain-rate. This is an important consideration when predicting the ballistic response of the fibers where high temperatures and high strain-rates are expected.

4.6.3 Ballistic Estimates for the Thermal and Mechanical Energy Dissipation

The actual Cunniff parameter results can be used to determine the effective temperature of fiber during a ballistic impact. To do this, the older generation of UHMPE fibers used by Cunniff for his V_{50} tests need to be calibrated to the newer generation of SK76 fibers used in this study. To calibrate, the same form of parameters used by Cunniff will be applied to the data in this study for a comparable V_{50} that can then be found on the 10^3 s^{-1} strain-rate actual Cunniff plot which used compliance corrected Young's moduli and actual failure toughness. The quasi-static and room temperature parameters for the Spectra® 1000 fibers used by Cunniff had a strain to failure of 3.5 %, failure strength of 2.57 GPa, and a compliance uncorrected Young's modulus of 120 GPa. The calculated Cunniff parameter was 801 m/s and the V_{50} data was fit best with a Cunniff parameter of 672 m/s. This is a decrease of approximately 16% from the calculated value to the fitted value. The 20 °C and 10^{-3} s^{-1} strain-rate average values can be used from this study for comparable testing conditions for fiber parameters. The Sk76 fibers have a strain to failure of 3.35 %, failure strength of 3.37 GPa (but an actual toughness of .0732 GJ/m³), and an uncorrected Young's modulus of 120 GPa. The calculated Cunniff parameter using actual toughness and corrected Young's modulus is 860 m/s. Assuming the fibers would behave similarly in a ballistic response, the V_{50} data would be fit best by a reduction of 16% resulting in a Cunniff parameter of 721 m/s. Following the actual Cunniff parameter results for the 10^3 s^{-1} strain-rate, which is the strain-rate closest to a ballistic impact, the 721 m/s corresponds to a temperature of approximately 130 °C. The fibers are behaving on average as though their temperature was approximately 130 °C at 10^3 s^{-1} strain-rate. This is the first use of experimental data

to estimate the average temperature of UHMMPE fibers during a ballistic impact. This estimate assumes an average temperature and strain-rate for all of the fibers contributing to the response of the ballistic projectile. There is more likely a higher temperature and strain-rate observed at the point of impact and both temperature and strain-rate decrease as distance from this point is increased. This estimate also assumed that the same percentage in reduction for the calculated Cunniff parameter and fitted V_{50} data. Which may not be accurate for the newer generation of SK76 fibers.

For ballistic response, the kinetic energy of the projectile must be absorbed by the fibers. The kinetic energy of the projectile can be used to both heat and stress the fiber. The simultaneous distribution of the heat, and stress-strain-rates throughout the region of ballistic impact has not been definitively studied. However, limits for each type of kinetic energy dissipation can be calculated and used as boundaries for the solution. Fibers with an average diameter of $18.5 \mu\text{m}$ and 10 mm in length can be used as the fiber unit element for mechanical and thermal dissipation. If all of the kinetic energy is dissipated through the mechanical failure of fibers with no heating, then the failure toughness of $.0725 \text{ GJ/m}^3$ at $20 \text{ }^\circ\text{C}$ and 10^3 s^{-1} strain-rate can be used to calculate the number of fibers required to stop the projectile using only mechanical means. Similarly, the specific heat of 1850 J/kg-K , total heat of fusion of approximately 250 kJ/kg (Smook) and a density of 980 kg/m^3 can be used to calculate how many fibers would have to be heated and melted from $20 \text{ }^\circ\text{C}$ to $150 \text{ }^\circ\text{C}$. A 9mm 115 grain (7.45 g) round with a muzzle velocity of 1150 fps (350.52 m/s) has a kinetic energy of 458 J will be used as the projectile in this calculation. 2.35×10^6 fibers are required to stop the projectile by purely mechanical means and 1.80×10^5 fibers to stop the projectile through purely thermal means.

Assuming a linear mass density of 1760 dtex, a yarn contains approximately 668 fibers and 3517 yarns are required to stop the projectile by physical failure and 530 to stop it by melting. These are over estimates due to the projectile losing velocity as it travels farther from the muzzle and that the fibers are the only material affecting the kinetic energy of the projectile, and the projectile must be brought to a complete halt for successful protection. However, this does demonstrate why ballistic vests are comprised of multiple layers of ballistic resistant material instead of just one.

Parameters can be used from the estimate of the fibers behaving as though they were at 130 °C and 10^3 s^{-1} strain-rate to determine if the number of fibers exists within these limitations. At these conditions, the failure toughness is 0.0505 GJ/m^3 . Using this value and assuming a heating from 20 °C to 130 °C with no phase transitions, each 10 mm fiber dissipated $6.72 \times 10^{-4} \text{ J}$ through both heating and mechanical failure. 6.82×10^5 fibers are required to completely stop the 9mm projectile or 1020 yarns. This is within the limitations set in the calculations above and it is estimated that approximately 80% of the energy dissipated is from heating the fiber and 20% is from the mechanical failure. Again, this estimate assumes an average temperature and strain-rate for all of the fibers contributing to the response of the ballistic projectile and it is more likely a distribution of temperatures and strain-rates is present that decrease in temperature and strain-rate as distance from the point of impact is increased.

4.7 Chapter Summary

In this chapter the potential chain mechanisms responsible for the fiber mechanical properties were discussed and the likelihood at different temperatures and strain-rates. The three major mechanisms discussed were chain scission, chain slippage,

and chain straightening. A fourth mechanism of CH₂ rotations is discussed at high temperatures and its effects on chain slippage.

The ΔE for the chain scission are estimated at 260 kJ/mol to 400 kJ/mol (Schnabel). The presence of scission products was found to be absent in the manufacturer as-received yarns and a small increase in oxidation products was observed at failure surfaces using micro-FTIR techniques. These results suggest that the scission mechanism occurs in at low frequencies primarily near the failure surface just before failure.

From this study the chain slippage ΔE was estimated at 112 kJ/mol, and was responsible for the temperature changes in stress-strain curves observed at the plateauing, necking, and non-failure transition temperatures for the quasi-static and intermediate strain-rates. The 10^0 s^{-1} strain-rate was observed to have a decreased change in strain to failure at the key temperature regions and was suggested to be close to the strain-rate limit where the slippage mechanism is no longer dominant. At the dynamic strain-rates, there were no changes in stress-strain curve shapes and strain to failure values were approximately 3 % for the temperature range of 20 °C to 145 °C.

At 148 °C, a phase transition from extended orthorhombic to hexagonal was observed and dramatic decreases in the failure strengths were observed for the dynamic strain-rates. The hexagonal phase changes the fiber system and new mechanisms regarding the trans to gauche rotations were proposed to explain the changes in mechanical properties.

The fibers were observed to stiffen at the necking and non-failure temperatures for the quasi-static and intermediate strain-rates and at all temperatures for the dynamic strain-rates. The stiffening was proposed to be caused by the conformational

straightening of tie molecules in the amorphous regions of the fiber. The stiffening reaches a maximum at approximately 0.5 % strain where the straightening of chains creates the maximum number of C-C bonds in the cross sectional area of the fiber. Assuming the straightening is symmetric about this maximum, it exists between strains of 0 % to 1 % and is dominant from 0 % to 0.5%. At low strain-rates and temperatures stiffening region of the stress-strain curve was not observed. The slippage and scission mechanisms are competing with the straightening mechanism and at these low strain-rates, the slippage mechanism has limited thermal energy to occur at a high rate. This allows the slippage mechanism to shield the observation of the straightening mechanism due to the slippage mechanism dominating the stress-strain behavior and dissipating the stress. Due to the competing effects of thermal expansion and thermal shrinkage in the straightening mechanism, there is not an estimation of the ΔE but it is expected to be lower than 112 kJ/mol before the tie chains are fully extended and then above 112 kJ/mol after the maximum in stiffness at 0.5%.

The change in dominant mechanism was proposed as:

- Chain slippage is dominant for the majority of conditions in this study except where scission and straightening are the dominant mechanism
 - At high temperatures for constrained fibers in the hexagonal phase, chain slippage occurs more frequently due to the trans to gauche conformation
- Chain scission is only dominant moments before fiber failure ($\epsilon \approx \epsilon_f$) and near the failure surface
- Chain straightening is only dominant at small strains (0 % to 0.5 %) and only temperatures greater than or equal to the strain-rate dependent necking temperatures for the quasi-static and intermediate strain-rates and at all temperatures for the dynamic strain-rates

5 Conclusions and Future Work

5.1 Contributions to Science

5.1.1 Elucidation of the Change in Dominant Mechanism that Determine the Mechanical Properties of Highly Oriented UHMMPE Fibers

A change in dominant mechanism was observed at different temperatures, strain-rates, and strain values. The potential mechanisms responsible for the observed changes in mechanical behavior are proposed for highly oriented UHMMPE Fibers. The main mechanisms proposed include chain scission, enthalpic chain slippage, and entropic chain straightening. Presented below is each mechanism, the proposed regions where it is dominant, and the experimental observation and deduction that led to each conclusion.

5.1.1.1 Chain slippage is the predominant at all temperatures, strain-rates, and strain values in this study except in the limited regions where scission and straightening are the dominant mechanism

A change in stress-strain curve shape was observed in quasi-static and intermediate strain-rates (10^{-3} s^{-1} to 10^0 s^{-1}). The shapes progressed from pseudo-brittle, to plateauing, to necking, and to non-failure with increasing temperature. The transition temperatures were observed to be strain-rate dependent and for similar mechanical behavior, a temperature-strain-rate equivalence was estimated between an increase in one decade of strain-rate and a decrease of approximately 20 °C. This estimate was investigated by creep-compliance plots of the stress-strain curve shape transition inverse temperature and natural log of strain-rate. The plots indicated similar ΔE of approximately 112 kJ/mol for each of the transitions, suggesting they are all dominated by the same mechanism. Since the mechanism allows for strains up to 25 % without failure at high temperatures and low strain-rates, the most probably mechanism is chain

slippage. The 10^0 s^{-1} strain-rate was observed to have a decreased change in strain to failure at the key temperature regions and was suggested to be close to the strain-rate limit where the slippage mechanism is no longer dominant. At the dynamic strain-rates, there were no changes in stress-strain curve shapes and strain to failure values were approximately 3 % for the temperature range of 20 °C to 145 °C, suggesting that the slippage mechanism is severely hindered by the short time scales for slippage events.

SEM imaging showed a decrease in the average diameter of the fiber near the failure surface compared to the average diameter before tensile testing for all temperature and strain-rates. This indicates there is strain localization near the failure surface. This study investigated the possibility of the minimum fiber diameter as the cause for the strain localization through the use of the minimum fiber diameter in the stress calculations. These calculations were compared to the common practice of using the average of at least five points along the gage length of the fiber. The results suggested that very similar trends are observed for the changes of failure strength and UTS with respect to temperature and strain-rate. Slightly larger standard deviations were observed for the minimum diameter method than the average diameter method. This suggests that the average diameter method provides more repeatable results with less variance and that the minimum diameter of the fiber is not the critical parameter for dictating failure mechanics. Whether there is correlation between the location minimum diameter region and the location of the failure surface was not determined and further investigation is needed.

5.1.1.2 Chain scission is dominant moments before fiber failure ($\epsilon \approx \epsilon_f$) at the failure surface

Chemical comparisons between the as-received yarns and the failure surfaces show a slight increase in oxidation products suggesting chain scission is present at low frequencies near the failure surfaces occurring primarily in the moments before failure. The ΔE for the chain scission are estimated from literature between 260 kJ/mol to 400 kJ/mol [41].

5.1.1.3 Chain straightening is dominant at small strains (0 % to 0.5 %) when the temperature greater than or equal to the strain-rate dependent necking temperatures for the quasi-static and intermediate strain-rates and at all temperatures for the dynamic strain-rates

Stiffening of the fiber was observed to occur at the necking and non-failure temperatures for the quasi-static and intermediate strain-rates and at all temperatures for the dynamic strain-rates. The stiffening is proposed to be caused by the conformational straightening of tie molecules in the amorphous regions of the fiber. The stiffening reaches a maximum at approximately 0.5 % strain where the straightening of chains creates the maximum number of C-C bonds in the cross sectional area of the fiber. Assuming the straightening is symmetric about this maximum, it exists between strains of 0 % to 1 % and is dominant from 0 % to 0.5%. Above .0.5 % strain, the slippage mechanism becomes dominant and the fibers become less stiff.

At low strain-rates and temperatures stiffening region of the stress-strain curve was not observed. The slippage and scission mechanisms are competing with the straightening mechanism and at these low strain-rates, the slippage mechanism has limited thermal energy to occur at a high rate. This allows the slippage mechanism to shield the observation of the straightening mechanism due to the slippage mechanism

dominating the stress-strain behavior and dissipating the stress. Due to the competing effects of thermal expansion and thermal shrinkage in the straightening mechanism, there is not an estimation of the ΔE but it is expected to be lower than 112 kJ/mol before the tie chains are fully extended and then above 112 kJ/mol after the maximum in stiffness at 0.5%.

5.1.1.4 A newly discovered gauche slippage mechanism is dominant in the hexagonal phase

The effects of strain-rate on the change in mechanical properties of the hexagonal phase were investigated for the first time in this study. Physical characterization of the fibers showed a highly oriented fiber system with few degrees of freedom at room temperature. A phase transition from the extended orthorhombic to hexagonal just below the melting temperature. This phase transition is a different morphological system than at lower temperatures. The free volume of the hexagonal phase is larger than the extended orthorhombic and CH_2 trans to gauche conformation changes become much more likely, to the point where 1/5 CH_2 bonds is in the gauche conformation. With the increase in free volume and the increase in the gauche conformational degree of freedom, a new mechanism to allow chain slippage becomes available. This gauche slippage mechanism occurs more frequently than the previously presented extended orthorhombic slippage mechanism.

Large decreases in the failure strengths were observed for the dynamic strain-rates between 145 °C to 148 °C. The 10^3 s^{-1} strain-rate also shows a linear stress-strain curve to failure at this temperature with an increase in the average strain to failure to approximately 5.5 %. The crystalline regions of the fiber are in the hexagonal phase at this temperature and the increase in free volume allows more frequent trans to gauche

rotations. The increased frequency of gauche slippage relieves stress in the system and is the proposed explanation for the sudden changes in mechanical properties at this temperature. Additionally, the 10^3 s^{-1} strain-rate is proposed to be close to the limit of strain-rate hindering the ability of the trans to gauche rotations from alleviating stress in the system. The gauche-gauche interactions increase the effective friction between adjacent chains that the high strain-rate does not allow the time required for the chains to rotate between trans and gauche to slip past one another. The hindrance of slippage from the gauche-gauche interactions are proposed to cause the linear stress-strain relationship that is observed at this temperature and strain-rate.

Additionally, the strain to UTS was observed to exhibit new mechanisms showing a large increase in the strain to UTS at the 10^{-1} s^{-1} and 10^3 s^{-1} strain-rates. The time-limitations of the gauche-gauche interactions possibly explain the sudden decrease in failure strength and the increase in strain to UTS for the 10^3 s^{-1} strain-rate. However, this mechanism does not explain the increase in strain to UTS observed at the 10^{-1} s^{-1} strain-rate and further investigation is needed.

In summary, the above mechanisms elucidated the following behavior observed in highly oriented UHMMPE fibers:

- Oxidation products at the failure surface (Scission)
- Changes in stress-strain curve shape as temperature increases for the quasi-static and intermediate strain-rates (Slippage)
- Regions of strain localization near the failure surface at all temperatures and strain-rates where failure occurs (Slippage)
- Stiffening of the fiber at approximately 0.5 % strain at the necking and non-failure temperatures for the quasi-static and intermediate strain-rates (Straightening)
- Stiffening of the fiber at approximately 0.5 % at all temperatures for the dynamic strain-rates (Straightening)
- Sudden decrease in failure strength at 148 °C in the dynamic strain-rates (Gauche Slippage)
- Linear stress-strain relationship at 148 °C and 10^3 s^{-1} strain-rate (Gauche Slippage)

5.1.2 Improved the Prediction of the Ballistic Response of UHMMPE Fibers

The tensile testing of the fibers in this study was conducted across a large range of temperatures and strain-rates. This provides experimentally determined mechanical properties across a large spectrum of temperatures and strain-rates that fibers are likely to experience during a ballistic impact. At the point of impact, the temperature and strain-rate is expected to be the highest. As distance from the point of impact is increased, the temperature and strain-rate are expected to decrease.

Failure toughness was confirmed to more accurately describe the energy required for mechanical failure of a viscoelastic fiber than the linear approximation of strain to failure and failure stress. Combined with the work conducted by Cunniff, this study estimated that during a ballistic impact the fibers behave on average as though they are at a 10^3 s^{-1} strain-rate at 130 °C.

Additionally, the mechanical properties from this study can be used to improve computational studies such as molecular dynamic simulations. More accurate force fields can be developed through fitting to the experimental mechanical properties from this study and will ultimately improve the modeled behavior of UHMMPE molecules.

5.1.3 Proposed a New Method for Calculating Average Fiber Strength

Diameter measurements were conducted at five locations on 437 Dyneema® SK76 single fibers providing a diameter distribution with a population of 2185 measurements. This is the first presentation of a single fiber distribution for ballistic UHMMPE fibers. The distribution was shown to be approximated by a Gaussian distribution with an average fiber diameter of 18.49 μm and a standard deviation of 1.15

μm . Outliers were removed from the distribution and have diameters smaller than 15 μm and larger than 23 μm corresponding to separated fibers or double fibers, respectively.

A negative correlation was observed to exist between average fiber diameter and failure strength. Linear fits between average fiber diameter and failure strength failure were calculated for all six strain-rates in this study at 20 °C. The slopes were observed to decrease (become more negative) with increasing strain-rate suggesting large diameter fibers exhibit more of a decrease in failure strength at high strain-rates than they do at low strain-rates.

The linear fits for the diameter-strength relationship were combined with the Gaussian fiber diameter distribution to calculate average fiber strength distributions at each strain-rate. The resulting average fiber strength was found to agree well with the experimental failure strength averages. The results suggest a method for modeling individual fiber strengths through a Gaussian distribution for a specific temperature and strain-rate. This could provide a valuable simplification of calculations to represent a fiber population for computational studies of higher echelon materials, such as UHMPE yarns, textiles, or fiber reinforces composites.

5.2 Future Work

5.2.1 Dynamic Strain-Rates

Throughout this study, larger standard deviations were observed for tensile tests conducted at the dynamic strain-rates using a fiber Split Hopkinson Tension Bar. Improvements in the experimental setup will provide more accurate and repeatable results. I have designed and built a new fiber Split Hopkinson Tension Bar for these

reasons and to also overcome issues of instrument availability. The new f-SHTB has been designed to have improved displacement measurement capabilities through an improved optical measurement system. Additionally, design of the thermal standoff is being conducted to minimize the strain-wave reflections in the system. Alternatively, the possibility of creating actively cooled grips are being explored that would eliminate the need for a thermal standoff.

Using this system and a synchrotron facility, the effect of strain and strain-rate on the formation of the hexagonal phase can be investigated in situ as well as the changes in fiber morphology of the amorphous phase as a function of average fiber diameter. Including high speed cameras and optics may also allow the capture of true stress-strain relationships and correlation of location of the strain localization to fiber diameter and local morphology.

5.2.2 Quasi-Static and Intermediate Strain-Rates

Additional tensile tests can be conducted at the 10^0 s^{-1} strain-rate with recorded force data to understand if the grip interface failures observed had lower than average failure strengths and to get a large population to calculate the success rate of fiber failures in the gage length. Also, the mechanism responsible for the increase in strain to UTS observed in the hexagonal phase at the 10^{-1} s^{-1} strain-rate will also be investigated.

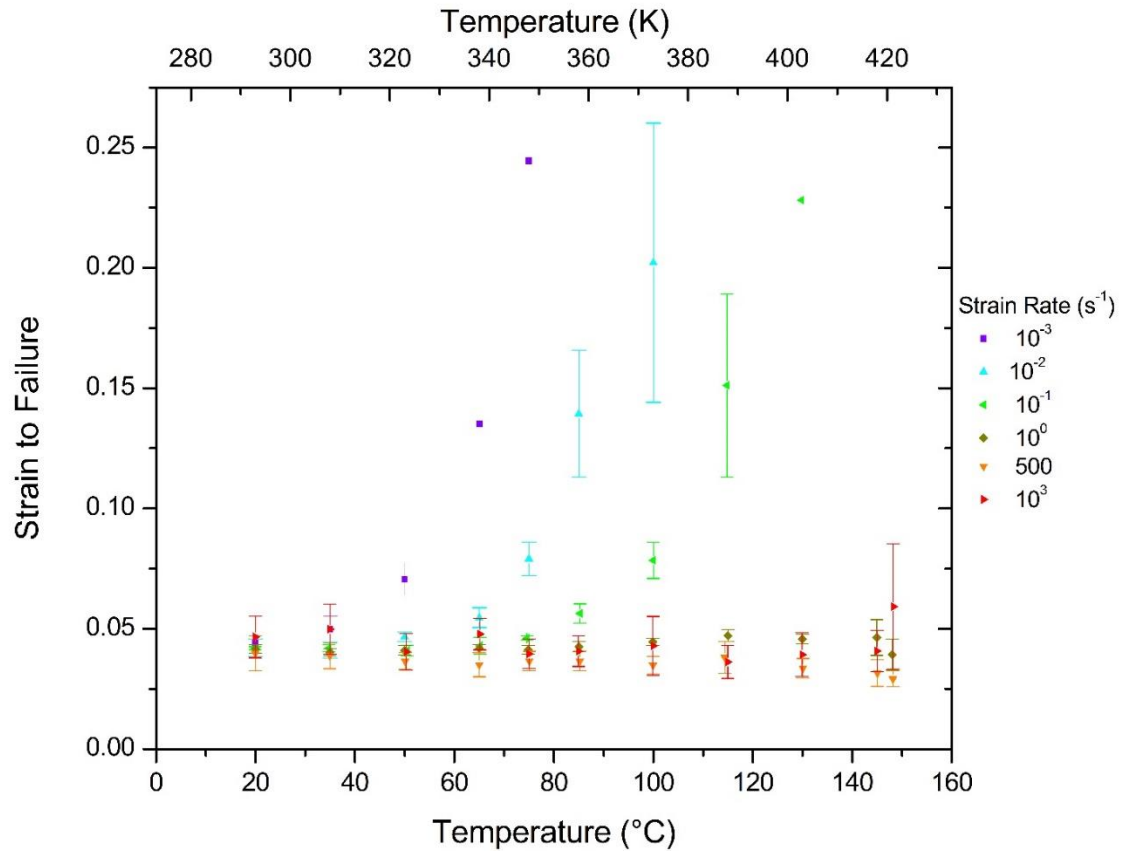
5.2.3 Structure-Property Relationships from Additional UHMMPE Fiber Systems

Different UHMMPE fibers can be investigated to determine the effects of fiber morphology on the changes in the mechanical properties. In particular, DSM has a new fiber that has failure strength close to 7 GPa to 8 GPa. Characterizing these new fibers

and conducting a similar temperature-strain-rate study will elucidate the effect of the morphology and phase composition on the mechanisms discussed in this study.

Appendices

A-1 Average Uncorrected Strain to Failure Plots



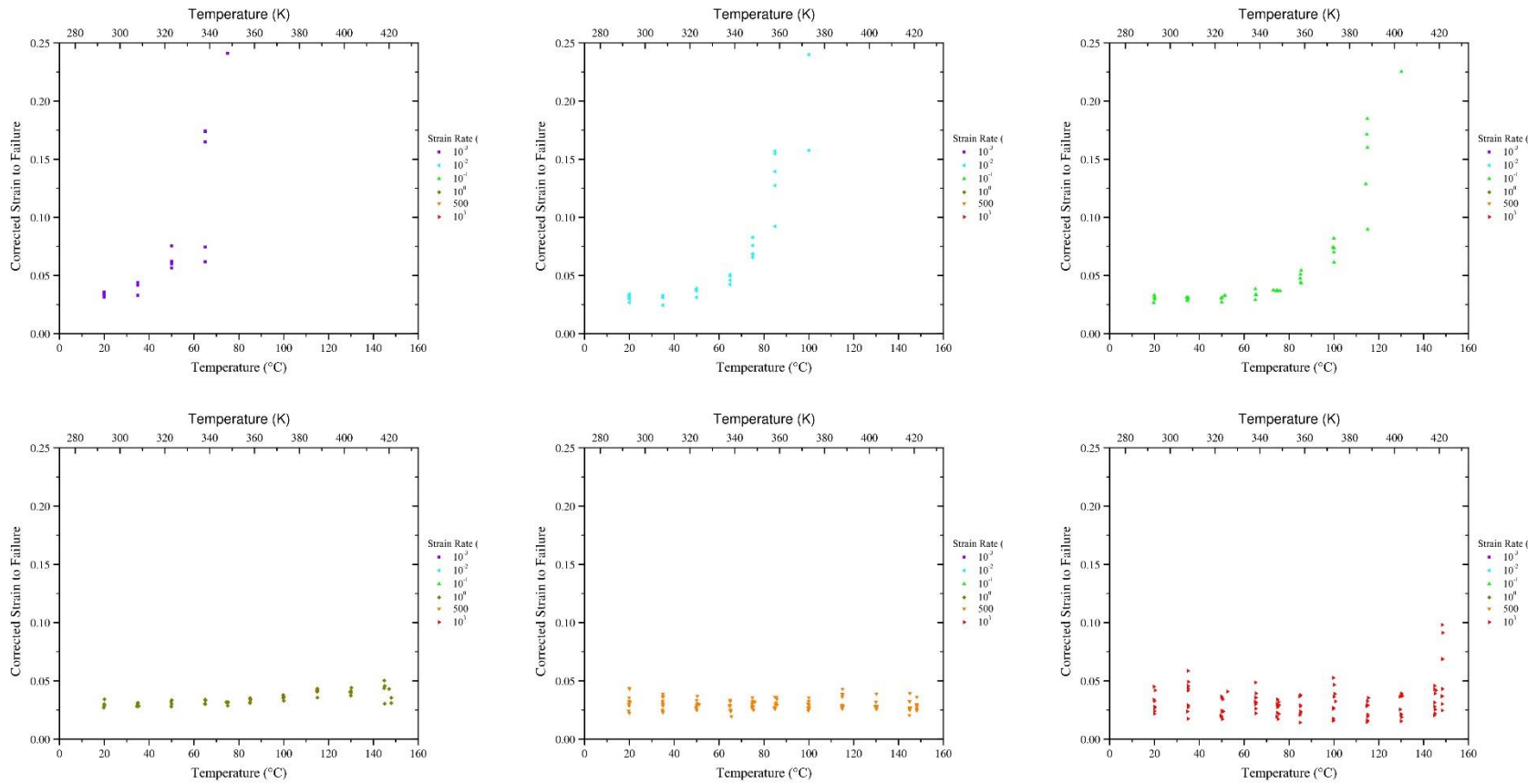
A-1: Plot of the average values of uncorrected strain to failure. The 10^{-3} s^{-1} , 10^{-2} s^{-1} , 10^{-1} s^{-1} , 10^0 s^{-1} , 500 s^{-1} , and 10^3 s^{-1} strain-rates are depicted in violet, blue, green, dark yellow, orange, and red, respectively. The averages are plotted with bars depicting \pm one standard deviation.

A-2 Average Uncorrected Strain to Failure Values

Strain-rate [s ⁻¹]	Temperature [°C]										
	20	35	50	65	75	85	100	115	130	145	148
10 ⁻³	4.43±.18	4.98±.55	7.07±.68	13.51±5.65	24.45±-	-	-	-	-	-	-
10 ⁻²	4.21±.36	4.10±.33	4.67±.20	5.46±.41	7.90±.70	13.93±2.64	20.21±5.80	-	-	-	-
10 ⁻¹	4.20±.06	4.19±.14	4.10±.22	4.29±.36	4.61±.08	5.64±.40	7.84±.75	15.11±3.81	22.82±-	-	-
10 ⁰	4.16±.18	4.02±.15	4.11±.19	4.18±.16	4.12±.18	4.26±.22	4.45±.15	4.71±.25	4.57±.21	4.64±.75	3.92±.65
550	3.98±.71	3.87±.54	3.65±.36	3.50±.50	3.66±.40	3.66±.40	3.48±.37	3.81±.66	3.36±.40	3.16±.56	2.92±.34
10 ³	4.66±.87	4.98±1.0 3	4.04±.77	4.77±.65	3.96±.61	4.06±.63	4.29±1.22	3.67±.68	3.93±.91	4.08±.86	5.92±2.6 0

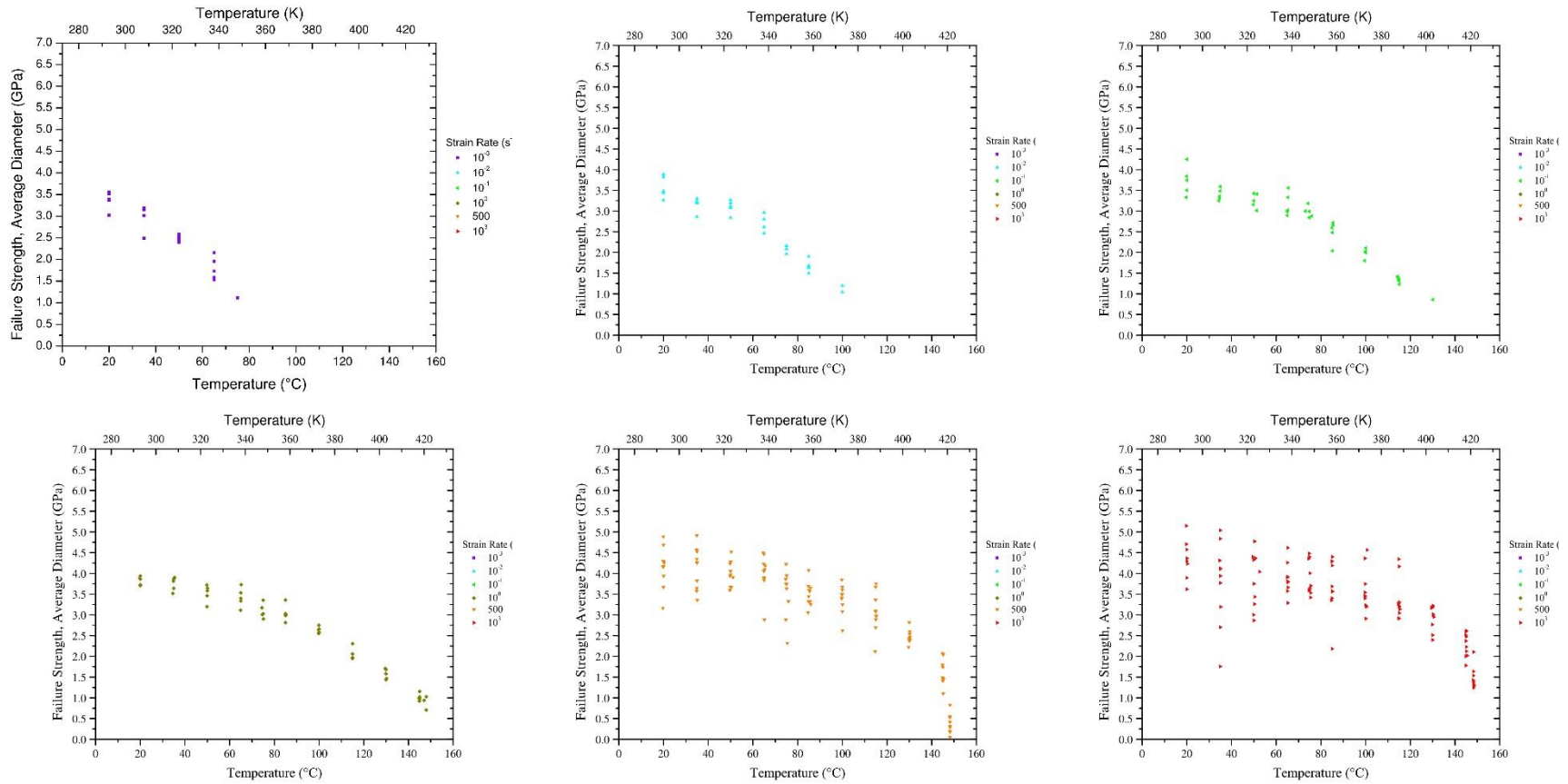
A-2: Average uncorrected strain to failure values.

A-3 Individual Corrected Strain to Failure Plots

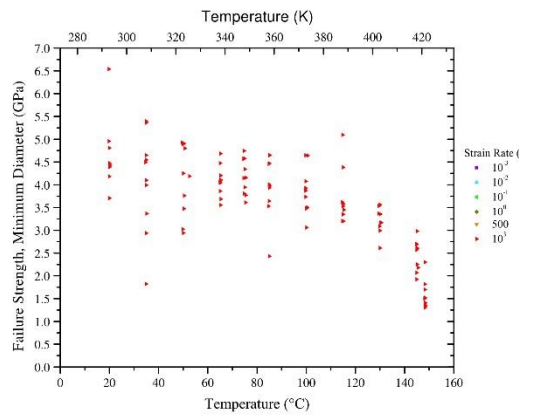
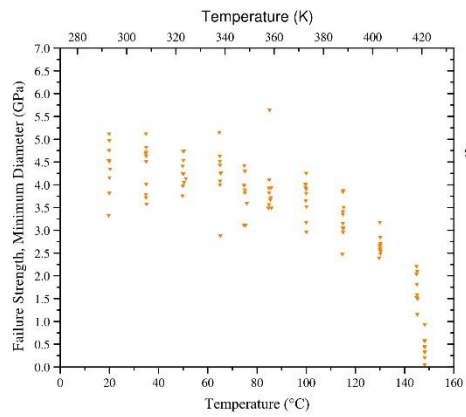
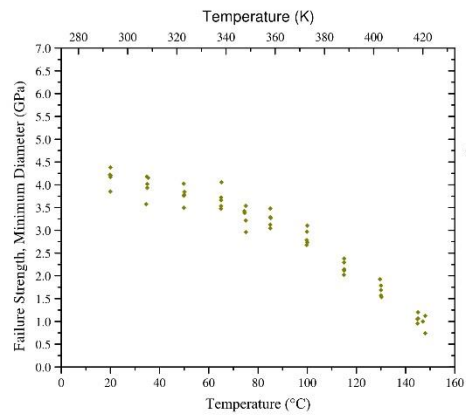
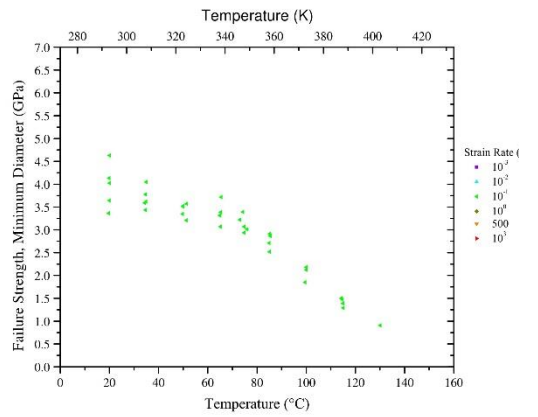
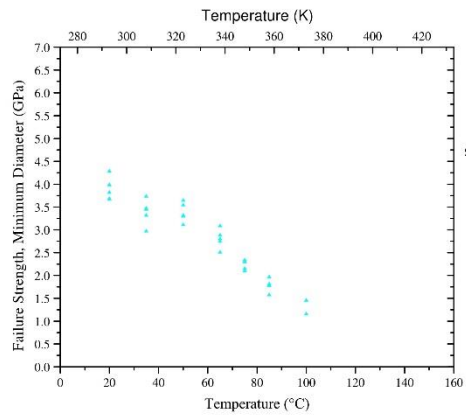
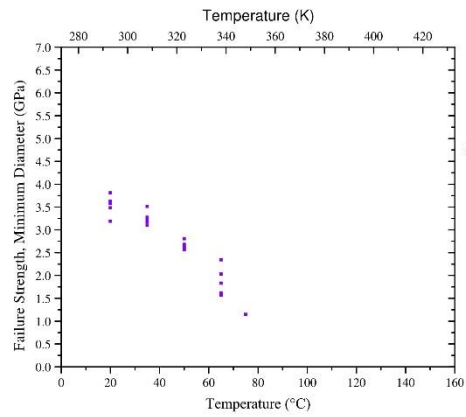


A-3: Plots of individual values of corrected strain to failure. The 10^{-3} s^{-1} , 10^{-2} s^{-1} , 10^{-1} s^{-1} , 10^0 s^{-1} , 500 s^{-1} , and 10^3 s^{-1} strain-rates are depicted in violet, blue, green, dark yellow, orange, and red, respectively.

A-4 Individual Failure Strength Plots

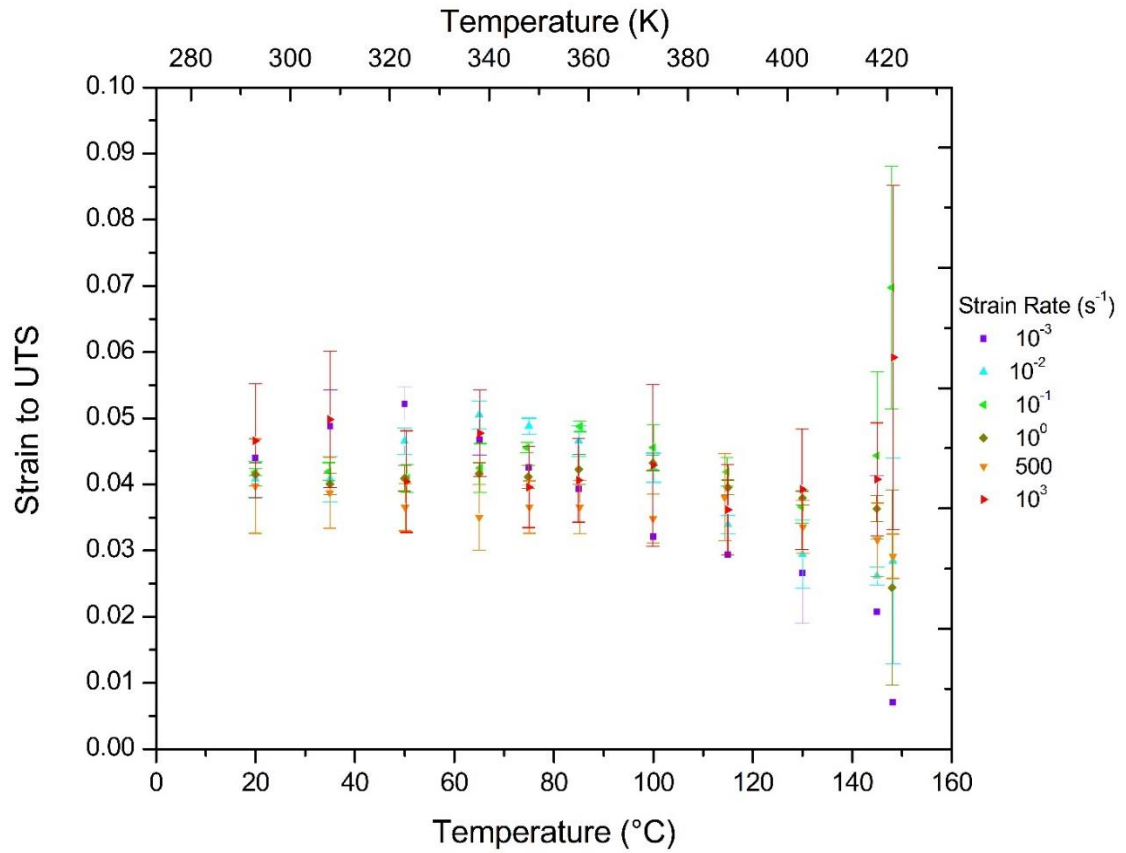


A-4: Plots of individual values of failure strength calculated with the average diameter method. The 10^{-3} s^{-1} , 10^{-2} s^{-1} , 10^{-1} s^{-1} , 10^0 s^{-1} , 500 s^{-1} , and 10^3 s^{-1} strain-rates are depicted in violet, blue, green, dark yellow, orange, and red, respectively.



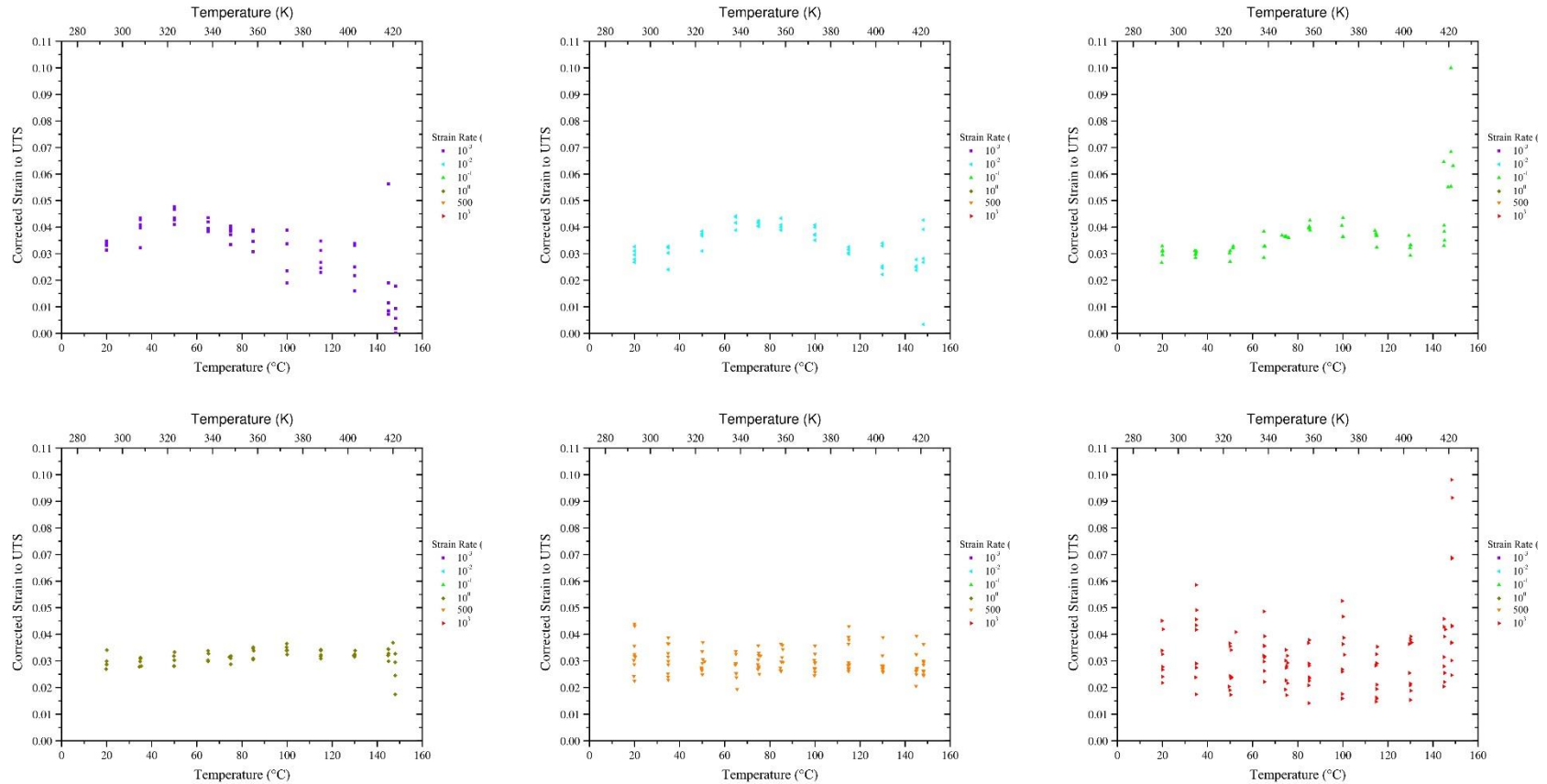
A-4 continued: Plots of individual values of failure strength calculated with the minimum diameter method. The 10^{-3} s^{-1} , 10^{-2} s^{-1} , 10^{-1} s^{-1} , 10^0 s^{-1} , 500 s^{-1} , and 10^3 s^{-1} strain-rates are depicted in violet, blue, green, dark yellow, orange, and red, respectively.

A-5 Average Uncorrected Strain to UTS Plots



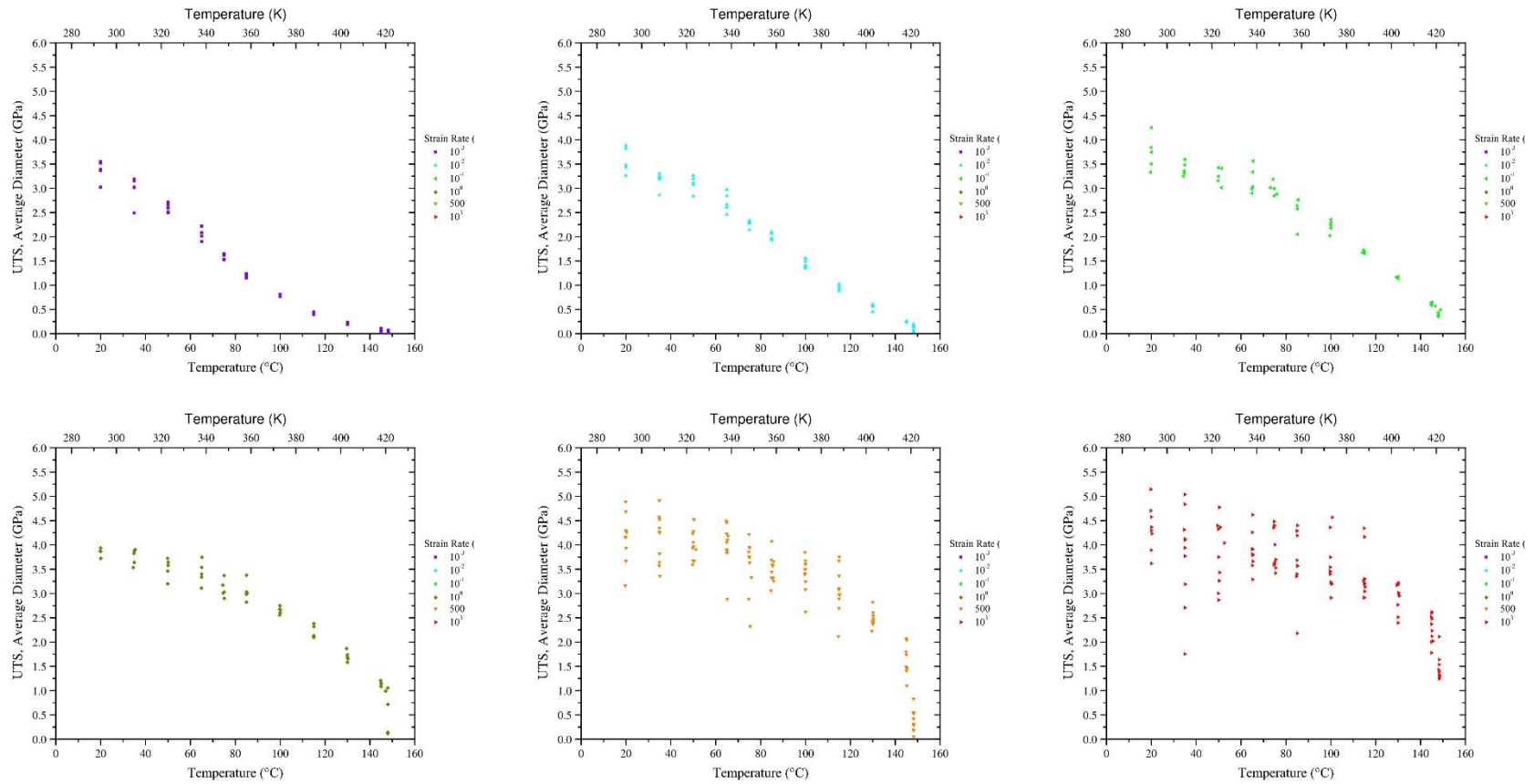
A:5: Plots of average values of strain to UTS. The 10^{-3} s $^{-1}$, 10^{-2} s $^{-1}$, 10^{-1} s $^{-1}$, 10^0 s $^{-1}$, 500 s $^{-1}$, and 10^3 s $^{-1}$ strain-rates are depicted in violet, blue, green, dark yellow, orange, and red, respectively. The averages are plotted with bars depicting \pm one standard deviation.

A-6 Individual Corrected Strain to UTS Plots

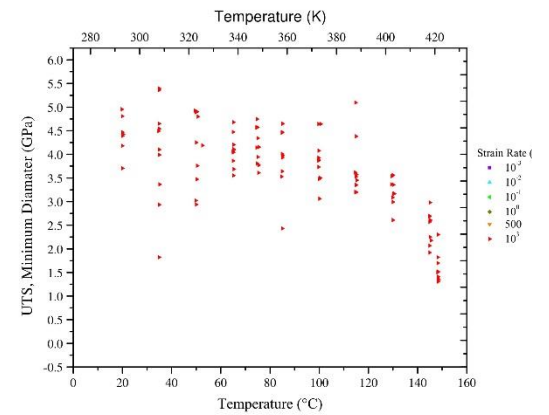
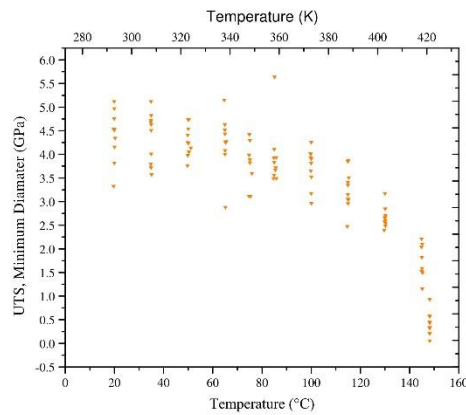
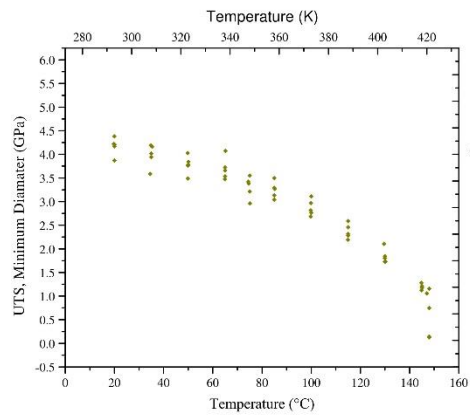
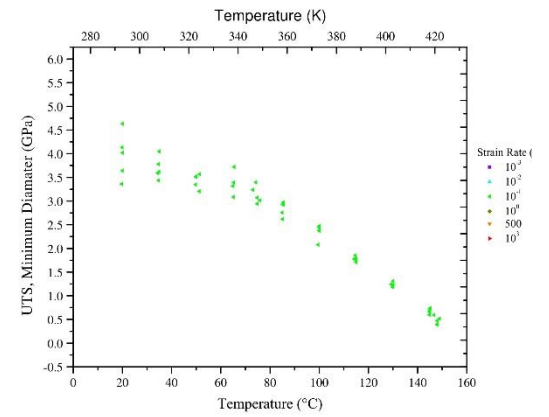
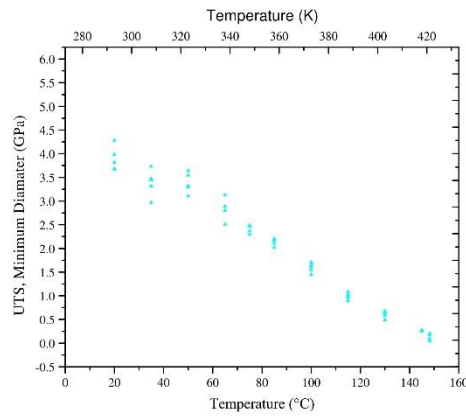
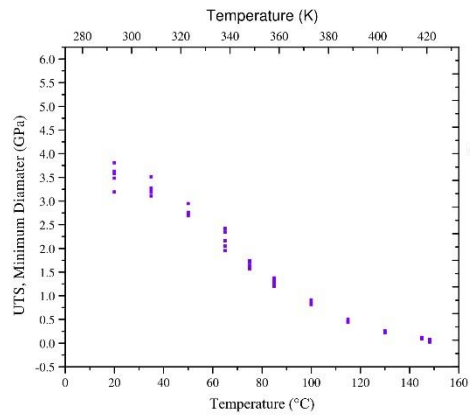


A-6: Plots of individual values of corrected strain to UTS. The 10^{-3} s⁻¹, 10^{-2} s⁻¹, 10^{-1} s⁻¹, 10^0 s⁻¹, 500 s⁻¹, and 10^3 s⁻¹ strain-rates are depicted in violet, blue, green, dark yellow, orange, and red, respectively.

A-7 Individual UTS Plots

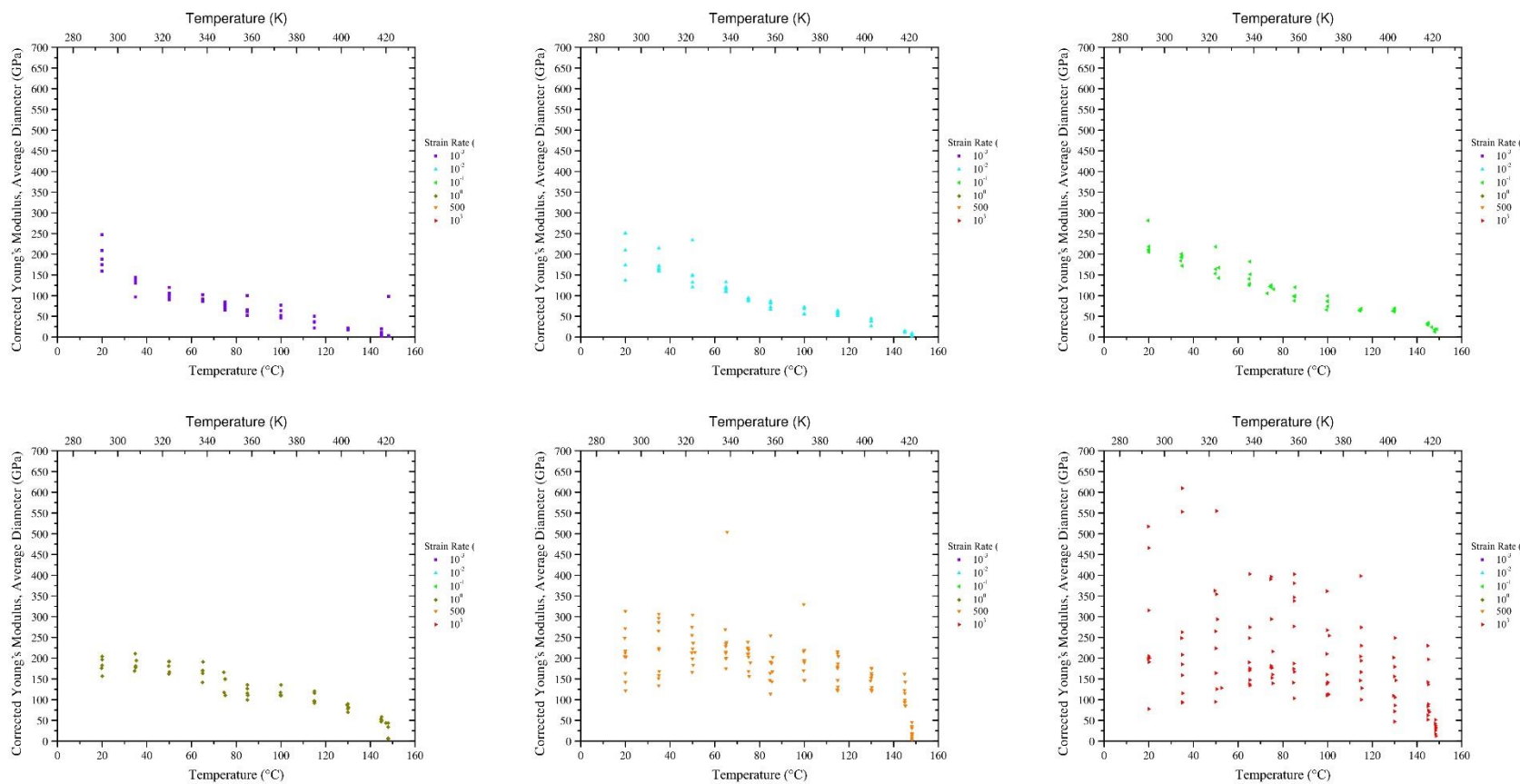


A-7: Plots of individual values of UTS using the average diameter method. The 10^{-3} s^{-1} , 10^{-2} s^{-1} , 10^{-1} s^{-1} , 10^0 s^{-1} , 500 s^{-1} , and 10^3 s^{-1} strain-rates are depicted in violet, blue, green, dark yellow, orange, and red, respectively.



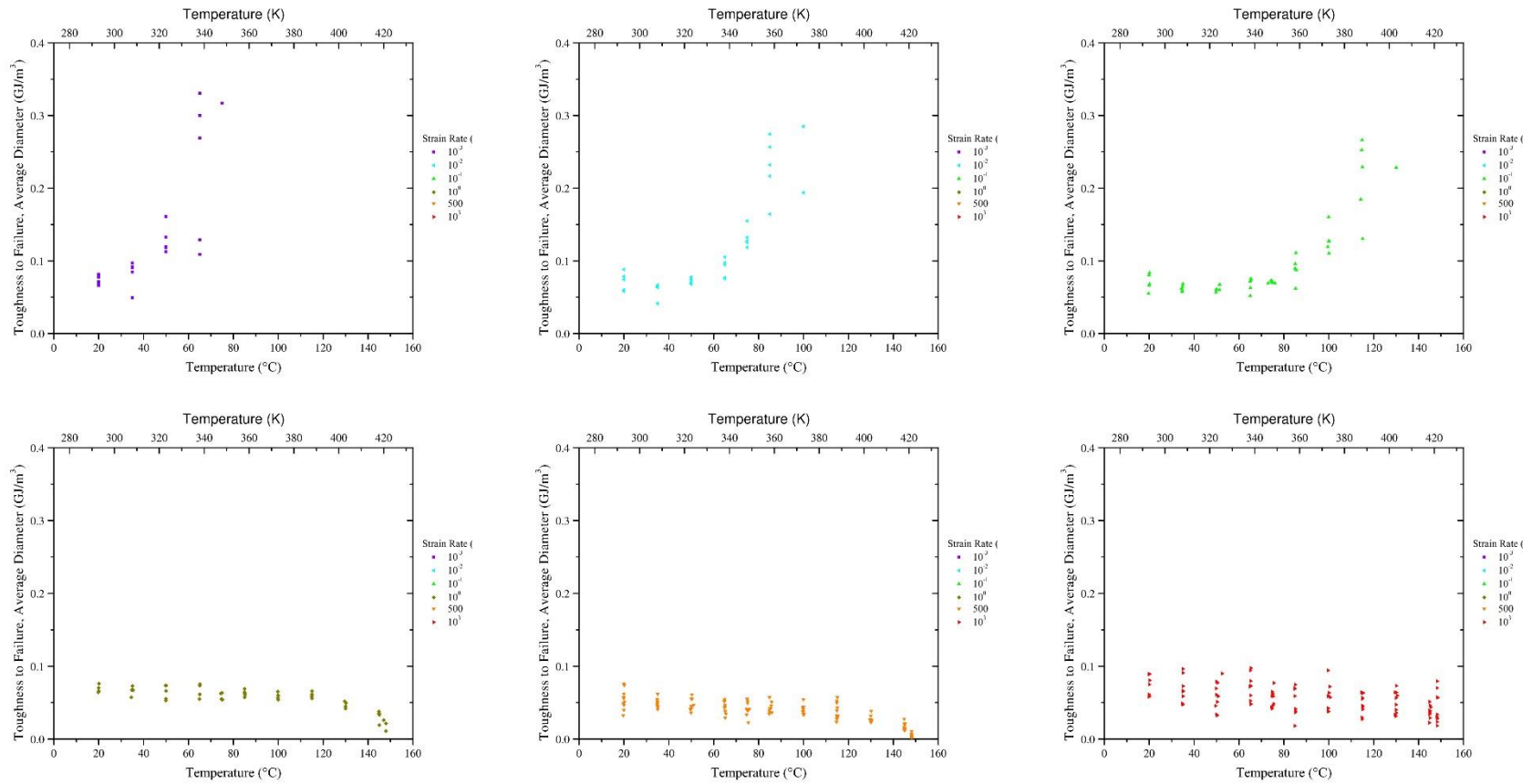
A-7 continued: Plots of individual values of UTS using the minimum diameter method. The 10^{-3} s^{-1} , 10^{-2} s^{-1} , 10^{-1} s^{-1} , 10^0 s^{-1} , 500 s^{-1} , and 10^3 s^{-1} strain-rates are depicted in violet, blue, green, dark yellow, orange, and red, respectively.

A-8 Individual Young's Modulus Plots



A-8: Plots of individual values of Young's modulus. The 10^{-3} s^{-1} , 10^{-2} s^{-1} , 10^{-1} s^{-1} , 10^0 s^{-1} , 500 s^{-1} , and 10^3 s^{-1} strain-rates are depicted in violet, blue, green, dark yellow, orange, and red, respectively.

A-9 Individual Failure Toughness Plots



A-9: Plots of individual values of failure toughness. The 10^{-3} s^{-1} , 10^{-2} s^{-1} , 10^{-1} s^{-1} , 10^0 s^{-1} , 500 s^{-1} , and 10^3 s^{-1} strain-rates are depicted in violet, blue, green, dark yellow, orange, and red, respectively.

Bibliography

- [1] MIL-STD662F. V₅₀ Ballistic Test for Armor. DoD Test Method Standard. 1997.
- [2] Mauchant, D., Rice, K. D., Riley, M. A., Leber, D., Samarov, D., & Forster, A. L. (n.d.). Analysis of Three Different Regression Models to Estimate the Ballistic Performance of New and Environmentally Conditioned Body Armor. Internal NIST report.
- [3] Cunniff, P. M. (15-19 November, 1999). Dimensionless Parameters for Optimization of Textile-Based Body Armor Systems. Unpublished paper presented at the 18th International Symposium on Ballistics, San Antonio, TX.
- [4] Phoenix, S. L., Porwal, P. K., (2003). A new membrane model for the ballistic impact response and V₅₀ performance of multi-ply fibrous systems. *International Journal of Solids and Structures*, 40, 6723-6765.
- [5] Kevlar Technical Guide. DuPont, n.d. Web. 15 June 2013.
- [6] Dyneema Comprehensive Fact Sheet; CIS YA100; DSM Dyneema LLC: Stanley, NC, January 2008. <http://issuu.com/eurofibers/docs/name8f0d44> (accessed 10 February 2016).
- [7] Kavesh, S., Prevorsek, D. C., (1995). Ultra high strength, high modulus polyethylene spectra fibers and composites. *International Journal of Polymeric Materials and Polymeric Biomaterials*, Vol. 30 Iss. 1-2, pp. 15-56.
- [8] Schaper, A., Zenke, D., Schulz, E., Hirte, R., Taege, M., (1989). Structure-property relationships of high-performance polyethylene fibres. *Phys Stat Sol A e Appl Res* 1989;116(1):179e95.
- [9] Grubb D, Keller A. Thermal contraction and extension in fibrous crystals of polyethylene. *Colloid Polym Sci* 1978;256:218e33.
- [10] Grubb DT, Li ZF. Molecular stress distribution and creep of high modulus polyethylene fibres. *Polymer* 1992;33(12):2587e97.
- [11] Litvinov, V. M., Xu, J., Melian, C., Demco, D. E., Möller, M., & Simmelink, J. (2011). Morphology, Chain Dynamics, and Domain Sizes in Highly Drawn Gel-Spun Ultrahigh Molecular Weight Polyethylene Fibers at the Final Stages of Drawing by

- SAXS, WAXS, and ^1H Solid-State NMR. *Macromolecules*, 44(23), 9254–9266.
doi:10.1021/ma201888f
- [12] Hu W-G, Schmidt-Rohr, K., (2000). Characterization of ultradrawn polyethylene fibers by NMR: crystallinity, domain sizes and a highly mobile second amorphous phase. *Polymer*, Vol. 41, Iss 8, pp 2979-2987.
- [13] Magonov SN, Sheiko SS, Deblieck R, Moller M. Atomic force microscopy of gel-drawn molecular weight polyethylene. *Macromolecules* 1993;26:1380e6.
- [14] Karacan, I. (2005). Structure-property Relationships in High-strength High-modulus Polyethylene Fibres. *Fibres & Textiles in Eastern Europe*, Vol 13 No. 4 (52).
- [15] Rubenstein, Michael. "Polymer Physics." Michael Rubinstein; Ralph H. Colby - Oxford University Press. N.p., 18 Feb. 2017. Web. 25 Feb. 2017.
- [16] Peacock, A.J. (2000) *Handbook of Polyethylene: Structures, Properties, and Applications*. New York City, New York: Marcel Dekker, Inc.
- [17] Fu, Y., Chen, W., Pyda, M., Londono, D., Annis, B., Boller, A., Habenschuss, A., Cheng, J., Wunderlich, B. (1996). Structure-Property Analysis for Gel-Spun, Ultrahigh Molecular Mass Polyethylene Fibers. *Macromolecule Science Physics*, B35(1), 37-87.
- [18] Mahendrasingham, A., Blundell, D. J., Wright, A. K., Urban, V., Narayanan, T., Fuller, W., (2004). Time resolved WAXS/SAXS observations of crystallization in oriented melts of ultra high molecular weight polyethylene. *Polymer*, 45, 5641-5652.
- [19] Hsieh, Y. L., Hu, X. P., (1997). Structural Transformation of Ultra-High Modulus and Molecular Weight Polyethylene Fibers by High-Temperature Wide-Angle X-Ray Diffraction. *Journal of Polymer Science Part B, Polymer Physics*, Vol.35, Issue 4, pp. 623–630.
- [20] Govaert, L. E., & Lemstra, P. J. (1992). Deformation behavior of oriented UHMW-PE fibers *Experimental A) Materials B) Techniques*, 464, 455–464.
- [21] Tashiro, K., Sasaki, S., & Kobayashi, M. (1996). Structural Investigation of Orthorhombic-to-Hexagonal Phase Transition in Polyethylene Crystal : The Experimental Confirmation of the Conformationally Disordered Structure by X-ray Diffraction and Infrared / Raman Spectroscopic Measurements, 9297(96), 7460–7469.

- [22] Drawing of PE. Digital image. N.p., n.d. Web. 5 Mar. 2016.
- [23] Hu, W., & Buzin, A. (2003). Annealing behavior of gel-spun polyethylene fibers at temperatures lower than needed for significant shrinkage. *Journal of Polymer Science Part B, Polymer Physics*, Vol. 41, Iss 4, pp 403-417.
- [24] Smook, J., Pennings, J. (1984). Influence of draw ratio on morphological and structural changes in hot-drawing of UHMW polyethylene fibres as revealed by DSC. *Colloid & Polymer Science*, 262(9), 712–722. doi:10.1007/BF01451543
- [25] Kwon, Y. K., Boller, A., Pyda, M., Wunderlich, B., (2000). Melting and heat capacity of gel-spun, ultra-high molar mass polyethylene fibers. *Polymer*, 41, 6237-6249.
- [26] Ratner, S., Weinberg, A., Wachtel, E., Moret, P. M., Marom, G., (2004). Phase Transitions in UHMWPE Fiber Compacts Studied by in situ Synchrotron Microbeam WAXS. *Macromolecules Rapid Communications*, 25, 1150-1154.
- [27] Yeh, J. T., Lin, S. C., Tu, C. W., Hsie, K. H., Chang, F. C., (2008). Investigation of the drawing mechanism of UHMWPE fibers. *Journal of Material Science*, 43, 4892-4900.
- [29] Spells, S. J., Coutry S., (2007). Mixed Crystal Infrared Spectroscopy of Uniaxially Drawn Polyethylene Films. *Applied Spectroscopy*, Vol 61 No 3.
- [29] Kausch, H. H. (Hans-Henning). *Polymer Fracture*. Berlin: Springer, 1987. Print.
- [30] "Dyneema® Fact Sheets." *Issuu*. N.p., n.d. Web. 14 Feb. 2017.
<https://issuu.com/eurofibers/docs/name8f0d44>
- [31] Lee, S., Rutledge, G. C., (2011). Plastic Deformation of Semicrystalline Polyethylene by Molecular Simulation. *Macromolecules*, 44, 3096-3108.
- [32] Yeh, I. C., Andzelm, J. W., Rutledge, G. C., (2015). Mechanical and Structural Characterization of Semicrystalline Polyethylene under Tensile Deformation by Molecular Dynamics Simulations. *Macromolecules*, 48, 4228–4239.
- [33] Coussens, B., van der Werff, H., (n.d.). Molecular modeling of chain pullout and scission for oriented polyethylene. Internal DSM Research report.
- [34] O'Connor, T. C., Andzelm, J. W., Robbins, M. O., (2016). AIREBO-M: A reactive model for hydrocarbons at extreme pressures. *The Journal of Chemical Physics* 142, 024903.

- [35] O'Connor, T. C., Robbins, M. O., (2016). Chain Ends and the Ultimate Strength of Polyethylene Fibers. *ACS Macro Letters*, 5, 263-267.
- [36] Wasiak, A., Sajkiewicz, P. (1993). Orientation distributions and melting behaviour of extended and folded-chain crystals in polyethylene. *Journal of Materials Science*, 28, 6409–6417.
- [37] Uehara, H., & Kanamoto, T. (1996). Real-Time X-ray Diffraction Study on Two-Stage Drawing of Ultra-High Molecular Weight Polyethylene Reactor Powder above the Static Melting Temperature, 1540–1547.
- [38] Keller A. (1994). An approach to the formation and growth of new phases with application to polymer crystallization : effect of finite size , metastability , and Ostwald ' s rule of stages. *Journal of Materials Science*, 29, 2579–2604.
- [39] Painter, Paul C. *Essentials of Polymer Science and Engineering*. Lancaster PA: DEStech Publications, 2009. Print.
- [40] Vincent, Julian F. V. *Structural Biomaterials*. Princeton: Princeton UP, 2012. Print.
- [41] Schnabel, Wolfram. *Polymer Degradation*. N.p.: n.p., 1981. Print.
- [42] Hsieh, C. Y., Nagarajan, S., & Zee, R. H. (1992). Infrared thermographic analysis of polymer composites during ballistic impact. *Review of Scientific Instruments*, 63(4), 2296. <http://doi.org/10.1063/1.1143153>
- [43] Prevorsek, D. C., Kwon, Y. D., Chin, H. B., (1994). Analysis of the Temperature Rise in the Projectile and Extended Chain Polyethylene Fiber Composite Armor During Ballistic Impact and Penetration. *Polymer Engineering and Science*, Vol. 34, No. 2. pp. 141-152.
- [44] Sanborn, B., Dileonardi, A.M., Weerasooriya, T.: Tensile properties of Dyneema SK76 single fibers at multiple loading rates using a direct gripping method; ARL-TR-6974; U.S. Army Research Laboratory: Aberdeen Proving Ground, MD, (June 2014).
- [45] Hudspeth, M., Nie, X., & Chen, W. (2012). Dynamic failure of Dyneema SK76 single fibers under biaxial shear/tension. *Polymer*, 53(24), 5568–5574. <http://doi.org/10.1016/j.polymer.2012.09.020>
- [46] Smook, J., Hamersma, W., & Pennings, A. J. (1984). The fracture process of ultra-high strength polyethylene fibres. *Journal of Materials Science*, 19(4), 1359–1373. <http://doi.org/10.1007/BF01120049>

- [47] Forster A. L., Forster A. M., Chin J. W., Peng JS, Lin CC, Petit S., Kang KL, Paulter, N, Riley M., Rice K. D., Al-Sheikhly, M. Long-term stability of UHMWPE fibers. *Polymer Degradation and Stability*; 114 45-51, April 2015.
<http://dx.doi.org/10.1016/j.polymdegradstab.2015.01.028>
- [48] Meulman, J. H., Werf, H. Van Der, Chabba, S., & Vunderink, A. (n.d.). Ballistic performance of Dyneema® at elevated temperatures. Internal DSM Research report.
- [49] Kim, J. H.; Heckert, A. N.; Leigh, S. D.; Rhorer, R. L.; Kobayashi, H; McDonough, W. G.; Rice, K. D.; Holmes, G. A. Statistical Analysis of PPTA Fiber Strengths Measured Under High Strain-rate Condition. *Composites Science and Technology* 2014, 98, 93–99.
- [50] Kim, J. H.; Heckert, N. A.; McDonough, W. G.; Rice, K. D.; Holmes, G. A. Single Fiber Tensile Properties Measured by the Kolsky Bar Using a Direct Fiber Clamping Method. In *Proceedings of Society for Experimental Mechanics Conference*, Lombard, IL, 3–5 June 2013.
- [51] Kim, J. H.; Heckert, N. A.; Leigh, S. D.; Kobayashi, H.; McDonough, W. G.; Rice, K. D.; Holmes, G. A. Effects of Fiber Gripping Methods on the Single Fiber Tensile Test: I. Non-Parametric Statistical Analysis. *Journal of Materials Science* 2013, 48, 3623–3673.
- [52] Chen, Weinong W., and Bo Song. *Split Hopkinson (Kolsky) Bar: Design, Testing and Applications*. New York: Springer, 2011. Print.
- [53] Zukas, Jonas A., Theodore Nicholas, Hallock F. Swift, Longin B. Greszczuk, and Donald R. Curran. *“Impact Dynamics”*. John Wiley & Sons. Web. 24 Aug. 2016.
- [54] Ramesh, K.T. (2008). High Strain Rate and Impact Experiments. In Sharpe, William N. , *Springer Handbook of Experimental Solid Mechanics* (Ch 33). New York: Springer.
- [55] Fakirov S., Krasteva B. On the Glass Transition Temperature of Polyethylene as Revealed by Microhardness Measurements, *Journal of Macromol. Sci-Phys.*, B39(2), 297-301 (2000).
- [56] Lin, S. P.; Han, J. L.; Yeh, J. T.; Chang, F. C.; Hsieh, K. H. Surface Modification and Physical Properties of Various UHMWPE Fiber Reinforced Modified Epoxy Composites. *Journal of Applied Polymer Science* 2007, 104, 655–665.

- [57] Umberger, P. D. Characterization and Response of Thermoplastic Composites and Constituents. Master's thesis, Virginia Polytechnic Institute and State University, Blacksburg, VA, 2010.
- [58] Russell, B. P; Karthikeyan, K.; Deshpande, V. S.; Fleck, N. A. The High Strain-rate Response of Ultra High Molecular Weight Polyethylene: From Fibre to Laminate. *International Journal of Impact Engineering* 2013, 60, 1–9.
- [59] Schwartz, P., Netravali, a., & Sembach, S. (1986). Effects of Strain Rate and Gauge Length on the Failure of Ultra-High Strength Polyethylene Fibers. *Textile Research Journal*, 56(8), 502–508. <http://doi.org/10.1177/004051758605600807>
- [60] Cochran, S.; Galvez, F.; Pintor, A.; Cendon, D.; Rosello, C.; Sanchez-Galvez, V. Characterization of Fraglight Non-Woven Felt and Simulation of FSP's Impact In It; R&D 8927-AN-01; Universidad Politecnica de Madrid (Spain) Escuela Tecnica Superior de Intenieros de Caminos, 2002; ADA408250.
- [61] Dijkstra, D., Prass, E., & Pennings, A. (1998). Temperature-dependent fracture mechanisms in gel-spun hot-drawn ultra-high molecular weight polyethylene fibres. *Polymer Bulletin*, 311, 305–311.
- [62] Huang, W., Wang, Y., & Xia, Y. (2004). Statistical dynamic tensile strength of UHMWPE-fibers. *Polymer*, 45(11), 3729–3734. <http://doi.org/10.1016/j.polymer.2004.03.062>
- [63] Languerand, D. L., Zhang, H., Murthy, N. S., Ramesh, K. T., Sansoz, F., (2009). Inelastic behavior and fracture of high modulus polymeric fiber bundles at high strain-rates. *Materials Science and Engineering A*, 500, 216-224.
- [64] Holmes, G. A., Kim, J. H., McDonough, W. G., Riley, M. A., Rice, K. D., (2009). A detailed investigation of the mechanical properties of polybenzoxazole fibers within soft body armor. *Journal of Material Science*, 44(14):3619-3625.
- [65] Holmes, G. A., Kim, J. H., Ho, D. L., McDonough, W. G., (2009). The role of folding in the degradation of ballistic fibers. *Polymer Composites*, Vol. 31, Issue 5, pp. 879–886.
- [66] McDonough, W. G., Kim, J. H., Liu, D. W., Kobayashi, H., Leigh, S. D., Forster, A. L., Rice, K. D., Holmes, G. A., (n.d.). Measuring the properties of ballistic fibers using two methods. NIST internal report.

- [67] Jenket II, D. R., Forster, A. M., Paulter Jr., N. G., Weerasooriya, T., Gunnarsson, C. A., Al-Sheikhly, M. (2016). An Investigation of the Temperature and Strain-Rate Effects on Strain-to-Failure of UHMWPE Fibers. In Antoun, B., Arzoumanidis, A., Qi, H. J., Silberstein, M., Amirkhizi, A., Furmanski, J., and Lu. H. Challenges in Mechanics of Time Dependent Materials, Volume 2: Proceedings of the 2016 Annual Conference on Experimental and Applied Mechanics (pp. 23-33). Cham: Springer International.
- [68] Bragg-Brentano Geometry. Digital image. N.p., n.d. Web. 10 Sept. 2015.
- [69] Gulmine, J. ., Janissek, P. ., Heise, H. ., & Akcelrud, L. (2002). Polyethylene characterization by FTIR. *Polymer Testing*, 21(5), 557–563.
[http://doi.org/10.1016/S0142-9418\(01\)00124-6](http://doi.org/10.1016/S0142-9418(01)00124-6)
- [70] Watanabe, S., Noda, I., Hu, Y., Ozaki, Y., (2007). Thermally induced conformational disordering process in high-density polyethylene crystal studied by generalized two-dimensional correlation mid-infrared spectroscopy. *Polymer*48, 6632-6638.
- [71] ASTM Standard C1557-03, 2008, “Standard Test Method for Tensile Strength and Young’s Modulus of Fiber,” ASTM International, West Conshohocken, PA, (2008).
- [72] Gafurov U. G., Novak I. I. *Polymer Mechanics* 6/1, 160-161 (1972).
- [73] Gulmine, J. V., Janissek, P. R., Heise, H. M., Akcelrud, L., (2003). Degradation profile of polyethylene after artificial accelerated weathering. *Polymer Degradation and Stability*, 79, 385-397.
- [74] Tavares, A. C., Gulmine, J. V., Lepienski, C. M., Akcelrud, L., (2003). The effect of accelerated aging on the surface mechanical properties of polyethylene. *Polymer Degradation and Stability*, 81, 367-373.
- [75] Kupper, L., Gulmine, J. V., Janissek, P. R., Heise, H. M., (2004). Attenuated total reflection infrared spectroscopy for micro-domain analysis of polyethylene samples after accelerated ageing withing weathering chambers. *Vibrational Spectroscopy*, 34, 63-72.
- [76] Mahdavi, H., Nook, M. E., (2008). Characterization and Microstructure Study of Low-Density Polyethylene by Fourier Transform Infrared Spectroscopy and

- Temperature Rising Elution Fractionation. *Journal of Applied Polymer Science*, Vol 109, 3492-3501.
- [77] Griffith A. A: *Phil. Trans. Roy. Soc.* 221, 163 (1921).
- [78] Williams M. L.: *Fracture of Solids*, D. C. Drucker and J. J. Gilman, eds. New York: Inter-science. 1963, p. 157.
- [79] Knauss: *Appl. Mechanics Rev.*, January 1973, p. 1.
- [80] Sauer J. A., Pae K. D.: *Colloid a. Polymer Sci.* 252, 680-695 (1974).
- [81] Dickie R. A., Smith T. L.: *J. Polymer Sci., A-2*, 7, 687 (1967).
- [82] Govaert, L., Brown, B., Smith, P., (1992). Temperature Dependence of the Young's Modulus of Oriented Polyethylene. *Macromolecules*, 25, 3480-3483.
- [83] Marko, J.F.; Eric D. Siggia (1995). "Stretching DNA". *Macromolecules*. 28: 8759–8770. Bibcode:1995MaMol..28.8759M. doi:10.1021/ma00130a008
- [84] Smith Jr., K. J., Wang, J., (1999). The breaking strength of imperfect (real) polymer fibers. *Polymer*, 40, 7251-7260.
- [85] Zhurkov S., Korskov V. E., (1974). *Journal of Polymer Science Physical Edition*, 122:385.
- [86] Dijkstra, D. J., Torfs J. C. M., Pennings A. J. (1989). *Colloid and Polymer Science*, 267:866.
- [87] Savitskii A. V., Gorshkova, I. A., Demicheva V. P, Frolova, I. L., Shimikk, G. N., (1984). *Polymer Science USSR*, 26:2007.
- [88] Govaert, L. E., Peijs, T. (1995). Tensile strength and work of fracture of oriented polyethylene fibre. *Polymer*, Vol 36, No 23.
- [89] Boyd, R. H., Gee, R. H., Han, J., Jin, Y., (1994). Conformational dynamics in bulk polyethylene: A molecular dynamics simulation study. *The Journal of Chemical Physics*, 101, 788.
- [90] McDaniel, P. B., Deitzel, J. M., & Gillespie, J. W. (2015). Structural hierarchy and surface morphology of highly drawn ultra high molecular weight polyethylene fibers studied by atomic force microscopy and wide angle X-ray diffraction. *Polymer*, 69, 148–158. <http://doi.org/10.1016/j.polymer.2015.05.010>